THE EFFECT OF PHYSICAL MOLECULAR FEATURES ON COMPLEX COACERVATION PHASE SEPARATION

BY

TYLER LYTLE

DISSERTATION

Submitted in partial fulfillment of the requirements
for the degree of Doctor of Philosophy in Chemistry
in the Graduate College of the
University of Illinois at Urbana-Champaign, 2019

Urbana, Illinois

Doctoral Committee:

Professor Nancy Makri, Chair
Assistant Professor Charles E. Sing, Director of Research
Associate Professor Joaquín Rodríguez-López
Professor Kenneth S. Schweizer

ABSTRACT

Complex coacervation is an associative liquid-liquid phase separation of oppositely-charged polyelectrolytes in aqueous salt solution. This phase separation is sensitive to chemical and physical molecular features making it attractive for a large number of applications. However, precisely tuning the phase behavior using specific chemistries is difficult, but physical molecular features, such as chain length, architecture, and chain polarity, can be used to precisely tune the phase behavior. To understand the link between phase separation and these molecular features, a copious amount of theoretical modeling of complex coacervates has been performed using a number of approaches such as Voorn-Overbeek theory, polymer field theory, counterion condensation and release, and liquid state theories. While these theories have given physical insights into coacervation, most of these approaches are not applicable to polymers with a high charge density, which is the relevant limit for most synthetic polyelectrolytes, and are difficult to extend to length scales associated with charge-driven self-assembly.

My work has led to the development of a transfer matrix theory that captures how molecular features affect complex coacervation in the high charge density limit. This theoretical approach maps the 3-dimensional system to a 1-dimensional adsorption model, and solves this 1-dimensional adsorption model using a transfer matrix approach. Inputs to the theory are determined using Monte Carlo simulation. Qualitative matching with simulation and experimental results is achieved for bulk phase separation. In order to capture how salt valency, chain stiffness, and chain architecture influence coacervation, this theory is modified using physically-motivated arguments. Results from these modifications suggest a combinatoric entropy gain is a driving force for coacervation. This means the presence of many different polyelectrolyte chains in the coacervate phase allows for a large number of ways for

them to adsorb onto each other causing an increase in entropy.

Additionally, precise charge sequence effects can be captured using this transfer matrix theory. Initial simulations demonstrated that the periodicity of the charge sequence affects counterion entropy gain, which is the entropy counterions gain upon being released from a polyelectrolyte. Chains with longer runs of charged monomers increasingly localize counterions compared to chains with shorter runs of charged monomers, resulting in an increased entropy gain upon coacervation. This observation is used to modify the transfer matrix theory to capture these trends in qualitative agreement with simulation and experiment. Further investigation of more charge sequences demonstrated that charge fraction, average length and relative positions of charged monomer 'runs' all influence coacervation phase behavior; this suggests precise charge sequence is a powerful method for designing coacervating systems.

Since this transfer matrix theory is a useful description of coacervation phase behavior, I use it to understand interfacial properties of coacervates. This importantly sets the foundation for understanding self-assembly driven by complex coacervation. Theoretic interfacial profiles showed qualitative matching with coarse-grained molecular dynamics simulations. Interfacial tension, interfacial width, and the interfacial excess of salt are calculated showing that adding salt to the system decreases the interfacial tension allowing the interfacial width to increase with a small concentration of salt adsorbing to the interface. Addition of a neutral polymer species drastically alters the phase separation behavior and interfacial properties due to the excluded volume interaction of this species. Morphological phase diagrams for coacervate-forming block copolymers are determined using a single chain in a mean field simulation, which show structures seen in neutral block copolymer systems. Large concentrations of salt and polymer can induce the formation of coexisting morphologies. Additionally, transitions from disorder to order upon addition of salt are observed.

The theoretical approach I have developed is broadly able to capture how physical molecular features affect coacervation phase behavior in the high charge density limit, and can be used to understand coacervate-driven self assembly. This theory is also capable of capturing the effect of monomer-level charge sequence effects, and a number of other ways to tune the phase behavior. This work provides a foundation to start considering more complex

sequence-defined coacervate systems, such as mixtures of sequence-defined polyelectrolytes and systems which undergo hierarchal self-assembly.

ACKNOWLEDGMENTS

This dissertation would not be possible without the guidance and support from a number of people. My advisor, Charles Sing, provided an environment in which I learned a large amount of science, specifically polymer physics. His mentoring helped me develop into a capable researcher.

My doctoral committee has provided important feedback throughout my graduate career, which I am grateful to have received. When the Sing research group first started, it was composed of 3 graduate students, including myself, and a postdoc. Michael Marvin provided support regarding simulation procedures. Mithun Radhakrishna helped me transition to researching complex coacervation. Kate Dahlke gave advice on many decisions that needed to be made throughout my graduate career. I would like to thank these 3 people for providing the foundation for this work. As time progressed the Sing research group became larger, and less senior graduate students have provided stimulating scientific discussions.

I would like to thank Dr. Todsapon Thananatthanachon and Dr. Gifford Brown for their tremendous impact on me during my undergraduate career. The first professor I performed research for was Todsapon, and this experience convinced me that I wanted to pursue scientific research as a career. Gifford is the reason I chose to become a double major in chemistry and physics, and allowed me to perform a couple of condensed matter physics projects with him.

I am grateful to my family and friends for their support throughout my graduate career. My mom, Cindy Lytle, has always been willing to do what she can to help me. Ben Fritch has provided me with friendship since we first met in our undergraduate careers. My wife, Brianna Lytle, has always supported me, and provided an incredible amount of knowledge about mathematics.

TABLE OF CONTENTS

CHAPTER 1

INTRODUCTION

Complex coacervation is a type of liquid-liquid phase separation, which has uses in a large number of applications in both synthetic and natural systems. This is due to the large number of ways to modulate the phase behavior by either tuning the polymer and salt chemistry or altering physical molecular features, such as chain length, architecture, and chain polarity. Physical molecular features are a controlled way to alter coacervation, and in order to understand these features, a large number of theoretical investigations have been performed to understand coacervation phase behavior. However, these methods are largely inadequate to describe the limit of high polymer charge density, which is present in most synthetic polyelectrolytes. The work in this dissertation describes a theoretical approach informed by coarse-grained molecular simulation to understand how physical molecular features alter coacervation in the limit of high charge density.

1.1 Complex Coacervation and Typical Phase Behavior

Complex coacervation is a macroscopic phase separation of oppositely-charged macromolecules is salt solutions [1, 2]. This phase separation forms a coacervate phase which contains most of the macromolecules in coexistence with a supernatant phase containing few of the macromolecules [2, 3]. Both phases contain salt and solvent, but the concentrations do not have to be equal in the phases [4, 5]. Usually, as the concentration of salt in the system is increased, the extent of phase separation, or the coacervate phase macromolecule concentration, decreases until the critical salt concentration, beyond which phase separation no longer occurs [1, 2]. Coacervate-forming systems investigated in this dissertation contain oppositely-charged polyelectrolytes in aqueous salt solutions.

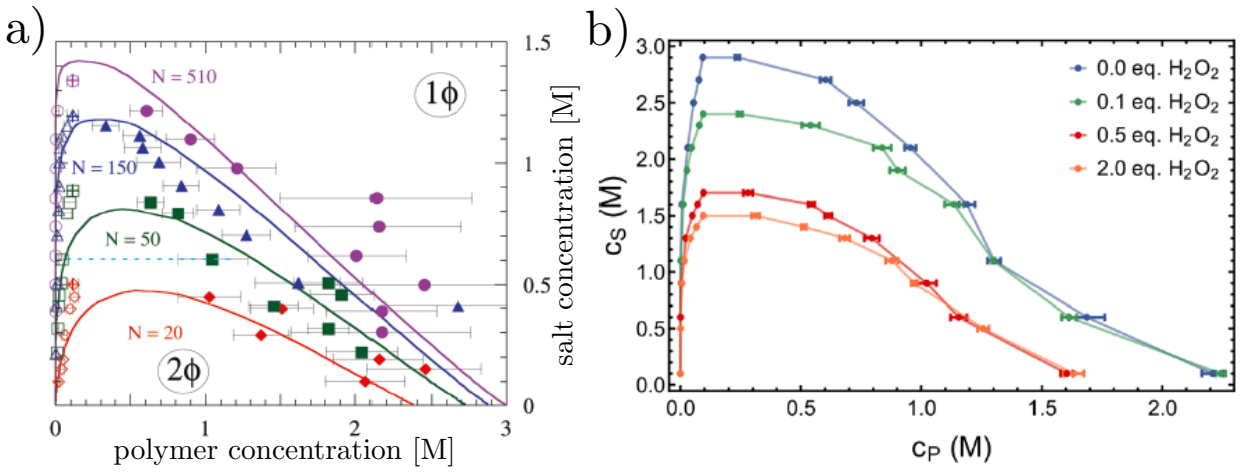

Figure 1.1: Example phase diagrams demonstrating how physical molecular features affect coacervation phase behavior. a) Reprinted with permission from [1]. Copyright 2010 American Chemical Society. The 2Φ region is where phase separation occurs, 1Φ is the region where the system is miscible. As the polymer length N is increased the phase separation region increases. b) Reproduced with permission from [6], which is available at https://pubs.acs.org/doi/abs/10.1021%acscentsci.8b00964. For further permissions related to the excerpted material should be directed to the ACS. Polymer concentrations, c_P, and salt concentrations, c_S, underneath the points phase separate. As salt is added to the system, the extent of phase separation decreases, until the critical salt concentration beyond which no phase separation is seen. Adding H_2O_2 increases the polymer polarity and decreases the phase separation region.

Typically, these systems contain a polycation and a polyanion species in an aqueous solution of monovalent cations and anions. Phase separation usually occurs at small concentrations of polymer and salt [1,4–6]. In the limit of no salt, the concentration of polyelectrolyte in the coacervate phase is at a maximum, and, as the salt concentration increases, the concentration of polyelectrolyte in the coacervate phase is decreased. At a certain concentration of salt, known as the critical salt concentration, the system no longer phase separates and is miscible [1,2]. The salt concentration in the coacervate phase is generally smaller than the concentration in the supernatant phase, but at extremely small overall salt concentration this salt partitioning can invert [4,5].

This phase behavior can be manipulated using a large number of parameters. Experimentally, polyelectrolyte and salt chemistry have been shown to alter the extent of phase separation [1,4,5,7]. The critical salt concentration tends to decrease with salt identity following a Hoffmeister series and increased salt valency [3,8]. Altering polyelectrolyte chemistry to

include short-range interactions, such as hydrophobicity and hydrogen-bonding, usually increases the extent of phase separation [1, 9]. However, precisely controlling coacervate phase behavior via alteration of chemical details remains difficult.

Alternatively, coacervation phase behavior can be modified by varying physical molecular features. Experiments have shown that chain length (Figure 1.1a), architecture, and polymer polarity (Figure 1.1b) alter the phase behavior in a controlled manner [1,6,10]. As the length of the polyelectrolyte chain increases, the translational entropy decreases, which stabilizes the chains in the coacervate phase [1]. Replacing linear polyelectrolyte chains with comb chains results in a decreased extent of coacervation [10], and increasing polymer polarity decreases the phase separation region [6]. In addition to chain length, architecture, and chain polarity, the polyelectrolyte charge sequence alters the phase behavior, which biological systems prevalently use to modulate a coacervate-like liquid-liquid phase separation [11, 12]. Since phase diagrams are available for experimental systems (a couple of examples are shown in Figure 1.1), we will calculate phase diagrams, using simulation and theory, as the main observable to understand coacervation phase behavior for a number of physical molecular features.

1.2 Industrial Applications of Complex Coacervation

Due to a number of useful properties, coacervation is prevalent in industrial applications. Since coacervation occurs without organic solvents or the need for extreme temperatures, it is useful for the food industry as an encapsulation motif [13–17]. Coacervates are usually formed at the interface between water and oil in emulsified systems, which thickens the interface and stabilizes the emulsion against flocculation [13, 17]. These microcapsules can be ruptured by mastication, or the coacervate phase can be dissovled via pH changes such as the acidic environment in the stomach [13,14,16,17]. Encapsulated agents include flavors [17], probiotics [16, 17], and aromas [14, 17].

In addition to being useful for food applications, coacervates are used in a number of cleaning applications [18–21]. Initial formulations contain concentrations of the species to make the system miscible, and, upon dilution with water, the concentration decreases into

the immiscible region and phase separation occurs [18–21]. These coacervates allow oils to be emulsified for cleaning applications [18–21] and can deliver complimentary agents for the application, such as fabric softener for laundry detergent [19]. Shampoos formulated with coacervates are able to deposit the coacervate onto hair, which can mend split-ends and improve wet combing [21].

1.3 Active Research on Coacervate Materials

1.3.1 Coacervation as a Self-Assembly Motif

A number of investigations have used coacervation as a way to drive self-assembly of block copolymers. Systems of diblock copolymers, polycation-neutral and polyanion-neutral, or triblock copolymers, polycation-neutral-polycation and polyanion-neutral-polyanion, form disordered, spherical micelles, body-centered cubic phases, and hexagonal packing phases, as well as a coexistence between a body-centered cubic phase and disordered micelles, shown in Figure 1.2a and b [22]. However, the polymer and salt concentrations over which these morphologies are stable depend on the number of blocks in the copolymer [22]. A more thorough investigation of the micelle phases revealed that the diblock copolymer can form dilute micelles at small polymer concentration, which can become jammed at a larger polymer concentration, shown in Figure 1.2b [23]c. At even larger polymer concentrations, the micelles order into a cubic lattice (Figure 1.2c) [23]. Triblock copolymers exhibit a different evolution of micelle phases upon increasing polymer concentration: a phase-separated gel phase, a percolated gel phase, and a cubic lattice of micelles (Figure 1.2c).

Similar to industrial applications, these block copolymers are used to encapsulate various agents, as shown in Figure 1.2d, and subsequently release the encapsulated agent when the environment changes, due to addition of salt or pH changes [24,25]. These coacervate systems are particularly attractive for protein encapsulation, because the protein does not become denatured upon encapsulation [26, 27]. The gel phases formed by triblock copolymers can encapsulate charged cargo,shown in Figure 1.2d, which can subsequently be released upon environmental changes, such as an increase in salt concentration [23, 24]. Gelation gives the

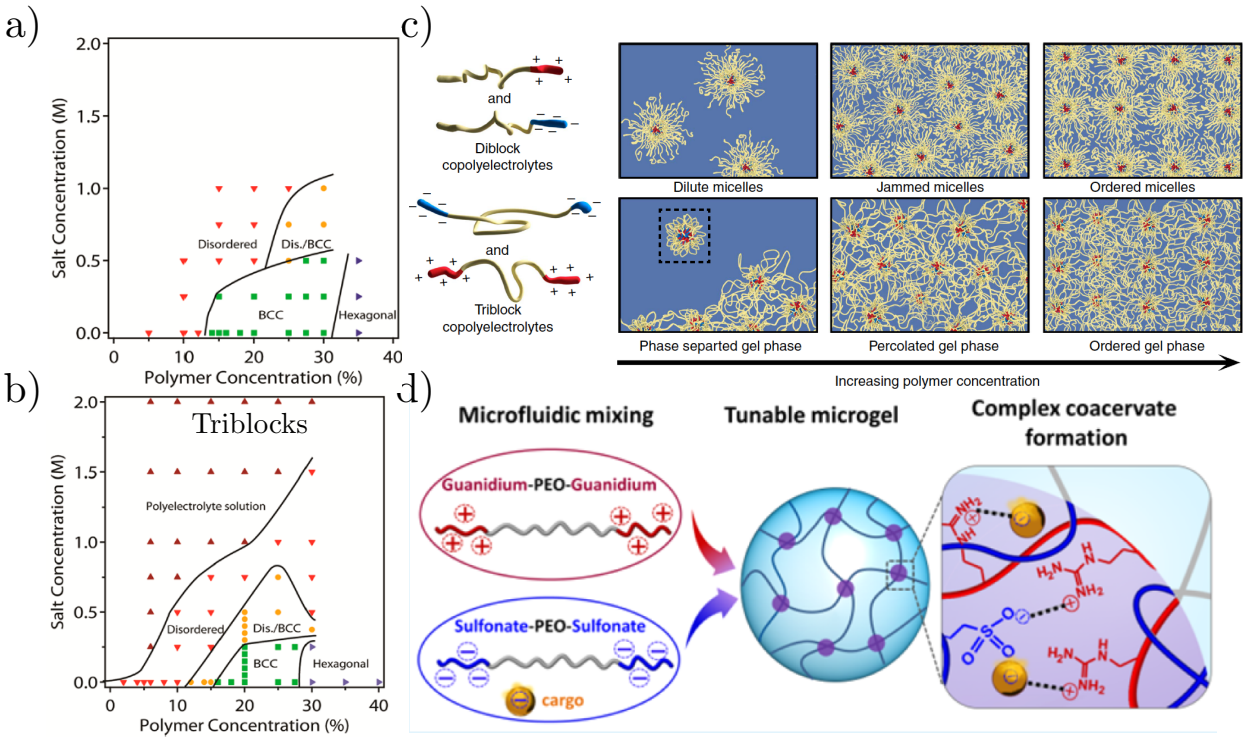

Figure 1.2: Examples of coacervate-driven block copolymer self-assembly. a) Reprinted with permission from [22]. Copyright 2014 ACS. Example diblock copolymer phase diagram showing disordered spherical micelles, body-centered cubic (BCC), and hexagonally packed phases, as well as a coexistence between BCC and disorderd micelles. b) Reprinted with permission from [22]. Copyright 2014 ACS. Example triblock copolymer phase diagram showing the same phases for the diblock in a), but at different salt and polymer concentrations. Additionally, the polyelectrolyte solution phase is a homogeneous mixture of the constituent components. c) Reproduced with permission from [23] under Creative Commons Attribution 4.0 International License, https://creativecommons.org/licenses/by/4.0/. Both diblock and triblock copolymers can form micelles, but triblocks can form a percolated gel phase before forming an ordered phase of micelles as a function of polymer concentration. d) Reprinted with permission from [24]. Copyright 2016 ACS. Example of a self-assembled triblock gel which encapsulates a charged cargo. Triblock copolymers form gels which are physcially crosslinked by the coacervate domains. These gels can dissolved upon addition of salt, allowing the cargo to be released.

.

self-assembled system more mechanical stability, and the physical crosslinks formed by the coacevating domains allow the gel to dissolve upon environmental changes [24].

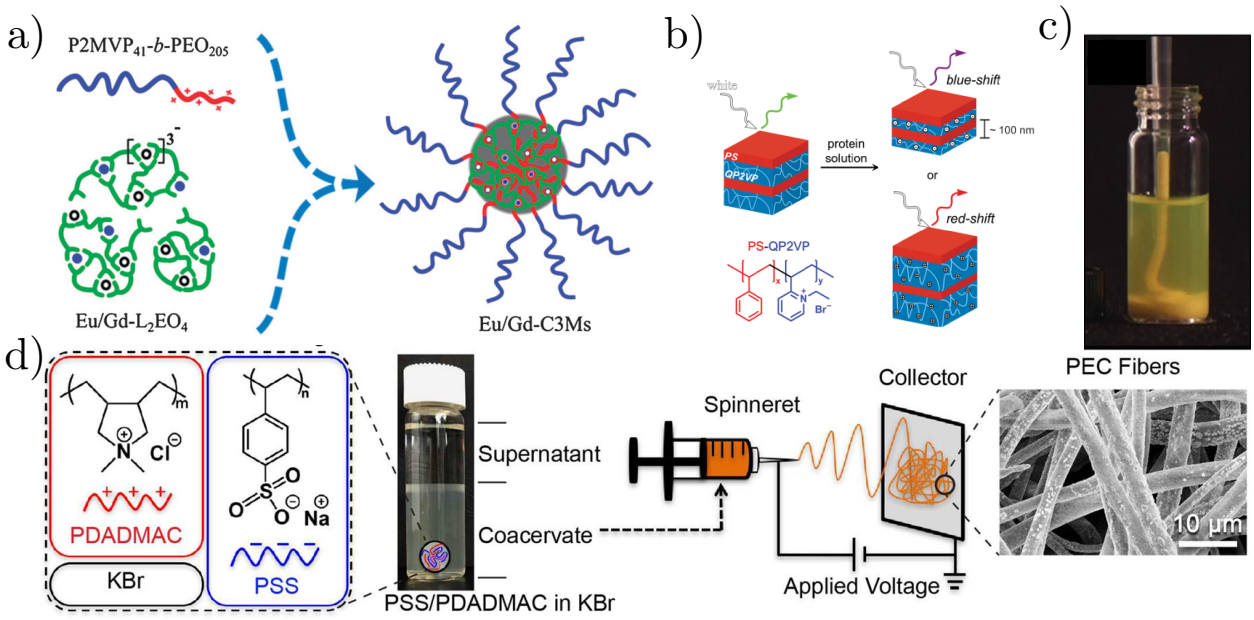

Figure 1.3: Example applications of coacervates. a) Reproduced from [28] with permission from the Royal Society of Chemistry. Example of a multimodal probe formed from a cationic-neutral block copolymer and an anion coordination polymer formed from coordination of europium(III) and gadolinium(III). The complex coacervate-core micelle allowed precise control of the ratio of metal ions to one another, which allows the probe to be tuned. b) Reprinted with permission from [29]. Copyright 2014 ACS. A cationic-neutral block copolymer was used to form a lamellar structure, which can form a coacervate upon addition of a protein. This coacervation can cause the lamellar spacing to shrink or swell depending on the protein properties. c) Reprinted from Advances in Colloid and Interface Science, Vol. 167, R. J. Stewart, C. S. Wang, and H. Shao, Complex coacervates as a foundation for synthetic underwater adhesives, Pages 85-93, Copyright 2011 with permission from Elsevier. [30]. An underwater adhesive made from a coacervate-forming system maintains a liquid-like structure in water, which allows it to wet a surface instead of beading up. d) Reprinted with permission from [31].Copyright 2017 American Chemical Society. A coacervate can be used to electrospin fibers in an aqueous solution of unentangled polymers, and the resulting fibers require no further crosslinking for stability.

1.3.2 Sensors from Self-Assembled Coacervate Systems

Self-assembled structures are also useful for sensing applications. A couple of demonstrative examples are multimodal probes and a protein sensor [28, 29, 32–34]. Multimodal probes are probes capable of being used for multiple measurement techniques simultaneously and can be formed from a diblock copolymer and a coordination polymer, which form a coacervate-core micelle (see Figure 1.3a) [28, 32, 34]. The coordination polymer is formed via coordination

of transition and lanthanide metal ions, which are active for a number of measurement techniques [28, 32, 34]. Using this approach, precise control of the ratio of the metal ions is achieved allowing alteration of the measured response [28,32]. A protein sensor was designed using coacervate-forming block copolymers in a lamellar morphology (see Figure 1.3b) [29]. This morphology has a spacing between lamellae sheets equal to a visible wavelength of light, and, upon addition of a protein solution, this spacing shrinks or expands depending on the charge of the protein [29]. Changing the lamellae spacing results in a change in the wavelength of light scattered, which allows visible light spectroscopy to determine the charge of a protein solution [29].

1.3.3 Coacervate as Underwater Adhesives and for Electrospinning

Not only are coacervates useful for electrospinning but also useful for underwater adhesives. It has been hypothesized that the adhesive secreted by the Sandcastle worm is formed, at least in part, by complex coacervation, and this observation has been used to develop underwater adhesives [30,35]. Coacervate-based adhesives exhibit the ability to wet a surface in water instead of beading up, shown in Figure 1.3c, [35] and could potentially be used as medical adhesive for tissue repair [30].

In addition to block copolymer applications, coacervation has been used for electrospinning, shown in Figure 1.3d [31, 36]. Coacervation provides a way to electrospin unentangled polymers in an aqueous solution [31, 36]. This also circumvents the need to chemically-crosslink the as-spun fibers, because the polyelectrolytes are physically crosslinked due to electrostatic interactions [31, 36]. Without organic solvents, the resulting fiber mat is benign and could potentially be used for tissue engineering scaffolds [31, 36].

1.4 Biological Uses of Complex Coacervation

Coacervates are not only used in synthetic systems, but also by natural processes, as shown in Figure 1.4. Intrinsically disordered proteins (IDPs) are proteins which have no definite structure and tend to have few hydrophobic groups, but an abundance of polar and charged

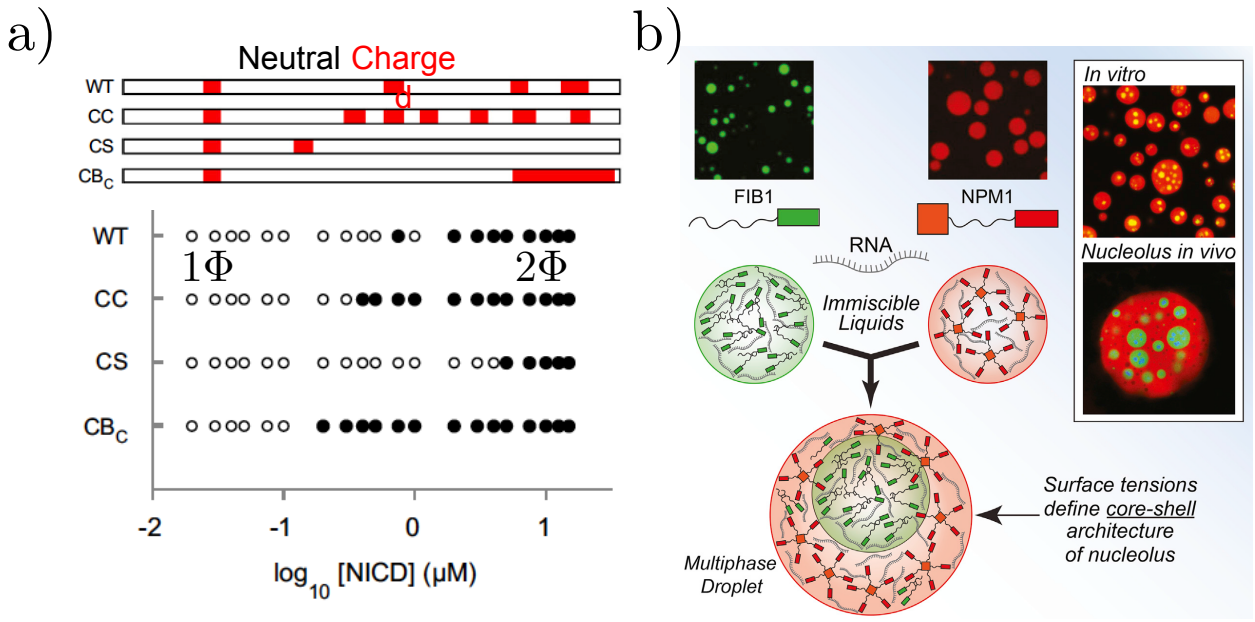

Figure 1.4: Biological analogues of complex coacervation. a) Reprinted from Molecular Cell, Vol 63, C. W. Pak, M. Kosno, A. S. Holehouse, S. B. Padrick, A. Mittal, R. Ali, A. A. Yuyus, D. R. Liu, R. V. Pappu, and M. K. Rosen, Sequence determinants of intracellular phase separation by complex coacervation of a disordered protein, Copyright 2016 with permission from Elsevier. [37]. 4 IDPs with different charge sequences (white is neutral and red is charged in top plot) exhibited different phase separation behavior, which demonstrates the effect of charge sequence on coacervation phase behavior. 1Φ is the miscible region (open symbols in bottom plot), and 2Φ is the phase separating region (closed symbols in bottom plot). b) Reprinted from Cell, Vol 165, M. Feric, N. Vaidya, T.S Harmon, M.M. Mitrea, L. Zhu, T.M. Richardson, R.W. Kriwacki, R.V. Pappu, and C.P. Brangwynne, Coexisting liquid phases underlie nucleolar subcompartments, Copyright 2016 with permission from Elsevier. [38]. Example membraneless organelle formed by coacervation of intrinsically disordered proteins (IDPs) with RNA. Subcompartments are liquid, and allow sequestration of active components without loss of function. Additionally, these function as nanoreactors capable of spatially and temporally regulating reactions.

groups [39–45]. It has been shown that these IDPs undergo a liquid-liquid phase separation similar to coacervation, which is dependent on the precise charge sequence of the IDP, shown in Figure 1.4a [39–45]. The sequence can be altered to encode the desired phase behavior, such as a lower critical solution temperature or an upper critical solution temperature phase behavior [41], and IDPs can form membraneless organelles upon coacervation [37, 46–62].

Commonly, IDPs interact with RNA to form membraneless organelles, shown in Figure 1.4b, which is a self-assembled structure with distinct subcompartments without the use of

membranes [37, 46–62]. This type of liquid-liquid phase separation is an active process that can respond to environmental stresses meaning subcompartments can be quickly formed and dissolved if required [48]. Upon coacervation, constituent components can be sequestered and concentrated, which allows reactions to occur without another regulatory event [46, 48]. These reactions can possibly change the concentration of involved species, which could alter the equilibrium phase behavior such that the subcompartment becomes miscible providing a method to temporally regulate reactions [63]. Photo-active molecules, catalytic nanoparticles, enzymes, and other active agents can be encapsulated in these subcompartments without loss of function [47, 54]. Additionally, these subcompartments can support protein refolding and facilitate the recovery of secondary structure [54].

Membraneless organelles formed by coacervation between different IDPs can form hierarchal structures depending on the amino acid sequence of each IDP [56]. IDPs with similar amino acid sequences can form a well-mixed coacervate, but, if the amino acid sequences are different, a layered, core-shell structure can be formed [56]. However, if the molecular weight of IDPs with different amino acid sequences is decreased, a well-mixed coacervate can be formed [56]. This type of hierarchal structure is not limited to membraneless organelles formed from IDPs, but also present in membraneless organelles formed from IDPs and RNA [64]. Mixing non-base pairing RNA can result in the formation of core-shell type structures, which were also observed by varying the mixing ratio of IDPs in the investigated system [64].

In order to design systems with desired phase behaviors, an understanding of how physical molecular features affect coacervation phase behavior is needed, because this understanding can guide how parameters are chosen for a specific application. Additionally, harnessing the previously discussed sequence dependent behaviors observed in biological systems with synthetic polymer systems, requires an understanding of how molecular-level charge sequence affects phase separation behavior. This could aid the design of synthetic systems able to perform complex tasks as discussed for membraneless organelles.

1.5 Theoretical Descriptions of Coacervation Phase Behavior

Complex coacervation is the subject of a large number of theoretical investigations employing a range of theoretical formalisms. Each of these theoretical formalisms has a certain range of applicability as a function of polyelectrolyte charge density, the fraction of monomers which are charged, and length scale. Initially, Voorn-Overbeek theory [65, 66] (Section 1.5.1) was used to describe coacervation phase behavior, but neglects charge correlations due to chain connectivity and the finite size of the charges, which affect phase behavior [67]. Chain connectivity correlations can be incorporated by using field theoretic techniques (Section 1.5.3), which can capture coacervation behavior in the small charge density limit, but describing self-assembly length-scales is difficult [68–79]. In the high charge density limit, coacervation might be described using counterion condensation and release (Section 1.5.4), but there are few theoretical descriptions that incorporate this information. Alternatively, liquid-state theory (Section 1.5.5) can be used to describe coacervation in the high charge density limit, but requires the use of an approximate closure relationship [80], and is difficult to use for self-assembly length scales. Thus, a theoretical description capable of describing coacervation in the high charge density limit and at longer length scales is needed.

1.5.1 Voorn-Overbeek Theory

The initial theoretical description of coacervation is Voorn-Overbeek theory [65,66,81], which defines the free energy of mixing as:

$$\frac{a^3 F}{V k_B T} = \sum_i \frac{\phi_i}{N_i} \ln \phi_i + \sum_i \sum_{j>i} \chi_{ij} \phi_i \phi_j - \alpha \left[\sum_i \sigma_i \phi_i \right]^{\frac{3}{2}} \tag{1.1}$$

where a^3 is the size of a monomer, V is the volume, k_B is Boltzmann's constant, and T is temperature. The first term is the Flory-Huggins mixing entropy of all species (polycation, polyanion, cation, anion,and water) where ϕ_i is the volume fraction of the ith species, and N_i is the degree of polymerization of this species with polymers having a degree of polymerization of N and non-polymeric species having a degree of polymerization of 1. Nonelectrostatic

interactions, such as Van der Waals and hydrophobicity, between species i and j are captured in the second term with an interaction strength of χ_{ij}, the Flory chi parameter. This parameter is usually positive and promotes phase separation between species i and j.

Electrostatic interactions are modeled using a Debye-Hückel approximation shown in the third term of Equation 1.1. σ_i is the charge density of species i, and α is the electrostatic interaction parameter:

$$\alpha = \frac{1}{12\pi}\left(\frac{e^2}{\epsilon_r \epsilon_0 k_B T}\right)^{\frac{3}{2}} \sqrt{\frac{1}{a^3}} \tag{1.2}$$

$$= \frac{2}{3}\sqrt{\pi}\left(\frac{l_B}{a}\right)^{\frac{3}{2}} \tag{1.3}$$

where e is the charge of an electron, ϵ_r is the relative dielectric constant, and ϵ_0 is the vacuum permittivity. Equation 1.3 rewrites this electrostatic interaction parameter in terms of a Bjerrum length, l_B. The Bjerrum length, $l_B = e^2/\left(4\pi\epsilon\epsilon_0 k_B T\right)$, is the separation between charged species at which the electrostatic interaction strength is equal to the thermal energy. These electrostatic interactions drive coacervation phase behavior in this theoretical model.

The free energy expression in Equation 1.1 is used to determine the phase coexistence by equating the electrochemical potentials, $\mu_i^\alpha = \mu_i^\beta + q_i\psi$, of each species i with charge q_i in the supernatant, β, and coacervate, α, phases [1, 66]. ψ is the electrical potential difference between the two phases, which allows calculation of phase coexistence in systems with nonstoichiometric ratios of polycations to polyanions. If this ratio is stoichiometric, the electric potential goes to 0 and the expression for chemical potential is recovered.

Phase diagrams from this theory have been calculated in both the polymer charge density-polymer volume fraction plane [66], in the limit of 0 salt concentration, and the salt volume fraction-polymer volume fraction plane [1, 65, 66]. This theory shows that as the molecular weight of the polyelectrolyte chains increases, the critical polymer charge density decreases and the volume fraction of polymer in the coacervate phase increases, because the total number of charges in the system is increasing [66]. Additionally, as the salt concentration increases, the concentration of polymer in the coacervate decreases, such that coacervation occurs at relatively small values of polymer and salt concentration [1, 65, 66]. This theory

predicts a slight excess of salt in the coacervate phase compared to the supernatant [1,65,66]. Investigations of nonstoichiometric ratios of polyelectrolytes revealed that as the asymmetry between the polyelectrolytes increases, the phase separating region decreases, due to an increased electric potential between phases [66].

1.5.2 Limitations of Voorn-Overbeek Theory

This theory can be used to fit experimental phase diagrams using χ_{ij} and σ_i as fitting parameters [1] . Usually, a χ parameter is introduced between the polyelctrolyte and water species to model hydrophobic interactions. σ_i is usually assumed to be the valency of the salt species, and is adjusted to fit the data for the polyelectrolyte species [1]. In addition to these 2 parameters, the sizes of the various species in the system have been used to fit experimental data. E. Spruijt, et. al. used a as a fitting parameter that was the same for all species [1]. An alternative procedure was used by P.K. Jha, et. al., which defined the size of a water molecule, and normalized the sizes of the non-water species by this value [3]. This was used to model how different salt species alter the phase separation behavior [3].

Even though this theory is capable of matching experimental phase diagrams, it does have a number of limitations. Chain connectivity is not explicitly included in this model, which will cause additional correlations between charges on polyelectrolyte chains due to being constrained to the chain [67]. Explicit excluded volume is also not included, which will limit the number of ways the charges can be arranged [67]. By neglecting both of these correlations a fortuitous cancellation of errors occurs, because chain connectivity causes an increase in the immiscible region and explicit excluded volume causes a nearly commensurate decrease in the immiscible region [67]. Treatment of the electrostatic interactions by the Debye-Hückel limiting law means the electrostatic interactions are only accurate at very small charge concentrations (<0.01 M) [3]. Replacing the electrostatic interaction term in Equation 1.1 by extended Debye-Hückel theory, which accounts for the finite size of an ion, does allow treatment of slightly larger charge concentrations, but these concentrations are still smaller than those typically observed for coacervate systems [3].

1.5.3 Field Theoretic Models of Complex Coacervation

A number of investigations have attempted to improve Voorn-Overbeek theory by capturing correlations using polymer field theory [68–79]. As an instructive example, consider a system composed of n_{P+} polycations and n_{P-} polyanion that each have a degree of polymerization N in aqueous solution of n_W water particles with n_+ cations and n_- anions. The canonical partition function for this system is:

$$Z_c \propto \prod_{i=1}^{n_{P+}+n_{P-}} \int \mathcal{D}\boldsymbol{r}_{p,i} \prod_{j\neq P+,P-}^{\alpha} \prod_{k=1}^{n_\alpha} \int d\boldsymbol{r}_k \exp\{-U_0\left(\boldsymbol{r}^{(n_{P+}+n_{P-})N}\right) - U_D\left(\boldsymbol{r}^{(n_{P+}+n_{P-})N+n_++n_-+n_W}\right) - U_{ES}\left(\boldsymbol{r}^{(n_{P+}+n_{P-})N+n_++n_-}\right)\} \tag{1.4}$$

where $\beta = 1/\left(k_B T\right)$. The integral over $\mathcal{D}\boldsymbol{r}_\alpha$ means the functional integration is performed for the positions of all the monomers in each chain α.

U_0 is the bonding potential for the polymer given by:

$$U_0\left(\boldsymbol{r}^{(n_{P+}+n_{P-})N}\right) = \frac{3k_BT}{2a^2} \sum_{\alpha}^{n_{P+}+n_{P-}} \int_0^N ds \left|\frac{d\boldsymbol{r}_\alpha\left(s\right)}{ds}\right|^2 \tag{1.5}$$

for a continuous, Gaussian chain. Nonelectrostatic interactions, U_D, are defined as:

$$U_D\left(\boldsymbol{r}^{(n_{P+}+n_{P-})N+n_++n_-+n_W}\right) = \frac{v_0 k_B T}{2} \int d\boldsymbol{r} \sum_i \sum_j \chi_{ij} \hat{\rho}_i\left(\boldsymbol{r}\right) \hat{\rho}_j\left(\boldsymbol{r}'\right) \tag{1.6}$$

where $\hat{\rho}_i\left(\boldsymbol{r}\right)$ is the density operator for species i at position $\boldsymbol{r}$. Electrostatic interactions are modeled using:

$$U_{ES}\left(\boldsymbol{r}^{(n_{P+}+n_{P-})N+n_++n_-}\right) = \frac{k_BT}{2} \int\int d\boldsymbol{r} d\boldsymbol{r}' \hat{\rho}_c\left(\boldsymbol{r}\right) \frac{l_B}{\left|\boldsymbol{r}-\boldsymbol{r}'\right|} \hat{\rho}_c\left(\boldsymbol{r}'\right) \tag{1.7}$$

where $\hat{\rho}_c\left(\boldsymbol{r}\right)$ is the microscopic charge density, which is defined as:

$$\hat{\rho}_c\left(\boldsymbol{r}\right) = \hat{\rho}_+ + \sigma\hat{\rho}_{P+} - \hat{\rho}_- - \sigma\hat{\rho}_{P-}. \tag{1.8}$$

This electrostatic interaction is dependent on the Bjerrum length.

This particle-based model can be converted to a field-based model via Hubbard-Stratonovich transformations [82] by the introducing chemical potential fields, ω, density fields, ϕ, and an electrostatic potential field, ψ which allow interactions to depend on field variables rather than particle positions [75, 76, 82]. Applying this transformation to Equation 1.4 results in the partition function:

$$\mathcal{Z}_c = \int \mathcal{D}\psi \prod_i \int \mathcal{D}\omega_i \int \mathcal{D}\phi_i \exp\left(-\mathcal{H}\left[\{\psi\}, \{\omega_i\}, \{\phi_i\}\right] / k_B T\right) \tag{1.9}$$

where $\mathcal{H}\left[\{\psi\}, \{\omega_i\}, \{\phi_i\}\right]$ is the Hamiltonian given by:

$$\begin{aligned}
\mathcal{H}\left[\{\psi\}, \{\omega_i\}, \{\phi_i\}\right] = & -n_{P+} \ln Q_{P+}\left[\omega_{P+}, \psi\right] - n_{P-} \ln Q_{P-}\left[\omega_{P-}, \psi\right] \\
& - n_+ \ln Q_+\left[\omega_+, \psi\right] - n_- \ln Q_-\left[\omega_-, \psi\right] - n_W \ln Q_W\left[\omega_W\right] \\
& + \rho_0 \int d\boldsymbol{r} \left[\frac{1}{2} \sum_i \sum_j \chi_{ij} \phi_i\left(\boldsymbol{r}\right) \phi_j\left(\boldsymbol{r}\right) - \sum_i \omega_i\left(\boldsymbol{r}\right) \phi_i\left(\boldsymbol{r}\right)\right. \\
& \left. + \sum_i q_i \phi_i\left(\boldsymbol{r}\right) \psi\left(\boldsymbol{r}\right) - \frac{\left|\nabla \psi\left(\boldsymbol{r}\right)\right|^2}{8\pi l_B}\right].
\end{aligned} \tag{1.10}$$

This formalism contains the same information as the partition function in Equation 1.4, but has a number of advantages compared to the particle-based model. Interactions are not pairwise and dependent on the particle positions, and Q_i is the single molecule partition function, which defines how each species interacts with the fields in the system [75, 76, 82]. Additionally, electrostatic interactions are no longer long-ranged $1/r$ potentials, but depend on the square gradient of the ϕ field [75, 76, 82]. Even with these advantages, this field-based partition function is not analytically solvable, but a number of approaches have been developed to use this partition function to study the thermodynamic behavior of coacervate-forming systems.

One approximation scheme for Equation 1.9 is the mean-field approximation, which assumes that only the most probable field configuration is needed to describe the system behavior [75, 76, 82]. This field configuration, denoted by ω_i^*, ϕ_i^*, and ψ^*, corresponds to

a saddle-point in the Hamiltonian, which is calculated by taking functional derivatives of Equation 1.10 with respect to each field and setting them equal to 0. The mean field partition function can be defined as $\mathcal{Z}_c^{MF} \approx \exp\left(-\mathcal{H}\left[\psi^*, \omega_i^*, \phi_i^*\right]/k_BT\right)$ [82]. However, this approach predicts no phase separation for these systems, because the positive charge density field exactly cancels the negative charge density field [70, 75, 76]. By assuming only 1 field configuration is needed, density fluctuations that could result in non-charge neutral configuration are ignored, and these configurations are needed to cause electrostatic interactions which drive coacervation [70, 75, 76].

A standard method to incorporate Gaussian-level fluctuations is the random phase approximation (RPA) [82]. Fields are written with the form $\phi_i(\boldsymbol{r}) = \phi_i^* + \delta\phi_i(\boldsymbol{r})$, and conversion to Fourier space, $\delta\phi_i(\boldsymbol{r}) = (2\pi)^{-3}\int d\boldsymbol{k}\delta\phi_i(\boldsymbol{k})\exp(i\boldsymbol{k}\cdot\boldsymbol{r})$ allows the partition function to be written as:

$$\mathcal{Z}_c^{RPA} \propto \mathcal{Z}_c^{MF}\int \mathcal{D}\delta\psi \prod_i \int \mathcal{D}\delta\omega_i \int \mathcal{D}\delta\phi_i \exp\left[\frac{1}{2k_BT}\sum_{j,l}\int \frac{d\boldsymbol{k}}{(2\pi)^3}\Omega_j(\boldsymbol{k})\boldsymbol{M}_{jl}(\boldsymbol{k})\Omega_l(\boldsymbol{k})\right] \tag{1.11}$$

where $\Omega_j(\boldsymbol{k}) = (\delta\omega_k, \delta\phi_k, \delta\psi)$ and $\boldsymbol{M}_{jl}(\boldsymbol{k}) = \delta^2\mathcal{H}/(\delta\Omega_j\delta\Omega_l)$. Since this is a second-order expansion, the integrals are Gaussian and can be evaluated over the non-density field variables, which gives:

$$\mathcal{Z}_c^{RPA} \propto \prod_i \int \mathcal{D}\delta\phi_i \exp\left(\frac{1}{2k_BT}\sum_{j,l}\int \frac{d\boldsymbol{k}}{(2\pi)^3}\delta\phi_j(\boldsymbol{k})S_{jl}^{-1}(\boldsymbol{k})\delta\phi_l(\boldsymbol{k})\right) \tag{1.12}$$

where $S_{jl}^{-1}(\boldsymbol{k})$ is the inverse structure factor.

This structure factor gives information about how the field fluctuations affect the mean field free energy at a length scale $\boldsymbol{k}$, and these fluctuations occur due to particles interacting through intermolecular potentials or through intramolecular potentials, such as the bonding potential [70, 75, 76]. Phase stability can also be analyzed using the structure factor. If the inverse structure factor is positive for all $\boldsymbol{k}$, phase separation does not occur [70]. At $\boldsymbol{k} = 0$, macrophase separation is predicted if $S_{jl}^{-1}(\boldsymbol{k}) < 0$, and microphase separation can be

predicted if $S_{jl}^{-1}(\boldsymbol{k}) < 0$ for $\boldsymbol{k} \neq 0$ [70].

Even though the RPA expansion is able to capture coacervation phase behavior, M. Castelnovo, et. al. demonstrated that fluctuations included beyond the RPA level can impact the resulting phase behavior [70]. Including fluctuations beyond the RPA level can be accomplished by modifying the inverse structure factor to depend on the field fluctuations, which is known as a 1-loop expansion [70]. This modification allowed the transition between segregative polymer phase separation and associative polymer phase separation to be determined [70]. Segregative phase separation occurs when the polymers phase separate into 2 phases: 1 phase contains most of the polycation and 1 phase contains most of the polyanion. Associative phase separation is coacervation phase behavior.

Even though these expansions are able to capture coacervation phase behavior, a number of complications need to be addressed. RPA and 1-loop expansion are numerically more expensive to implement than the mean field approximation, and using these expansions for inhomogeneous systems, such as block copolymers, is challenging [68, 74–76]. A technique that attempted to overcome these limitations is the embedded self-consistent mean field technique [68]. Using the observation that only fluctuations in the electrostatic potential are necessary to qualitatively capture coacervation behavior, this technique uses the 1-loop electrostatic interaction potential in the mean field approximation to combine the efficiency of the mean field approximation with the driving force for coacervation from fluctuating field theory methods [68]. This technique was used to model coacervate-driven block copolymer self assembly, and achieved qualitative matching with experimentally-determined phase diagrams [68].

Another limitation of these expansion techniques is the limit of systems with high charge density [70]. In principle, expansions could be performed to include fluctuations beyond the Gaussian-level, but this increases the numerical cost of these types of calculations. As an alternative to an increasing number of expansion terms, the full partition function in Equation 1.9 can be utilized in a field theoretic simulation [82]. Monte Carlo simulations are performed to evolve the fields according to the partition function, and the continuous integrals are usually approximated as a sum on a grid [82]. All field configurations can be sampled using this technique, but applications to polymers with high charge density are

lacking. Since the correlations for these polyelectrolytes are on small length scales, the grid discretization needs to be small, but this increases the computational cost. Additionally, these simulations usually smear the charge along the polymer backbone, which may affect the predicted phase behavior [77].

1.5.4 Counterion Condensation and Release

Heretofore theoretical descriptions of coacervation have assumed that electrostatic interactions drive the phase separation, but experimental investigations suggest coacervation is driven by an increase in entropy upon phase separation, particularly for polymers with a high charge density, and is due to counterion condensation and release [11, 83–87]. To minimize the effective charge density along a polyelectrolyte chain, salt ions will adsorb onto the chain [88]. If an oppositely-charged chain is present, the adsorbed salt ions will be replaced by the polyelectrolyte, because the polyelectrolyte translational entropy is less than the salt ions, and this results in the salt ions gaining translation entropy, which drives the phase separation [11, 83–86].

Theoretical models incorporating counterion condensation and release into Voorn-Overbeek and random phase approximation based models have been developed by treating counterion condensation and release as a series of reaction equilibria describing ion binding between the various species, as well as including the autodissociation of water [6, 89, 90]. The equilibrium constants are experimentally determined, and used to calculate a free energy contribution [6, 89, 90]. Theoretically-determined phase diagrams show at least qualitative agreement with experimentally-determined phase diagrams [6, 89, 90]. While this model includes counterion condensation and release, the relation between molecular features, counterion condensation and release, and phase behavior is not direct.

1.5.5 Liquid State Theory

A different approach to coacaervation has been liquid state theory. This theory uses the Ornstein-Zernike Equation [80]:

$$\hat{h}_{ij}(\boldsymbol{k}) = \hat{c}_{ij}(\boldsymbol{k}) + \sum_{l} \phi_l \hat{c}_{il}(\boldsymbol{k}) \hat{h}_{lj}(\boldsymbol{k}) \tag{1.13}$$

where $\hat{h}_{ij}(\boldsymbol{k})$ is the total correlation function between species i and j. $\hat{c}_{ij}(\boldsymbol{k})$ is the direct correlation function due to species i interacting with species j [80]. The second term in Equation 1.13 is a convolution between the total correlation function and the direct correlation function, and captures indirect correlations [80]. Indirect correlations occur when species i directly interacts with species l, and species l interacts either directly or indirectly with species j [80]. These correlation functions can be used to calculate thermodynamic information such as chemical potentials and pressures [80].

The Ornstein-Zernike Equation has 2 unknown variables, $\hat{h}_{ij}$ and $\hat{c}_{ij}$, and requires another Equation linking these 2 variables, which is known as the closure relationship, which can alter the accuracy of calculated thermodynamic properties [80]. A number of different closure relationships exist that depend on the particular system under investigation, and choosing an accurate closure is not straightforward [80]. However, several investigations have utilized liquid state theory to examine coacervate phase behavior.

Application of Equation 1.13 to polymer systems is known as polymer reference interaction site model, which has been applied to coacervate systems [67]. This investigation demonstrated that the salt partitioning such that the salt concentration in the supernatant is larger than the salt concentration in the coacervate, which is also seen in experimental systems [67]. This was attributed to the increased excluded volume in the coacervate phase due to the polymer [67]. Excluded volume and chain connectivity correlations were explored, which demonstrated that errors incurred due to neglecting these correlations cancel, and contribute to how Voorn-Overbeek fits experimental data [67]. Additionally, this theoretical approach suggested a counterion condensation and release mechanism for coacervation [67].

An alternative approach used Equation 1.13 to calculate the excess free energy for a system

of charged hard spheres, and included excluded volume interactions and bonded interactions via perturbation expressions [91, 92]. This theory also qualitatively captured the experimental salt partitioning, but attributed this to a larger exchange chemical potential, which is the free energy change for connecting N small ions, in the supernatant phase compared to the coacervate phase [92]. Since Voorn-Overbeek theory neglects charge connectivity, the exchange chemical potential is 0, which causes a slight excess of salt in the coacervate phase [92]. In addition to salt partitioning, this theory was used to investigate coacervate systems with nonstoichiometric concentrations of polyelectrolytes [91]. This showed that the excess polyion favors the supernatant phase, because the counterions required for charge neutrality have more translational entropy in the supernatant phase compared to the coacervate phase [91].

1.6 My Contributions to Complex Coacervation Modeling

In this dissertation, I focus on systems containing high charge densities, because this is where most theoretical treatments are least valid; yet, most synthetic polyelectrolytes have a high charge density, and this regime is where there is the most opportunity to design at a molecular level. To this end, we have developed a theoretical description of complex coacervation, described in Chapter 2, which treats the polyelectrolyte as a one dimensional adsorption model with a salt ion, a polymer chain, or remaining bare as potential adsorption states for each monomer. This is based on the observation that correlations in coacervating systems with high charge densities are largely local, and between nearest neighbors. Phase diagrams calculated with this theory show nearly quantitative agreement with simulation phase diagrams. Using physically-motivated arguments, this theory is modified to investigate charge spacing and nonstoichiometric mixtures of polyelectrolytes in Chapter 2. Chain stiffness, salt valency, and chain architecture effects are investigated in Chapter 3.

These molecular feature modifications suggest that a combinatorial entropy for having a large number of ways for polymer chains to adsorb onto each other is another driving force for coacervation. Chain stiffness and salt valency both decrease the number of ways for polyelectrolytes to adsorb onto each other, which causes the extent of coacervation to

decrease. Comb polymers alter the entropy gain of salt ions upon counterion condensation and release.

Once a theoretical understanding of the manner in which these molecular features alter the phase behavior has been developed, investigation of how charge sequence affects complex coacervation is undertaken in Chapter 4. Initially, this was investigated using Monte Carlo simulation and comparing to experimental results, which showed charge sequence alters the magnitude of the entropy gain when counterions are released upon coacervation. In order to incorporate this information into the transfer matrix theory, the local electrostatic environment as a function of monomer position is used as an input for the transfer matrix, described in Chapter 5. Phase diagrams thus calculated show nearly quantitative matching with simulation phase diagrams and qualitative matching with experimental results, and reveal the interplay of how charge blockiness, charge fraction, and charged block position affect complex coacervation phase behavior.

Using the information about how molecular features alter macroscopic coacervation phase behavior, we want to understand how these molecular features affect block copolymer self-assembly behavior. The investigations undertaken establish some of the foundation for understanding self-assembly behavior. We use our transfer matrix theory as an input for self consistent field theory in order to calculate interfacial properties in Chapter 6. Comparison with interfacial profiles generated via molecular dynamics simulations showed qualitative agreement. A neutral polymer species is added to the coacervating system, which almost completely segregates into the supernatant phase. This increases the extent of coacervation, increases the interfacial tension, decreases the interfacial width, and increases the amount of salt partitioning to the interface between the two phases. We attribute these changes to the increased excluded volume in the supernatant phase, which results in an increased pressure on the coacervate phase, which causes the coacervate to be more stable.

Initial morphological phase diagrams for coacervate-driven block copolymer self-assembly were determined using the field theory technique theoretically-informed Monte Carlo with an input calculated from particle-based Monte Carlo simulations, described in Chapter 7. We show that at large polymer and salt concentrations a morphological coexistence is observed, and salt can induce transitions from disordered to ordered phases.

CHAPTER 2

MONTE CARLO SIMULATION AND TRANSFER MATRIX THEORY MODEL OF COMPLEX COACERVATION

2.1 Introduction

In this chapter, we develop a Monte Carlo simulation method to determine complex coacervation phase separation. Monte Carlo simulations are used to calculate an excess free energy contribution, which captures all correlations contained in the simulation. The form of this excess free energy is incorporated into a polymer field-theory type free energy to calculate the phase behavior. Resulting phase diagrams are compared to phase diagrams calculated from Gibbs Ensemble Monte Carlo simulations, and show nearly quantitative matching.

In order to further understanding of coacervation phase separation behavior, we develop a transfer matrix theory for determining the phase separation behavior of complex coacervates. A method to map the 3-dimensional simulation to a 1-dimensional adsorption model is presented. This 1-dimensional adsorption model can be solved via a transfer matrix, which allows calculation of the partition function. From the partition function, the free energy can be determined and phase diagrams can be calculated. We show this transfer matrix theory matches simulation results nearly quantitatively, and this theory is modified to examine how charge spacing and nonstoichiometric mixtures affect the coacervation phase behavior.

2.2 Simulation

Our overall approach is to assume a *separation of length scales* between the local, molecular features and the larger length-scale phase separation of complex coacervates. For the local, molecular features we use Monte Carlo (MC) techniques; thermodynamic values can be obtained from these simulations that are then useful at larger length scales. For the larger length-scale phase separation, we use a numerical method to determine the compositions of coexisting phases.

Simulation captures the local structure and correlations without approximation, albeit with non-negligible computational cost. The common limitation with these simulations will be our invocation of the restricted primitive model (RPM) that does not resolve atomistic detail [80, 94]. The RPM treats ions as hard-sphere beads that can be connected to form polyelectrolytes, all of which interact via Coulomb potentials in a continuum medium with the solvent dielectric constant.

Limitations associated with RPM are well-known, [95] such as the neglect of specific ion effects and the nuances of water structure in aqueous systems. This prevents quantitative prediction. RPM simulations also neglect potential variations in the relative dielectric constant, which has been shown to vary at large concentrations of salt or polymer [96–98]. Dielectric constant plays an especially large role in polyelectrolytes in the melt state, [99,100] and can become important in solution [101, 102]. We justify neglecting this possible effect by noting the high concentration of water in typical coacervate systems ($\sim 60 - 80\%$) [1]. Previous RPM simulations have shown reasonable agreement with experimental measurement, [4] to the extent that it is possible to qualitatively match trends due to architecture and sequence.

2.2.1 RPM Model of Coacervation

MC simulations are performed with $N_P \times n_{P+}$ polycation monomers, $N_P \times n_{P-}$ polyanion monomers, n_+ cations, and n_- anions. Each bead is considered as monovalent, and these species are at positions $\mathbf{r}_i^\alpha$, where i is the index specifying the monomer or ion and α

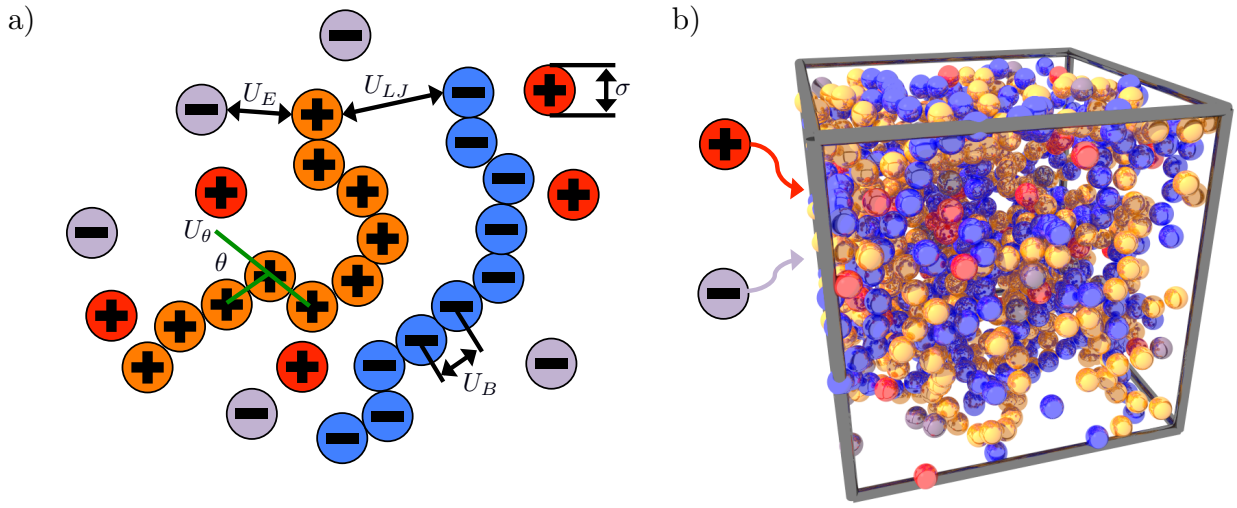

Figure 2.1: (a) Schematic of the simulation model used in this paper. The RPM is used, with all hard-sphere particles of diameter σ and electrostatic interactions between all charged species U_E. Polymers are connected charges with a bonding potential U_B and a bending potential U_θ. (b) Simulation snapshot of a coacervate phase using our model. A method known as Widom insertion measures the energy change associated with adding pairs of charged particles into a simulation box, yielding excess chemical potentials that can be integrated to calculate f_{EXC}.

specifies the type ($P+, P-, +, -$ for polycation, polyanion, cation, and anion). Polycations and polyanions both have degree of polymerization N_P. Water is modeled as an implicit solvent with a relative dielectric constant, $\epsilon_r = 78.5$. See Figure 2.1a for a schematic of our model. All beads have a hard core diameter σ. Monomers and ions are explicit, and contribute to the overall system energy U given by:

$$U = U_{HS} + U_E + U_B + U_\theta + U_{LJ} \tag{2.1}$$

U_{HS} is the hard sphere energy that prevents overlap of the beads:

$$U_{HS} = \sum_{\alpha,\beta} \sum_{i,j} u_{HS}(r_{ij}^{\alpha,\beta}) \tag{2.2}$$

Here, $r_{ij}^{\alpha,\beta} = |\mathbf{r}_i^\alpha - \mathbf{r}_j^\beta|$ is the distance between beads i and j on species α and β, and the individual pair potential u_{HS} is given by:

$$u_{HS}(r_{ij}^{\alpha,\beta}) = \begin{cases} \infty & r_{ij}^{\alpha,\beta} < \sigma \\ 0 & r_{ij}^{\alpha,\beta} \geq \sigma \end{cases} \tag{2.3}$$

U_E is the charged Coulomb potential:

$$U_E = \frac{1}{2} \sum_{\alpha,\beta} \sum_{i,j} \frac{q_\alpha q_\beta}{4\pi\epsilon_0\epsilon_r r_{ij}^{\alpha\beta}} \tag{2.4}$$

where $q^\alpha = z^\alpha e$, the per-bead charge of species α with valency z^α, e is the charge of an electron, and ϵ_0 is the vacuum permitivitty. Ewald summation is used to calculate electrostatic interactions in the simulation. U_B is the bonding potential between beads along the polymer chains:

$$U_B = \sum_{\alpha=P+,P-} \sum_i {}^* u_B(r_{i,i-1}^{\alpha,\alpha}) \tag{2.5}$$

We constrain α to only be along connected polymer chains, and the asterisk in the second summation indicates that we omit terms where $i \bmod N = 0$. The pair potential u_B is given by:

$$u_B(r_{i,i-1}^{\alpha,\alpha}) = \begin{cases} 0 & \Delta\sigma \leq r_{i,i-1}^{\alpha,\alpha} < \Delta\sigma + 0.1\sigma \\ \infty & \text{otherwise} \end{cases} \tag{2.6}$$

Here we can adjust the spacing by a factor of Δ. An angle potential contribution U_θ is applied to the polymer chains:

$$U_\theta = \sum_{\alpha=P+,P-} \sum_i {}^{**} u_\theta(\mathbf{r}_i^\alpha, \mathbf{r}_{i-1}^\alpha, \mathbf{r}_{i-2}^\alpha) \tag{2.7}$$

The double asterisk in the second summation indicates that we omit terms where $i \bmod N = 0$ or 1. The pair potential u_θ is given by:

$$u_\theta(\mathbf{r}_i^\alpha, \mathbf{r}_{i-1}^\alpha, \mathbf{r}_{i-2}^\alpha) = \frac{\kappa_\theta}{2} \theta_{i,i-1,i-2}^2 \tag{2.8}$$

κ_θ is a constant determining the strength of the bond angle potential, and $\theta_{i,i-1,i-2}$ is the angle between the adjacent bond vectors. Dispersive interactions are included via Lennard-Jones potentials given by:

$$U_{LJ} = \frac{1}{2}\sum_{\alpha,\beta}\sum_{i,j}\epsilon_{LJ}\left[\left(\frac{\sigma}{r_{ij}^{\alpha\beta}}\right)^{12} - 2\left(\frac{\sigma}{r_{ij}^{\alpha\beta}}\right)^{6}\right] \tag{2.9}$$

where ϵ_{LJ} is the depth of the Lennard-Jones potential.

For our MC simulations, we use the values $\sigma = 4.25$Å, $T = 298$K, $N_P = 20$, $n_{P-} = n_{P+} = 5$, $\epsilon_{LJ} = 0.25k_BT$, and $\kappa_\theta = 3.3k_BT$, where k_B is the Boltzmann constant. κ_θ is chosen so that the polymer chains are flexible, with an uncharged persistence length of 2.8 beads. We ran multiple simulation box sizes to check that we had no finite box size effects, shown in the right inset of Figure 2.2.

2.2.2 NVT and Gibbs Ensemble MC Simulations

Standard MC techniques are used to simulate coacervates in the constant particle, volume, and temperature (NVT) ensemble [103,104]. Particles in our NVT-ensemble MC simulations undergo random translational movements. The change in U for each particle movement determines whether or not the move is accepted, using the standard Metropolis criterion $p_{acc} = \min[1, \exp(-\Delta U/(k_BT))]$ [103, 104]. These simulations are useful for calculating thermodynamic parameters, in particular the excess chemical potential $\mu_{EXC,i}$ that is the non-ideal portion of the full chemical potential $\mu_i = \mu_{IG,i} + \mu_{EXC,i}$ (where $\mu_{IG,i} = \ln\rho_i$ is the ideal chemical potential for a species i number concentration ρ_i) [80]. This is calculated using Widom insertion, which determines $\mu_{EXC,i}$ using the change in energy associated with random placement of a test particle of type i averaged over all microstates $\{\mathbf{r}\}$ and positions $\mathbf{r}_i^T$ in the system $\mu_{EXC,i} = -k_BT\ln\langle\exp(-\beta\Delta U_{MC})\rangle_{\mathbf{r}_i^T,\{\mathbf{r}\}}$ [103,104]. For $\mu_{EXC,i}$ of polymeric species, we use Widom insertion to place a bead at the end of the chain only, which has been shown to reproduce the appropriate thermodynamics for sufficiently long chains [105, 106]. For both polymer and salt ions, both positive and negative species are inserted jointly or not at all to maintain electroneutrality.

NVT-ensemble calculations are performed [107] for single-phase mixtures of the charged components; however, it is possible for the system to undergo spontaneous phase separation into a polymer deficient and polymer rich phase. To determine the concentrations of salt and polymer where this phase separation will occur, we carry out Gibbs-Ensemble Monte Carlo (GEMC) calculations [104, 108]. GEMC simulations were performed on the same system as in the NVT-ensemble (U given by Equations 2.1-2.9), using standard particle exchange and volume change moves [104, 108]. Polymeric species are assumed to reside in a single box, due to the near-negligible translational entropy associated with moving two oppositely-charged polyelectrolytes into the supernatant phase. This simplifies particle exchange by restricting it to simply the anion and cation species, which undergo a joint particle exchange to maintain electroneutrality in both phases. Figure 2.2 demonstrates the results of a standard GEMC calculation, with a binodal that demarcates a two-phase coacervation region from a one-phase miscible polyelectrolyte solution.

2.2.3 Free Energy Landscapes Calculated From Monte Carlo

We seek to calculate the excess free energy $\mathcal{F}_{EXC}(\phi_S, \phi_P)$ as a function of the volume fractions of salt ϕ_S, and polyelectrolyte ϕ_P in the system. Volume fractions are directly proportional to the number of particles, $\phi_S = 2(\pi\sigma^3 n_S)/(6V)$ and $\phi_P = 2(\pi\sigma^3 n N_P)/(6V)$. $\mathcal{F}_{EXC}(\phi_S, \phi_P)$ can be determined from NVT-ensemble MC calculations, where Widom insertion is used to calculate $\mu_{EXC,i}(\phi_S, \phi_P)$. We note that both $\mu_{EXC,i}$ and $\mathcal{F}_{EXC}$ values obtained from MC simulations are dependent on both the composition of the system as well as the underlying molecular MC model (N_P and U).

It is difficult to access $\mu_{EXC,i}$ in the two-phase coexistence regions of the phase diagram, where Widom insertion would be into one of two coexisting phases leading to a $\mu_{EXC,i}$ that is a linear combination of the value in both phases. We instead desire the value of $\mu_{EXC,i}$ for the unstable homogeneous phase, which is important in heterogeneous polymer systems (for example, polymer interfaces) where the local concentration may pass through these macroscopically unstable states. To obtain these values, we note that the region of complex coacervate coexistence shrinks when N_P is decreased (see e.g. experimental phase

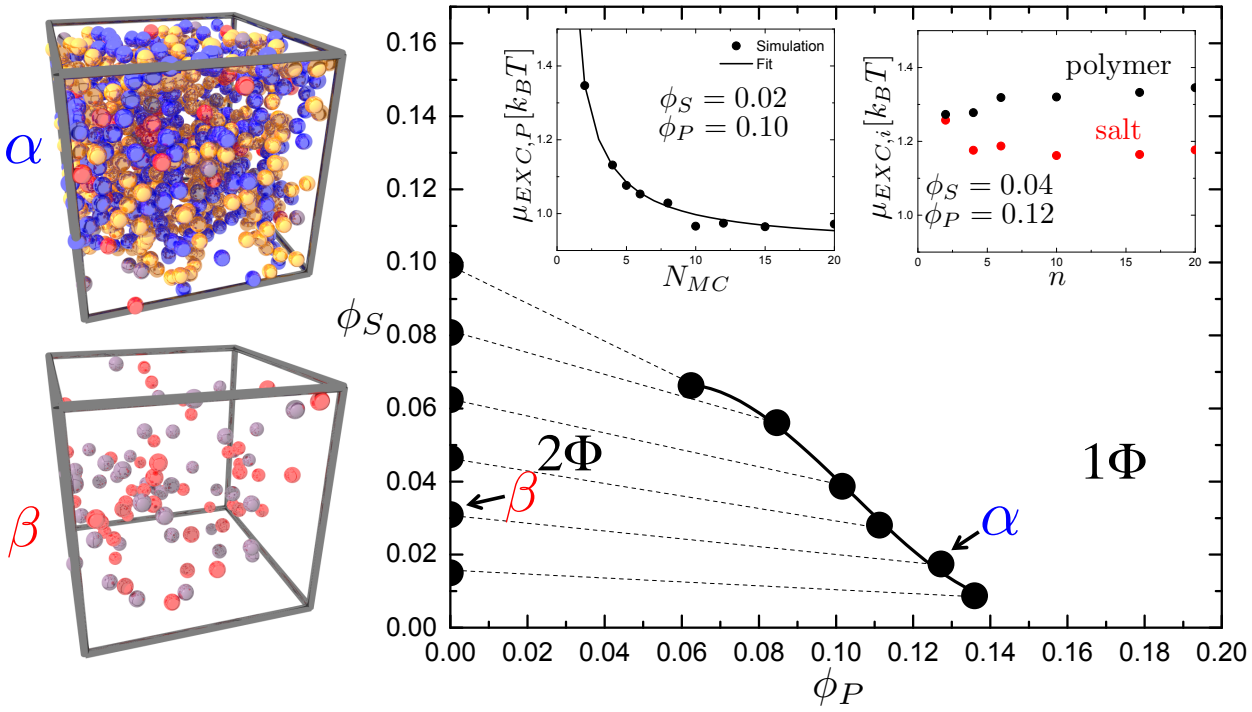

Figure 2.2: GEMC simulation snapshots, demonstrating a polymer-rich α-phase and a polymer deficient β-phase that are in equilibrium. A phase diagram of salt concentration ϕ_S versus polymer concentration ϕ_P shows the binodal curve calculated via GEMC, indicating the points associated with simulation snapshots. Tie lines demonstrate the difference in salt concentration ϕ_S between the coacervate (α) and supernatant (β) phase. (Left inset) Widom insertion can be used to calculate the excess chemical potential of all the species, in this case the polymer ($\mu_{EXC,P}$). In the coexistence region ($\phi_S = 0.02$ and $\phi_P = 0.1$), this is performed at a number of different chain lengths N_P and the value of $\mu_{EXC,P}(N_P)$ is extrapolated to the desired chain length N_P based on equation 2.10. This calculates the value of the excess chemical potential for a *homogeneous* system, which would otherwise be unstable at large N_P. (Right inset) Excess chemical potentials calculated in miscible region ($\phi_S = 0.04$ and $\phi_P = 0.12$) for a number of system sizes (number of polymer chains, $n = n_{P+} + n_{P-}$). Significant deviations from large-n behavior are observed only at very small system sizes $n < 6$.

diagrams [1]). This is primarily due to the increased translational entropy of shorter chains, reflected in the $1/N_P$ contribution to the Flory-Huggins mixing entropy. In principle, excess contributions to the free energy beyond the translational entropy will also change with N_P; however, so long as these interactions are local compared to the chain dimensions, a chain segment far from the chain end will be *independent* of the length of the chain. Thus, the excess contribution to the free energy will only be dependent on N_P via the presence of chain end segments, which see a different environment than mid-chain segments.

Correlation functions for the charged polymer/salt species in the MC simulations (not pictured) demonstrate that correlations are on the order of a few bead radii, reflecting the high salt concentrations considered. The excess chemical potentials $\mu_{EXC,i}$ for both the salt and the polymer thus vary weakly with N_P, with variation primarily related to the number of chain end segments. We postulate the form:

$$\mu_{EXC,i}(N_P) = \mu_{EXC,i}(N_P \to \infty) + \frac{(\mu_{EXC,i}(N_P = 1) - \mu_{EXC,i}(N_P \to \infty))}{N_P} \tag{2.10}$$

The significance of this equation is that we do not need to calculate $\mu_{EXC,i}$ in the coexistence region that is large for large N_P. Rather, it is possible to extrapolate from values of $\mu_{EXC,i}$ calculated at small values of N_P (where the coexistence region is small or nonexistent) to obtain the unstable homogenous state $\mu_{EXC,i}$. We demonstrate this extrapolation in the coexistence 2Φ region, shown in the left inset of Figure 2.2. Indeed, the form of equation 2.10 almost exactly fits *all* values of the excess chemical potential $\mu_{EXC,i}(N_P)$, with only a single fitting parameter $\mu_{EXC,i}(N_P \to \infty)$. Care is taken to extrapolate from low $N_P < 7$ values, which provides enough data to accurately determine the $N_P = 20$ value to match the 1Φ portion of the excess chemical potential calculation.

We note that this calculation is distinctly suited to charge dense coacervates, where high concentrations of the species ($\phi_P, \phi_S \sim 0.1-3$M) lead to highly screened interactions. This is reflected in the insensitivity of the system to box size changes. In the right inset of Figure 2.2, we vary the number n of $N_P = 20$ chains while maintaining the same concentration. The value of $\mu_{EXC,i}$ only deviates significantly at very small box sizes at typical concentrations used in this manuscript. The low charge-density limit may require larger system sizes, but would then be suitable for other field theory approaches [68, 78].

With the values of $\mu_{EXC,i}(\phi_S, \phi_P)$ for both the polymer and ion species, it is possible to reconstruct the free energy from a reference point. We arbitrarily choose our reference point to be $\phi_S^0 = 0.0$ and $\phi_P^0 = 0.0$. An excess free energy density $f_{EXC}(\phi_S, \phi_P) = \mathcal{F}_{EXC}(\phi_S, \phi_P)/V$ is then calculated from these points:

$$f_{EXC}(\phi_S, \phi_P) = \int_{\phi_S^0, \phi_P^0}^{\phi_S, \phi_P^0} \mu_{EXC,S}(\phi_S', \phi_P) d\phi_S' + \int_{\phi_S, \phi_P^0}^{\phi_S, \phi_P} \mu_{EXC,P}(\phi_S, \phi_P') d\phi_P' \tag{2.11}$$

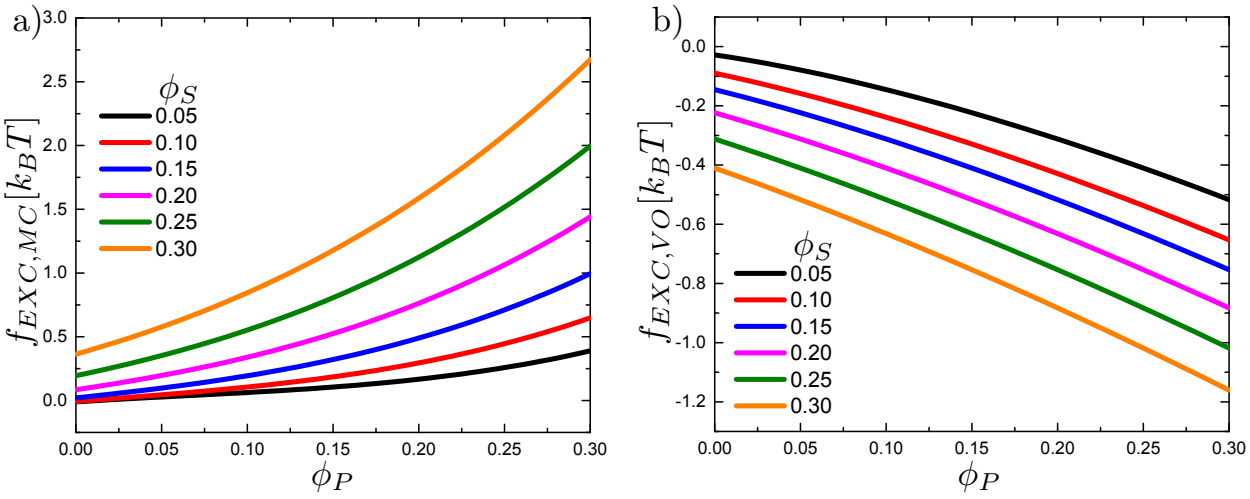

Figure 2.3: (a) Excess free energy landscape $f_{EXC,MC}$ calculated from MC simulations. We note that low values of ϕ_P and ϕ_S shows a region of negative curvature, which drives coacervation. Large ϕ_P and ϕ_S eventually show positive curvature due to the presence of excluded volume interactions. Calculated from Equation 2.11. (b) Excess free energy landscape $f_{EXC,VO}$ predicted by Voorn-Overbeek theory.

Figure 2.3a demonstrates this excess free energy landscape calculated using this method ($f_{EXC,MC}$). We note that this landscape captures both the entropic and energetic contributions to the free energy, with the exception of translational contributions (or conformational, for polymeric species). The value f_{EXC} is thus in the form that is useful for inclusion in field theories.

2.2.4 Numerical MC Technique

In order to determine the coacervation phase diagram, a Flory-Huggins-like theory is developed. The system has an average polymer volume fraction, $\langle\phi_P\rangle$, and an average salt volume fraction, $\langle\phi_S\rangle$. At certain salt and polymer volume fractions, phase separation occurs creating a coacervate phase, denoted as co, with polymer volume fraction, $\phi_{P,co}$, and salt volume fraction, $\phi_{S,co}$. Coexisting with the coacervate phase is a supernatant phase, denoted as su, with polymer volume fraction, $\phi_{P,su}$, and salt volume fraction, $\phi_{S,su}$. Both phases are incompressible with a volume fraction of water given by $\phi_{W,i} = 1 - \phi_{P,i} - \phi_{S,i}$ where i denotes either the coacervate phase or the supernatant phase. The free energy of

the system is

$$F = F_0 + F_{EXC} \tag{2.12}$$

where F_0 is the translational entropy contribution to the overall free energy, and F_{EXC} is the excess free energy contribution. Both F_0 and F_{EXC} are calculated for the phase separated system.

The entropy of mixing is given by

$$\begin{aligned} F_0 = \frac{\Omega}{\langle\phi_P\rangle}\Bigg\{\left[1-\frac{pN_P\langle\phi_P\rangle}{\Omega\phi_{P,co}}\right]\left[\phi_{S,su}\ln\phi_{S,su}+\frac{\phi_{P,su}}{N_P}\ln\phi_{P,su}\ +\phi_{W,su}\ln\phi_{W,su}\right] \\ +\frac{pN_P\langle\phi_P\rangle}{\Omega\phi_{P,co}}\left[\ \phi_{S,co}\ln\phi_{S,co}\ +\frac{\phi_{P,co}}{N_P}\ln\phi_{P,co}+\phi_{W,co}\ln\phi_{W,co}\right]\Bigg\} \end{aligned} \tag{2.13}$$

where Ω is the total number of monomers in the system, and p is the total number of chains in the coacervate phase. The first term describes the entropy of mixing in the supernatant phase, and the second term describes the entropy of mixing in the coacervate phase. $\frac{pN_P\langle\phi_P\rangle}{\Omega\phi_{P,co}}$ gives the ratio of the coacervate phase volume to the total system volume, $1-\frac{pN_P\langle\phi_P\rangle}{\Omega\phi_{P,co}}$ gives the ratio of the supernatant phases's volume to the system's total volume, and $\frac{\Omega}{\langle\phi_P\rangle}$ gives the total number of monomer-equivalent volumes in the system.

The excess free energy contribution is given by:

$$F_{EXC} = \frac{\Omega}{\langle\phi_P\rangle}\left\{\left[1-\frac{pN_P\langle\phi_P\rangle}{\Omega\phi_{P,co}}\right]f_{EXC}(\phi_{P,su},\phi_{S,su})\ +\frac{pN_P\langle\phi_P\rangle}{\Omega\phi_{P,co}}f_{EXC}(\phi_{P,co},\phi_{S,co})\right\} \tag{2.14}$$

where f_{EXC} is the excess free energy density obtained in Equation 2.11.

F is minimized with respect to $\phi_{P,co}$, $\phi_{P,su}$, and $\phi_{S,so}$. p can be calculated using $\langle\phi_P\rangle = \frac{pN_P\langle\phi_P\rangle}{\Omega\phi_{P,co}}\phi_{P,co}+\left(1-\frac{pN_P\langle\phi_P\rangle}{\Omega\phi_{P,co}}\right)\phi_{P,su}$, and $\phi_{S,su}$ can be calculated using $\langle\phi_S\rangle = \frac{pN_P\langle\phi_P\rangle}{\Omega\phi_{P,co}}\phi_{S,co}+\left(1-\frac{pN_P\langle\phi_P\rangle}{\Omega\phi_{P,co}}\right)\phi_{S,su}$. The minimized value of F is compared to the free energy of a homogeneous state, F_{HOM}, given by

$$\begin{aligned} F_{HOM} = \frac{\Omega}{\langle\phi_P\rangle}\Big[\langle\phi_S\rangle\ln\langle\phi_S\rangle+(1-\langle\phi_P\rangle-\langle\phi_S\rangle)\ln(1-\langle\phi_P\rangle-\langle\phi_S\rangle) \\ +\frac{\langle\phi_P\rangle}{N_P}\ln\langle\phi_P\rangle+f_{EXC}(\langle\phi_P\rangle,\langle\phi_S\rangle)\Big]. \end{aligned} \tag{2.15}$$

If the minimized value of F is less than F_{HOM}, the system undergoes phase separation to the concentration values which minimized F.

2.2.5 Relationship to the Voorn-Overbeek Limit

We provide a link to previous theory by directly comparing this work to the Voorn-Overbeek theory predictions [1,65,66,109]. In our system, we can replace the excess free energy density f_{EXC} with the prediction of Voorn-Overbeek theory that uses results from Debye-Hückel theory [1]:

$$f_{EXC,VO} = -\alpha \sum_i \left(\lambda_i \phi_i(\mathbf{x})\right)^{\frac{3}{2}} \tag{2.16}$$

λ_i is the charge density of species i, and α controls the strength of electrostatic interactions [1]:

$$\alpha = \frac{2}{3}\sqrt{\pi}\left(\frac{l_B}{\sigma}\right)^{\frac{3}{2}} \tag{2.17}$$

where l_B is the Bjerrum length (0.7 nm for water). We plot the landscape $f_{EXC,VO}(\phi_S, \phi_P)$ in Figure 2.3b, which demonstrates markedly different behaviors when compared to the landscape determined from molecular MC calculations shown in Figure 2.3a. This is due to the neglect of important polymer-based connectivity and the excluded volumes of charges correlations in Voorn-Overbeek theory [1]. Indeed, the use of $f_{EXC,VO}$ can be shown to directly compare to phase diagrams calculated in the literature [1, 109].

Figure 2.4a shows the phase diagram for a system using the Voorn-Overbeek term $f_{EXC,VO}$. This reproduces Figure 4 in Spruijt et al. [1], using their fit values ($\alpha = 0.9$, $\lambda_P = 0.95$, and $\lambda_S = 1.0$) and a variety of chain lengths N_P. Spruijt et al. used the 'fixed salt approximation', where the values of ϕ_S are kept constant in both the coacervate and supernatant phases [1]. Assuming that $\phi_i = 1$ when the concentration $c_i = 7.9$M, we are able to plot this in terms of the molarity of salt c_S and polymer c_P in quantitative matching with Spruijt et al. [1] This thus reproduces the result that the chain length has a measurable effect on the size of the coexistence region, which can be attributed to the change in the translational entropy of the polymer chains.

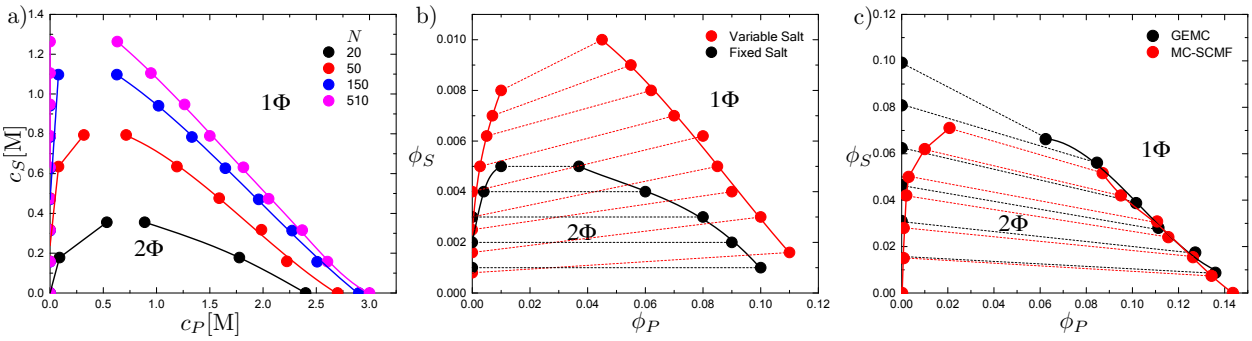

Figure 2.4: (a) Plot of c_S versus c_P using the Voorn-Overbeek excess free energy $f_{EXC,VO}$ and the fixed salt approximation with parameters α=0.90, λ_P=0.95, and λ_S=1.0 for a variety of molecular chain lengths. The points, each a separate simulation, form the binodal curve. The area below the binodal is the immiscible region (2Φ) and above the binodal is the miscible region (1Φ). This demonstrates that our method can reproduce the results of Spruijt, et al. [1] (b) Plot of ϕ_S versus ϕ_P based on Voorn-Overbeek theory with parameters N_P=100, α=3.655, λ_P=0.24, and λ_S=1.0. The points, each a separate simulation, form the binodal for the constant salt approximation and allowing the salt to vary between phases. The area below the binodal is the immiscible region (2Φ) and above the binodal is the miscible region (1Φ). This demonstrates that our method can reproduce the results of Qin, et al. [109] (c) Coacervation phase diagram from GEMC calculations (black) matches well with the MC numerical predictions using $N_P = 20$ (red), including the locations of the tie lines. The primary difference is the presence of a non-zero supernatant portion of the binodal for the numerical MC results, because this does not use the $\phi_P^\beta = 0$ assumption that is used for the GEMC. Both methods share a related origin (Monte Carlo simulation), so this provides a self-consistent verification of the accuracy of the numerical scheme for MC results. In contrast to the Voorn-Overbeek predictions, the mumerical MC calculation predicts that the tie lines tilt toward a lower salt concentration in the coacervate phase.

Figure 2.4b reproduces the results in Figure 2c of Qin, et al., [109] using their fit values ($N = 100$, $\alpha = 3.655$, $\lambda_P = 0.24$, and $\lambda_S = 1.0$). This result demonstrates the effect of the 'fixed salt approximation', showing that the ability of salt to repartition between the phases has a sizable effect on the extent of the coexistence region [109]. We also include tie lines in the non-fixed case, which demonstrate that the salt concentration is predicted to be larger in the coacervate phase in Voorn-Overbeek [109].

Our model is thus capable of reproducing standard theoretical results in the simplified Voorn-Overbeek case. This provides the basis to include local charged structure via molecular MC simulation results.

2.2.6 Numerical MC Consistency and Salt Partitioning

In Figure 2.4c, we plot a comparison between the GEMC result and the numerical MC result. The latter uses the landscape in Figure 2.3a and the numerical MC technique. GEMC and numerical MC are both based on the same RPM MC simulation, and thus this is a test of self-consistency. For a simple coacervate-forming polymer system, the phase diagram should be essentially identical. The only approximation is that there is no polymer in the supernatant for the GEMC calculation, whereas for numerical MC this approximation is unnecessary. Thus, other than the position of the supernatant portion of the binodal at high salt, the MC-SCMF follows the GEMC result in both the binodal curve and the salt partitioning (i.e. the tie lines).

The tie lines indicated in Figure 2.4c are significant when compared to the Voorn-Overbeek predictions. While the phase diagram from the numerical MC calculation is qualitatively similar to Voorn-Overbeek, the upward slope of the tie lines in Figure 2.4b contrast with the numerical MC results. This indicates that salt prefers the supernatant over the coacervate phase (downward slope of the tie lines in Figure 2.4c). This expulsion of salt from the coacervate is also observed in the GEMC simulations, and is attributed to the excluded volume of the dense polymer in the coacervate phase.

2.2.7 Simulation Parameters for Theory Comparison

We will now use this numerical MC technique to inform and test our theory, but modify simulation parameters for a simpler coacervate model to elucidate the physics of the system. The length of polymer is increased to $N_P = 100$ and the number of chains is increased to $n_{P-} = n_{P+} = 6$. Additionally, $\epsilon_{LJ} = 0.00 k_B T$ to remove dispersive interactions. Other simulation parameters remain the same.

2.3 Theory

2.3.1 Multicomponent Charge Condensation Along a Test Chain

We consider a test polyelectrolyte in the bulk of a coacervate phase, with monomers i that proceed from $i = 1$ to $i = N$. We will explore the environment along the contour of this chain, where the oppositely-charged species can 'adsorb' to the linear test molecule. Accounting for these adsorbing molecules will enable calculation of the free energy of interaction of a polyelectrolyte with its surroundings. The counterion C and the oppositely-charged polymer P are possible adsorbing species. As the contour coordinate of the chain is traversed, we further distinguish between an initial polymer unit in a run of adsorbed monomers, P', and the subsequent monomers P that are adjacent along the adsorbed chain (i.e. not from a different, competing chain). Figure 2.5 schematically demonstrates these distinctions, and shows that each adsorbed species (C, P', and P) are each associated with a single monomer along the test chain. There is also a possibility that there are no species that are nearby a given monomer within an arbitrary cutoff r_C, which we designate as 0. We note that this is relatively infrequent, because we focus on applying this model under conditions where most monomers are 'paired'. This is a limitation of our approach, which we expect will be most accurate in the high charge-density limit where counterion condensation is strong.

2.3.2 Interaction Free Energy

The system of interest is the immediate volume surrounding the test chain, which has an open boundary to the oppositely charged chains and counterions in the environment. For now, we consider the polymer and salt species in the environment to be at chemical potentials μ_P and μ_S respectively. Similarly, we assign a penalty ϵ for *not* having a paired charge (0) adjacent to a monomer on the test chain. This phenomenological parameter is related to the entropic cost associated with having a charged monomer without a nearby pair within the arbitrary distance r_C. This is left as a fit parameter in our model, and we observe that it remains unchanged over all conditions considered in this paper. We write the grand

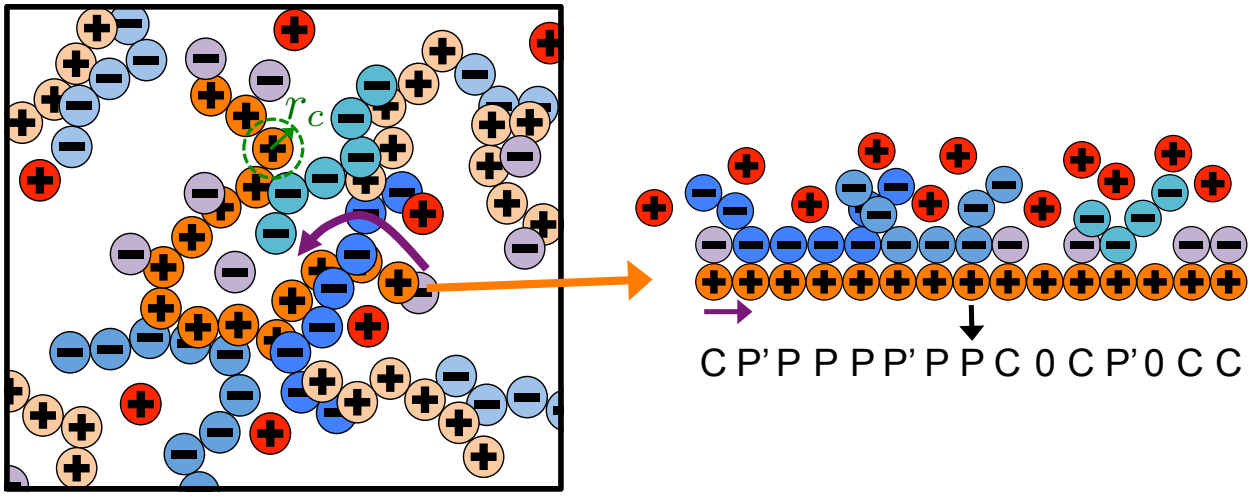

Figure 2.5: Our theoretical model uses a coordinate that is along the contour of a test polymer (left, dark orange). We assign to each monomer of this test polymer a 'nearest neighbor' particle of the opposite charge, which can be a counterion C, a polymer P or P' (right top). It is also possible that there is no nearby neighbor, so we consider the monomer unpaired 0, using a cutoff r_C (green circle). These assignments are converted into a sequence (right bottom) describing the state of the test particle; our model of interactions is built around determining the free energy associated with the many sequence possibilities.

canonical partition function for a test chain with N monomers by:

$$\Xi(N) = \sum_{\{s_i\}} \exp\Bigg[-\beta \sum_j{}^{*} \Big(\epsilon\delta_{s_j,0} - \mu_P\delta_{s_j,P'} - \mu_S\delta_{s_j,C} - \\ -k_BT\delta_{s_{j-1},P'}\delta_{s_j,P} \ln 2E - k_BT\delta_{s_{j-1},P}\delta_{s_j,P} \ln E \Big)\Bigg] \tag{2.18}$$

Here, the indices j denote locations along the chain, each with a state $s_j = C, P, P', 0$ that represents the immediate environment. The asterisk on the sum denotes the constraint that it is not possible to have adjacent sites where $s_j = P$ and $s_{j-1} = C$ or $s_j = P$ and $s_{j-1} = 0$. E represents a single-particle partition function associated with the confinement of adsorbed monomers after the first monomer has been adsorbed; we initially set this to be $E = 1$, which sets the otherwise arbitrary reference states of the chemical potential terms μ_P, μ_S, and the energy ϵ. The factor of 2 in the $\ln 2E$ term is associated with the degeneracy of choosing a direction to adsorb the second monomer P after initially adsorbing the chain P'. This contrasts with the $\ln E$ term, which is due to the propagation of the adsorbed chain (P to

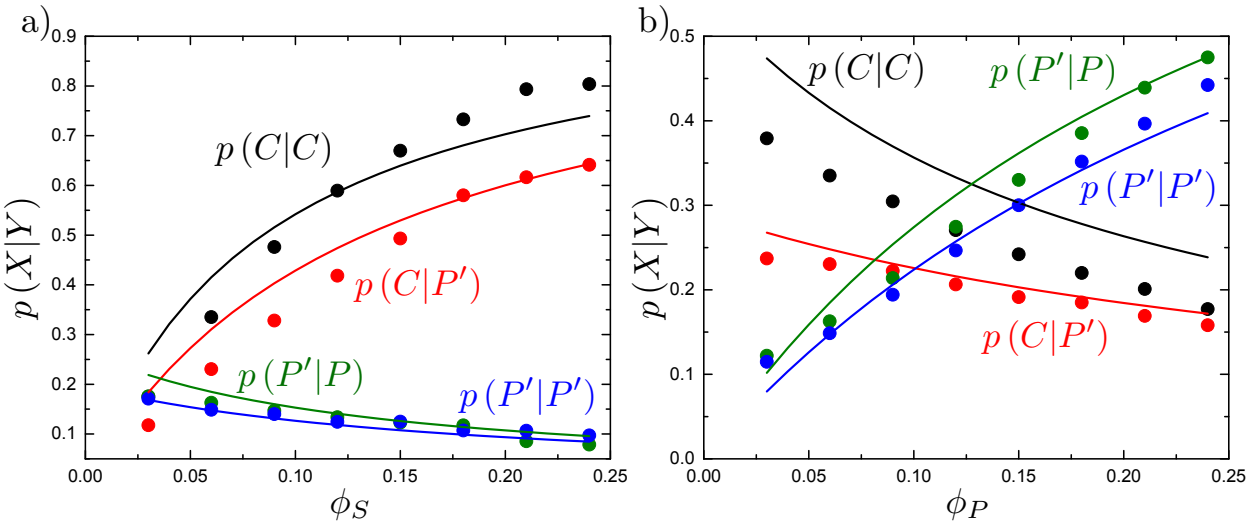

Figure 2.6: Simulation (points) and theory (curves) describing the adsorption sequence statistics in various coacervate-forming systems at a number of values of ϕ_P and ϕ_S. (a) The conditional probabilities $p(X|Y)$ of having a monomer with adsorbed state of type X immediately following a monomer with adsorbed state of type Y. $p(C|C)$, $p(C|P')$, $p(P'|P)$, and $p(P'|P')$ as a function of salt concentration ϕ_S at constant $\phi_P = 0.06$. (b) The same conditional probabilities as a function of polymer concentration ϕ_P for constant $\phi_S = 0.06$. For both (a) and (b) there is near-quantitative fitting between theory and simulation, indicating that this formalism describes the environment surrounding a test chain.

P). In this case, continuation must be along a direction along the adsorbing chain already determined by the initializing P' to P step.

This partition function is more concisely written using the transfer matrix formalism. Here, we note that the partition function at a number of monomers $N+1$ is related to the partition function of a chain with N monomers. For example, if the last monomer in the chain is $s_{N+1} = P$, then the partition function $\Xi\,(N+1, s_{N+1} = P)$ can be written as:

$$\Xi\,(N+1, s_{N+1} = P) = \Xi\,(N, s_N = P)\, e^{-\beta[-k_B T \ln E]} + \\ + \Xi\,(N, s_N = P')\, e^{-\beta[-k_B T \ln 2E]} \tag{2.19}$$

The bracketed terms in the exponential factors correspond are deliberately written to correspond to contributions to the sum in the exponent of Equation 2.18. Similar relationships can be written for all possible values of s_{N+1}. We generalize this by representing the expo-

nential factors (such as those in Equation 2.19) in matrix form; we define the contribution to the partition function for an adsorption state s_i at monomer 'site' i given the adsorption state s_{i-1} at the previous monomer site $i-1$ using a matrix $\mathbf{M}(s_i, s_{i-1})$:

$$\mathbf{M}(s_i, s_{i-1}) = \begin{bmatrix} CC & CP & CP' & C0 \\ PC & PP & PP' & P0 \\ P'C & P'P & P'P' & P'0 \\ 0C & 0P & 0P' & 00 \end{bmatrix} = \begin{bmatrix} A & A & A & A \\ 0 & E & 2E & 0 \\ B & B & B & B \\ D & D & D & D \end{bmatrix} \tag{2.20}$$

The first version of the matrix describes the states $s_i = C, P, P', 0$ and $s_{i-1} = C, P, P', 0$, pairs of which contribute to the partition function. The second version of the matrix assigns each element to the factors $A = e^{\tilde{\mu}_S}$, $B = e^{\tilde{\mu}_P}$, $D = e^{-\tilde{\epsilon}}$, and $E = 1$ where tildes denote normalization by the thermal energy k_BT. The partition function can be rewritten using this matrix:

$$\Xi = \psi^T \mathbf{M}^N \psi \tag{2.21}$$

where the vectors ψ are comprised of ones. For sufficiently large N, the largest eigenvalue of the matrix $\mathbf{M}$ (ξ) dominates this partition function, and has an analytical form:

$$\Xi = \xi^N = \left[\left(A + B + D + E + \sqrt{(A + B + D + E)^2 - 4E(A - B + D)}\right)/2\right]^N \tag{2.22}$$

This partition function is directly related to a free energy of interaction between N monomers of a coacervate chain and its surroundings:

$$\mathcal{F}_{int} = -k_BT \ln \Xi = -Nk_BT \ln \Big[A + B + D + E + \\ + \sqrt{(A + B + D + E)^2 - 4E(A - B + D)}\Big] + Nk_BT \ln 2 \tag{2.23}$$

The last term is simply an additive constant that we will neglect for the rest of this paper. This equation is a function of μ_S, μ_P, and ϵ that determine A, B, D, and E respectively. These parameters connect this tagged polymer chain to the surrounding environment.

2.3.3 Chain Environment

We assume a straightforward expression for the chemical potentials, $\tilde{\mu}_S = \tilde{\mu}_S^0 + \ln \phi_S = \ln (A_0 \phi_S)$ and $\tilde{\mu}_P = \tilde{\mu}_P^0 + \ln \phi_P = \ln (B_0 \phi_P)$, where $\tilde{\mu}_S^0$ and $\tilde{\mu}_P^0$ are reference chemical potentials and $A_0 = \exp \tilde{\mu}_S^0$ and $B_0 = \exp \tilde{\mu}_P^0$. This is an assumption that the environment surrounding the tagged polymer is near-ideal [110]. We conceptually justify this by observing that, in simulations of these dense Coulombic environments, correlations do not extend significantly beyond the immediate neighbors of the test molecule (which are included in the transfer matrix method) [4].

We can demonstrate the suitability of this method by directly determining the adsorbed species along chains in coacervate simulations. We show our method schematically in Figure 2.5. Along test chains, the nearest oppositely charged particle within a cutoff radius of $\tilde{r}_C = 3\sigma/2$ around each monomer is assigned to each indexed bead. Assignments are unique, so that every neighboring particle is only used for a single monomer. This allows us to determine from simulation the sequence of 'adsorbed' species $\{s_i\}$ which consists of C, P, P', and 0 designations. P and P' are defined such that an adsorbed monomer is considered to be from a new chain if it is more than 3 monomers from the previous adsorbed monomer.

Figure 2.5 shows a characteristic sequence description of the test chain environment. We quantify the statistics of this sequence by calculating the conditional probability of observing an adsorbed species s_i at monomer i given that we previously had an adsorbed species s_{i-1} at monomer $i-1$, $p(s_i|s_{i-1})$. These conditional probabilities are directly calculable from the transfer matrix elements:

$$p(s_i|s_{i-1}) = \frac{\mathbf{M}(s_i, s_i - 1)}{\sum_{s_i} \mathbf{M}(s_i, s_{i-1})} \tag{2.24}$$

As such, our predictions can be compared to simulation results and thus to molecular structure. For example, we can calculate $p(C|P) = A/(A+E+B+D) = A_0\phi_S/(A_0\phi_S + B_0\phi_P + e^{-\tilde{\epsilon}} + 1)$. Figure 2.6 shows how a number of these conditional probabilities compare between the theory and the simulation as ϕ_S is changed at constant ϕ_P (Figure 2.6a) and as ϕ_P is changed at constant ϕ_S (Figure 2.6b). Qualitative matching shows that we are capturing key attributes of the local chain correlations with this simple model. We allow ϵ to be a fit parameter that is constant regardless of the environment or molecular features. This

matching with experiments enable parameterization, with $A_0 = 20.5$, $B_0 = 12.2$, and $\tilde{\epsilon} = 0$. We use these values for all of the subsequent results in this chapter.

2.3.4 Free Energy of Coacervation

We combine the expression for the free energy of interaction term (Equation 2.23) with an entropic mixing contribution, and a phenomenological contribution to capture the excluded volume of all the non-water species:

$$\frac{\mathcal{F}}{Vk_BT} = \frac{\phi_P}{N}\ln\phi_P/2 + \phi_S\ln\phi_S/2 + \phi_W\ln\phi_W - \frac{\phi_P}{2}\ln\Big[1 + A_0\phi_S + B_0\phi_P + e^{-\tilde{\epsilon}} + \\ + \sqrt{(1 + A_0\phi_S + B_0\phi_P + e^{-\tilde{\epsilon}})^2 - 4(A_0\phi_S - B_0\phi_P + e^{-\tilde{\epsilon}})}\Big] + \kappa(\Lambda\phi_P + \phi_S)^3 \quad (2.25)$$

We have introduced a constant κ that parameterizes the strength of the excluded volume contribution. This term is third order to distinguish from the interaction term, which includes the two-body interactions (chain-salt and chain-chain interactions) that are represented by the interaction term. The constant $\Lambda = v_{e,P}/v_{e,S}$ accounts for the difference in excluded volumes v_e between the polymer versus salt species. The region of excluded volume around a salt ion is $v_{e,S} = 4\pi\sigma^3/3$, associated with the closest-approach distance of another species. This is different for the polymer, because the connectivity between the polymer beads forces overlap between their respective excluded volume regions. Polymer beads thus exclude less volume, and for excluded volume radius σ around beads that are connected with bonds separated by a distance σ, $\Lambda = 0.6875$. We discuss this term in more detail in section 2.4.3.

The last two terms of equation 2.25 correspond to the excess free energy $f_{EXC} = \mathcal{F}_{EXC}/V$, which is the portion of $\mathcal{F}$ that does not include the configurational mixing entropy. This prediction can be tested by comparison to the values for f_{EXC} that are calculated from thermodynamic integration of simulations according to equation 2.11. In Figure 2.7, we plot free energy landscapes from both simulation and theory. These exhibit near-quantitative matching for $\kappa = 19.0$, except at high values of ϕ_P and ϕ_S that likely reflects the approxi-

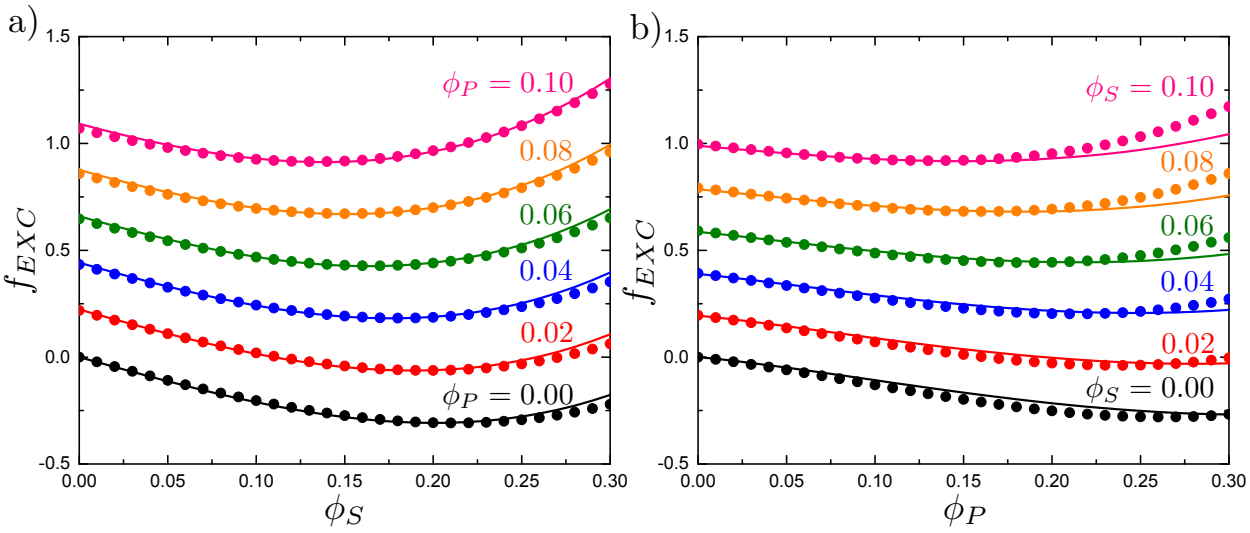

Figure 2.7: Excess free energy f_{EXC} calculated using the final two terms in Equation 2.25 (lines) and comparison with simulation values (points). (a) Constant ϕ_P curves as a function of ϕ_S and (b) constant ϕ_S curves as a function of ϕ_P. For (a) and (b), each curve is shifted vertically by a value $f^S_{EXC} = 0.25$ for visual clarity. We note that there is excellent quantitative agreement between all values of ϕ_P and ϕ_S.

mation of using a simple third-order term to describe excluded volume effects. We note that matching between simulation and theoretical f_{EXC} curves is aided by linear contributions that tilt the f_{EXC} landscape ($f_{EXC} = f^0_{EXC} + M_1\phi_S + M_2\phi_P$, with constants M_1 and M_2). This has no impact on thermodynamic properties.

2.4 Coacervation Predictions and Comparison to Simulation

To motivate a number of assumptions in the above derivation, we provided some comparison to simulation. In particular, we demonstrated that the chosen form for the chemical potentials of the tagged polymer environment was motivated by comparing the adsorption sequence statistics. Furthermore, we were able to show that the f_{EXC} calculated from theory matched well with simulation calculations. We now demonstrate that the predictions of this theory are consistent with the current state of understanding of coacervation physics, including aspects that are not described by VO or related theoretical approaches [4, 65, 67, 111].

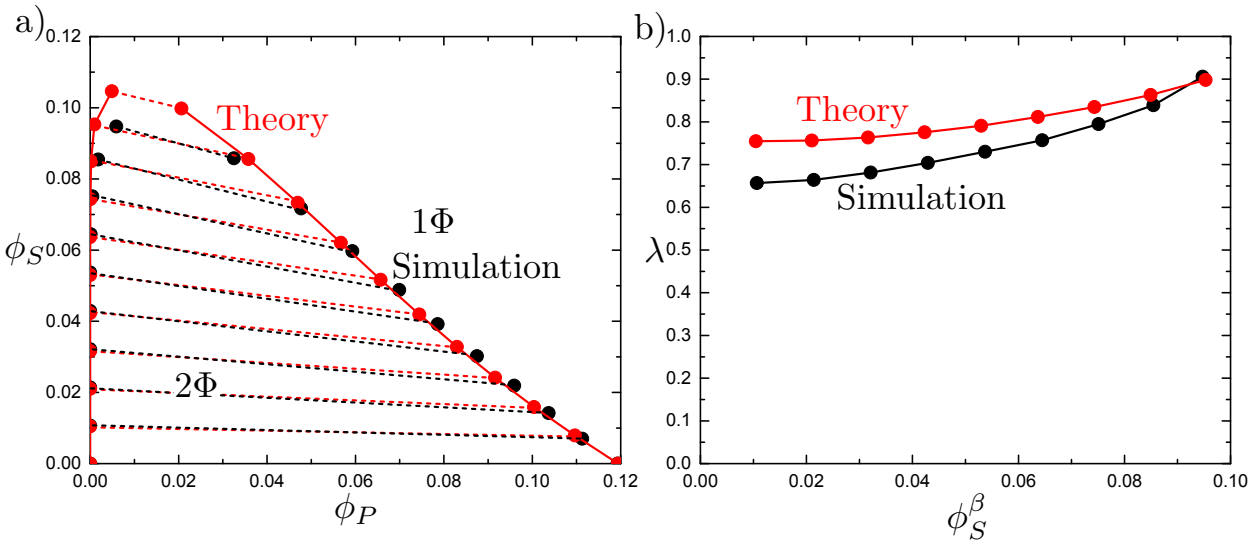

Figure 2.8: (a) Phase diagram in the salt concentration ϕ_S versus polymer concentration ϕ_P plane calculated from both simulation and theory, with the binodal curves demarcating the two phase 2Φ region where coacervation occurs. Tie lines are drawn, denoting the equilibrium between the low-ϕ_S coacervate phase (right branch of the binodal) and the high-ϕ_S supernatant phase (left branch of the binodal). (b) Tie lines indicate a difference in salt partitioning between the coacervate (α) and supernatant (β) phases. We plot $\lambda = \phi_S^\alpha/\phi_S^\beta$ as a function of the supernatant salt concentration ϕ_S^β. For all ϕ_S^β, $\lambda < 1$ indicating that salt is depleted from the coacervate phase.

2.4.1 Phase Separation

Figure 2.8a demonstrates a coacervation phase diagram, in the salt concentration versus polymer concentration plane. Consistent with previous observations of coacervate phase behavior, [1, 4, 65] there is a two phase region at low ϕ_S and ϕ_P where the mixture will spontaneously phase separate into polymer-rich coacervate and polymer-dilute supernatant phases. We use the values of A_0, B_0, $\tilde{\epsilon}$, and κ determined previously, and we likewise include simulation results for the binodal curve on the same plot. We find that both results match nearly quantitatively. This is perhaps not entirely surprising, given the use of simulation to determine the fitting constants; however, we note that these constants are parameterized by *molecular* features rather than simply matching the phase diagram.

One important feature of this prediction is the slope of the tie lines that connect the coexisting supernatant and coacervate phases. In most coacervate theories, these are non-horizontal to reflect the uneven partitioning of salt into the two phases [65]. Voorn-Overbeek

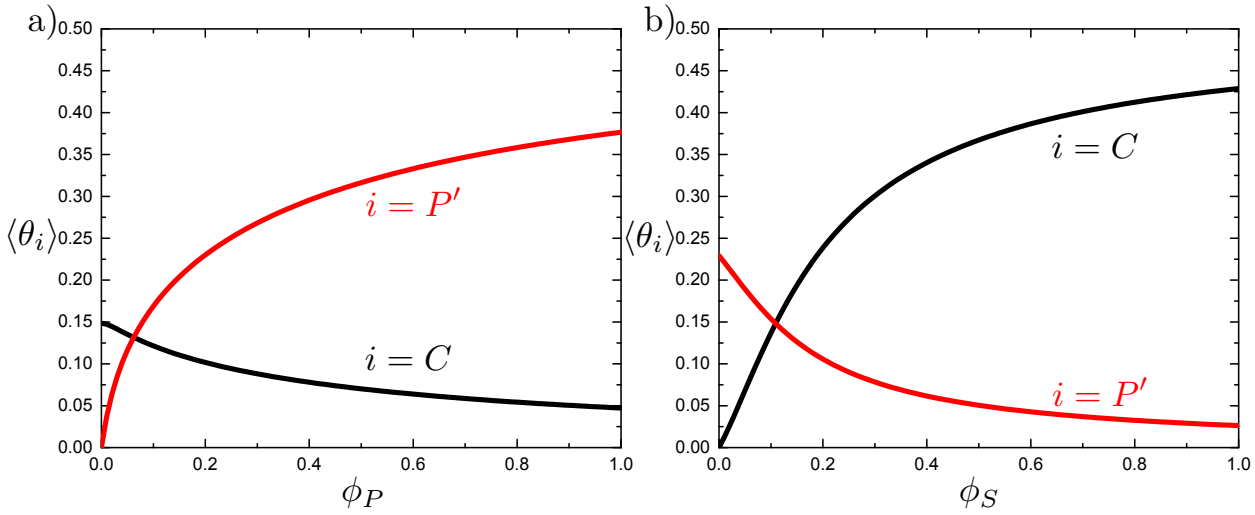

Figure 2.9: Fraction of monomers with 'adsorbed' species i, $\langle\theta_i\rangle$, as a function of (a) ϕ_P (at constant $\phi_S = 0.09$) and (b) ϕ_S (at constant $\phi_P = 0.09$). $\langle\theta_C\rangle$ is a measure of the number of condensed counterions, and monotonically decreases as the concentration of of polymer ϕ_P is increased. This reflects the traditional counterion release driving force for coacervation. The amount of condensed counterions increases with ϕ_S, reflecting the increased abundance of salt ions. The number of new polymer interactions per monomer, $\langle\theta_{P'}\rangle$, monotonically increases as the concentration of polymer ϕ_P is increased. This is a further driving force for coacervation, due to the increased entropy of having a large number of combinations of possible polymer-polymer interactions.

predicts an excess of salt in the coacervate phase, leading to a positively-sloped tie line [65, 78, 89]. However, recent simulation and theory work by the authors, [4, 67, 112] in line with experimental results, [4] demonstrates that the tie line will typically have a negative slope. The physical motivation for this negative slope is that the high polymer density in the coacervate phase excludes the volume accessible to the salt, which will subsequently prefer to be in the polymer-dilute supernatant phase. Our theory predicts this behavior, and we quantify the extent of this partitioning by plotting in Figure 2.8b the ratio of the salt concentration between the two phase, $\lambda = \phi_S^\alpha/\phi_S^\beta$, where α denotes the coacervate phase and β denotes the supernatant phase. In Figure 2.8, quantity λ is plotted versus ϕ_S^β, and is always $\lambda < 1$ indicating that salt preferentially partitions to the supernatant phase. Simulation and theory agree qualitatively, and are consistent with previous simulation and experimental results [4, 67].

2.4.2 Counterion Release and Chain-Chain Interactions

We can quantify how this phase separation is related to the mechanism of counterion release, one of the traditional concepts of coacervation. The average fraction of monomers with a condensed salt ion $\langle\theta_C\rangle$ can be calculated from the partition function Eq. 2.22:

$$\langle\theta_C\rangle = k_BT\left(\frac{\partial \ln \xi}{\partial \mu_S}\right) = \frac{A_0\phi_S}{2\xi}\Bigg[1 + \\ + \frac{A_0\phi_S + B_0\phi_P + e^{-\tilde{\epsilon}} - 3}{\sqrt{\left(A_0\phi_S + B_0\phi_P + e^{-\tilde{\epsilon}} + 1\right)^2 - 4\left(A_0\phi_S - B_0\phi_P + e^{-\tilde{\epsilon}}\right)}}\Bigg] \tag{2.26}$$

This is a function of salt and polymer concentration, and is plotted alongside simulation values in Figure 2.9 as a function of polymer concentration ϕ_P (Figure 2.9a) and ϕ_S (Figure 2.9b). Indeed, at low ϕ_P there are significantly more adsorbed counterions, which monotonically decreases with ϕ_P. This is indicative of a counterion condensation and release effect. Increased salt concentration ϕ_S leads to a monotonic increase of $\langle\theta_C\rangle$ due to the prevalence of salt ions.

The entropic driving force for coacervation is only partly driven by counterion release. There is another entropic driving force due to the increasing number of interactions between the polymers. We also plot this in Figure 2.9, by calculating the average number of new polymers P' per chain $\langle\theta_{P'}\rangle$:

$$\langle\theta_{P'}\rangle = k_BT\left(\frac{\partial \ln \xi}{\partial \mu_P}\right) = \frac{B_0\phi_P}{2\xi}\Bigg[1 + \\ + \frac{A_0\phi_S + B_0\phi_P + e^{-\tilde{\epsilon}} + 3}{\sqrt{\left(A_0\phi_S + B_0\phi_P + e^{-\tilde{\epsilon}} + 1\right)^2 - 4\left(A_0\phi_S - B_0\phi_P + e^{-\tilde{\epsilon}}\right)}}\Bigg] \tag{2.27}$$

The monotonic increase in the quantity $\theta_{P'}$ with ϕ_P is due to the increasing abundance of options for polymer-polymer interactions, which is entropically favorable. This is one way in which coacervation is different from the behavior of isolated pair complexes. Pair complexes occur in the dilute limit where two oppositely-charged polyelectrolytes interact via the counterion release mechanism; however, these polyelectrolytes only have the option of interacting each other over the entire length of their respective chain contours. As concen-

tration increases, there is an entropic benefit of each polyelectrolyte interacting with more than one chain. A similar effect is found in physical gelation, [113] polymer solution phase behavior, [114] and dense polyelectrolytes [115]; in all of these examples there is a strong entropic contribution to the free energy due to the number of possible interactions.

2.4.3 Charge Density Effects

Previous work by the authors has demonstrated the importance of local charge density, with drastic reductions in the two-phase coexistence region as the spacing between charges is increased [4,67]. We consider two molecular effects that contribute to charge spacing, which can be incorporated directly into this formalism.

We first consider the entropy of adsorbing subsequent monomers, which affects the factor E. We postulate a form $E = \Delta^{-2}$ where Δ is the normalized spacing between adjacent charges. This scaling is related to the entropic penalty of confining a single monomer along a run of monomers, which would otherwise sweep the surface of a sphere $\sim \Delta^2$ but instead must be nearby the chain (see schematic in Figure 2.10a). Thus, as spacing increases, the entropic penalty to adsorb a monomer (after placing the initial monomer) becomes more significant due to the larger area that the monomer can sweep out in our RPM-based model.

We demonstrate that this effect captures the local structure in simulation. Figure 2.10b shows the calculation of the quantity $p(P|P) = E/(A + B + D + E) = \Delta^{-2}/(A_0\phi_S + B_0\omega_\Delta\phi_P/\omega_1 + v_1 e^{-\tilde{\epsilon}}/v_\Delta + \Delta^{-2})$ plotted alongside simulation calculations of the same quantities from the adsorption sequence for a number of charge spacings Δ and volume fractions ϕ_P. Without changing the parameters A_0, B_0, or $\tilde{\epsilon}$, we can fit the entire set of curves.

Charge spacing further impacts the excluded volume associated with the polymer. The proximity of neighboring polymer beads decreases the effective excluded volume, because they jointly occupy regions that would otherwise separately prevent the approach of salt ions (see schematic in Figure 2.10c). This was previously captured by $\Lambda = v_{e,P}/v_{e,S}$, which we can write as a function of bead spacing along the polymer. A single salt bead occupies a volume $v_{e,S} = 4\pi\sigma^3/3$. For a polymer, half of the overlap volume must be subtracted because it is shared between any pair of adjacent beads; however, this is multiplied by two

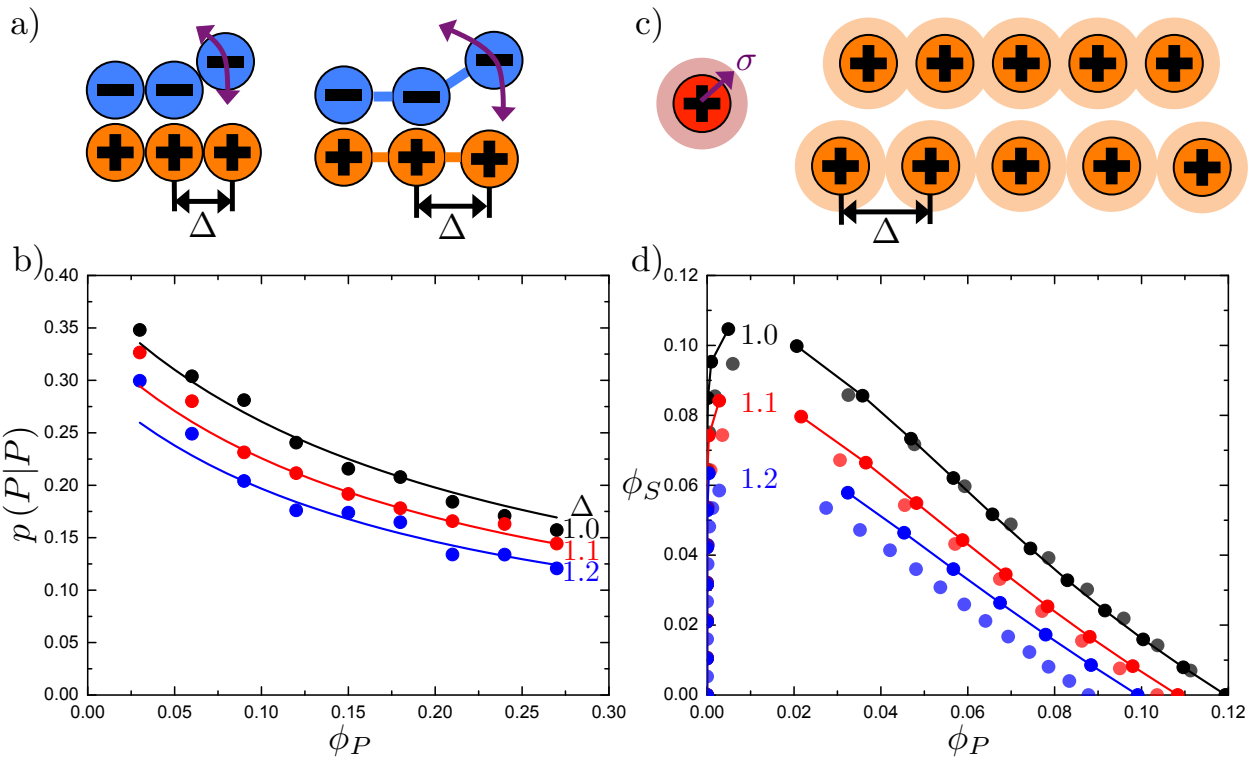

Figure 2.10: (a) As the spacing Δ between charges increases, then the entropic penalty for continued adsorption of monomers increases; this is due to the larger angle swept by a non-adsorbed charge, which corresponds to a larger phase space. (b) The sequence probability $p(P|P)$ as a function of Δ and ϕ_P (constant $\phi_S = 0.06$). Theory that accounts for the entropic penalty for chain adsorption captures the trend in simulation describing the local environment around a test chain. (c) Spacing affects the volume excluded by the charged species. An isolated salt ion excludes a volume within a diameter of the particle (light red circle). In a chain, the polyelectrolyte charges exclude a smaller volume (light orange circle), which is a function of Δ. (d) Phase diagrams from both simulation and theory, including different values of Δ. The combined contribution of chain adsorption entropy and excluded volume leads to a marked decrease in the coexistence region, which is qualitatively demonstrated in both simulation (unconnected, lighter symbols) and theory (connected, bold symbols).

adjacent beads. This leads to the result $v_{e,P} = 4\pi\sigma^3/3 - \frac{\pi}{12}(4\sigma + \Delta\sigma)(2\sigma - \Delta\sigma)^2$, providing an expression for Λ:

$$\Lambda = 1 - \frac{(4+\Delta)(2-\Delta)^2}{16} \tag{2.28}$$

We demonstrate the combined strength of these effects by calculating the phase behavior for a series of polymer $\Delta = 1.0 - 1.2$ in Figure 2.10d for both simulation and theory. We observe the expected decrease in the coexistence region as the charge spacing is increased,

which is qualitatively consistent between simulation and theory. We note that matching becomes less quantitative as Δ is increased, which represents a limitation of this model. The increase in charge spacing moves the system away from a high charge-density limit, where charged interactions are highly screened and neighboring 'adsorbed' molecules drive the thermodynamics. As Δ increases and charge density is decreased, long-range correlations become more important and field theoretic methods become increasingly appropriate [70, 72, 73, 75, 78, 79].

2.4.4 Electrostatic Strength

One surprising result of this theory is that Equation 2.25 is not explicitly dependent on the strength of the electrostatic interactions (via the Bjerrum length $\lambda_B = e^2/(4\pi\epsilon_r\epsilon_0 k_B T)$). This stems from the high charge-density limit considered in this work, where nearly all charges are effectively 'paired' in our framework. Within this limit, we can demonstrate that λ_B does not play a role. We do this by changing the relative dielectric constant ϵ_r from $\epsilon_r = 78.5$ to $\epsilon_r = 60$, which increases the strength of the Coulomb interaction by ca. 31%. The simulation results are plotted in Figure 2.11a, which show essentially no difference in the phase behavior, despite the considerable change in the strength of the Coulomb interaction. Similarly, the test chain neighbor conditional probabilities $p(X|Y)$ match between the different values of ϵ_r, and are shown in Figure 2.11b. These results are consistent with experimental observation that coacervation is primarily an entropic process, with calorimetry consistently showing only small enthalpic changes during coacervate formation [84, 85].

2.4.5 Non-Stoichiometric Coacervation Phase Diagrams

Most existing coacervate theory considers stoichiometric mixtures of polycation and polyanion, where there is equal number of polycation charges and polyanion charges, [111] with a few exceptions [116–118]. We can extend this theory to capture the phase behavior as an excess of polycation or polyanion charges is present in the system. This involves changing the interaction free energy to be rewritten with explicit reference to the polyelectrolyte species

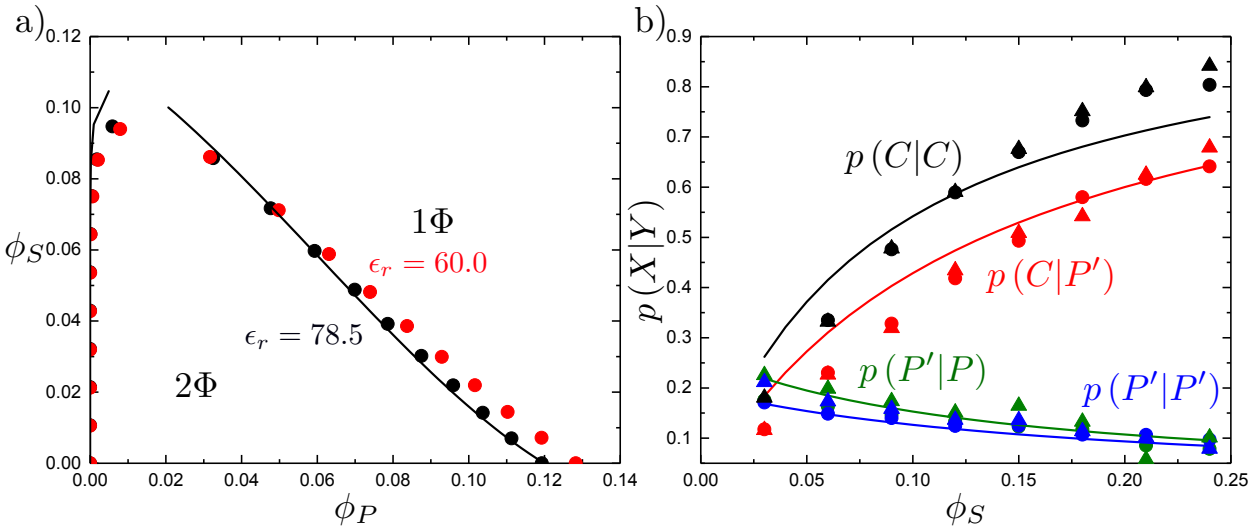

Figure 2.11: (a) Phase diagram for both $\epsilon_r = 78.5$ (black points) and $\epsilon_r = 60.0$ (red points), along with theory (black line). We note that both phase diagrams are almost exactly the same, despite electrostatic interactions being 31% stronger for the red points. This is predicted by our theory, which does not have a dependence on ϵ_r except in the assumption that we are at the high charge-density limit. (b) Example test chain probabilities $p(X|Y)$ for both $\epsilon_r = 78.5$ (circles) and $\epsilon_r = 60$ (triangles). These representative results demonstrate that a test chain experiences the same environment regardless of the strength of the electrostatic interactions, in this limit of high charge-density.

of interest:

$$\frac{\mathcal{F}_{int,\pm}}{Vk_BT} = -\frac{\phi_{P\pm}}{2}\ln\Big[1 + 2A_0\phi_{S\mp} + 2B_0\phi_{P\mp} + e^{-\tilde{\epsilon}} + \\ + \sqrt{(1 + 2A_0\phi_{S\mp} + 2B_0\phi_{P\mp} + e^{-\tilde{\epsilon}})^2 - 4(2A_0\phi_{S\mp} - 2B_0\phi_{P\mp} + e^{-\tilde{\epsilon}})}\Big] \tag{2.29}$$

We note that the prefactor includes the volume fraction of the test polymers, while the natural log term is concerned with the concentrations of the surrounding *oppositely-charged* species. The final free energy is therefore:

$$\frac{\mathcal{F}}{Vk_BT} = \frac{\phi_{P+}}{N_{P+}}\ln\phi_{P+} + \frac{\phi_{P-}}{N_{P-}}\ln\phi_{P-} + \phi_{S+}\ln\phi_{S+} + \phi_{S-}\ln\phi_{S-} + \\ + \phi_W\ln\phi_W + \frac{\mathcal{F}_{int,+}}{Vk_BT} + \frac{\mathcal{F}_{int,-}}{Vk_BT} + \kappa(\Lambda\phi_P + \phi_S)^3 \tag{2.30}$$

We plot the results of this calculation in Figure 2.12 on a plot of ϕ_S^* versus ϕ_{P+} and

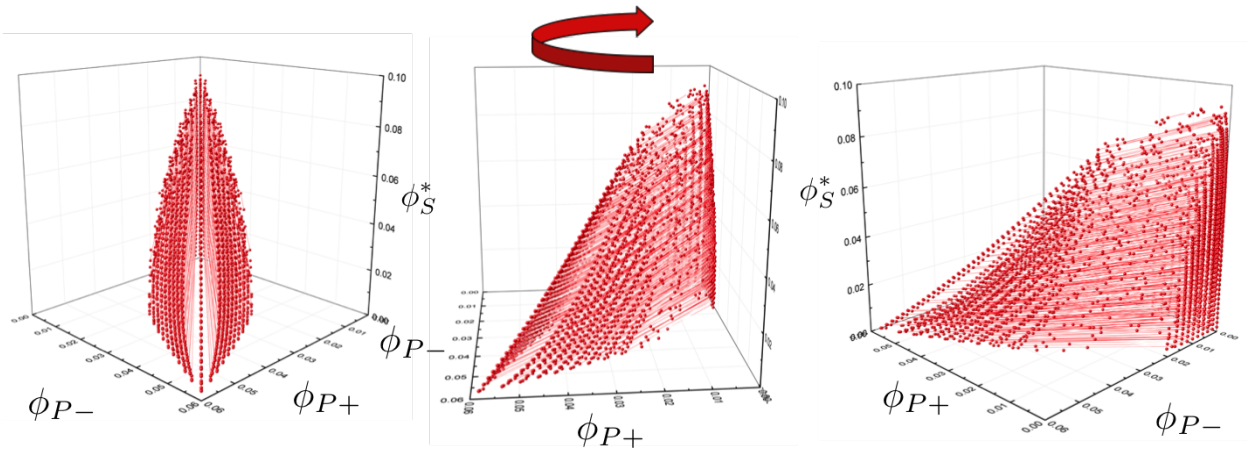

Figure 2.12: Three-dimensional phase diagram showing phase behavior as the concentration of polycation (ϕ_{P+}) and polyanion (ϕ_{P-}) are varied independently. ϕ_S^* is the concentration of excess salt, beyond the excess cations or anions required to balance the charges on the polyelectrolytes. All plots are the same, only from different angles. Deviations from the $\phi_{P+} = \phi_{P-}$ line quickly decrease the coexistence region. Points are calculated phase coexistences connected by tie lines, which show a decrease in salt concentration ϕ_S^* in the coacervate phase as compared to the supernatant phase, consistent with the two-dimensional phase diagram in Figure 2.8a. The far left plot demonstrates that these tie lines move away from the $\phi_{P+} = \phi_{P-}$ line as they move toward the coacervate phase, demonstrating that the coacervate phase accommodates more disparity in the polyelectrolyte stoichiometry than the supernatant phase.

ϕ_{P-}. The asterisk on ϕ_S^* denotes that this is the salt added beyond the counterions that are needed to make up the difference between ϕ_{P+} and ϕ_{P-}. We obtain results that are consistent with the previous literature, [2] with a region around $\phi_{P+} \approx \phi_{P-}$ that phase separates and shrinks as salt is added. In Figure 2.12, the points shown forming the surface in the ϕ_S^0-ϕ_{P+}-ϕ_{P-} space represent individual calculations of phases in equilibrium, separated by tie lines. Similar to results in Figure 2.8, the downward slope of the tie lines denotes that salt preferentially partitions to the supernatant phase. However, in off-stoichiometric mixtures the coacervate phase accommodates more of the un-matched polyelectrolyte, as indicated by the tie lines moving away from $\phi_{P+} = \phi_{P-}$ as they move toward the coacervate phase. This preference for the unmatched polyelectrolyte and its counterions to partition into the coacervate phase is unsurprising; the excess counterions will be condensed to the unmatched polyelectrolyte in the supernatant phase, which is entropically unfavorable compared to the coacervate phase where the counterions will no longer be condensed.

2.5 Conclusion

Here we presented a theory for complex coacervation that incorporates molecular aspects that are known to be crucial to understanding the thermodynamics of these materials. Specifically, we base this model on counterion condensation and release concepts [84,88,89,119,120] in order to capture the effect of local correlations due to the connected polyelectrolyte charges [67]. The results of this model are compared to the local environment around a test chain as determined in simulation, demonstrating that the assumptions that we make are appropriate for the salt and polymer concentration regimes relevant to complex coacervation [1, 8]. We see near-quantitative agreement between the results of this theory and the phase behavior of complex coacervates in simulation, including features such as the behavior of the tie lines and the influence of charge density on coacervation.

We note that this model relies on the short range of correlations due to high charge density. This allowed us to use simplistic arguments for the values of μ_P and μ_S, and an assumption that longer-range correlations are able to be neglected at distances further along the polyelectrolyte chain. For the latter assumption, the current transfer matrix model only accounts for monomers that are immediately adjacent along the chain. This may not be adequate in dilute systems where the electrostatic correlations will cause an adsorbed counterion/chain at monomer i to strongly affect nonadjacent monomers $|j - i| > 1$. We speculate that some combination of this model with standard field theoretic approaches [70,72,73,75,78] may be useful to capture these long-ranged correlations in the dilute regime.

The advantage of this model is that it considers local connectivity-based correlations, such as the local alignment of oppositely-charged chains, in a fashion that is analytically tractable and motivated by structure known from molecular simulation. The excess free energy expression f_{EXC} can be used as an input for more complicated theoretical arguments, such as those for coacervate-driven self-assemblies; indeed, this is the limiting aspect of most current models for coacervate-driven assembly, [68, 75] which either use field theory results [68] or full molecular simulation [112] to determine the local effect of electrostatic attractions and correlations.

The simulation and theoretical techniques contained herein are the standard techniques

we use to study coacervation phase behavior, and modifications of these techniques will be discussed in the relevant chapters. In the subsequent chapter, we extend these methods to understand the effects of chain stiffness, chain architecture, and salt valency.

CHAPTER 3

TUNING CHAIN INTERACTION ENTROPY IN COMPLEX COACERVATION USING POLYMER STIFFNESS, ARCHITECTURE, AND SALT VALENCY

Reproduced from Ref. [121] with permission from the Royal Society of Chemistry.

3.1 Introduction

This chapter describes how polymer architecture, polymer stiffness, and salt valency affect complex coacervation by using the transfer matrix theory and coarse-grained simulation developed in Chapter 2. These are molecular attributes that are widely known to be important for polyelectrolyte systems. For example, chain flexibility is known to affect DNA packing into virus capsids, [122–124] and affects its complexation with polyanions in drug delivery vehicles known as 'polyplexes' [125–130]. Similarly, dendrimers [131] and brushes [132] are polymer architectures that exhibit rich polyelectrolyte physics beyond linear chains, and there is experimental and simulation evidence that branches play an important role in coacervation [10] and complexation [125, 126]. Finally, valency is known to strongly affect polyelectrolyte properties in a wide variety of systems, ranging from single chains [133] to brushes, [134, 135] gels, [136, 137] and solutions [138, 139].

We will demonstrate that all these features - architecture, stiffness, and counterion valency - indeed affect complex coacervation, driving significant changes in phase behavior. We demonstrate that the phase behavior of comb polymers are affected by a combination of excluded volume and counterion condensation considerations, and qualitatively matching simulation and a modified version of our transfer-matrix coacervation model. We also show how increasing polymer stiffness suppresses coacervation, due to the entropic penalty of aligning neighboring polyelectrolyte chains. Finally, we extend our theory to account for multivalent effects, by accounting for the combinatoric entropy of counterion pairing. This

overall model provides the physical basis for understanding how complex coacervate phase behavior can be tuned on a molecular level.

3.2 Comb Polymer Model

N_P is the degree of polymerization of both the polycation and the polyanion. For linear polymers, we assume all monomers are charged, so $N_P = N$. Comb polymers have N_0 uncharged backbone monomers in addition to the N_P charged beads, so that a comb polymer has $N = N_0 + N_P$ total beads. The degree of polymerization of the branch is given by N_b, so the number of branches is given by N_P/N_b and the number of uncharged backbone monomers between branches is $N_s = N_0 N_b/N_P$. Additionally, we assume the N_0 backbone beads have no excluded volume. We show schematics of both the linear and comb polymers in Figure 3.1. Simulation parameters modified for the molecular features under consideration are discussed in the corresponding results subsection.

3.3 Results and Discussion

We study comb polymer architecture, polymer stiffness, and salt valency by comparing to a baseline coacervate-forming system. In Chapter 2 we used linear polymers with $N = 100$ and $\kappa_\theta = 3.3 k_B T$, which are shown to be well described by the transfer-matrix theory [93]. For the transfer matrix theory, we use the values $A_0 = 20.5$, $B_0 = 12.2$, and $D = 1$.

3.3.1 Chain Stiffness

Coacervates can be made using a wide range of polymers and biopolymers, [2] spanning highly flexible synthetic polymers such as Poly(Acrylic Acid) to stiff polymers such as ds-DNA. We can tune the polymer stiffness in our simulation model by adjusting the value of κ_θ in equation 2.8, with larger values of κ_θ leading to stiffer polymers with longer persistence lengths. We plot phase diagrams for $\kappa_\theta = 0.8 k_B T$ to $\kappa_\theta = 13.0 k_B T$ in Figure 3.3a. In the flexible polymer limit $\kappa_\theta \to 0$, changes in κ_θ do not significantly affect phase behavior. This

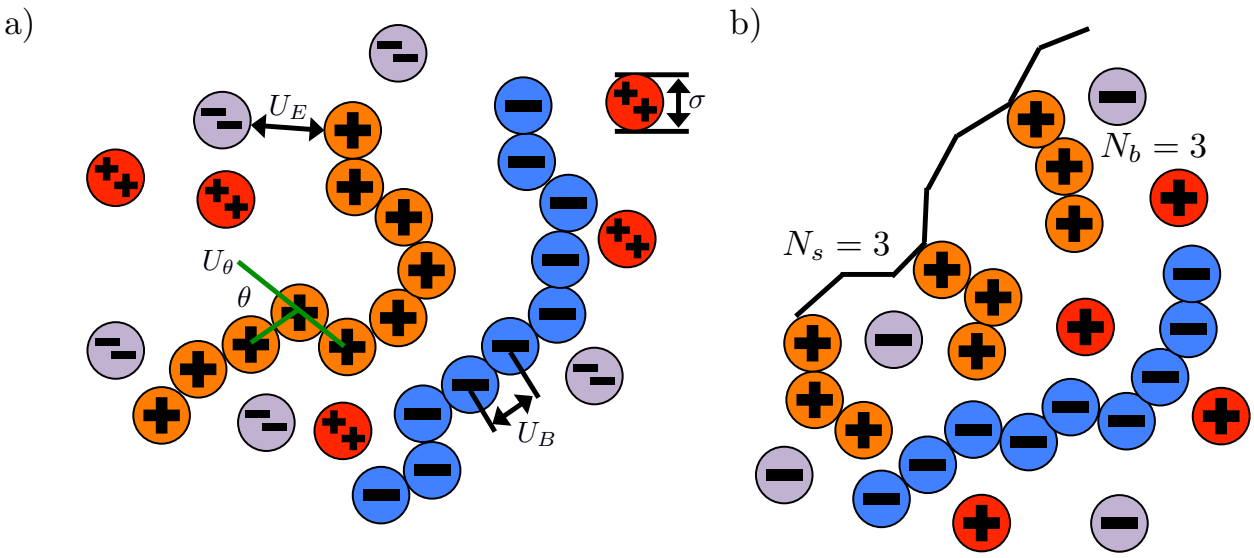

Figure 3.1: Schematics illustrating the coacervate models used in our Monte Carlo simulation. (a) Linear polyelectrolytes are modeled as a series of charged beads connected together at a distance of σ, which is also the bead diameter. Chain stiffness is included via an energetic penalty for bending angles θ. Salt valency can be changed, with divalent salts shown in this figure. (b) Comb polymers are modeled with branches of N_b charges each, positioned every N_s backbone monomers. In this work, we focus on coacervates formed from comb polycations and linear polyanions.

is also reflected in the salt partitioning, which is plotted in Figure 3.3b. Here we use a parameter $\lambda = \phi_S^\alpha/\phi_S^\beta$, which quantifies the depletion ($\lambda < 1$) of salt from the coacervate phase. This as a function of the supernatant salt concentration $\phi^{**}_{S,\text{sup}}$, which is normalized by the largest measured salt concentration (approximately the critical salt concentration) [4, 67]. Larger values of the polyelectrolyte chain stiffness κ_θ ($\kappa_\theta \geq 6.6k_BT$) demonstrate significantly smaller two-phase regions and less salt depletion (i.e. larger λ) in the coacervate phase, when compared to smaller values of κ_θ.

To understand this phase behavior from a molecular viewpoint, we consider the along-the-chain correlation of two neighboring, oppositely-charged polyelectrolytes. We assign adsorption states to all polymers in our MC simulations; each monomer has an environment characterized by the nearest unclaimed opposite charge within a cutoff radius $r_C = 1.5\sigma$, so that it is in one of the states C, P', P, or 0. We define the correlation function, $C_{P'P}$:

$$C_{P'P}(\Delta s) = \frac{\langle \delta_{s,P'}\delta_{s+1,P}\delta_{s+2,P}\cdots\delta_{s+\Delta s,P}\rangle}{\langle \delta_{s,P'}\rangle} \tag{3.1}$$

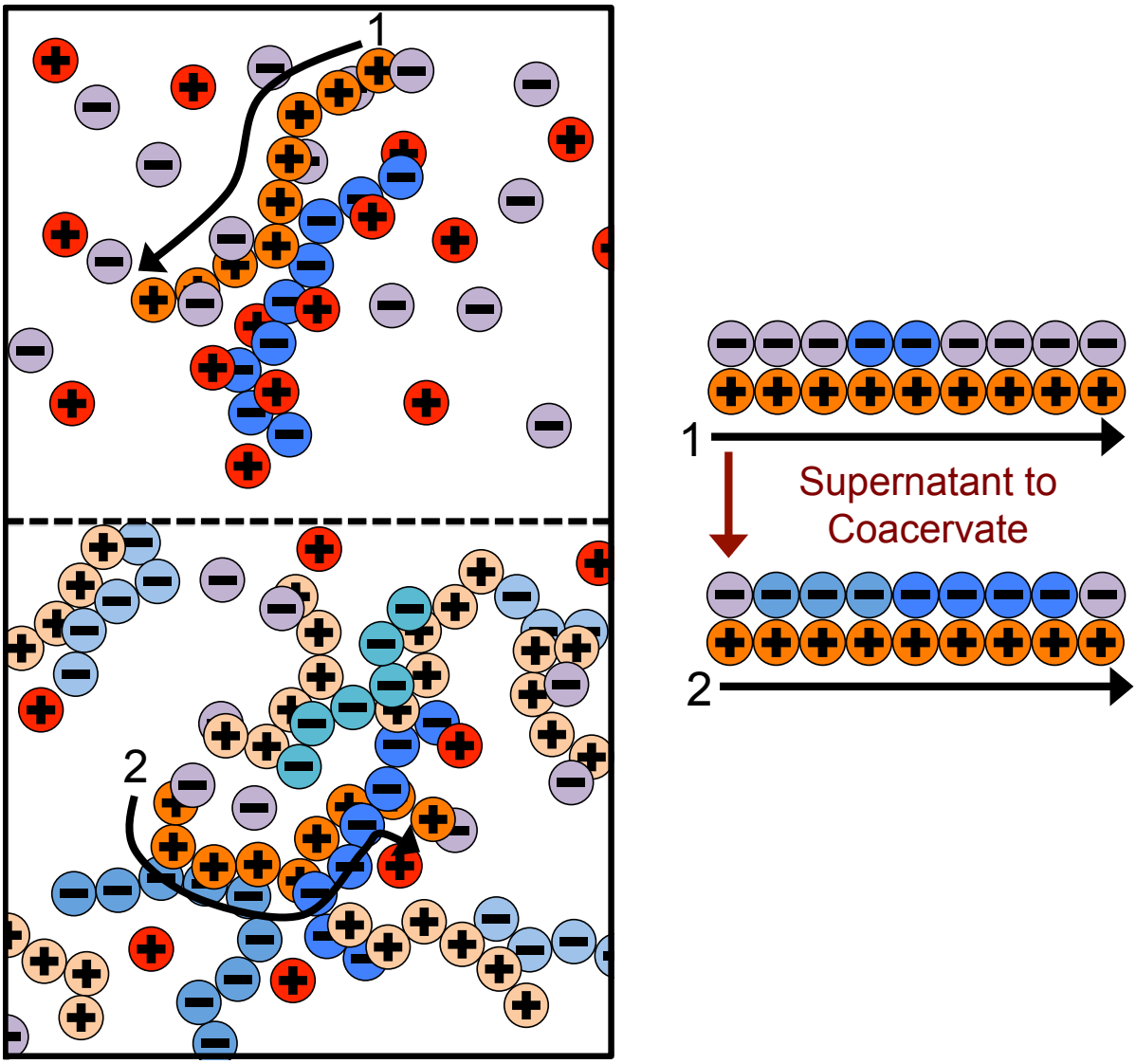

Figure 3.2: Schematic illustrating the transfer matrix theory of coacervation. We keep track of the environment around a test chain (orange polycation) by assigning neighboring charges as 'adsorbed' to the test chain. In the supernatant (1), these adsorbed charges are associated primarily with a single oppositely-charged polyelectrolyte partner with a few interspersed salt ions. In the coacervate (2), there are many neighboring polyelectrolytes and salt ions. The test chain prefers to be in the coacervate for entropic reasons; there are more configurations in state (2) due to the many adsorbing species.

Here, $\delta_{s,X} = 1$ if the state at adsorption site s is X, and $\delta_{s,X} = 0$ otherwise. This correlation function quantifies the distribution of aligned segments along neighboring polyelectrolyte chains. Figure 3.4a plots $C_{P'P}$ determined from simulation, and demonstrates that stiffness strongly affects this length distribution due to an increasingly slower decay of $C_{P'P}(\Delta s)$

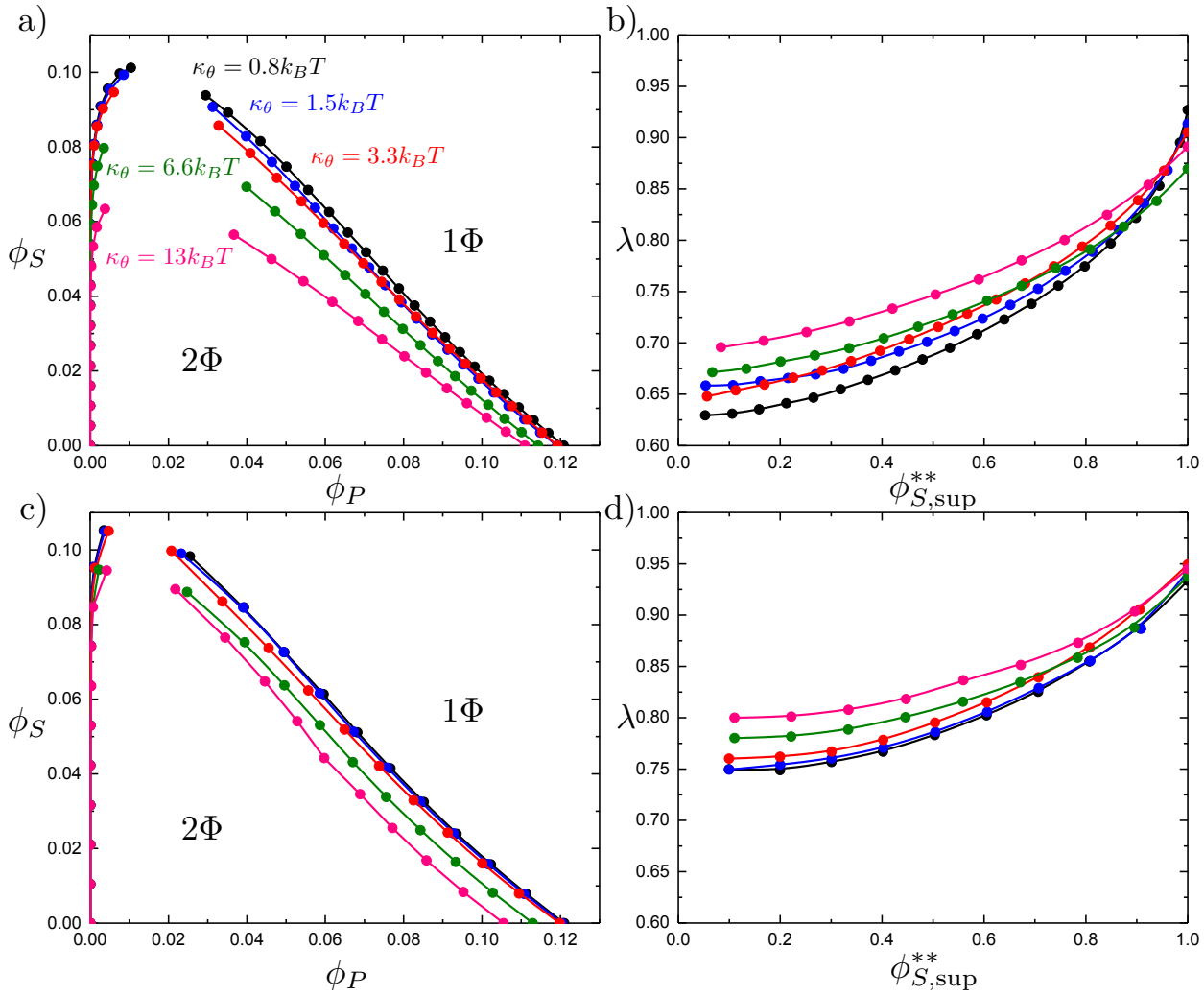

Figure 3.3: Coacervate phase behavior, with varying values of the chain stiffness κ_θ for both polyelectrolyte species. (a) Phase behavior as a function of ϕ_S and ϕ_P, calculated from simulation. As chain stiffness increases, the two-phase region begins to shrink. At small polymer flexibilities $\kappa_\theta < 6.6k_BT$, these changes are modest, but much more stiff chains $\kappa_\theta \geq 6.6k_BT$ demonstrate significant changes in the location of the binodal. (b) The salt partitioning λ for all coacervation processes are such that there is less salt in the polymer-dense coacervate phase than the supernatant phase; concomitant with a decrease in the 2-phase region, this depletion of salt from the coacervate phase decreases in magnitude with an increase in stiffness κ_θ. We demonstrate qualitatively similar effects in our modified coacervate theory, for both phase behavior (c) and salt partitioning (d). Differences are apparent, likely reflecting differences in salt contributions to the free energy not included in our current model.

as κ_θ is increased. For this plot, we chose $\phi_P = 0.09$ and $\phi_S = 0.03$, which is near the binodal curve for all values of κ_θ. This stiffness effect extends over all ϕ_P and ϕ_S values,

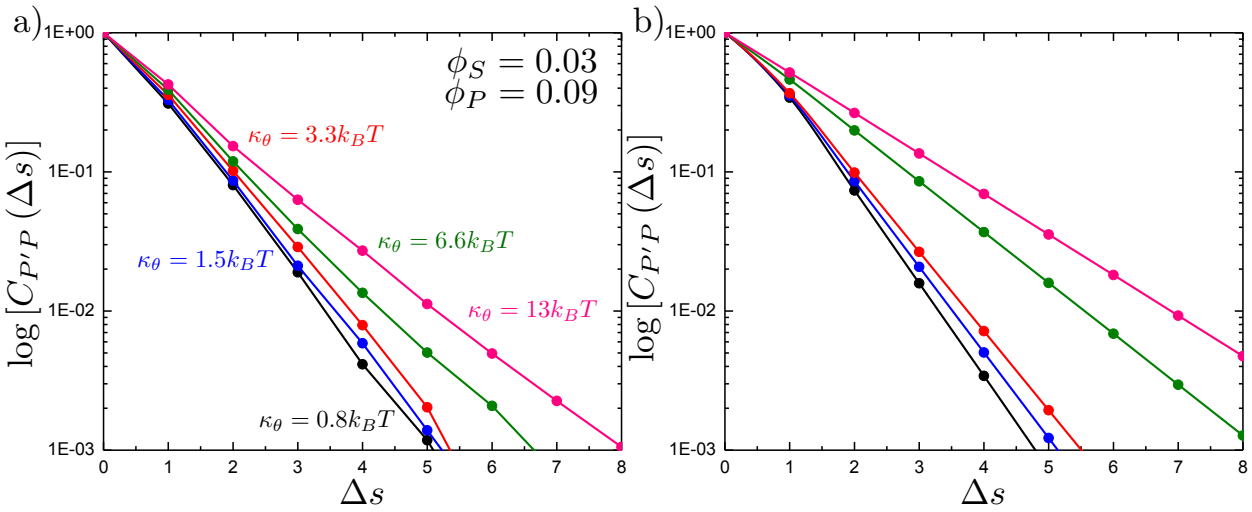

Figure 3.4: Our model attributes stiffness-related differences in coacervate phase behavior to longer runs of polycation/polyanion interactions for stiffer polyelectrolytes. These longer runs lead to a decrease in the number of polycation/polyanion interactions, decreasing the entropic driving force for coacervates. We capture these longer runs in both simulation (a) and theory (b) by plotting the length distribution $C_{P'P}(\Delta s)$ of aligned polycation/polyanion segments for a coacervate near the binodal curve ($\phi_S = 0.03$ and $\phi_P = 0.09$). Both demonstrate the same qualitative trend, with larger values of κ_θ exhibiting longer runs of aligned polyelectrolytes.

which we demonstrate by considering a single related value $C_{PP}(\Delta s = 1, \phi_S, \phi_P)$ that is the propagation probability of a neighboring chain along the test polyelectrolyte. This is plotted Figure 3.5 for as a function of both ϕ_S (Figure 3.5a) and ϕ_P (Figure 3.5b), which shows that C_{PP} monotonically increases with κ_θ. This demonstrates that adsorbed chains tend to preferentially propagate when the chain is stiff (high κ_θ).

We modify the transfer matrix theory to account for this chain alignment effect, informed by the increase in $C_{P'P}$ observed in simulation. Our conceptual argument is that, absent any competing polymers or counterions, which can 'condense' without significantly perturbing the original adsorbed polymer, the polymer can only either propagate or bend to allow an unbound state 0 at the next site. We propose a simple two-state model, based on the energy required to undergo this bending deformation, $U_B \sim \kappa_\theta \theta^2/2$ (see schematic in Figure 3.6). We can thus write a relationship based on the conditional probabilities that a site has a

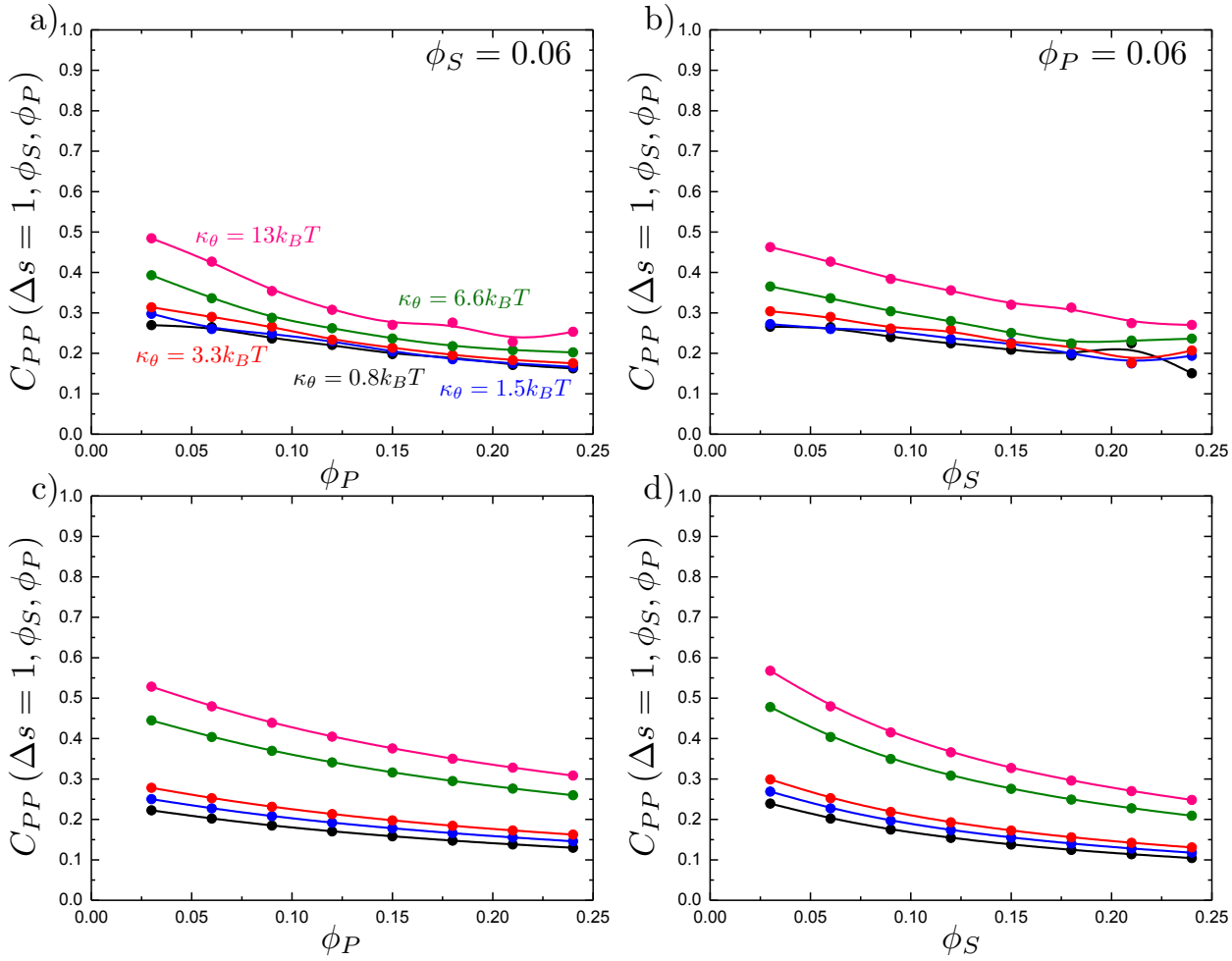

Figure 3.5: The probability of propagation $C_{PP}(\Delta s = 1, \phi_S, \phi_P)$ as a function of ϕ_P for $\phi_S = 0.06$ (a) and as a function of ϕ_S for $\phi_P = 0.06$ (b). Stiff polymers with large κ_θ are more likely to propagate along the chain, leading to longer runs of polycation/polyanion interaction for all salt and polymer concentrations, when compared to small κ_θ. Theory reproduces this observation, as demonstrated in (c) and (d) that are at the same conditions as (a) and (b) respectively.

state Y given the previous site has a state X, $p(Y|X)$:

$$\frac{p(P|P)}{p(P|P) + p(0|P)} = \frac{1}{1 + e^{-\beta\kappa_\theta \langle\theta\rangle^2/2}} \tag{3.2}$$

We choose an average angle $\langle\theta\rangle \sim 0.7$ that represents the extent of polymer bending in order for the next site is in state 0. This parameter is chosen within a reasonable range of θ to qualitatively match simulation. We assume that the adsorption statistics of competing polymers or counterions are not affected significantly by changes, so we calculate changes

in transfer matrix quantities such that $\mathbf{M}(P,P) + \mathbf{M}(0,P) = \text{Constant}$. This uniquely sets these respective values of the transfer matrix as a function of κ_θ. Finally, we make the assumption that we simultaneously decrease the likelihood of 0 due to rigidity even once the first monomer P' is adsorbed; thus we equate $\mathbf{M}(0,P) = \mathbf{M}(0,P')$. We test this model by calculating the theoretical distribution of aligned segments $C_{P'P}$ (Figure 3.4b) and $C_{PP}(\Delta s = 1, \phi_S, \phi_P)$ (Figure 3.5c and d), qualitatively matching the corresponding simulation values. Figure 3.3c and d demonstrate that the coacervation phase diagram and salt partitioning λ calculated from this theory qualitatively match simulations, based solely on these molecular correlation-informed changes in the transfer matrix.

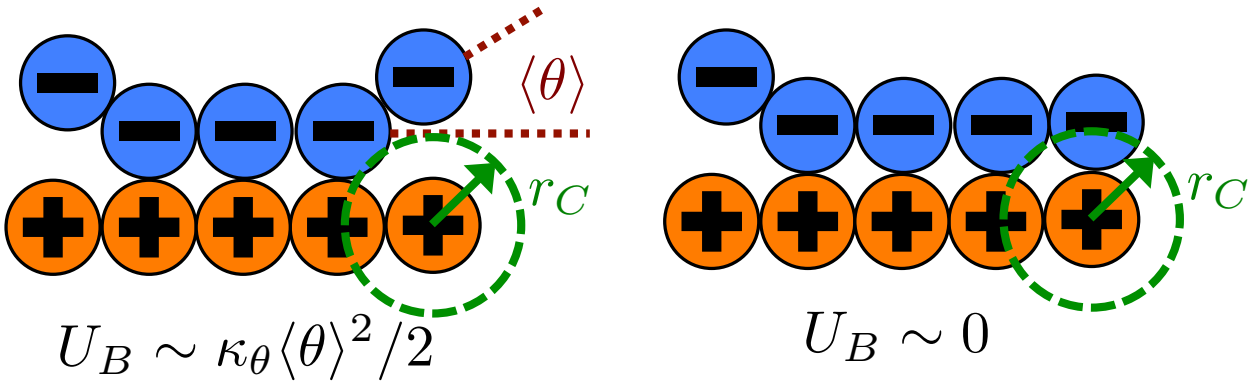

Figure 3.6: We consider a two-state model to determine the propagation of runs of polycation/polyanion interactions. A bent configuration (left) can end these runs, leading to the formation of a test chain monomer without a condensed opposite charge. This has an energetic penalty U_B associated with κ_θ. The continuing propagation (right) does not have an energetic penalty $U_B \sim 0$. The relative weight of these choices is used to determine how κ_θ affects D and E in our model.

This combination of simulation and theory provides conceptual insight into how stiffness affects complex coacervation. In the high charge-density limit, a primary driver of coacervation is the combinatoric entropy of each polyelectrolyte chain interacting with increasing numbers of oppositely-charged polyelectrolytes. The dilute supernatant has very few polyelectrolytes, because in this limit they exist as exclusive polycation/polyanion pairs. Stiffness affects the number of oppositely-charged polymers and counterions that a given test chain interacts with, due to the long, aligned runs of paired monomers. This lessens the entropic driving force for coacervation.

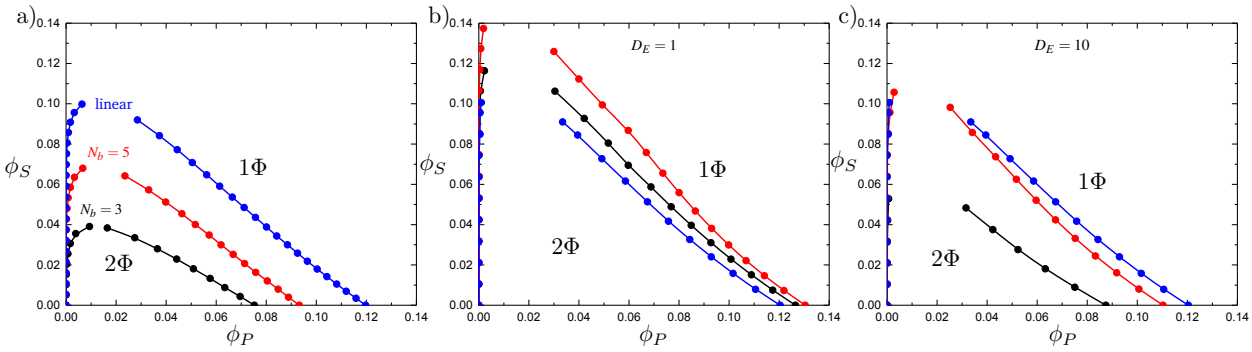

Figure 3.7: Complex coacervation phase behavior for branched polymers and linear polymers. (a) Simulation phase diagrams for N_b values of 3 (black) and 5 (red). A linear-linear system with an equivalent number of charged monomers is shown for comparison in blue. Comb polymers and linear polymers have a smaller immiscible region than an equivalent linear-linear system. (b) Phase diagrams generated from theory using increased values of Λ. The qualitative difference between different branch lengths does not sufficiently reflect the different size of the immiscible region seen in simulation. (c) By considering decreased counterion condensation on the branch ends, the qualitative trends from simulations are better matched.

3.3.2 Comb Polymer Architecture

Comb polymers, where the branches are charged, have been investigated previously in experimental studies on coacervation [10]. While comb polyelectrolytes can form coacervates when paired with linear counterparts, the two-phase region is significantly smaller than for coacervates formed from two linear polyelectrolytes [10]. Preliminary simulation results from our group were parameterized to match these experimental observations [10].

We now study comb polyelectrolytes that are parameterized to match the polymer models used in this paper, and use theory to provide a mechanistic argument for this architectural effect. Figure 3.7a demonstrates the phase diagrams for coacervates formed from a linear polyelectrolyte and a comb polyelectrolyte, with $N_b = 3$ and $N_b = 5$, compared to coacervates formed from two linear polyelectrolytes. In agreement with previous experiment and simulation, [10] a decrease in branch length considerably shrinks the two-phase coacervation region of the phase diagram.

We use transfer matrix theory to understand these drastic changes in the coacervate phase behavior of branched polymers. We consider a comb polymer to be equivalent to *uncorrelated* segments of length N_b. Each overall polymer still has only a single contribution

to the translational entropy, however the individual branches interact as if they were shorter segments. To incorporate this into our theory, we rewrite the partition function for a test comb polymer as:

$$\Xi = \left(\xi_{(N_b)}\right)^{N/N_b} \tag{3.3}$$

Where the value of $\xi_{(N_b)}$ is a transfer matrix-based quantity associated with a single branch of length N_b:

$$\xi_{(N_b)} = \vec{\psi}_0^T \mathbf{M}_E(s_{N_b-1}, s_{N_b-2}) \cdots \mathbf{M}(s_3, s_2)\mathbf{M}(s_2, s_1)\vec{\psi}_E \tag{3.4}$$

In this case, we distinguish between the transfer matrices $\mathbf{M}$ and $\mathbf{M}_E$, with the latter representing a different transfer matrix that specifically considers the branch end. The vector $\vec{\psi}_E$ has also been changed from the $\vec{\psi}$ in Equation 2.21 to account for the other end of the charged branch. To distinguish $\mathbf{M}$ and $\mathbf{M}_E$, and $\vec{\psi}$ and $\vec{\psi}_E$, we alter the weights for forming a vacant adsorption site ($D \to D \times D_E$). This represents the effects of decreased counterion condensation at the ends of the branch.

Branch ends also play a role in excluded volume, via the parameter Λ in $\kappa(\Lambda\phi_P + \phi_S)^3$. Λ accounts for the difference in the effective volume of polymer chains, which have overlapping spheres of excluded volume in our model. In previous work, we calculated this to be $\Lambda = 0.6875$. Branch ends are unconnected on one side, however, and have more accessible excluded volume. We calculate this to be $\Lambda_E = 0.8438$. In the comb-linear coacervate systems, the effective excluded volume for the overall system is a weighted average $\langle\Lambda\rangle$ that is dependent on the relative ratio of branch ends to non-branch-end monomers. For our system, we find that $\langle\Lambda\rangle = \left[(N_B - 1)\Lambda + \Lambda_E\right]/N_B$.

In Figure 3.7b we first demonstrate the effect of changing the excluded volume parameter Λ. Indeed, the increased excluded volume parameter $\langle\Lambda\rangle$ from branched polymers noticeably changes the two-phase coacervate region of the phase diagram; however, it is not sufficient to qualitatively reproduce the effects seen in simulation, and in fact leads to an increase in the two-phase coacervate forming region of the phase diagram. Instead, we require $D_E > 1$ to demonstrate the decreased driving force for counterion condensation at the branch ends. This is shown in Figure 3.7c for $D_E = 10$, qualitatively demonstrating that decreased counterion condensation at branch ends leads to a significantly smaller two-phase coacervate region.

This mechanism is related to the combinatoric justification for the effect of stiffness on coacervation. For stiff polymers, longer runs of polyelectrolyte decrease the number of possible configurations that condensed species can have. In comb polymers, the mechanism is primarily related to the diminished condensation on branch ends. This similarly limits the number of possible configurations of condensed species, by making it increasingly likely that these adsorption sites are vacant and thus not contributing to the number of adsorption configurations. In both cases, either by increasing κ_θ or decreasing N_b, the end result is that there are fewer numbers of chain-chain interactions; this decreases the entropic driving force for coacervation, which is reflected in the simulation results.

3.3.3 Divalent Ions

We consider the case that one or both of the salt ions are divalent. Mutlivalent ions can present a challenge for polyelectrolyte theory, because they can exhibit behavior inconsistent with standard Poisson-Boltzmann theory. For example, DNA can be condensed with multivalent counterions, [133] because electrostatic correlations induce like-charge attraction between DNA strands [138,139]. This is just one of a whole range of correlation effects, including multivalent-induced brush collapse [134, 135] and like-charge attraction between surfaces [140]. Coacervates exhibit significant electrostatic correlations, in particular due to the connectivity between polyelectrolyte charges; our transfer matrix theory includes this connectivity, and indeed we can extend this theory to describe the effects of divalent salt ions.

To include divalent ions, we include a new possibility in the transfer matrix. Instead of having only a state (that we now call C') to designate a bound counterion, we consider the possibility that the next monomer is also condensed with the same counterion (in a state we call C, see schematic in Figure 3.8). We thus use the following matrix $\mathbf{M}_{2+}(s_i, s_{i-1})$, with

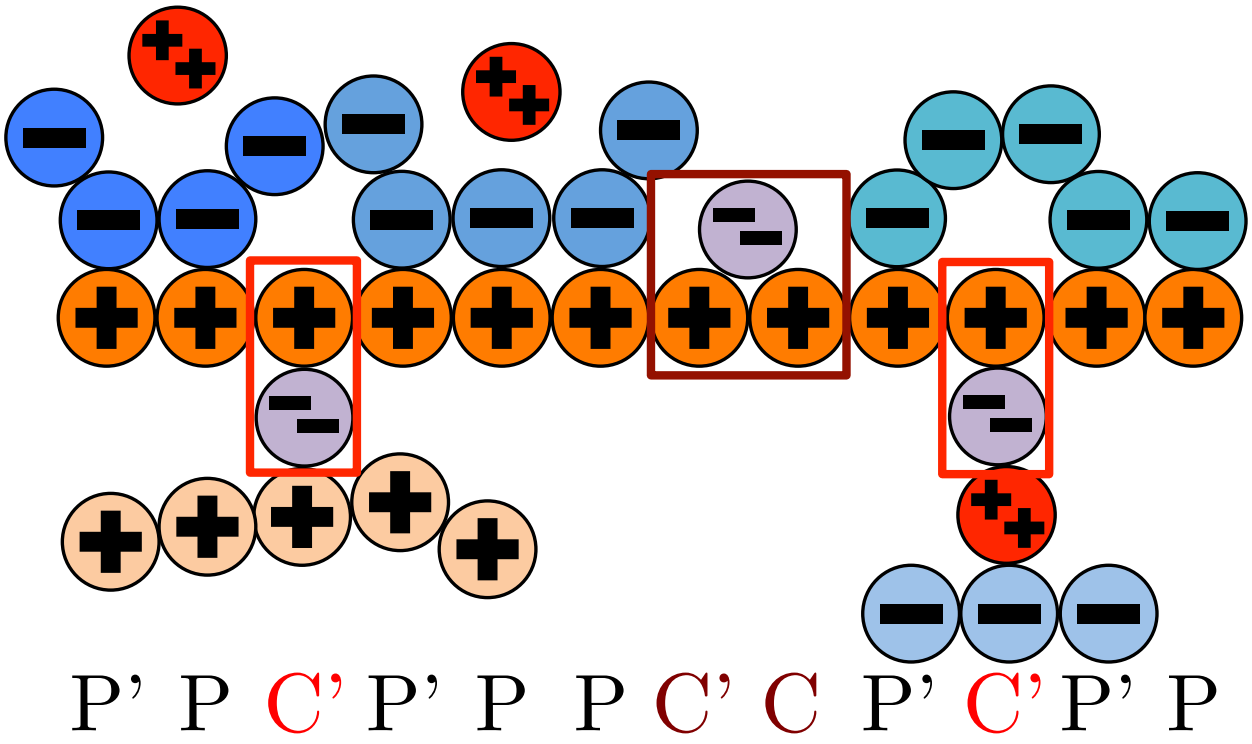

Figure 3.8: Our model for a polyelectrolyte interacting with divalent ions. We describe the environment around the test polycation (orange) as including adsorbed polyanions (P' or P) or divalent ions (C' or C). The first monomer with an adsorbed polymer is denoted with the prime (P'), following our previous notation [93]. We now do this also for the divalent ions, which can only be adsorbed to a single polyelectrolyte monomer (singly adsorbed, with only a single C', light red) or to two adjacent monomers (doubly adsorbed, with a $C'C$ pair, dark red).

the subscript 2+ denoting that the test polymer has divalent counterions:

$$\mathbf{M}_{2+}(s_i, s_{i-1}) = \begin{bmatrix} CC & CC' & CP & CP' & C0 \\ C'C & C'C' & C'P & C'P' & C'0 \\ PC & PC' & PP & PP' & P0 \\ P'C & P'C' & P'P & P'P' & P'0 \\ 0C & 0C' & 0P & 0P' & 00 \end{bmatrix} = \begin{bmatrix} 0 & F & 0 & 0 & 0 \\ A & A & A & A & A \\ 0 & 0 & E & 2E & 0 \\ B & B & B & B & B \\ D & D & D & D & D \end{bmatrix} \tag{3.5}$$

This introduces the possibility that there are both singly- and doubly-adsorbed, divalent counterions. Singly-adsorbed divalent counterions only neutralize a single polyelectrolyte charge on a given chain, with the other charge neutralizing either a different polyelectrolyte

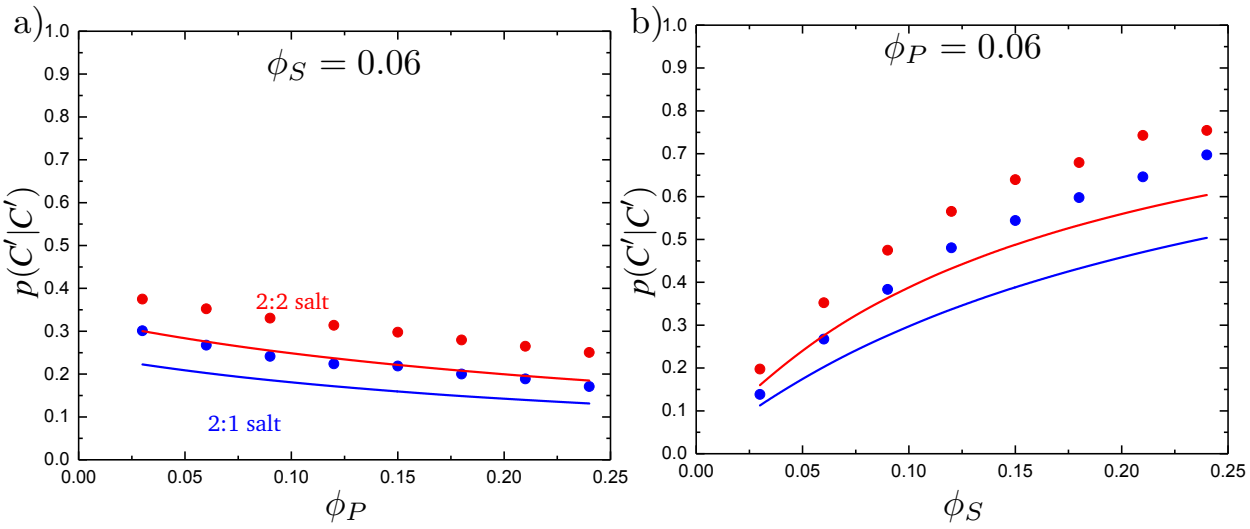

Figure 3.9: The probability of transitioning between singly-condensed salt ions, $p(C'|C')$, as a function of (a) ϕ_P and (b) ϕ_S. Points are simulation values and lines are theoretical calculations.

or the oppositely charged ion (see light red boxes in Figure 3.8). Doubly-adsorbed divalents neutralize an equivalent two charges on the polyelectrolyte (see dark red boxes in Figure 3.8). The factor F is chosen to reproduce the balance of both singly- and doubly-adsorbed possibilities as determined by simulation. By introducing the two adsorption possibilities for the divalent counterions, an additional combinatorial entropy must be included to consider how the divalent counterions can be 'chosen' to be either singly or doubly-adsorbed. We define a fraction Θ of doubly-adsorbed divalent counterions, and use it to write a free energy expression for the divalent cation/divalent anion $(2:2)$ case:

$$\begin{aligned}\frac{\mathcal{F}_{2:2}}{Vk_BT} &= \tfrac{\phi_P}{N}\ln\phi_P/2 + \phi_S\ln\phi_S/2 + \phi_W\ln\phi_W - \\ &-\tfrac{\phi_P}{2}\ln\xi_{2+} + \phi_P\theta_{C'}\left[\Theta\ln\Theta + (1-\Theta)\ln(1-\Theta)\right] + \\ &+\kappa(\Lambda\phi_P + \phi_S)^3 \end{aligned} \tag{3.6}$$

Here, we define a test-chain partition Ξ_{2+} function as:

$$\Xi_{2+} = \vec{\psi}_0^T\mathbf{M}_{2+}^N\vec{\psi} = \xi_{2+}^N \tag{3.7}$$

Correspondingly, the value of Θ can be given by:

$$\Theta = \left(\frac{\partial \ln \xi_{2+}}{\partial \ln F} \right) / \theta_{C'} \tag{3.8}$$

Where $\theta_{C'} = (\partial \ln \xi_{2+} / \partial \ln A)$ is the fraction of polymer sites with initially-adsorbed divalent ions. A similar expression can be derived for the free energy of a 2 : 1 salt, by replacing the $-\phi_P \ln \xi_{2+}/2$ term with $-\phi_{P-} \ln \xi_{2+}/2 - \phi_{P+} \ln \xi/2$, and including a factor of 1/2 on the divalent singly/doubly adsorbed entropy term. Here, only one of the two polyelectrolyte species includes the transfer matrix and entropic contribution associated with the divalent salt.

We test this model by comparing with simulation. Local correlations are described by the sequence of species adsorbed along the test molecule, and we specifically consider the probability of having a C' immediately following another C', $p(C'|C')$. This is plotted in Figure 3.9 for both the 2 : 1 and 2 : 2 salt cases, as a function of ϕ_P (Figure 3.9a) and ϕ_S (Figure 3.9b). Both theory and simulation are plotted, demonstrating excellent agreement. We also consider the fraction of the adsorbed counterions that are doubly-adsorbed Θ, which can again be directly determined from simulation and calculated from theory. We plot Θ in Figure 3.10, again with both 2 : 1 and 2 : 2 salts. Both theory and simulation match nearly quantitatively as a function of ϕ_P and ϕ_S.

Figure 3.11a plots phase diagrams in the ϕ_S-ϕ_P plane, calculated from simulation. Consistent with experimental observations, [8] increased salt valency drastically decreases the two-phase coacervation region. Along with this decrease, there is a marked change in the salt partitioning. For 1 : 1 salts, $\lambda < 1$ indicates that salt is depleted from the coacervate phase. However, for 2 : 1 this depletion is significantly weaker and for 2 : 2 salts $\lambda > 1$, indicating that the divalent salts prefer the coacervate phase. Our theory reproduces these simulation observations, shown in Figure 3.11c and d; we see the shrinking of the coacervation region upon inclusion of divalent salts, and also show that $\lambda > 1$ for 2 : 2 salts.

These observations are well-explained using an entropic argument. For monovalent (1 : 1) ions, entropy is increased during coacervation due to the increased configurations of polymers and ions that are adsorbed to the test chain. This entropic increase is large with

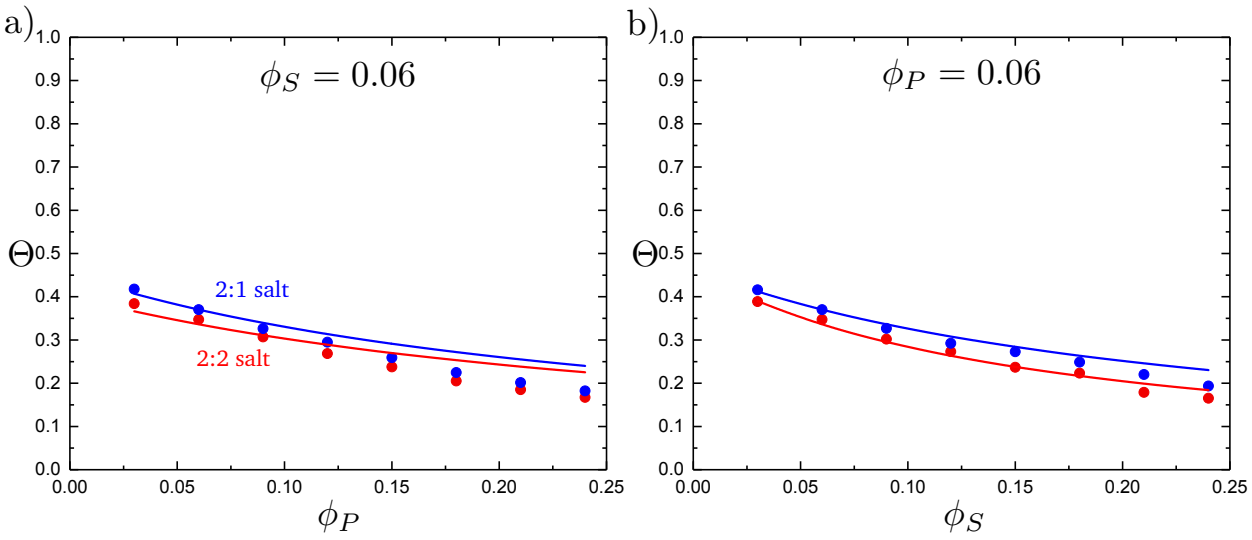

Figure 3.10: The probability of a salt ion double condensing, Θ, as a function of (a) ϕ_P and (b) ϕ_S. Points are simulation values and theoretical calculations are represented by lines.

monovalent ions, because there are many configurations when a single charged monomer can be neutralized by a single salt ion. To contrast, a divalent ion neutralizes two charged monomers, significantly reducing the number of configurations of charged species adsorbed to the test chain. In this sense, a divalent ion is equivalent to two monovalent ions *if* those monovalent ions were constrained to be adsorbed next to each other along the chain. This decreases the entropic driving force for coacervation.

The inversion of λ, which shows that monovalent salt is depleted from the coacervate while divalent salt is depleted from the supernatant, is also entropically driven in theory. This is driven by the $\phi_P \theta_{C'}[\Theta \ln \Theta + (1-\Theta)\ln(1-\Theta)]$ term in Equation 3.6, which accounts for the ways in which the adsorbed divalent charges can be neutralized by the surrounding polyelectrolyte chains. A given divalent charge is essentially only neutralized by individual opposite charges in the polymer-dilute supernatant, but in the coacervate any combination of polyelectrolyte or counterions can be used to neutralize the divalent charge.

Both of these effects are conceptually related to the behaviors of polyelectrolyte chains, with the divalent ion behaving essentially the same as a polyelectrolyte of length $N = 2$. For example, the phase behavior is similar to the effect of polyelectrolyte stiffness, where longer runs of aligned polyelectrolytes limit the number of adsorption configurations for the test chain. In the divalent case, the neutralization of two monomers at a time similarly

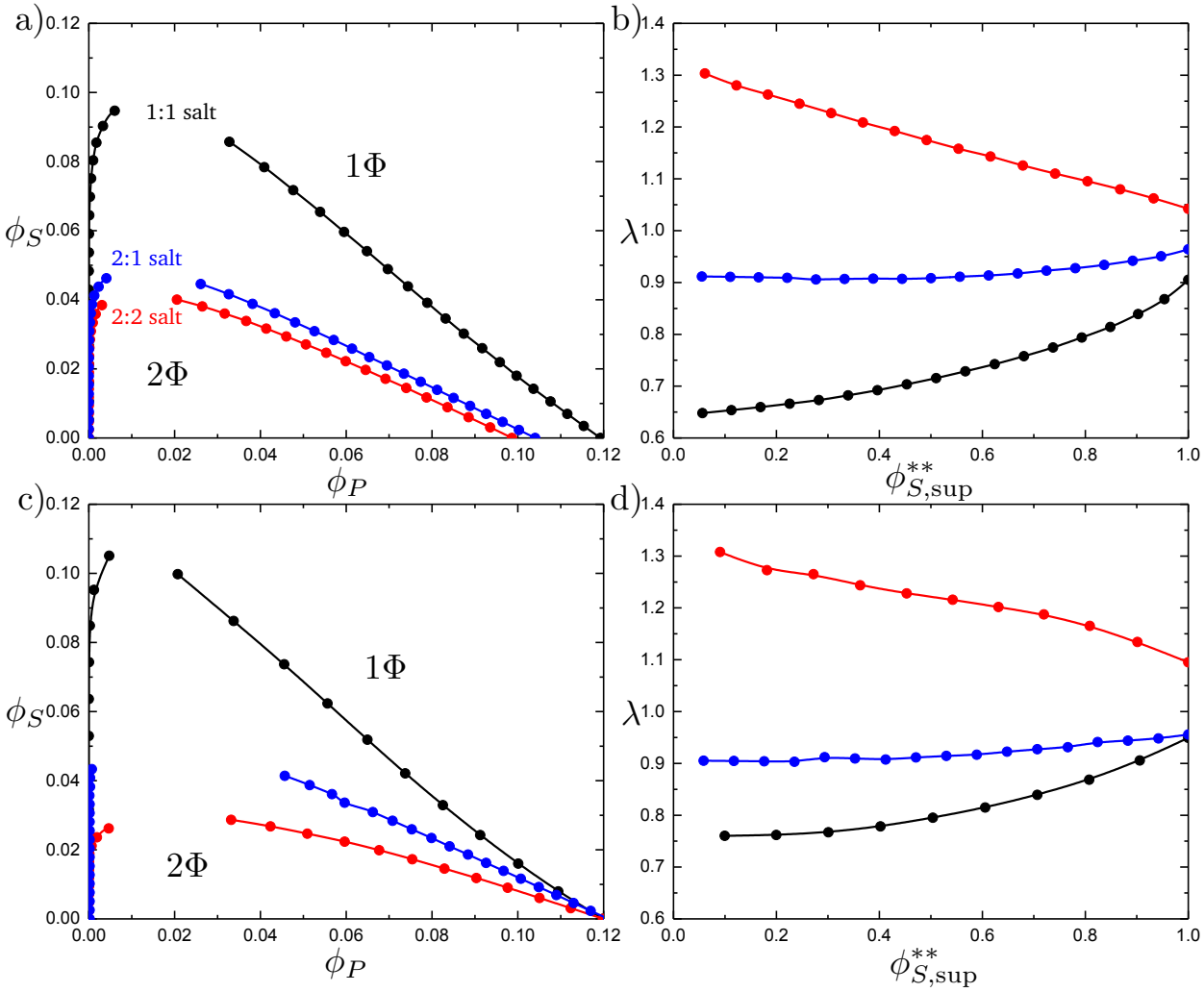

Figure 3.11: Complex coacervation phase diagrams with different salt valencies. (a) Simulation phase diagrams for a monovalent salt (1 : 1 black), a divalent salt (2 : 2 red), and a salt with one divalent species and one monovalent species (2 : 1 blue). Increased salt valency causes the immiscible region to shrink. (b) Simulation calculated salt partitioning for the various salt valencies. The 1 : 1 salt favors the supernatant phase as does the 2 : 1, but not to the same extent. The 2 : 2 salt favors the coacervate phase. (c) Theoretical phase diagrams for the various salt valencies. The same qualitative phase behavior is observed as seen in simulation. (d) Theoretically calculated salt partitioning shows the same qualitative trends as the simulation. This model of complex coacervation suggests the reason for the change in salt partitioning is due to ions double condensing onto the polymer chain. F, from the transition matrix $\mathbf{M}_{2+}(s_i, s_{i-1})$, has a value of 1.5, which was determined by matching simulation data.

limits the number of configurations and leads to less entropic driving force for coacervation.

The entropic driving force for divalents to partition to the coacervate is also similar to the

underlying driving force for coacervation, where the species (in this case the divalent ion, but in the coacervate case the polyelectrolyte) finds it entropically favorable to interact with many configurations of neighboring, oppositely charged species.

3.4 Conclusion

We have used a combination of simulation and theory to explore ways in which polymer physical features (chain stiffness, architecture, and salt valency) play a role in complex coacervation. We not only demonstrate that these features *can* have marked effects on coacervate phase behavior, but we use theoretical results to provide a mechanistic understanding of *how* molecular structure influences charged polymers. We show that this is related to how these molecular features affect the configurational entropy of condensation on test polymers. Phase behavior is indeed linked to the 'number' of species that are condensed, either via long runs of aligned polymer-polymer chains, via weak counterion condensation in short branches, or via divalent salt ions.

These combinatoric principles have limitations, in particular outside the limit of high charge density. It is unclear how to systematically modify this theory for lower charge densities, and transition to coacervate theories that focus on charge fluctuation-driven attractions. We also note the limitations on the model due to simplifications of the salt interactions, which are not explicitly included except in a phenomenological cubic term to capture excluded volume. We justify this assumption due to the significant screening of these small molecule species, however we will have to reevaluate our assumptions if electrostatic interactions become stronger or short-range interactions become significant.

Despite these approximations, we capture how polymer physical behaviors influence coacervation for polyelectrolyte systems with experimentally relevant charge densities and electrostatic interaction strengths. This builds upon a simulation and theoretical model that qualitatively matches with experimental results in previous literature, and provides new physical intuition to guide experiment and molecular design in this active area of polymer research.

Now that the utility of the transfer matrix theory for investigating molecular features has

been established, we proceed to study charge sequence effects along the polymer backbone. Initial investigations focus on modifying our simulation methods to qualitatively capture experimental trends, discussed in Chapter 4. In Chapter 5, we extend this transfer matrix theory to study a large number of charge sequence effects.

CHAPTER 4

MONTE CARLO SIMULATION INVESTIGATION OF SEQUENCE-DEFINED COACERVATION

The contents of this chapter are based on the publication L. Chang, T.K. Lytle, M. Radhakrishna, J.J. Madina, J. Vélez, C.E. Sing, S.L. Perry, *Nat. Comm.* 2017, 8, 1273 [11].

4.1 Introduction

Polymer properties follow primarily from their one-dimensional nature, with their length distinguishing them from other soft materials. This length is due to the end-to-end connection of monomer units; the precise sequence of these monomers is capable of encoding information along the backbone [141, 142]. However, interactions between these long chains are typically described in synthetic polymers by coarse-grained 'effective' interactions between immediate neighboring molecules. [143] Polymer physics relies on the use of the these interactions, described by a parameter χ, which has its origins in average, pairwise, short-range interactions [143, 144]. Biological materials, however, use a richer array of polymer-polymer interactions where this sort of 'averaging' may obscure relevant physical properties [50] and limit our ability to understand the complicated biological structure-function relationships encoded at the molecular level. The use of charge in sequence-controlled biopolymers is ubiquitous. [37,38,145] For example, charge sequence is shown to dictate the conformational behavior of intrinsically-disordered proteins (IDPs), [39] and theoretical work has similarly connected IDP sequence to charge-driven phase separation [146]. Sequence is correspondingly a key aspect of intracellular compartmentalization via membrane-less organelles [37].

While solid-phase synthesis methods [147] have long been used to prepare sequence-controlled polymers, recent advances in synthetic polymer chemistry have expanded the palette of sequence-defined polymerization methods [141, 142, 148–150]. For instance, ad-

vances in chemical synthesis have enabled the evaluation of precise charge spacing effects in ionomers [151, 152]. However, a general understanding of the physics of sequence-defined polymer materials remains underdeveloped.

Initial efforts have begun to elucidate how monomer sequence physically influences polymer material properties. In particular, the continuum of behaviors between block and random copolymers has been probed in terms of equilibrium properties (e.g., phase behavior, [153,154] compatibilization [155]) using coarse-grained modeling and theory. These works consider portions of a vast sequence parameter space, using monomer sequence correlations (i.e., 'blockiness'), [153, 154] sophisticated machine learning methods, [155] or sequence gradients [156]. These situations focus on short-range dispersive interactions, where monomers interact primarily with their immediate neighbors. Charge interactions differ from short-range interactions, leading to different types of design rules; this difference can be tied to both the long-range nature of electrostatic interactions, and the complementarity between positive and negative charges suppressing like interactions and promoting partner interactions.

In this chapter, we demonstrate that sequence specificity of charged monomers can be used to precisely control the self-assembly and thermodynamics of a class of materials known as complex coacervates [65]. Charge-based sequence control allows for dramatic modulation of polymer-polymer interaction strengths without changing the overall monomer composition. We experimentally and computationally demonstrate the effects of charge patterning, and establish the physical picture and design rules necessary to show why charge patterning has such a profound effect on coacervate phase behavior.

4.2 Methods

4.2.1 Coacervation of Sequence-Controlled Peptides

Polypeptides were prepared via solid-phase synthesis using microwave-enhanced, automated synthesis (Liberty Blue, CEM Corp.) using standard methods [147]. Poly(glutamate) and the poly(glycine-co-lysine) polymer for $\tau = 16$ were synthesized using amino acids of alter-

nating (D and L) chirality to mitigate inter-peptide hydrogen bond formation. [157–159] All other peptides were composed of only L amino acids. See synthesis details in [11].

Complexation was performed using stoichiometric quantities of positive and negatively charged polypeptides at a total charged residue concentration of 5 mM at pH 7.0 unless otherwise specified. Samples were prepared by first mixing a concentrated solution of NaCl with MilliQ water in a microcentrifuge tube (1.5 mL, Eppendorf), followed by the polyanion. The resulting mixture was then vortexed for 5 s before addition of the polycation to a final volume of 120 μL. The final mixture was vortexed for at least 15 s immediately after the addition of polycation to ensure fast mixing. The effect of salt was examined over the range of 0 to 520 mM NaCl. All samples were prepared immediately before analysis and studied at room temperature (25°C). Optical microscopy was used to identify the CSC.

ITC experiments were performed at 25°C on a MicroCal Auto-iTC200 system (Malvern Instruments, Ltd.) All experiments were performed by injecting a 5 mM solution of the charge-patterned polycation (with respect to the number of lysines) into the sample cell containing 0.625 mM polyanion. Both solutions were prepared at a salt concentration of 25 mM NaCl and pH = 7.0 so as to minimize interference associated with heats of dilution. An initial injection of 0.5 μL was performed, followed by 24 injections of 1 μL each. An injection duration of 2 s followed by a 180 s equilibration time was used. Constant stirring speed was applied at a rate of 1000 rpm. All experiments were performed in triplicate. Analysis of ITC data was performed using the method reported previously [85]. Additional details are available in [11].

4.2.2 Monte-Carlo Model for Sequence Coacervate Systems

The simulation model used for this is a modification of the model in Section 2.2 to account for sequence-defined polycations and homopolyanions. Sequence-defined polycations have both neutral monomers and charged monomers within the same chain with a sequence that will be specified in Section 4.3. We fix the degree of polymerization, N, to be 48 beads for all chains. Polycations are patterned with 24 neutral beads and 24 charged beads. n_{P+} is twice the value of n_{P-} to ensure the polymers are charge neutral without additional

salt. Charged beads, including all salt ions and polymer charges, have a hard core diameter $\sigma = 4.25\mathring{A}$. Neutral beads have smaller diameter $\sigma_0 = 0.25\sigma$, motivated by the absence of a hydration shell that is implicitly included in the hard core radius of the charged species in the RPM. Practically, the neutral bead size does have a measurable effect on the magnitude of coacervate phase behavior; we have parameterized this value to match experimental and computational phase behavior. To incorporate the different bead sizes into the model, the appropriate hard sphere potential is:

$$u_{HS}(r_{ij}^{\alpha,\beta}) = \begin{cases} \infty & r_{ij}^{\alpha,\beta} < (\sigma_i + \sigma_j)/2 \\ 0 & r_{ij}^{\alpha,\beta} \geq (\sigma_i + \sigma_j)/2 \end{cases} \tag{4.1}$$

where σ_i is the hard core diameter of bead i. All other potentials remain the same.

4.2.3 Widom Insertion to Calculate Free Energy Landscape

The excess chemical potentials, $\mu_{EXC,i}$ for all species $i = P+, P-, +, -, 0$ were calculated using Widom insertion as described in Section 2.2. However, modification of the Widom insertion technique was necessary to calculate the polyelectrolyte excess chemical potential due to the monomer sequence, illustrated schematically in Figure 4.1. The polycation pattern is shifted along the various chains in the system so each monomer in the charge pattern has representative chain ends. Widom insertion is performed on each of the different types of chain ends, and, if the inserted polycation monomer is charged, a corresponding polyanion monomer is inserted. The chemical potentials thus calculated are added together and divided by the total number of monomers inserted for all of the chain ends. This gives each monomer's excess chemical potential, which can be integrated via Equation 2.11 to yield the excess free energy.

4.2.4 Along-The-Chain Correlation Functions

We characterize the structure and sequence behaviors of charge sequences using a pair of correlation functions, C_1 and C_2, that characterize spatial and sequence-based structure

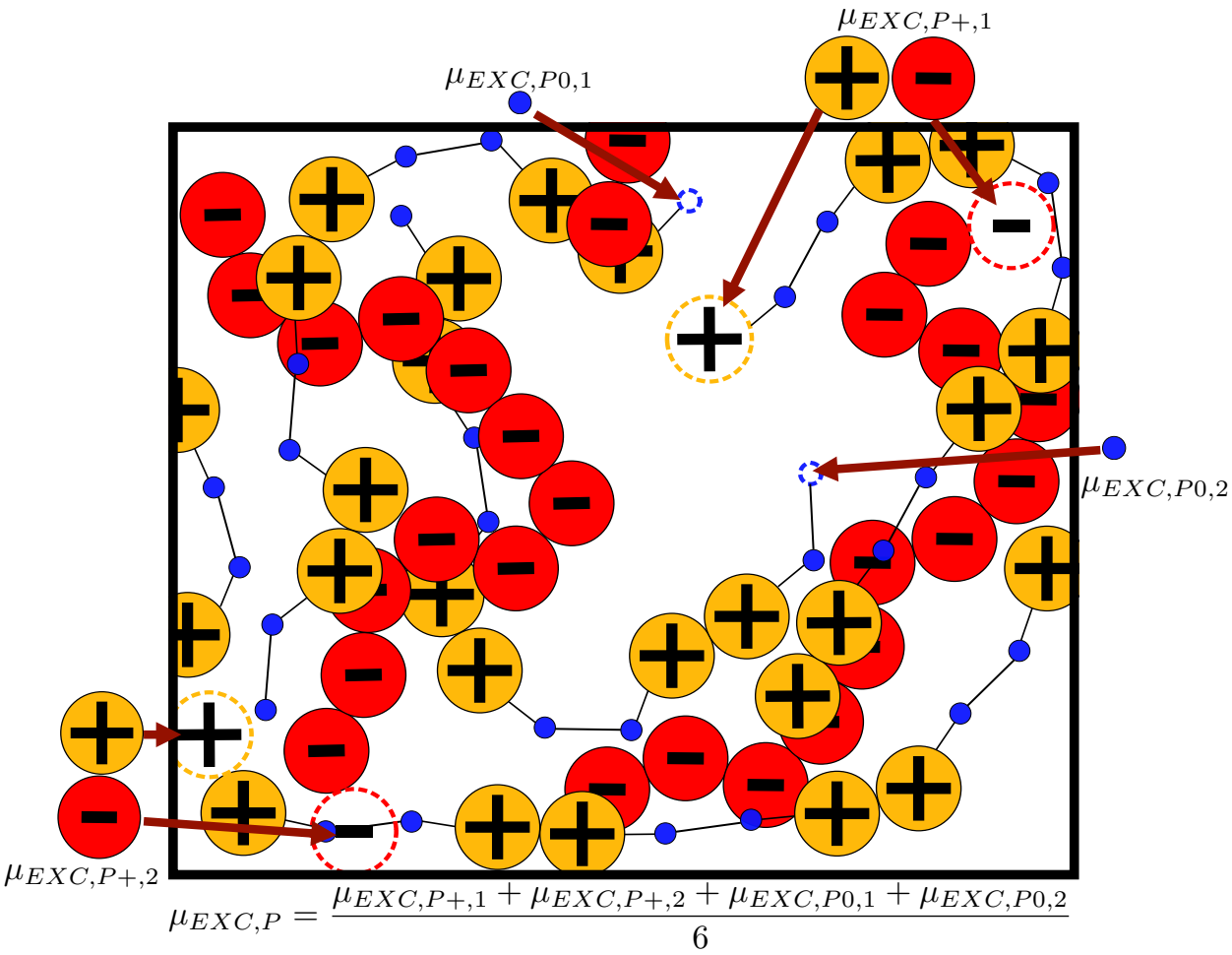

Figure 4.1: Example calculation for the polymer excess chemical potential with a $\tau = 4$ repeating pattern. Charged polycation monomers are orange, neutral polycation monomers are blue, and polyanion monomers are red. Bonds are denoted by solid lines. Sequence-defined polycation chains are generated such that each bead in the repeating pattern is represented by a chain end. In this case, polycation chain ends correspond to the first charged bead, the second charged bead, the first neutral bead, and the second neutral bead. Widom insertion is then performed on the different chain ends, and, if the inserted polycation monomer is charged, a polyanion monomer is also inserted. For this particular pattern, the four excess chemical potentials are $\mu_{EXC,P+,1}$, $\mu_{EXC,P+,2}$, $\mu_{EXC,P0,1}$, and $\mu_{EXC,P0,2}$. These correspond to insertion of the first charged polycation monomer with a polyanion monomer, the second charged polycation monomer with a polyanion monomer, the first neutral polycation monomer, and the second neutral polycation monomer, respectively. These excess chemical potentials are added together and divided by the total number of monomers inserted for all excess chemical potentials. For this pattern, the total number of monomers inserted for all excess chemical potentials is 6. This scheme can be generalized to any pattern size.

respectively. Both consider an initial pair of oppositely-charged monomers, i and j, that are

separated by a distance less than or equal to a cutoff r_{CC}. We then characterize properties of two beads a constant number of monomers Δs along the chain contour, $i+\Delta s$ and $j+\Delta s$.

$C_1(\Delta s)$ provides a structural measure of looping among neighboring polyelectrolytes. We calculate the probability that $i + \Delta s$ and $j + \Delta s$ are also within the cutoff r_{CC}, *if* both monomers are charged. Formally, this is given by the equation:

$$C_1(\Delta s) = \frac{\langle \sum_i \sum_j \delta(z_i-1)\delta(z_j+1)\delta(z_{i+\Delta s}-1)\delta(z_{j+\Delta s}+1)\Theta(r_{CC}-r_{ij})\Theta(r_{CC}-r_{i+\Delta s,j+\Delta s})\rangle}{\langle \sum_i \sum_j \delta(z_i-1)\delta(z_j+1)\delta(z_{i+\Delta s}-1)\delta(z_{j+\Delta s}+1)\Theta(r_{CC}-r_{ij})\rangle} \tag{4.2}$$

Here the function $\Theta(x)$ is the Heaviside function that is $\Theta(x) = 1$ for $x \geq 0$ and $\Theta(x) = 0$ for $x < 0$. The average denoted by the angle brackets $\langle \cdots \rangle$ represents ensemble averages taken over the course of a simulation, and $\delta(x)$ is the Dirac delta function. This is a measure of conformational correlations by determining the subset of polyelectrolyte charges that loop over a number of monomers Δs.

This measure of $C_1(\Delta s)$ between charged particles has some values that are necessarily 0 due to the periodicity of the pattern; these are removed from representations of this function for clarity.

$C_2(\Delta s)$ is a related measure of the sequence correlations:

$$C_2(\Delta s) = \frac{\langle \sum_i \sum_j \delta(z_i-1)\delta(z_j+1)\delta(z_{i+\Delta s}-1)\delta(z_{j+\Delta s}+1)\Theta(r_{CC}-r_{ij})\Theta(r_{CC}-r_{i+\Delta s,j+\Delta s})\rangle}{\langle \sum_i \sum_j \delta(z_i-1)\delta(z_j+1)\Theta(r_{CC}-r_{ij})\Theta(r_{CC}-r_{i+\Delta s,j+\Delta s})\rangle} \tag{4.3}$$

The difference here is that we are now considering the subset of loops that consist of charged monomers. For this work, we set $r_{CC} = 1.5\sigma_+$.

4.2.5 One-Dimensional Absorption Model

We can use simulation data of a single, dilute polyelectrolyte chain in a salt solution to calculate the entropic driving force for counterion release. To do this, we map simulation data to a one-dimensional adsorption model where each monomer of the polyelectrolyte chain is a 'site' that can contain a condensed counterion. These adsorbed counterions are in equilibrium with the external solution that is a constant chemical potential μ reservoir of salt

ions. Each adsorbed ion 'feels' an effective binding energy ϵ_i that is due to the electrostatic characteristics of the chain and the surrounding condensed charges, and is a function of the chain index i. The grand canonical partition function for adsorption on to a chain of length N is thus:

$$\Xi = \prod_{i}^{N} \left(1 + e^{-\beta(\epsilon_i - \mu)}\right) \tag{4.4}$$

Standard statistical mechanics leads to expressions for both the average number of adsorbed counterions $\langle n_i \rangle$ at a given index i and the overall entropy of the adsorbed counterions S_{ads}:

$$\sum_{i} \langle n_i \rangle = k_B T \left(\frac{\partial \ln \Xi}{\partial \mu} \right)_T = \sum_{i} \frac{e^{-\beta(\epsilon_i - \mu)}}{1 + e^{-\beta(\epsilon_i - \mu)}} \tag{4.5}$$

$$S_{ads} = k_B \left(\frac{\partial T \ln \Xi}{\partial T} \right)_\mu = k_B \left[\sum_{i} \ln \left(1 + e^{-\beta(\epsilon_i - \mu)}\right) + \frac{\epsilon_i}{k_B T} \left(\frac{e^{-\beta(\epsilon_i - \mu)}}{1 + e^{-\beta(\epsilon_i - \mu)}} \right) \right] \tag{4.6}$$

This calculation requires determining the parameters of this model; namely, the values of the energy ϵ_i along the chain and the chemical potential of the reservoir. We use simulation to determine the former, and keep the latter as a parameter that is constant for all systems at a given salt concentration.

4.2.6 Determination of Counterion Condensation

We first determine the number and distribution of condensed counterions. We use a methodology described in Ou and Muthukumar to characterize the extent of counterion condensation along a dilute polyelectrolyte chain [120]. In this methodology, a cutoff distance r_C is chosen to represent the near-chain region; salt ions that are within r_C from a polyelectrolyte bead are considered condensed. We choose $r_C = 1.5\sigma_{P+}$. This is somewhat arbitrary, however we find that our results are not strongly affected by the specific choice of r_C. We schematically demonstrate this method in Figure 4.2. Condensed counterions are assigned to an index, i, which is the nearest polyelectrolyte chain's monomer. Averaged over a simulation run, we obtain a value of $\langle n_i \rangle$.

The size difference between charged and neutral beads causes the value of $\langle n_i \rangle$ to be

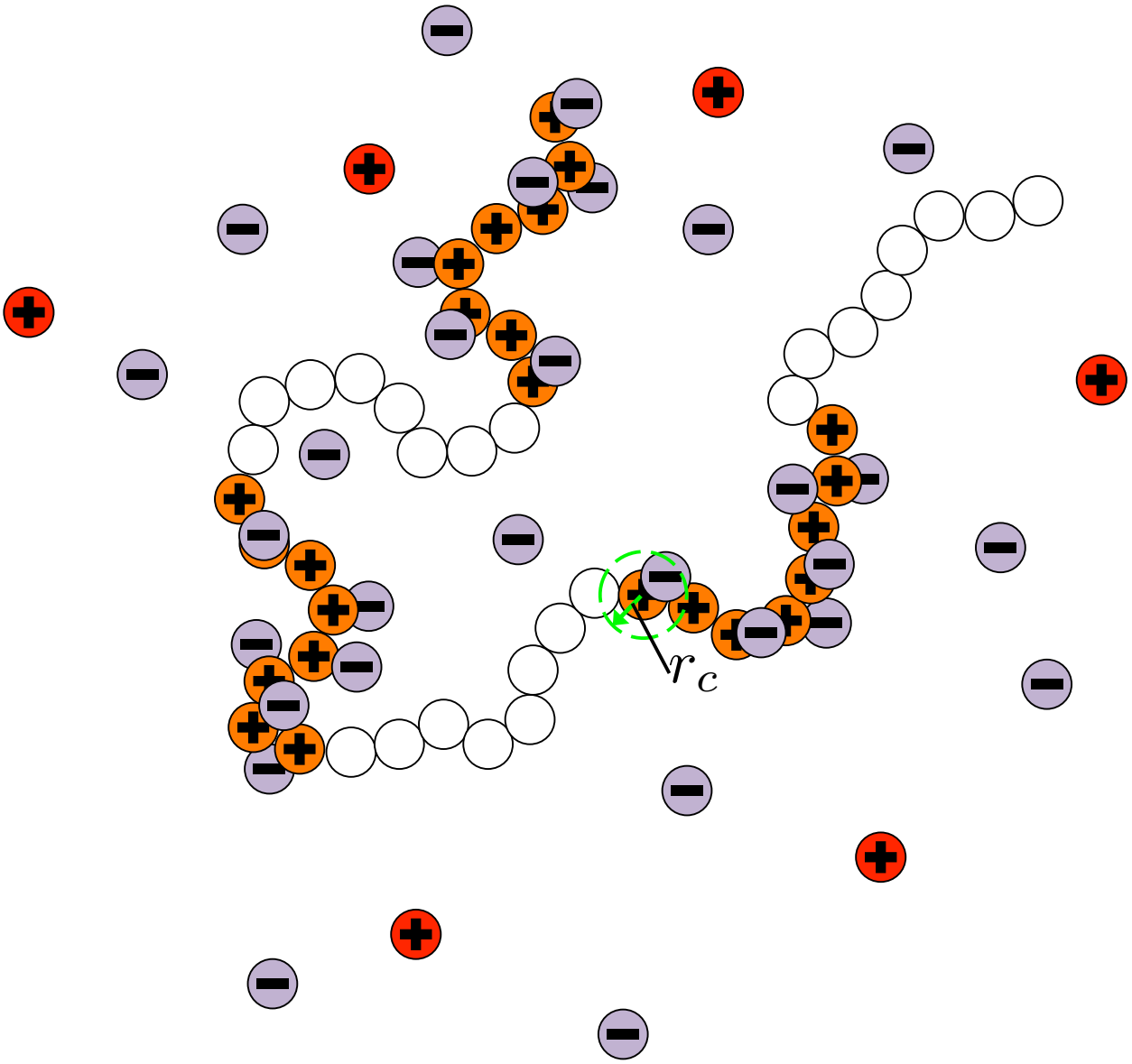

Figure 4.2: Simulation schematic of counterion condensation simulation. A single polyelectrolyte is simulated in a dilute salt solution. If an oppositely-charged salt ion is separated from a monomer by a distance r_C (green, dashed circle), it is considered condensed.

significantly different for a fixed r_C. $\langle n_i \rangle$ for a charged bead will typically be smaller than for a neutral bead because there is less unoccupied volume. This does not, however, represent a physically meaningful difference, but rather due to the arbitrary definition of r_C. Rather than vary r_C, we choose to normalize $\langle n_i \rangle$ to remove this disparity by calculating a value $\langle n_i^0 \rangle$ that is determined from simulations where the polyelectrolyte charge is taken to $z_{P+} = 0$. This establishes the number of counterions that would fit the definition of a condensed charge

for a neutral chain, which also varies with the different-sized beads. Indeed, this variation introduces the same effect as for a charged chain, so a ratio $\langle n_i \rangle / \langle n_i^0 \rangle$ removes effects due to the difference in unoccupied volumes between the two bead types.

4.2.7 Effective Binding Energy

We can convert the number of counterion beads into an effective ϵ_i. We do so using the previously determined relationship:

$$\langle n_i \rangle = \frac{e^{-\beta(\epsilon_i - \mu)}}{1 + e^{-\beta(\epsilon_i - \mu)}} \tag{4.7}$$

The effective energy ϵ_i is defined as the effect of the charged polyelectrolyte chain and the condensed counterions. We can thus set $\epsilon_i \to 0$ for the uncharged polyelectrolyte chains, leading to the relationship:

$$\langle n_i^0 \rangle = \frac{e^{\beta\mu}}{1 + e^{\beta\mu}} \tag{4.8}$$

We can thus define the relationship:

$$\frac{\langle n_i \rangle}{\langle n_i^0 \rangle} = \frac{e^{-\beta(\epsilon_i - \mu)} \left(1 + e^{\beta\mu}\right)}{e^{\beta\mu} \left(1 + e^{-\beta(\epsilon_i - \mu)}\right)} \tag{4.9}$$

The quantities $e^{\beta\mu} \ll 1$ and $e^{-\beta(\epsilon_i - \mu)} \ll 1$ for the cases we consider in this chapter (an *a posteriori* observation). We can thus simplify the relationship to the following expression for the effective ϵ_i:

$$\epsilon_i \approx -k_B T \ln \left(\langle n_i \rangle / \langle n_i^0 \rangle \right) \tag{4.10}$$

This enables the calculation of the entropy of counterion condensation, via equation 4.6, via the conversion of simulation data for n_i to the effective binding energy.

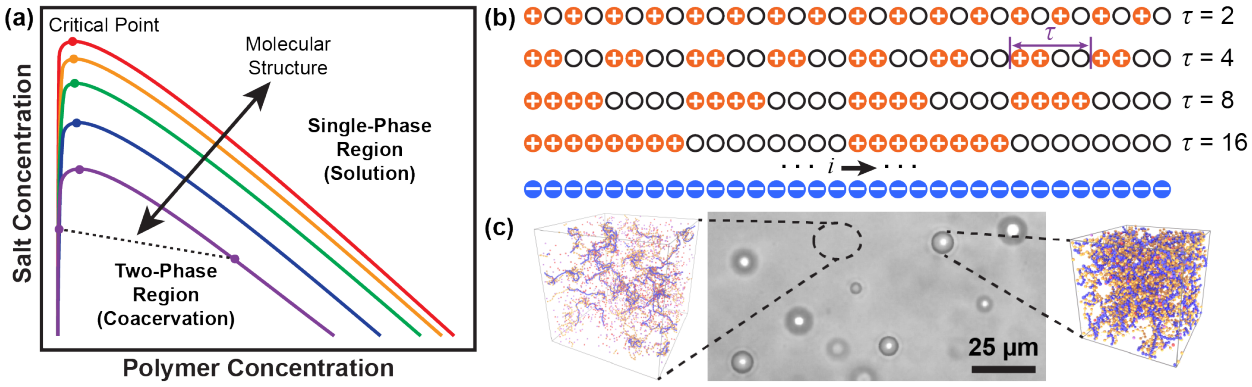

Figure 4.3: Molecular structure and sequence affects charge-driven phase separation (a) Qualitative sketch of a typical phase diagram of complex coacervate-forming polyelectrolytes. Coacervation occurs at low salt and polymer concentrations, where oppositely-charged polyelectrolytes undergo a liquid-liquid phase separation into polymer dense (coacervate) and polymer dilute (supernatant) phases. The different curves qualitatively represent how the immiscible region changes with different molecular features (charge monomer sequence, spacing, ion size, degree of polymerization, valency, etc.). (b) We show that charge monomer sequence is a molecular, feature which can be used to tune coacervation behavior. This simulation and experimental result is based on coacervation between a homopolyanion and a series of model, sequence-defined polycations with half of their monomers charged. These polycations are characterized by the periodic repeat of the monomer sequence, τ. (c) Coacervation is experimentally observed as droplets of a polymer-dense 'coacervate' dispersed in a polymer-dilute 'supernatant' phase. Simulation images correspond to conditions (salt concentration, 25 mM and $\tau = 2$) shown in Figure 4.4. Scale bar is 25 μm.

4.3 Results

4.3.1 Oppositely-Charged Polymers Drive Self-Assembly

Figure 4.3a schematically illustrates a standard complex coacervate phase diagram, in the space spanned by salt concentration c_S and polymer concentration c_P. At low salt and polymer concentrations, in the coexistence region (2Φ) underneath the *binodal* curve, the system spontaneously undergoes a phase separation into the high-c_P coacervate phase and the low-c_P supernatant phase. The coacervate and supernatant states are connected along a tie line, which is sloped to denote a difference in c_S between the two phases. Beyond the coexistence region, the system becomes completely miscible. Previous work has demonstrated that this phase diagram is extremely sensitive to molecular-level structure [4, 67]. Changes in bond length and charge size can drastically expand or shrink the coexistence region, reflecting

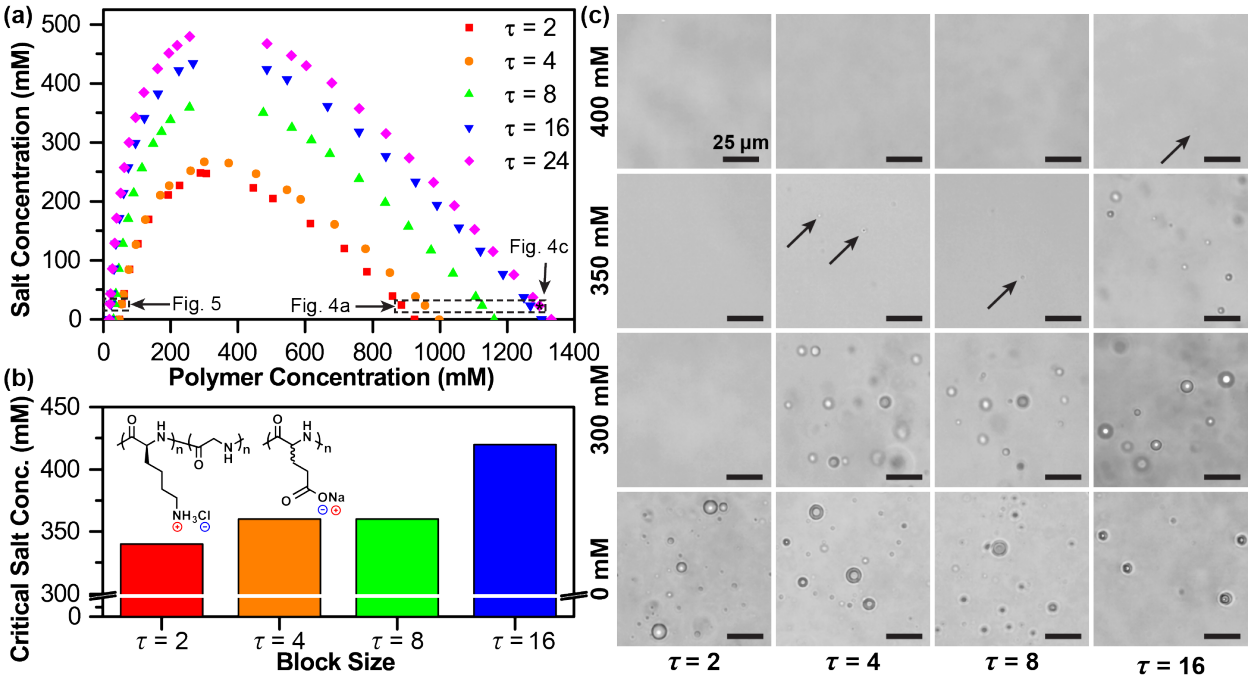

Figure 4.4: Coacervate phase behavior is affected by charge sequence in both simulation and experiment (a) Simulations demonstrate that the size of the coexistence region 2Φ increases with τ. Simulation conditions for Figs. 4.6, 4.7, and 4.8 are specified by asterisks/boxes, which denote points along the binodal curves at 25 mM NaCl. These points are considered, because the salt concentration values correspond to those used for isothermal titration calorimetry. (b) The experimental critical salt concentration (CSC) for sequence-defined coacervates at a variety of total charged monomer concentrations (solid 1 mM, stripes 5 mM, crosshatch 50 mM), plotted as a function their periodic block size ($\tau = 2$ to $\tau = 24$). Increasing τ leads to a marked increase in the CSC, qualitatively changing by as much as $50 - 150$ mM, consistent with simulations in (a). Error bars reflect the intervals between samples in these experiments. (c) A selection of optical micrographs corresponding to the data in (a), highlighting that the region of coacervation increases with τ. Arrows indicate the presence of tiny coacervate drops. Scale bars are 25 μm.

differences in local charge correlations that arise between the highly connected, oppositely-charged polyelectrolytes [4]. However, it is difficult to experimentally demonstrate these effects in a controllable fashion. Instead, changing charge monomer sequence provides both a way to experimentally observe the interplay between electrostatics and molecular structure, and enables the sequence-driven design of coacervate-based materials.

4.3.2 Tuning Molecular Interactions via Patterning

We use the 1-D pattern of charged monomers along a polymer backbone to controllably tune the local arrangement of charges, and thus the strength of charge interactions between coacervate-forming chains. Experimentally, we consider coacervation between an anionic homopolymer of poly(glutamate) and sequence-specific cationic copolymers of poly(glycine-co-lysine). These are prepared in aqueous solution with NaCl salt at pH 7.0. All polymers have the same degree of polymerization $N = 50$; because the sequence-specific polycations have a charge monomer fraction of $f = 0.5$, there are twice as many polycation molecules as polyanion molecules to balance the number of charges on these species.

Figure 4.3 demonstrates our scheme for the homopolyanion and sequence-specific copolycation. The homopolyanion and copolycation both consists of chains of $N = 48$; similar to experiment, twice as many polycations are present per polyanion. Copolycation sequences for both simulation and experiment are defined by their periodicity τ. A copolycation with a sequence that alternates between charged and neutral monomers would have a value $\tau = 2$, while a copolycation that has 8 charged monomers followed by a block of 8 neutral monomers has a periodicity $\tau = 16$ (see Figure 4.3b). For all sequences, the copolycation has the same number of charged and neutral monomers.

Figure 4.4a shows the coacervation phase diagrams for a series of patterned copolycations interacting with unpatterned homopolyanions, calculated from simulation. These phase diagrams exhibit a drastic, monotonic increase in the size of the coexistence region. In fact, the critical salt concentration (CSC) nearly doubles from $\tau = 2$ to $\tau = 24$.

Changes in the size of the coexistance region determined from simulation are reflected experimentally by trends in CSC as a function of τ at a constant polymer concentration, (Figure 4.4b,c) with qualitative agreement. While matching between the simulation and experimental results is in part dependent on the choice of simulation parameters such as bead radii, the trend observed here persists regardless of the choice of reasonable parameterization values. We note that this effect persists even when the solvent is changed, with a similar effect of τ on the CSC in a water/isopropanol solvent mixture (see [11]).

4.3.3 Thermodynamics of Sequence-Defined Coacervation

We use isothermal titration calorimetry (ITC) as a tool to experimentally probe the thermodynamics of complex coacervation (Figure 4.5) [85]. A two-step model of coacervation enables analysis of ITC data and its separation into entropic and enthalpic contributions; 'ion pairing' between oppositely-charged polymers is followed by a 'coacervation' step that results in phase separation (fit to raw data shown in Figure 4.5a inset) [85].

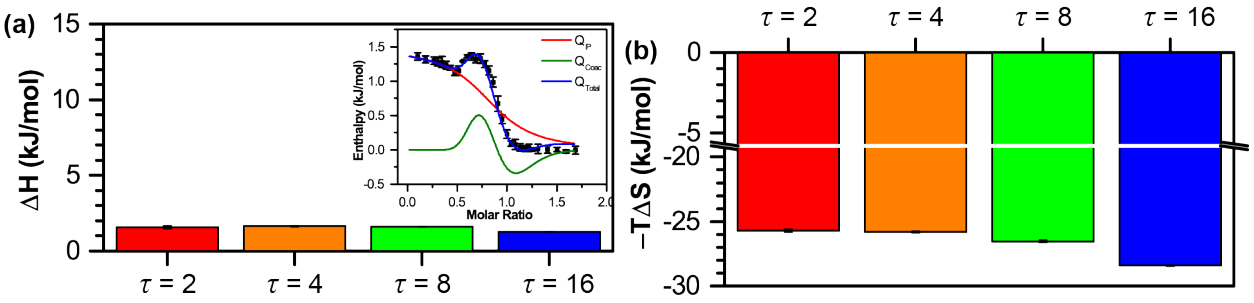

Figure 4.5: Isothermal titration calorimetry (ITC) shows that sequence effects in coacervation are entropically driven (a) The enthalpic contribution to coacervation as a function of τ is small, positive, and does not show significant differences between sequences. Isothermal titration calorimatry captures this thermodynamic value via a fit to an established two-step coacervation model (inset) that distinguishes between enthalpic contributions from ion pairing (IP) and coacervation (Coac) steps [85]. (b) The entropic contribution to the coacervation free energy is large, negative, and attributed to counterion release. Clear differences are observed as a function of τ, with an increasing entropic driving force with increasing blockiness (larger τ).

ITC measurements show a small, positive enthalpic contribution to coacervation, consistent with the results of previous investigations (Figure 4.5, see [11]) [84, 85]. Variations between different sequences are difficult to resolve due to the small magnitude of this term. In contrast, and as expected, entropy is the primary driving force for coacervation [84, 85, 120]. Calculated values for $-T\Delta S$ are both negative and an order of magnitude larger than the observed enthalpies. Furthermore, the entropic driving force for coacervation increases with increasing τ, concomitant with the changes in the width of the coexistence region and the CSC observed in simulation and experiment. Furthermore, the magnitude of the entropic differences are significant, spanning $\sim$ 3 kJ mol^{-1}. This is on the order of thermal energy ($\sim 1 - 2k_BT$), which can significantly compete against the translational entropy of the

polymer chains. This is conceptually consistent with the observed differences in the phase behavior of the different sequences.

4.3.4 Correlations and Sequence Alignment in Coacervation

We use simulation to understand the role of charge sequence in determining molecular structure of the coacervate phase. We first consider pair correlations under conditions of constant salt concentration (25 mM) corresponding to the high polymer concentration points on the binodal curves (boxed points in Figure 4.4a). These polymer concentrations are relevant for the thermodynamics of coacervation, because they are obtained when coacervation occurs within the two-phase region. The polymer concentration thus depends on the sequence due to the changes in the phase diagram with τ. We focus on the polyanion-polycation correlations $g_{P+/P-}(r)$ shown in Figure 4.6a. Peaks corresponding to chain connected structure are seen, [4, 67] but there is no clear trend as τ is changed. This is consistent with a calcuation of the energy of coacervation in Figure 4.6b, calculated from $U_i = 2\pi \sum_j \rho_j \int_0^\infty dr r^2 v_{ij}(r) g_{ij}(r)$ [80]. This summates the energy that a species i 'feels' due to contributions from all other species j, each with a number density ρ_j and an interaction with i via a pair potential v_{ij} [80]. The overall change in energy $\Delta U = \Delta U_{P+} + \Delta U_{P-}$ for coacervation matches with experimental ITC measurements, demonstrating only a small, positive increase that does not depend on τ. This is consistent with the experimental observation that enthalpic effects tend not dominate the coacervation process [84, 85].

While the coacervate process is not strongly affected by enthalpic effects in coacervation, the structure of coacervates still exhibits non-trivial correlations associated with the monomer sequences. We use a second comparison where dense phases (denoted with an asterisk in Figure 4.4a) for all values of τ are considered at the same polymer and salt concentrations. This permits a direct comparison between systems with exactly the same components - such as the number of charged/neutral monomers and salt ions - with the only change being the order in which the monomers are connected. Pair correlations $g_{P+/P-}(r)$ are shown in Figure 4.7a for all values of τ, demonstrating a distinct change in the second peak adjacent to the initial polyanion/polycation pair.

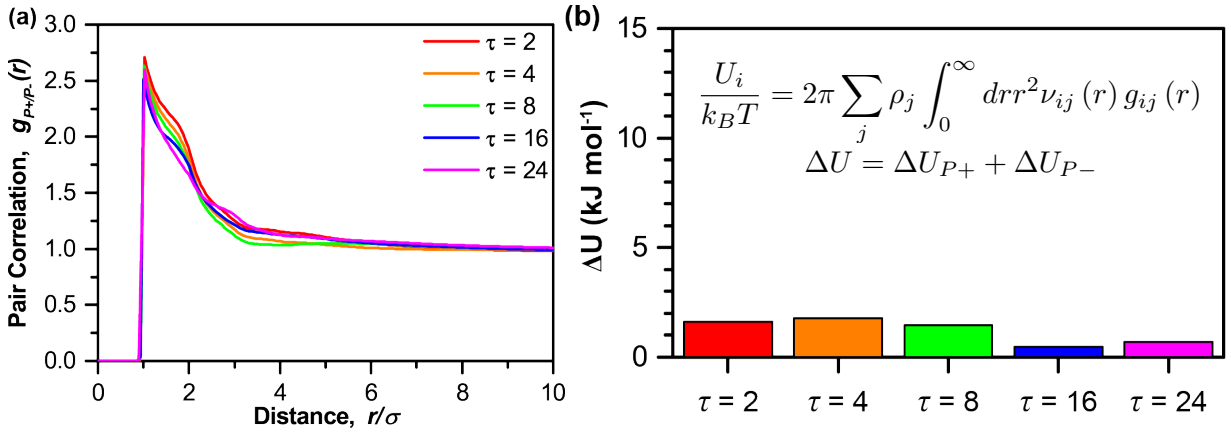

Figure 4.6: Phase separating coacervate structure and energy shows no significant sequence effect (a) Polycation/polyanion pair correlation function for the coacervate phase at various τ (boxed points in Figure 4.4a). Correlations do not show strong dependence on τ. (b) Calculation of the change in electrostatic energy for the polycation (from $g(r)$ such as in (a)) show small, positive increases in energy during coacervation. This is qualitatively consistent with experimental data in Figure 4.5.

The change in this peak can be interpreted through the use of a set of along-the-chain correlation functions $C_1(\Delta s)$ and $C_2(\Delta s)$, which are a function of the distance along a chain contour Δs described by the index s. We show schematics in Figure 4.7b and provide rigorous definitions in Section 4.2.4. Both functions start with a pair of polycation/polyanion charges that are within a cutoff radius r_{CC} from each other, and measure conditional probabilities for two monomers that are Δs monomers away from original pair. $C_1(\Delta s)$ is the probability that these two new monomers are within r_{CC} from each other *given* that they are both charged, while $C_2(\Delta s)$ is the probability that these two new monomers are both charged *given* they are within r_{CC} from each other. Conceptually, C_1 is a measure of the contour length over which two nearby chains of opposite charge remain aligned, which we call a 'looping' correlation. To contrast, C_2 is a measure of how much the charged monomers on the patterned chain prefer to be along segments aligned with the opposite polyelectrolyte, which we call a 'sequence alignment' correlation.

$C_1(\Delta s)$ shows a decrease in looping potential with increasing distance along the chain and very little dependence on the value of τ (Figure 4.7c). This indicates that neighboring

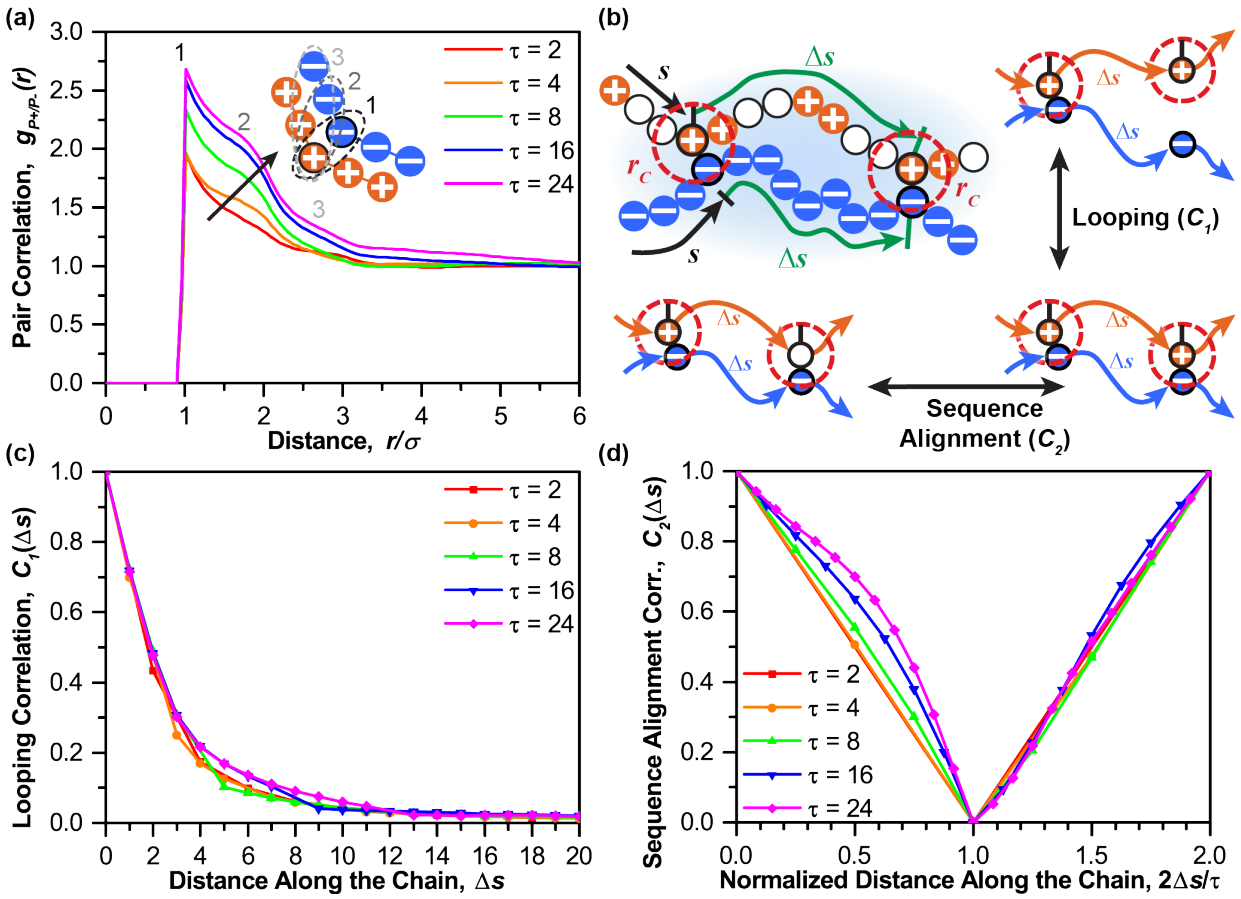

Figure 4.7: Blocky sequences exhibit strong charge correlations due to sequence alignment at same concentrations (a) Polycation/polyanion pair correlations for the dense phase at a single salt/polymer concentration denoted with an asterisk in Figure 4.4a. When species concentrations are kept constant, there is a clear increase in polyelectrolyte correlations. (b) We use a set of pair correlations that capture the extent that two nearby chains interact; we follow their contour s and check for both spatial proximity within a cutoff r_{CC} and monomer charge. C_1 determines the probability that charged monomers separated along their respective contours Δs 'loop'. C_2 determines the probability that 'looped' monomers are both charged. (c) Spatial 'looping' correlations are measured by C_1, which demonstrates negligible differences between different values of τ. However, there is a tendency for interacting polyelectrolytes to feature runs of charged monomers, whose sequence alignment is quantified by C_2 (d). We attribute pair correlations in (a) to this effect.

chains align for approximately the same number of monomers regardless of sequence. A larger correlation effect is apparent in C_2 (Figure 4.7d). Here, the abscissa (Δs) has been normalized by $\tau/2$ in order to highlight the primary difference between values of τ, which is that the probability of finding another charged monomer after a shift of Δs initially decreases much more quickly with small values of τ. In the extreme, for $\tau = 2$, there is by

definition no chance of finding a charged monomer for $\Delta s = 1$. To contrast, the likelihood of finding an adjacent charged monomer is very high for large τ, due to the blockier monomer sequence. Beyond this primary probabilistic effect, which is captured by the normalization of Δs, larger values of τ still show a slower C_2 decay. We attribute this secondary effect to a preference for aligned chain segments to include the charged portion of the patterns. Both of these behaviors are due to the electrostatic benefit of aligning charged monomer sequences, such that opposite charges are in close proximity.

These structural changes at the molecular level do not directly influence the macroscopic thermodynamics of coacervation, as evidenced by the small and τ-independent values of ΔU. Instead, C_2 shows that opposite polyelectrolytes tend to 'align', which entropically confines polyelectrolyte chains in the coacervate phase. This entropic effect is best seen through the lens of counterion release, and is the main driving force for sequence-dependence in coacervation.

4.3.5 Tuning the Entropy of Counterion Release

The large entropy change upon coacervation observed in ITC is consistent with traditional counterion release arguments for coacervation [88, 120]. In the dilute phase, counterions *condense* along the backbone of a highly-charged polyelectrolyte to decrease the local electrostatic energy [88]. This counterion condensation occurs at the expense of the counterion translational entropy. During coacervation, oppositely-charged polymers can condense upon each other, similarly lowering the local electrostatic energy. Meanwhile, the previously-condensed counterions regain their translational entropy [88, 89, 93, 120]. We use a modified version of this counterion release argument to explain how τ can strongly affect coacervation phase behavior.

We use simulation to characterize counterion condensation in the dilute phase. We use a method developed by Liu and Muthukumar, [119] where condensed counterions are located within a cutoff radius r_C from any monomer along a dilute chain. Each condensed counterion is assigned to its nearest monomer, such that each monomer i has an average number $\langle n_i \rangle$ of counterions condensed (Figure 4.8b). The smaller, neutral monomers have a larger accessible

counterion volume with this method. A number is therefore defined for each bead using the condensed counterions $\langle n_i^0 \rangle$ for an uncharged chain. The ratio $\langle n_i \rangle / \langle n_i^0 \rangle$ thus gives a normalized measure of the condensed counterions. We relate this ratio to an effective energy $\epsilon_i = -k_B T \ln \left(\langle n_i \rangle / \langle n_i^0 \rangle \right)$ in a one-dimensional adsorption model that is suited to the high charge densities considered in this work (see Sections 4.2.5 through 4.2.7). The quantity $\ln \left(\langle n_i \rangle / \langle n_i^0 \rangle \right)$ is plotted as a function of monomer index i for a number of different values of τ (Figure 4.8a). The distribution of counterions along the backbone varies greatly, with low τ polymers showing relatively uniform condensation while high τ polymers have condensed counterions clustered near the charge blocks (Figure 4.8c).

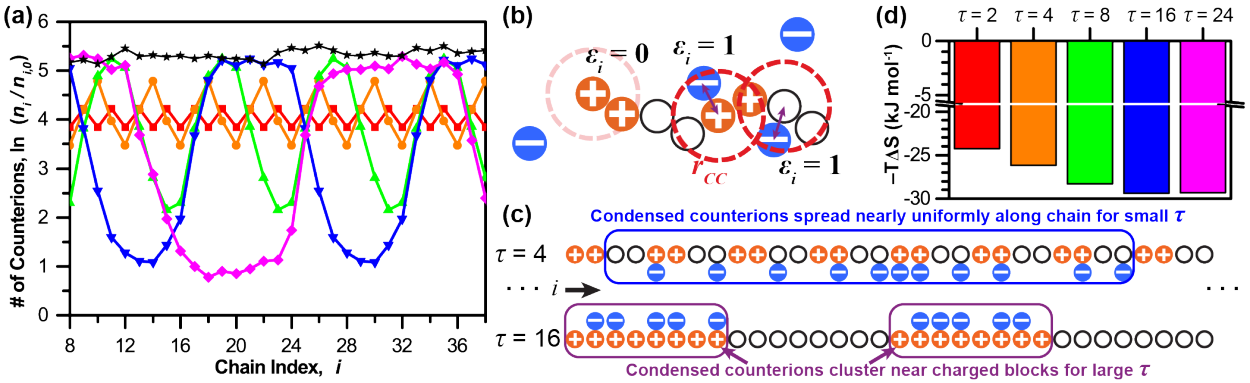

Figure 4.8: Charge sequence effects in coacervation can be explained by 1-D counterion confinement entropy (a) The number of counterions n_i condensed as a function of chain index i, relative to the counterions present near an uncharged chain, $n_{i,0}$. Salt concentration is 25 mM, at boxed supernatant points in Figure 4.4a. The value $\ln (n_i/n_{i,0})$ is related to an *effective* binding energy used in a 1-D adsorption model. Colors same as Figure 4.4a and (d), black curve for homopolyanion. (b) The criterion for a condensed counterion is one that is within r_C of a polyelectrolyte charge; it is 'condensed' along the nearest polymer bead of index i. (c) Conceptual schematic demonstrating the origin of the charge sequence effect on coacervation. Condensed counterions are uniformly distributed along polyelectrolyte chains with low τ, however at high τ these condensed counterions are confined along the chain contour near the charged blocks. This additional confinement increases the entropic driving force for counterion release. (d) This 1-D confinement is reflected in the entropic contribution to the free energy, $-T\Delta S$, as calculated from the 1-D adsorption model and in near-quantitative matching with ITC data (Figure 4.5b).

To evaluate the effect of this distribution of condensed counterions on the counterion release entropy, we use an expression for the entropy calculated from the same one-dimensional

adsorption model (energies normalized by k_BT denoted with a tilde):

$$\frac{S}{k_B} = \sum_i \left[\ln\left(1 + e^{-(\tilde{\epsilon}_i - \tilde{\mu})}\right) + \tilde{\epsilon}_i \left(\frac{e^{-(\tilde{\epsilon}_i - \tilde{\mu})}}{1 + e^{-(\tilde{\epsilon}_i - \tilde{\mu})}} \right) \right] \tag{4.11}$$

In this model, simulation data serves as the primary input of $\tilde{\epsilon}_i$, while the external chemical potential $\tilde{\mu}$ is set at a constant value for all τ and i for a given salt concentration.

Using a single value of $\tilde{\mu}$, we obtain values for the entropic contribution to coacervation in near-quantitative agreement with ITC data (Figure 4.8d). Thus, accounting for the distribution of counterions condensed onto individual polyelectrolytes in the supernatant phase yields a prediction for the sequence-dependence of coacervation. This is a one-dimensional confinement effect. Low-τ systems show an even distribution of condensed counterions along the length of the polyelectrolyte chain (Figure 4.8c, $\tau = 4$). However, as τ is increased, the counterions are increasingly confined near the charged blocks (Figure 4.8c, $\tau = 16$). Counterions that are more confined consequently gain more entropy upon release, leading to the increasingly negative values of $-T\Delta S$ with increasing τ observed in Figs. 4.5b and 4.8d.

4.4 Conclusion

We used a combination of experiment, theory, and simulation to demonstrate the profound effect of polyelectrolyte monomer sequence on charge-driven materials structure and thermodynamics. Sequence-defined polypeptides were used to evaluate this monomer sequence effect, demonstrating qualitative matching with simulation. This sequence effect is due to differences in entropic confinement of condensed counterions along the polymer, which changes drastically with the blockiness of the sequence. Experimental thermodynamic measurements are consistent with this picture, showing that entropy dominates coacervation while enthalpic contributions are negligible.

We emphasize that this charge patterning effect does not rely on subtle chemical or solvent-specific effects, and trends can be recapitulated using coarse-grained electrostatic models. However, we note that such effects would be important to obtain quantitative predictions. Implications for these charge patterning effects extend from biological polymers to materials

design. Sequences featuring runs of similarly-charged macromolecules may provide a way to tune biophysical interactions, with long, charge-dense sequences exhibiting stronger charge interactions than patterns with less-blocky runs of the same charge.

For materials design, charge patterning represents a way to deliberately tune charge interactions in coacervate-driven assembly. This is one way that sequence *information* may be included into the backbone of a polymer chain that is distinct from i.e., random copolymerization or block copolymerization. This mechanism is not an averaging of dispersive effects, but rather a precise tuning of the local arrangements of charge. Indeed, by combining with the aforementioned sequence effects we envision a number of sequence-scales that can be used to tune charge-driven assembly. We foresee this as one way to utilize the development of sequence-specific synthesis to reach ever-more complex assemblies.

In the next chapter, we extend the transfer matrix description of coacervation to develop a molecular-level understanding of how charge sequence affects complex coacervation. This uses simulation to calculate the binding energy as developed in Section 4.2, which captures how the local electrostatic environment changes along the polymer backbone. Not only are the sequences studied in this chapter considered but also a wider range of sequence effects are investigated, demonstrating that the transfer matrix theory can capture precise, monomer-level charge sequence effects.

CHAPTER 5

TRANSFER MATRIX THEORY INVESTIGATION OF SEQUENCE-DEFINED COACERVATION

5.1 Introduction

Understanding the role of monomer sequence on the physical properties of long-chain macromolecules remains a grand challenge in the field of polymer science, [141, 160] due to the utility of sequence as a tool to store information and drive structure formation in biological polymers such as proteins, RNA, and DNA [142]. This takes place in a number of ways; for example, molecular storage of genomic data is encoded in DNA via a sequence of four different base pairs which can then be read by the protein machinery of the cell. Proteins leverage sequences incorporating any number of roughly twenty amino acids, that then often undergo hierarchical assembly into highly complex and precise three-dimensional structures. A subclass of proteins known as intrinsically-disordered proteins (IDPs) are subtly different, in that they tend not form secondary or higher-order structures; however, IDPs remain crucial to biological structure and function [40, 161]. Despite this lack of hierarchical order, recent work has shown that the precise sequence of charged amino acids still plays a defining role in the structure and function of IDPs [39–45]. This suggests that the physical effects of charged monomer sequences are generally relevant for a broad range of polymeric materials, not limited to biological molecules; however, the underlying physics of these sequence-dependent electrostatic interactions is not well understood.

In Chapter 4, we demonstrated how 'blockiness' affects complex coacervation phase behavior by comparing Monte Carlo simulations to experimental results. As the blockiness

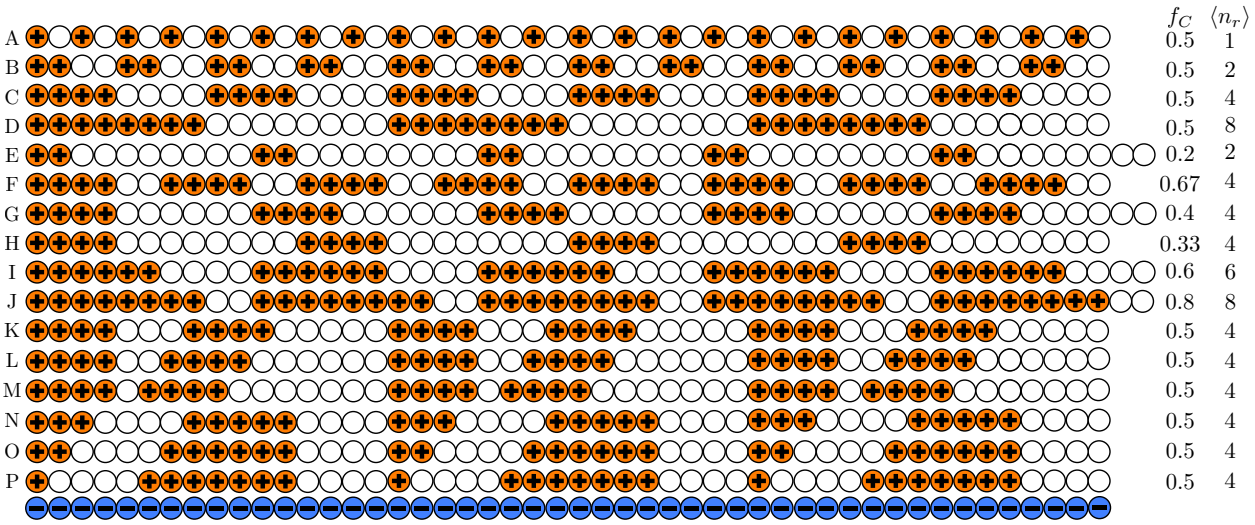

Figure 5.1: The sequences used in this paper (A-P), along with the homopolyanion (blue) that is partnered with the polycation sequences. Sequences can be characterized by parameters such as charge fraction f_C and average 'run' length $\langle n_r \rangle$, however sequences are not uniquely characterized by these two parameters.

of a polyelectrolyte increases, the size of the immiscible region increases due to increasing entropic gain upon counterion release as a consequence of stronger counterion localization along the polymer backbone as blockiness increases. This demonstrates that the local electrostatic environment along the polymer backbone is a physical feature which needs to be included in theory to capture sequence effects.

We show in Figure 5.1d a schematic of the total range of polycation sequences we use in this paper, along with the fully-charged homopolyanion that was paired with the polycations in each coacervate. All of these sequences have between 48-50 monomers, with a variety of charge fractions f_C and an average length 'run' of charged monomers $\langle n_r \rangle$, indicated on Figure 5.1d. We note that these types of averaged variables do not uniquely define a sequence; for example, sequences C, L, M, and N have the same total number and type of runs, only spaced out with different combinations of neutral monomer runs, or 'spacers'. Therefore, to identify the different sequences, we assign a letter to them in Figure 5.1d that will be used to denote points associated with a given sequence later in the paper. We do point out a few sequence-based trends that we will focus on: (**Blockiness**) we change the periodicity of sequence polymers with the same number of charged, neutral monomers in runs

(A-D). This trend was the basis of our prior work [11]. (**Constant Runs**) we examine a constant set six runs of four adjacent, charged monomers, and change how the neutral spacer monomers are distributed in-between (C,K-M, D). (**Constant Spacers**) we keep a constant set of six runs of four neutral monomer spacers, and change how the charged monomers are distributed in-between (C,N-P,D). Finally, (**Constant Runs, Constant Number of Charges**) we keep a constant set of runs of four adjacent, charged monomers, and change the number of neutral monomer spacers while keeping the overall number of charges per chain constant (not included in Figure 5.1d, but represented later). We note that, for this chapter, all polymers are monodisperse in size *and* sequence in both theory and simulation, and have very low polydispersity in experiments. We compare transfer matrix results directly with experiment and simulation, and observe qualitative agreement for a wide variety of test sequences. We thus demonstrate how subtle changes in monomer sequence can affect the strength of electrostatic interactions between oppositely-charged polyelectrolytes, and the resulting phase behavior.

5.2 Methods

For the investigations in this chapter, we use the Monte Carlo simulation model described in Section 4.2.2, and a modification of the transfer matrix theory in Section 2.3. However, the simulation excess free energy will be calculated using the excess pressure instead of the polyelectrolyte excess chemical potential.

5.2.1 Pressure Calculation

Pressure, p, was calculated using phantom box volume changes [162] in Monte Carlo simulations with no salt ions. For each instance of calculating pressure both a compressive and expansive volume change is performed. These volume changes have the same magnitude, but different directions. Since these are phantom volume changes, the volume of the simulation

box does not change throughout the simulation. Pressure can be calculated via [162]:

$$\frac{p\Delta V_+}{k_BT} = (Nn_{P+} + Nn_{P-}) \ln\left(1 + \frac{\Delta V_+}{V}\right) + \ln\left\langle \exp\left(-\frac{\Delta U_+}{k_BT}\right)\right\rangle - \ln\left\langle \exp\left(-\frac{\Delta U_-}{k_BT}\right)\right\rangle \tag{5.1}$$

Here V is the volume of the box. ΔV_i is the size of the volume change, and i denotes the direction of the volume change, with + being expansive and − being compressive. ΔU_i is the change in potenial energy due to the volume change, i. The first term on the right hand of Equation 5.1 is the pressure due to an ideal gas of monomers. The second and third terms are the monomer excess pressure, but the desired quantity is the chain excess pressure. This quantity allows thermodynamic integration to yield the excess free energy.

To accomplish this, we use arguments found in K.G. Honnell, *et al.* [163]. The monomer excess pressure, p^m_{EXC}, is defined as:

$$p^m_{\mathrm{EXC}} = \ln\left\langle \exp\left(-\frac{\Delta U_+}{k_BT}\right)\right\rangle - \ln\left\langle \exp\left(-\frac{\Delta U_-}{k_BT}\right)\right\rangle \tag{5.2}$$

As the concentration approaches 0, the intermolecular forces should become negligible, which means the pressure should approach the value for an ideal gas of chains. For this to be true, Equation 5.2 has to approach $\{[(n_{P+} + n_{P-})\, k_BT/V] - [(Nn_{P+} + Nn_{P-})\, k_BT/V]\}$ in this limit. If this expression is subtracted from equation 5.2, then the chain excess pressure, p^c_{EXC}, is recovered:

$$p^c_{\mathrm{EXC}} = \ln\left\langle \exp\left(-\frac{\Delta U_+}{k_BT}\right)\right\rangle - \ln\left\langle \exp\left(-\frac{\Delta U_-}{k_BT}\right)\right\rangle - \{[(n_{P+} + n_{P-})\, k_BT/V] - [(Nn_{P+} + Nn_{P-})\, k_BT/V]\} \tag{5.3}$$

This excess pressure can be used to calculate excess free energies.

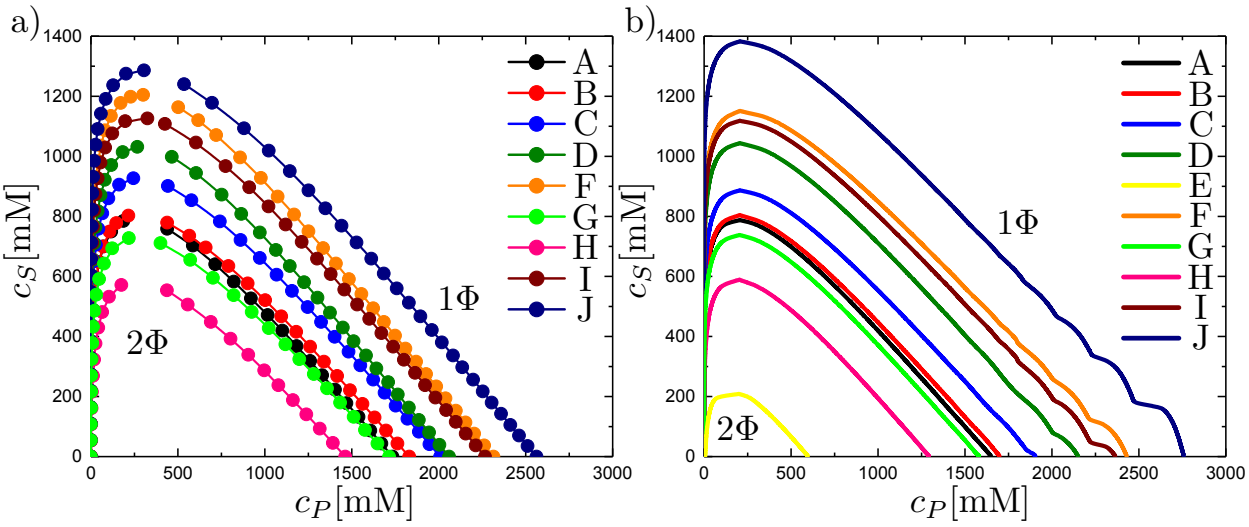

Figure 5.2: Phase diagrams for the investigated patterns. The 2Φ region is the immiscible part of the phase diagram, and the 1Φ region is the miscible part of the phase diagram. (a) Simulation phase diagrams calculated using equation 5.5. (b) Theoretical phase diagrams calculated using the transfer matrix theory. The letters corresponding to each phase diagram denote the pattern in Figure 5.1. Both simulation and theory show alterations in phase behavior as charge fraction and the average length of the run of charged monomers is changed.

5.2.2 Phase Diagram Calculation from Simulation

The excess free energy per volume can be defined as:

$$f_{\mathrm{EXC}}\left(\{\phi_i\}\right) = \frac{F_{\mathrm{EXC}}\left(\{\phi_i\}\right)}{Vk_BT} = \phi_P \int_{\phi_S^0,\phi_P^0}^{\phi_S^0,\phi_P} \frac{Vp^c_{\mathrm{EXC}}\left(\phi_S^0,\phi'_P\right)}{N_{\mathrm{pat}}k_BT\phi'_P} d\phi'_P + \int_{\phi_S^0,\phi_P}^{\phi_S,\phi_P} \mu_{\mathrm{EXC},S}\left(\phi'_S,\phi_P\right) d\phi'_S \tag{5.4}$$

where $N_{\mathrm{pat}} = f_C n_{P+} N + (1-f_C) n_{P+} N \left(\sigma_0/\sigma_\pm\right)^3 + n_{P-} N$. ϕ_i^0, with $i = S$ for salt and $i = P$ for polymer, is the reference volume fraction, which we set to 0, and, $\mu_{\mathrm{EXC},S}$ is the salt chemical potential, calculated via Widom insertion of a pair of salt ions [164]. This excess free energy can be used as an input into a total free energy expression:

$$\frac{\mathcal{F}}{Vk_BT} = \sum_i \frac{\phi_i}{N_i} \ln \phi_i + f_{\mathrm{EXC}}\left(\{\phi_i\}\right) \tag{5.5}$$

The first term on the right hand side of this equation is the mixing entropy of all species, and the second term is the simulation-calculated excess free energy. This free energy can be used to calculate phase diagrams, shown in Figure 5.2 for patterns A-J as described in Figure 5.1.

Comparison of these phase diagrams with those contained in the previous chapter [11] reveals some differences. We attribute the discrepancy to the different techniques used to calculate the excess free energy. Previously, the excess free energy was calculated via:

$$f_{\mathrm{EXC}}\left(\{\phi_i\}\right) = \int_{\phi_S^0,\phi_P^0}^{\phi_S^0,\phi_P} \mu_{\mathrm{EXC},P}\left(\phi_S^0,\phi_P'\right) d\phi_P' + \int_{\phi_S^0,\phi_P}^{\phi_S,\phi_P} \mu_{\mathrm{EXC},S}\left(\phi_S',\phi_P\right) d\phi_S' \tag{5.6}$$

Here, excess chemical potentials are calculated for the polymer using incremental Widom insertion [105]. In order to adapt this technique to the patterned polycation, the pattern is shifted along the polymer backbone to capture the contribution of the charged and neutral monomers to the excess chemical potential [11]. This resulted in phase diagrams with a larger polymer concentration in the supernatant phase compared to the current results. However, both techniques qualitatively capture the observed patterning trends.

5.3 Results and Discussion

5.3.1 Simulation and Experiment Exhibit Sequence-Dependent Coacervation

In looking to understand the nuanced effects of chemical sequence, we first performed a direct comparison between simulation and experiment. Coacervate phase diagrams were calculated using thermodynamic integration of Monte Carlo simulations [104] using a combination of box size-changes [162,163] and Widom insertion [104,164] to calculate the excess free energy along both the polymer (polyanion and sequenced polycation) and salt species respectively (see Sections 5.2.1 and 5.2.2). This approach uses the same simulation model as detailed in Section 4.2.2 [4,11,121,165]. We then compared the binodal phase diagrams resulting from these simulations to experimentally determined measures of the phase behavior (Figure 5.3).

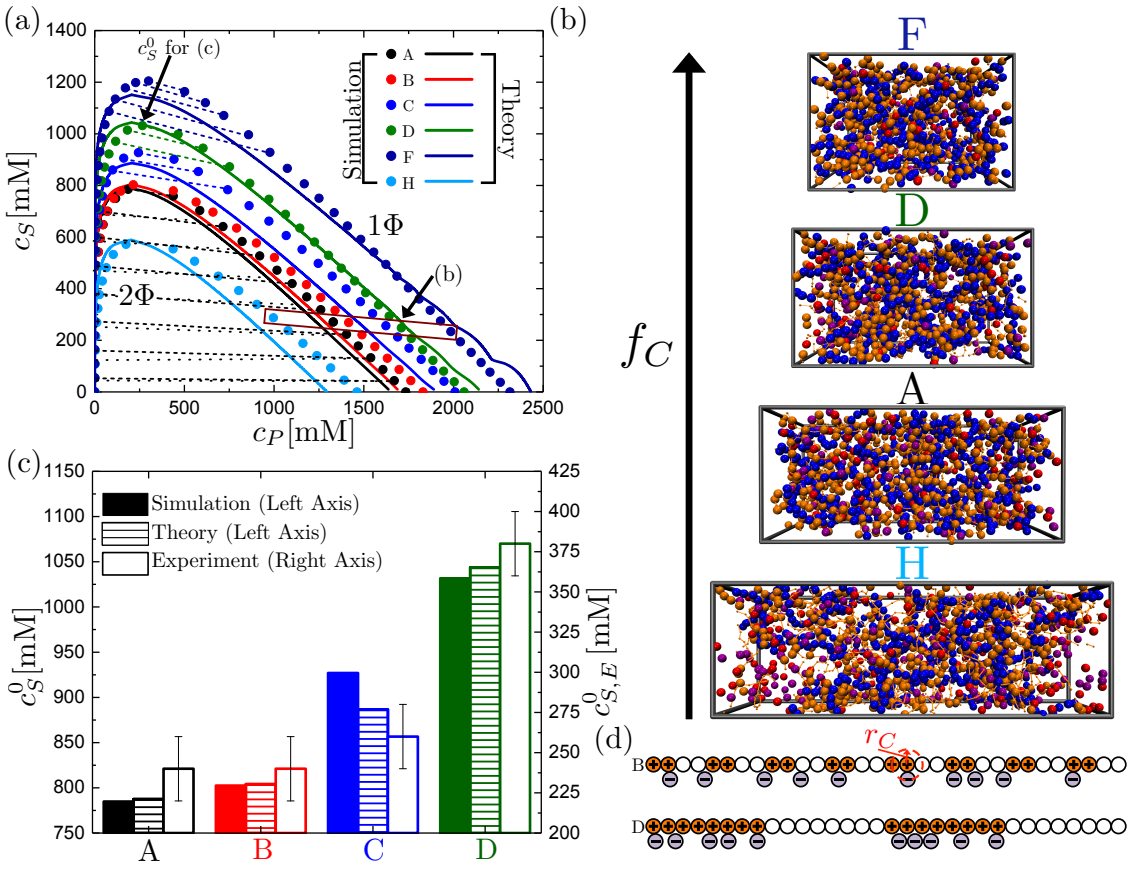

Figure 5.3: (a) Salt concentration c_S versus polymer concentration c_P phase diagram of coacervation measured from simulation (points) and transfer matrix theory (lines) for polycations with sequences A-D, F, and H interacting with a homopolyanion. An example set of tie-lines are shown for sequence A (dashed line, simulation and dotted line, theory), with both exhibiting a small negative slope consistent with prior literature [4, 5]. Simulation tie-lines are also shown for other sequences at concentrations outside the binodal of sequence A, demonstrating that sequence does not alter the sign of the slope. The critical salt concentration as measured by theory c_S^0 is measured at the largest concentration of salt observed in the supernatant phase for each sequence. (b) Simulation snapshots representative of the points in (a) for sequences H, A, D, and F. The polycation is orange, the polyanion is blue, the cation is purple, and the anion is red. Neutral beads for the polycation are shown with smaller beads connected by rods. (c) Simulation and theory values for salt resistance (left axis, c_S^0) qualitatively compare well with experimentally-measured values of $c_{S,E}^0$ obtained at 1 mM polymer for sequences A-D, showing that we can use theory and simulation to capture sequence variations described by an increase in charge block size (Blockiness). (d) Schematic highlighting counterion localization for two different sequences. For a sequence with a large $\langle n_r \rangle$ (D), the counterions are locally confined near the charged blocks. In contrast, counterions are more uniformly localized along the chain for sequences with a small $\langle n_r \rangle$ (B). The red circle represents the cutoff radius, r_C. If a salt ion is within this r_C of a monomer, the salt ion is considered localized.

The phase boundaries in Figure 5.3a exhibit the same trend observed in Chang *et al.*, [11] with minor differences due to the different methods for calculating phase diagrams (see discussion in Section 5.2.2). Our results highlight that an increase in blockiness $\langle n_r \rangle$ and charge fraction f_C generally leads to a marked increase in the two-phase region of the phase diagram, indicating that phase separation is enhanced by stronger electrostatic attractions. Figure 5.3b shows characteristic snapshots from simulations performed at a constant number of charged monomers for sequences H, A, D, and F, visually highlighting how an increased value of c_S^0 leads to stronger phase separation and a denser coacervate phase.

Further analysis of simulation results also suggested that electrostatic cooperativity resulting from an increase in $\langle n_r \rangle$ enhances the localization of counterions at high charge-density locations along the polyelectrolyte chain (Figure 5.3d). An important consequence of this increase in counterion confinement is a commensurate increase in the entropy resulting from the release of these bound counterions upon complexation with an oppositely-charged polymer [11] .

Due to the correlation between increases in the strength of the electrostatic attraction, counterion localization, and the size of the two-phase region, we can use the highest salt concentration where we observe phase separation, c_S^0, as a simple descriptor of the system (Figure 5.3a). This parameter also allows for comparison with experimental data. While c_S^0 represents the highest salt concentration for the overall phase diagram, experimental measurements of this 'salt resistance' were performed at a fixed overall polymer concentration $c_P = 1$ mM. Therefore, we expected to observe similar qualitative trends for these two parameters, but not quantitative matching. Figure 5.3c demonstrates that the size of the two-phase region, as measured by either the salt resistance $c_{S,E}^0$ from experiments or c_S^0 from simulations, systematically increased with increasing blockiness $\langle n_r \rangle$ for constant charge fraction f_C, (*i.e.*, sequences A to D).

The results in Figure 5.3a also include example tie-lines connecting coexisting coacervate and supernatant phases. It is noteworthy that we observe tie-lines with a negative slope, indicating that coacervate phase has a lower salt concentration than the supernatant [4, 5, 93, 121, 165, 166]. This preferential partitioning of salt out of the dense, polymer-rich coacervate phase has been previously attributed to the excluded volume of the polyelectrolyte

species, [4, 5, 93, 121, 165, 166] and has been confirmed experimentally [4, 5].

5.4 Theory of Monomer Sequence in Polymeric Complex Coacervation

Results from simulations suggested that we can capture the relevant physics dictating the effects of charge sequence on coacervate phase behavior by considering how counterions interact with a single polymer chain. Therefore, we extend the transfer matrix theory of complex coacervation to include the effects of charged monomer sequence [93,121,165] .This method is particularly applicable because, for most coacervates, the concentration of charged species is sufficiently high that standard Debye-Hückel or Poisson-Boltzmann electrostatics are no longer applicable, [4,110,167] and correlations are primarily due to charge connectivity and nearest-neighbor pairing [4, 94].

To extend the transfer matrix formalism to describe sequence effects in coacervation, the electrostatic association strength ϵ becomes a function of the specific monomer position along the test polycation chain. This accounts for the variation in local electrostatic environment, and specifically the energetic penalty for an unpaired ion, for a particular monomer sequence [93, 165]. Thus, the $D_{homo} = D_0 \exp(-\epsilon_0)$ that in the homopolyelectrolyte theory contains a constant ϵ_0, now is written with a contribution ϵ_1 that depends on the monomer index s, $D_{pattern} = D_{homo} \exp(-\epsilon_1(s))$.

To calculate the value of $\epsilon_1(s)$, we use Monte Carlo simulations of single polyelectrolytes in a dilute salt solution (see the Sections 4.2.6 and 4.2.7). The localization of counterions near charged polycation blocks, and thus the local strength of electrostatic interactions, is calculated by defining a region around the chain defined by a cutoff radius r_C (Figure 5.3d) [119]. This charge localization is energetically favorable due to electrostatic attractions, [88,101,119] and there is thus an increased number density $n_C(s)$ of opposite charges within r_C at a given chain monomer s [11]. We define an electrostatic energy that accounts for this increase in local correlations as the aforementioned $\epsilon = \epsilon_0 + \epsilon_1(s)$. We demonstrate that $\epsilon(s)$ can be determined from simulation using the relationship $\epsilon(s) = -\ln n_C(s)/n_{C,0}(s)$ (see Section 4.2.7), where $n_{C,0}(s)$ is the number density of opposite charges within r_C in

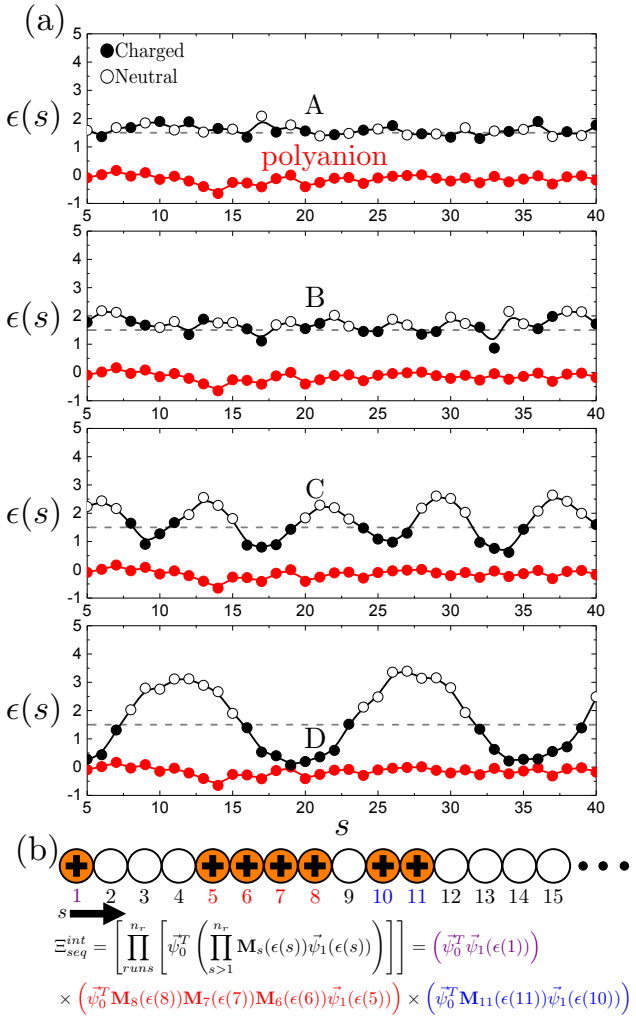

Figure 5.4: (a) Monomer-dependent energy $\epsilon(s)$ as a function of the chain index, measured by single-polyelectrolyte simulations in dilute salt solution. Variations in $\epsilon(s)$ reflect the different electrostatic environments associated with monomers in different positions along the chain. $\epsilon(s)$ is plotted here for sequences A-D, which reflects variation in sequence periodicity ranging from alternating charged/uncharged monomers (A) to blocks of 8 charged/uncharged monomers (D). Filled symbols represent charged monomers in the sequence, and open symbols represent neutral monomers. The homopolyanion is also plotted as the dark red line in each graph. We note that, for the blockiest polycation sequences, $\epsilon(s)$ approaches the homopolyanion behavior in the center of the block. (b) Schematic illustrating how the variation in $\epsilon(s)$ is incorporated into the transfer matrix theory. Ξ_{seq}^{int} is the grand canonical partition function associated with polymer-polymer interactions. It is composed of products of 'runs' of charge, as shown explicitly in the expression given below the schematic; here, the colors are associated with the indicated charged monomer runs: 1 (purple), $5-8$ (red), and $10-11$ (blue)

the absence of electrostatic interactions. This method thus only requires two single-chain simulations (one with electrostatics and one without) at low salt concentrations. Figure 5.4a shows typical landscapes ($\epsilon(s)$) for patterns A-D, as well as the homopolyanion, where we denote charged monomers with closed symbols and neutral monomers with open symbols. We take $D_0 = 1$ and $\epsilon_0 = 0$, in agreement with the theory for homopolyelectrolyte coacervates [93].

As expected, there is a large variation in electrostatic attraction along the contour of the chain due to the precise sequence of monomers. For the sequences plotted in Figure 5.4a, sequence D exhibits the most marked variations in $\epsilon(s)$. In this case, long runs of adjacent, charged monomers (*e.g.*, $s = 16-23$ and $s = 32-39$) have a value of $\epsilon(s)$ that is similar to ϵ_0 for a homopolymer. As the sequence transitions from a charged run to a neutral spacer (*e.g.*, $s = 22$ to 26), there is a concomitant increase in $\epsilon(s)$ that we attribute to the weakening of the driving force for charge localization. $\epsilon(s)$ decreases once more as the neutral spacer transitions back to a charged run (*e.g.*, $s = 30$ to 34). In contrast, short runs of charge or isolated, charged monomers (such as in sequences A or B) show weak localization. This is indicated by a larger value of $\epsilon(s)$ with weaker oscillations. These energy landscapes $\epsilon(s)$ inform our model of sequence effects in complex coacervation.

We define a new transfer matrix, that now depends on the monomer index via the sequence-dependent epsilon:

$$\mathbf{M}_s(\epsilon(s)) = \begin{bmatrix} A_0\phi_S & A_0\phi_S & A_0\phi_S & A_0\phi_S \\ 0 & 1 & 2 & 0 \\ B_0\phi_P & B_0\phi_P & B_0\phi_P & B_0\phi_P \\ D_0e^{-\epsilon(s)} & D_0e^{-\epsilon(s)} & D_0e^{-\epsilon(s)} & D_0e^{-\epsilon(s)} \end{bmatrix} \tag{5.7}$$

This transfer matrix is specifically for monomers that contain a *charge*, in contrast to neutral monomers along the chain. We consider neutral monomers to only affect the free energy of coacervation through (1) excluded volume of the monomer units and (2) through their spacing of charges and its effect on $\epsilon(s)$ for those monomers. Neutral monomers are otherwise not required to 'pair' with an opposite charge, and their contribution to the transfer matrix

calculation is as an identity matrix $\mathbf{M}_n = \mathbf{I}$. We can use this set of matrices to write a new grand canonical partition function $\Xi_{seq}^{int} = \prod_s^{N_P} (\mathbf{M}_s(\epsilon(s))(1-\delta_{z_s}) + \mathbf{M}_n\delta_{z_s})$. This can be simplified, since when $\delta_{z_s} = 1$ for neutral monomers, the product is simply an identity matrix. This means that the system can be divided into a product over a series of charge 'runs', or adjacent charges, of length n_r.

$$\Xi_{seq}^{int} = \left[\prod_{runs}^{n_r} \left[\vec{\psi}_0^T \left(\prod_{s>1}^{n_r} \mathbf{M}_s(\epsilon(s))\vec{\psi}_1(\epsilon(s))\right)\right]\right] \tag{5.8}$$

We schematically show how this calculation is carried out in Figure 5.4b. The new interaction free energy contribution for a patterned polymer (in this case, a polycation) is $\mathcal{F}_{seq}^{int}(\{\epsilon(s)\})/(Vk_BT) = \phi_{P+}\ln(\Xi_{seq}^{int})/2f_CN_{P+}$. We thus use the free energy for the overall system:

$$\begin{aligned}\frac{\mathcal{F}_{seq}}{Vk_BT} &= \frac{\phi_{P+}}{N_{P+}}\ln\phi_{P+} + \frac{\phi_{P-}}{N_{P-}}\ln\phi_{P-} + \phi_W\ln\phi_W + \\ &+\phi_{S+}\ln\phi_{S+} + \phi_{S-}\ln\phi_{S-} + \frac{\phi_{P+}}{2f_CN_{P+}}\ln\left[\Xi_{seq}^{int}(\{\epsilon(s)\})\right] + \\ &+\frac{\phi_{P-}}{2N_{P-}}\ln\left[\psi_0^T\mathbf{M}_0^{N_{P-}}\psi_1\right] + \zeta\left(\phi_S + \Lambda_{P+}\phi_{P+} + \Lambda_{P-}\phi_{P-}\right)^3\end{aligned} \tag{5.9}$$

Here, the sequence-dependence is almost completely contained within the interaction term for the polycation, while the homopolyanion is treated as in the previous transfer matrix theory [93]. In this paper we use the parameters $A_0 = 35.0$, $B_0 = 11.5$, $\Lambda_{P+} = \Lambda_{P-} = 0.84375$, and $\zeta = 16.0$; these are similar to values in prior work, [93,165] but with small changes reflecting slight differences in how we model Λ. The same parameters are used for all sequences considered in this paper.

5.4.1 Sequence-Based Transfer Matrix Theory Can Match Experimental and Computational Phase Behaviors

Full theoretical phase diagrams are calculated for the polyelectrolyte patterns. These demonstrate excellent, nearly-quantitative matching with the full simulation phase diagrams shown in Figure 5.3a and Figure 5.3. In particular, we can capture how the phase diagram changes

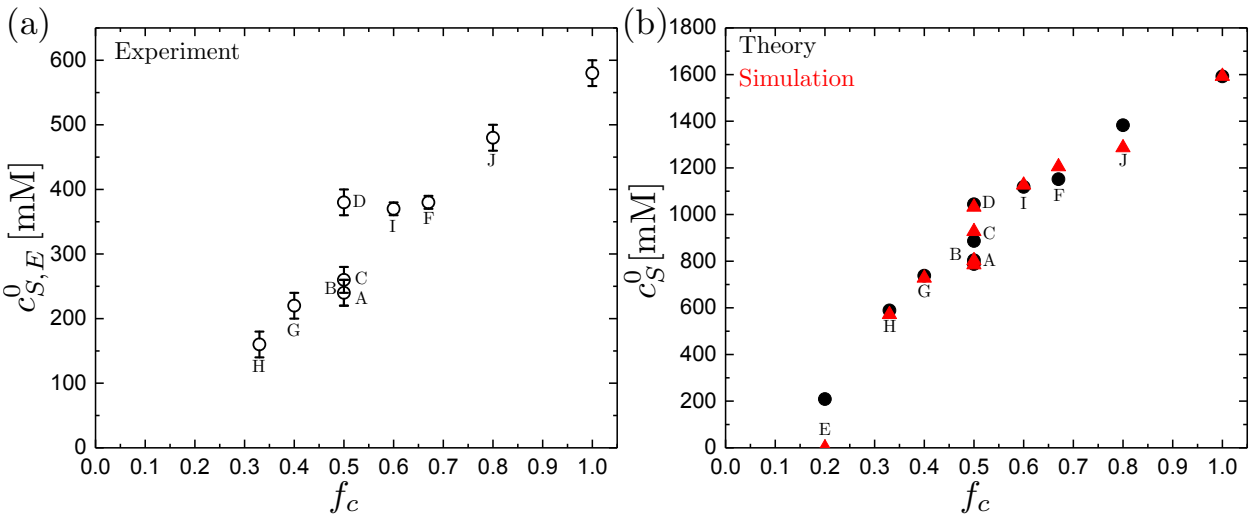

Figure 5.5: (a) Experimental salt resistance $c^0_{S,E}$ as a function of charge fraction f_C for sequences $A-J$ shown in Figure 5.1d, and also a homopolyelectrolyte coacervate $f_C = 1$. We note that experimental data for sequence E is not included, because only solid precipitation is observed and thus $c^0_{S,E}$ is not accessible. (b) Theoretical (black circles) and simulation (red triangles) salt resistance c^0_S as a function of charge fraction f_C for sequences $A-J$. We note that simulation and theory are in nearly quantitative agreement, and both qualitatively agree with the experimental trends in (a).

with increasing **blockiness** for the constant $f_C = 0.5$ sequences (A-D) in simulation, experiment, and theory. This is shown in Figure 5.3c. In particular, this matching includes the significant jumps in c^0_S from B to C and C to D, concomitant with the emergence of significant variations in $\epsilon(s)$ in Figure 5.4a.

We showed this charge **blockiness** effect in simulation in Change, *et al.*, [11] which was attributed to the one-dimensional confinement of charges localized along the backbone. This emerges from our theory, because the energetic parameter $\epsilon(s)$ (Figure 5.4a) corresponds a local one-dimensional confinement potential for counterions along the chain.

We extend this matching to the entire set of sequences considered in Figure 5.1d. In Figure 5.5a, we plot the experimental $c^0_{S,E}$ as a function of the overall charge fraction f_C for sequences A-J. We observe large variations in $c^0_{S,E}$, ranging from 160 to 580 mM NaCl, showing that charge patterns can significantly alter the strength of electrostatic interactions. We obtain the values of c^0_S from simulation and theory for this same, extended set of sequences (see Figure 5.3 for full phase diagrams) and also plotted versus f_C in Figure 5.5b. Both simulation and theory results exhibit nearly-quantitative matching, and exhibit qualitative

matching with the experimental values observed in Figure 5.5a.

Experiment, theory, and simulation all exhibit the same trends. Broadly speaking, high values of f_C lead to larger values of $c_{S,E}^0$ (experiment) and c_S^0 (theory and simulation), corresponding to higher strengths of electrostatic interactions. This is expected, given that there are more charges per chain and thus more electrostatic attraction to the oppositely-charged polymeric species. Nevertheless, we note that even among the same charged fraction there can be a wide variation in $c_{S,E}^0$ and c_S^0, as apparent in the **blockiness** trend at $f_C = 0.5$. The opposite situation is also true, with similar values of c_S^0 being observed for different values of f_C. For example, we note that the trio D, I, and F or the pair G and A show a similar value of $c_{S,E}^0$ despite having different charge fractions. These particular cases generally represent a trade-off between blockiness and charge fraction, with less f_C needed if the sequences have longer blocks. We are able to accurately capture this effect of precise charge sequence on the phase behavior of complex coacervates with both theory and simulation, because our theory considers the particular charge sequence rather than average sequence metrics such as charge fraction f_C or blockiness $\langle n_r \rangle$.

5.4.2 Sequence-Based Trends

Having looked at the effect of **blockiness**, we tested the ability of this theory to capture non-regular sequences. In particular, we show this by keeping the total charge fraction $f_C = 0.5$ constant, and maintaining constant runs of four charges while varying neutral spacers (sequences C, K-M, and D *i.e.*, **constant runs**). These systematically shrink the length of one neutral spacer while increasing the length of another (see schematic in Figure 5.6a). We do this for charge runs of length $n_r = 4$, which represents a transition between $\langle n_r \rangle = 4$ and $\langle n_r \rangle = 8$ (sequences C and D) at the extremes. Despite controlling for both f_C and $\langle n_r \rangle$, this variation results in a marked change in the values of c_S^0 and $c_{S,E}^0$ for theory and experiment. This is plotted in Figure 5.6a (circular symbols) as a function of the larger neutral linker length ν, and demonstrates that there is a transition from C to D where intermediate values of c_S^0 are observed. We attribute this change to the proximity of charge runs, which still affect each other even when separated by a few neutral monomers, a cooperative effect that

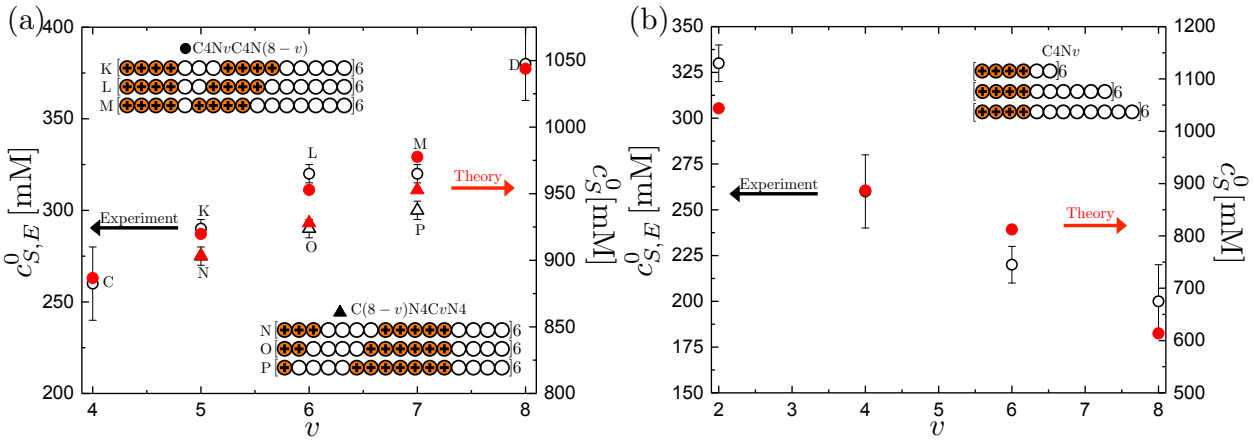

Figure 5.6: (a) Salt resistance c_S^0 for $f_C = 0.5$ with varying length neutral spacers, denoted by v and $8 - v$, between runs of four charges (circles) and with varying length charge blocks, denoted by v and $8 - v$, separated by spacers of four neutral monomers (triangles). Experiment (black) and theory (red) exhibit qualitative matching, showing the complicated interplay between charge block separation and length. (b) Salt resistance for polycations with 24 total charged monomers, separated by increasingly long neutral spacers, denoted by v.

decreases with increasing length of the neutral spacer. Indeed, this is observed in both experiment (open, black points, $c_{S,E}^0$) and theory (filled, red points, c_S^0).

The next set of sequences we highlight are C, N-P, and D. This **constant spacers** trend is the inverse of the **constant run** trend, and is characterized by constant spacer length (4 neutral monomers) with variation in charged runs at a constant $\langle n_r \rangle = 4$ and $f_C = 0.5$. Here we observe a similar transition between the limiting sequences C and D, plotted in Figure 5.6a as triangular symbols.

We note for both the **constant run** and **constant spacer** trends, the increase in $c_{S,E}^0$ and c_S^0 is more abrupt as the longer charge-run length ν is increased from $\nu = 7$ to $\nu = 8$, which is again observed in both experiment and theory. This demonstrates that there is a large differential effect of moving an isolated charged (P to D) or neutral monomer (M to D) in a larger run of the other monomer type. This is especially apparent in the P to D transition, which we attribute to the lack of electrostatic cooperativity of the isolated charged monomer with respect to its neighbors in P; upon 'promoting' that monomer to be in the long, charged block in D it gains the cooperative electrostatic attractions associated with these blocks.

We consider a final **constant runs, constant number of charges** trend, where runs of four adjacent charges along the polycation have differing numbers of neutral monomers, only now the chain length N_{P+} is increased to have a constant number of charged positive charges along the polycation. This runs from 2 to 8 monomers between groupings of four charged monomers. We plot $c^0_{S,E}$ and c^0_S for these sequences in Figure 5.6b, and show that they decrease with the number of neutral monomers ν for both the experiment and theory values. This further clarifies that the values of n_r and the total *number* of charges per chain do not, by themselves, dictate the strength of electrostatic interactions. The neutral spacers, despite not being directly involved with the electrostatic interactions, affect the local charge correlations sufficiently to cause significant changes in c^0_S and correspondingly the strength of the electrostatic attractions between the oppositely-charged polyelectrolytes.

5.5 Conclusion

We have developed a theoretical framework for understanding the role of polyelectrolyte charge sequence in complex coacervates. This framework builds on a transfer matrix approach [93] that explicitly accounts for the local electrostatic environment along a sequenced polyelectrolyte via an effective energy $\epsilon(i)$. We can capture the effects of sequence in complex coacervates, including charge fraction and charge blockiness, as well as the more subtle variations in charge associated with non-regular sequences. Furthermore, we show close matching between experiment, simulation, and theory for the wide range of sequences considered. The emerging physical picture is that there is a tradeoff between the number of charges per chain and the blockiness of the sequence, however the relative position of these blocks also plays a significant role in determining phase behavior.

This computational, experimental, and theoretical effort provides the foundation to study a whole range of polyelectrolytes and biopolyelectrolytes with charge sequence. The next step is to incorporate other molecular interactions into this theoretical framework, such as hydrogen bonding, short-range χ-interactions and hydrophobicity, and ion-pi interactions. This is particularly relevant to biological systems such as IDPs, which are known to form phase-separated structures in the cell that are sensitive to sequence. However, this may

also open the door to engineering charge sequence in synthetic polymers, and to inform the self-assembly or phase behavior of soft materials.

Since the utility of this transfer matrix theory to describe a number of physical molecular features, including charge sequence, has been demonstrated, this theory will now be used to investigate interfacial properties of complex coacervates. Examining interfacial properties will start to build the foundation for understanding coacevate driven self-assembly. Additionally, a neutral polymer species will be added to the system to demonstrate the alteration to the phase behavior and interfacial properties, which will need to be considered if examining a system containing a neutral species, such as a block copolymer.

CHAPTER 6

ELUCIDATING INTERFACIAL PROPERTIES OF COMPLEX COACERVATES USING SIMULATION AND THEORY

Reproduced from T.K. Lytle, A.J. Salazar, C.E. Sing, *The Journal of Chemical Physics* 2018, 149, 163315, with the permission of AIP Publishing.

6.1 Introduction

Most theoretical/simulation studies on interfacial properties have been developed using either Voorn-Overbeek theory [109] , discussed in Section 1.5.1, or field theoretic simulations [75, 79], discussed in Section 1.5.3. These efforts provide an initial glimpse at how interfacial tension changes with salt, however both carry the limitations of their underlying methods.

In this chapter, we show that the transfer matrix (TM) approach developed in Chapter 2, combined with self consistent field theory (TM-SCFT), can lead to predictions about the interface that are consistent with both Monte-Carlo-informed SCFT (MC-SCFT) [112] and full coarse-grained Molecular Dynamics (MD) simulations. All three methods quantitatively match with regards to both coacervate bulk thermodynamics and the structure of the interface, demonstrating the efficacy of field theory techniques developed by the authors [112]. We subsequently demonstrate that the two SCFT-based methods, informed either by theory or simulation, exhibit the same interfacial thermodynamics; this includes the surface tension, interfacial width, and the surface excess of salt ions. We modify both MC-SCFT and TM-SCFT to include a neutral polymer, to understand interfaces similar to those found in block copolyelectrolytes. We show that increasing neutral polymer density drastically increases the immiscible region of the phase diagram due to the interplay between excluded volume of the polymeric species. Indeed, this can lead to large regions of small, but pos-

itive, surface tension; this understanding is crucial to understand the thermodynamics of coacervate-driven assembly.

6.2 Theoretical and Computational Methods

We use a combination of theoretical and computational methods to study complex coacervate interfaces, in part to explore their limitations and capabilities. Specifically, the MD simulations require the fewest assumptions, because all chains and salt ions are explicitly represented; however, this comes at a significant computational cost. SCFT is far more efficient, however it comes with the trade-off that all chains are treated at a mean-field level. However, we use methods (both TM and MC) that provide information about the local charge correlations that are crucial to understanding coacervate thermodynamics [67, 94]. TM and MC provide different routes to this correlation information, with MC accounting for charge correlations directly from simulation via the method outlined in 2.2 [4, 10, 112] while TM reflects a theoretical model developed in Section 2.3 [93, 121].

6.2.1 Self-Consistent Field Theory (SCFT)

We consider a system composed of polyelectrolytes, neutral polymers, salt, and water, and use SCFT methods standard in the literature [82, 168–170]. To simplify our SCFT calculation, we assume both local electroneutrality and charge stoichiometry between both polymers and ions; therefore, we only need one polyelectrolyte species representing both polycations and polyanions, and one salt species representing both cations and anions. This is a standard assumption common to most coacervate models, [65,111], and is used to simplify experiments; this can in principle be relaxed [121]. For this chapter, the of polymerization is $N = 100$ and is the same for both the polyelectrolyte and the neutral polymer. Species-specific quantities are denoted with subscripts; A for polyelectrolytes, B for neutral polymers, S for salt, and W for water. We thus define a set of volume fractions $\phi_i(\boldsymbol{x})$, where $i = A, B, S, W$ that is a function of a spatial position $\boldsymbol{x}$.

The homogeneous free energy F of a coacervate system can be written as [78, 112]:

$$\frac{F}{k_B T V} = \frac{f}{k_B T} = \frac{\phi_A}{N} \ln \phi_A + \frac{\phi_B}{N} \ln \phi_B + \phi_S \ln \phi_S + \phi_W \ln \phi_W + f_{EXC}\left(\phi_j\right) \tag{6.1}$$

Here we introduce the per-volume free energy f. The first four terms on the right side account for the translational entropies of all the species. The fifth term is an excess free energy that accounts for all remaining contributions to F, and is generally a function of the set of volume functions ϕ_j. $f_{EXC}\left(\phi_j\right)$ is the excess free energy which accounts for the *local* charge interactions that drive coacervation. This term will not be given here in its explicit form; however, we describe how to obtain explicit forms for values $f_{EXC}\left(\phi_j\right)$ in Section 2.2 (for MC) or 2.3 (for TM). Derivatives of $f_{EXC}\left(\phi_j\right)$ will be discussed in subsequent subsections. We note that this term is assumed to be completely local, based on the observation that coacervation takes place at high salt/polymer concentrations where we expect very local charge correlations to dominate. This theory thus differs from alternative field theoretic formalisms that directly include the Coulomb interaction in the Hamiltonian, simplifying the SCFT calculation but introducing an assumption that we can use a free energy associated with charge correlations while neglecting how they may be affected by concentration gradients that arise in inhomogeneous polymer systems.

The homogeneous free energy F in Equation 6.1 corresponds to a Hamiltonian functional $\mathcal{H}$ [82]:

$$\begin{aligned}\mathcal{H}\left[\{\phi_j\},\{\omega_j\}\right] = &-n_A \ln Q_A\left[i\omega_A\right] - n_B \ln Q_B\left[i\omega_B\right] - n_S \ln Q_S\left[i\omega_S\right] - n_W \ln Q_W\left[i\omega_W\right] \\ &+ \rho_0 \int d\mathbf{r} \left[f_{EXC}\left(\{\phi_j\left(\mathbf{r}\right)\}\right) + \frac{\xi}{2}\left(\sum_k \phi_k\left(\mathbf{r}\right) - 1\right)^2 - i\sum_k \omega_k\left(\mathbf{r}\right)\phi_k\left(\mathbf{r}\right)\right]\end{aligned} \tag{6.2}$$

The Hamiltonian is a functional of the position dependent density fields $\phi_j\left(\mathbf{r}\right)$ and auxiliary fields $\omega_j\left(\mathbf{r}\right)$ for of the species [82]. ρ_0 is the bulk number density. The single chain partition functions Q_A and Q_B, along with the single particle partition functions Q_S and Q_W are functionals of their respective auxiliary fields $i\omega_j\left(\mathbf{r}\right)$ [82]. The first term in the integral is

the local excess free energy, to be calculated from MC or TM, and the second term in the integral ensures that the sum of the volume fractions is 1 with a coefficient ξ that is set to be large. In writing this Hamiltonian for inhomogeneous coacervate systems, we introduce an ansatz that a homogeneous value of the excess free energy $f_{EXC}\left(\{\phi_j\}\right)$ can be used locally at points $\mathbf{r}$, leading to a position-dependent $f_{EXC}\left(\{\phi_j\left(\mathbf{r}\right)\}\right)$. This term is thus approximated as a local contribution to the Hamiltonian, based on the observation that coacervation takes place at high salt/polymer concentrations where we expect local charge correlation to dominate [1, 4, 5]. We do not justify this "local homogeneity" ansatz *a priori* because electrostatic correlations in MC simulations are loner-range than the field theory grid spacing; we will instead justify *a posteriori* through comparison to particle-based MD. This theory thus differs from alternative field theoretic formalisms that directly include the Coulomb interaction in the Hamiltonian, [75, 79] simplifying the SCFT calculation but introducing an assumption that we can use a free energy associated with charge correlations while neglecting how they may be affected by concentration gradients that arise in inhomogeneous polymer systems [82].

The goal of SCFT is to find the 'saddle point,' or sets of fields $\phi_j^*\left(\mathbf{r}\right)$ and $\omega_j^*\left(\mathbf{r}\right)$ where the Hamiltonian is at an extremum [82]:

$$\left(\frac{\delta\mathcal{H}\left[\{\phi_j\},\{\omega_j\}\right]}{\delta\omega_j\left(\mathbf{r}\right)}\right)_{\omega_j^*}=\left(\frac{\delta\mathcal{H}\left[\{\phi_j\},\{\omega_j\}\right]}{\delta\phi_j\left(\mathbf{r}\right)}\right)_{\phi_j^*}=0 \tag{6.3}$$

These functional derivatives with respect to the auxiliary fields lead to the expression for the density in terms of the propagators [82, 168–170]:

$$\left(\frac{\delta\mathcal{H}\left[\{\phi_j\},\{\omega_j\}\right]}{\delta\omega_j\left(\mathbf{r}\right)}\right)_{\omega_j^*}=0=-in_j\frac{\delta\ln Q_j\left[i\omega_j\right]}{\delta\left(i\omega\left(\mathbf{r}\right)\right)}-i\rho_0\phi_j\left(\mathbf{r}\right) \tag{6.4}$$

For the polymer components, this becomes [82, 168–170]:

$$\phi_{j=A,B}\left(\mathbf{r}\right)=\frac{\langle\phi_j\rangle}{Q_j\left[W_j\right]}\int_0^N dsq_j\left(\mathbf{r},N-s;\left[W_j\right]\right)q_j\left(\mathbf{r},s;\left[W_j\right]\right) \tag{6.5}$$

For the water and salt components, this becomes [82, 168–170]:

$$\phi_{j=S,W}\left(\mathbf{r}\right)=\frac{\langle\phi_j\rangle}{Q_j\left[W_j\right]}\mathrm{e}^{-W_j(\mathbf{r})} \tag{6.6}$$

Here, we have defined a field $W_j = i\omega_j$, and the quantity $q_j\left(\mathbf{r},s;\left[W_j\right]\right)$ in Equation 6.5 is a propagator that represents the probability that a sub-chain of length s has its terminal chain end located at a position $\mathbf{r}$ in a field W_j. These are calculated via the diffusion equation, which in one dimension ($\mathbf{r}\rightarrow x$) [82, 168–170]:

$$\frac{\partial q_j\left(x,s;\left[W_j\right]\right)}{\partial s}=\frac{a^2}{6}\frac{\partial^2 q_j\left(x,s;\left[W_j\right]\right)}{\partial x^2}-W_j\left(x\right)q_j\left(x,s;\left[W_j\right]\right) \tag{6.7}$$

We also consider the functional derivatives of the Hamiltonian (in Eqution 6.4) with respect to the density fields [82, 168–170]:

$$\left(\frac{\delta\mathcal{H}\left[\left\{\phi_j\right\},\left\{\omega_j\right\}\right]}{\delta\phi_j\left(\mathbf{r}\right)}\right)_{\phi_j^*}=0=\rho_0\frac{\partial f_{EXC}\left(\mathbf{r}\right)}{\partial\rho_j\left(\mathbf{r}\right)}+\xi\left(\sum_k\phi_k\left(\mathbf{r}\right)-1\right)-i\omega_j\left(\mathbf{r}\right) \tag{6.8}$$

The partial derivative is the local excess chemical potential $\mu_{j,EXC}\left(\phi_i\left(\mathbf{r}\right)\right)$, calculated with respect to the number density ρ_j of species j. This leads to the result:

$$W_j\left(\mathbf{r}\right)=\mu_{j,EXC}\left(\phi_i\left(\mathbf{r}\right)\right)+\xi\left(\sum_k\phi_k\left(\mathbf{r}\right)-1\right) \tag{6.9}$$

In this chapter, the value of $\mu_{j,EXC}\left(\phi_i\left(\mathbf{r}\right)\right)$ is determined from either MC or TM using the set of values $\phi_i\left(\mathbf{r}\right)$. A self-consistent scheme is used to calculate the saddle point. This consists of calculating the fields $W_j\left(\mathbf{r}\right)$ using the species densities $\phi_j\left(\mathbf{r}\right)$ via Equation 6.9. These fields are then used to calculate the propagators for the polymer species $q_j\left(x,s;\left[W_j\right]\right)$ in Equation 6.7, and subsequently the species densities $\phi_j\left(\mathbf{r}\right)$ using Equations 6.5 and 6.6. These densities can once more be used to calculate $W_j\left(\mathbf{r}\right)$, and this process repeats until all of the fields have converged to their saddle point values $W_j^*\left(\mathbf{r}\right)$ and $\phi_j^*\left(\mathbf{r}\right)$. For this chapter, we use the value $\xi = 1000k_BT$.

6.2.2 MC-SCFT

MC simulations were performed using the system described in Section 2.2 with the addition of n_B neutral polymer chains with the same degree of polymerization as the polyelectrolytes, which are included to model how the neutral species affects the phase separation and interfacial profiles of complex coacervates. This neutral species has the same angle, bond, and hard sphere potentials as the polyelectrolytes. Modification of Equation 2.11 to include the neutral species yields:

$$\begin{aligned} f_{EXC}\left(\phi_S,\phi_A,\phi_B\right) = &\int_{\phi_S^0,\phi_A^0,\phi_B^0}^{\phi_S,\phi_A^0,\phi_B^0} \mu_{EXC,S}\left(\phi_S^{'},\phi_A^0,\phi_B^0\right) d\phi_S^{'} \\ &+ \int_{\phi_S,\phi_A^0,\phi_B^0}^{\phi_S,\phi_A,\phi_B^0} \mu_{EXC,A}\left(\phi_S,\phi_A^{'},\phi_B^0\right) d\phi_A^{'} \\ &+ \int_{\phi_S,\phi_A,\phi_B^0}^{\phi_S,\phi_A,\phi_B} \mu_{EXC,B}\left(\phi_S,\phi_A,\phi_B^{'}\right) d\phi_B^{'} \end{aligned} \tag{6.10}$$

where we have included the chemical potential of the neutral polymer species, $\mu_{EXC,B}$. These f_{EXC} values can be fit with a third order polynomial using orthogonal distance regression. Simulations to determine chemical potential values in the limit of $\phi_B = 0.00$ were performed with $n_{A+} = n_{A-} = 6$, where n_{A+} is the number of polycation chains and n_{A-} is the number of polyanion chains, and simulations to determine chemical potential values with neutral polymer used $n_B = 12$. This f_{EXC} serves as an input to MC-SCFT.

6.2.3 TM-SCFT

The transfer matrix described in Section 2.3 is modified to include the neutral species:

$$f_{EXC}\left(\{\phi_i\}\right) = \frac{-\phi_A}{2}\ln\Theta + \kappa\left(\Lambda\left(\phi_A+\phi_B\right)+\phi_S\right)^3 \tag{6.11}$$

Here, the function Θ is [93, 121]:

$$\begin{aligned} \Theta = 1 + A_0\phi_S + B_0\phi_A + \mathrm{e}^{-\tilde{\epsilon}} + \\ + \sqrt{\left(1 + A_0\phi_S + B_0\phi_A + \mathrm{e}^{-\tilde{\epsilon}}\right)^2 - 4\left(A_0\phi_S - B_0\phi_A + \mathrm{e}^{-\tilde{\epsilon}}\right)} \end{aligned} \tag{6.12}$$

Inclusion of the neutral polymer species is completely contained in the phenomenological cubic term $\kappa\left(\Lambda\left(\phi_A+\phi_B\right)+\phi_S\right)^3$, because the neutral polymer only interacts with the other species via the hard sphere potential. We use this form for this chapter, but more generally it is possible to numerically calculate the interaction free energy via the Equation 2.23 if the transfer matrix is no longer analytically tractable.

We can rewrite Equation 6.12 as:

$$\Theta = \theta_0 + \theta_1 \tag{6.13}$$

$$\theta_0 = 1 + A_0\phi_S + B_0\phi_A + e^{-\tilde{\epsilon}} \tag{6.14}$$

$$\theta_1 = \sqrt{\theta_0^2 - 4\left(A_0\phi_S - B_0\phi_A + e^{-\tilde{\epsilon}}\right)} \tag{6.15}$$

For the species in the system, we can write the chemical potentials:

$$\begin{aligned}\frac{\mu_S}{k_BT} = \ln\phi_S + 1 - \phi_S - \phi_W - \frac{\phi_A}{N_A} - \frac{\phi_B}{N_B} + \\ + \frac{\phi_A}{\theta_1}\left[\frac{\theta_0 - A - 1}{2} - \frac{A\phi_S - B\phi_A - A}{\Theta}\right] + \\ + \kappa\phi_{TOT}^2\left(3 - 2\phi_{TOT}\right)\end{aligned} \tag{6.16}$$

$$\begin{aligned}\frac{\mu_A}{k_BT} = \frac{\ln\phi_A}{N_A} + \frac{1}{N_A} - \phi_S - \phi_W - \frac{\phi_A}{N_A} - \frac{\phi_B}{N_B} + \\ + \frac{\phi_A}{\theta_1}\left[\frac{\theta_0 - B - 1}{2} - \frac{A\phi_S - B\phi_A + B}{\Theta}\right] - \\ - \ln\Theta/2 + \kappa\phi_{TOT}^2\left(3\Lambda - 2\phi_{TOT}\right)\end{aligned} \tag{6.17}$$

$$\begin{aligned}\frac{\mu_B}{k_BT} = \frac{\ln\phi_B}{N_A} + \frac{1}{N_B} - \phi_S - \phi_W - \frac{\phi_A}{N_A} - \frac{\phi_B}{N_B} + \\ + \frac{\phi_A}{\theta_1}\left[\frac{\theta_0 - 1}{2} - \frac{A\phi_S - B\phi_A}{\Theta}\right] - \\ + \kappa\phi_{TOT}^2\left(3\Lambda - 2\phi_{TOT}\right)\end{aligned} \tag{6.18}$$

$$\frac{\mu_W}{k_B T} = \ln \phi_W + 1 - \phi_S - \phi_W - \frac{\phi_A}{N_A} - \frac{\phi_B}{N_B} + \\ + \frac{\phi_A}{\theta_1}\left[\frac{\theta_0 - 1}{2} - \frac{A\phi_S - B\phi_A}{\Theta}\right] - \\ -2\kappa\phi_{TOT}^3 \tag{6.19}$$

Here we have defined:

$$\phi_{TOT} = \phi_S + \Lambda(\phi_A + \phi_B) \tag{6.20}$$

These expressions for μ_i can be used in Equation 6.9 to incorporate the transfer matrix theory into the SCFT calculation.

6.2.4 Molecular Dynamics Simulations (MD)

Molecular dynamics (MD) simulations were performed on a system consisting of n_{A+} polycations and n_{A-} polyanions, modeled as connected, monovalently charged beads with diameter σ. Both polymers have the same degree of polymerization, N. n_{S+} cations and n_{S-} anions are modeled as monovalently charged beads, also with a diameter σ. Water is included as an implicit solvent with a relative dielectric constant, $\epsilon_r = 78.5$. These simulations were performed using the Large-scale Atomic/Molecular Massively Parallel Simulator (LAMMPS) with a Langevin thermostat [171]. See Figure 6.1 for a schematic of our model. The overall potential energy is given by:

$$U = U_E + U_B + U_\theta + U_{LJ} \tag{6.21}$$

U_E models the electrostatic interactions:

$$U_E = \frac{1}{2}\sum_{i,j} \frac{q_i q_j}{4\pi\epsilon_0\epsilon_r r_{ij}} \tag{6.22}$$

where q_i is the charge on bead i, ϵ_0 is the permittivity of free space, and r_{ij} is the separation between beads i and j. Standard Ewald summation is used to account for the long-range interactions in periodic boundary conditions [104]. The polymers are bound together with

a bond potential U_B:

$$U_B = \sum_i \frac{\kappa_B}{2} \left(r_{i,i-1} - r_0\right)^2 \tag{6.23}$$

For this contribution, κ_B is the strength of the bond potential, and r_0 is the equilibrium bond distance. In addition to the bond potential the polymers have a bending potential U_θ:

$$U_\theta = \sum_i \frac{\kappa_\theta}{2} \left(\theta_{i,i-1,i-2} - \theta_0\right)^2 \tag{6.24}$$

Here, κ_θ is the strength of the bending potential, $\theta_{i,i-1,i-2}$ is the angle between the two bond vectors, and θ_0 is the equilibrium angle between bond vectors. The excluded volume of the beads is modeled by a Lennard-Jones potential U_{LJ}:

$$U_{LJ} = \sum_{ij} 4\epsilon_{LJ} \left[\left(\frac{\sigma_{LJ}}{r_{ij}}\right)^{12} - \left(\frac{\sigma_{LJ}}{r_{ij}}\right)^{6} \right] \qquad r_{ij} < r_c \tag{6.25}$$

where ϵ_{LJ} is the depth of the potential well, σ_{LJ} is the interparticle separation at which U_{LJ} becomes zero, and r_c is the cutoff distance of this potential [104].

For this simulation, the degree of polymerization is kept at $N = 100$. We choose parameters consistent with our previous efforts; [4, 112] κ_B=250k_BT, $r_0 = 1.05\sigma$, $\kappa_\theta = 1.65k_BT$, and $\theta_0 = \pi$. Lennard-Jones parameters to model excluded volume were $\epsilon_{LJ} = 10.75k_BT$, $\sigma_{LJ} = \sigma$, and $r_c = \sigma$. This mimics the hard-sphere potential in the MC simulations by having the interparticle excluded volume potential at zero until the particles overlap. The bead diameter σ was taken as 4.25 Å.

6.3 Results and Discussion

6.3.1 Molecular Dynamics and Self Consistent Field Theory Comparison

We use MD simulations and SCFT to capture the physics of this coacervate system, with the latter informed by both MC simulations and TM theory. We can show that all methods, while they provide different levels of resolution and assumptions, exhibit nearly-quantitative

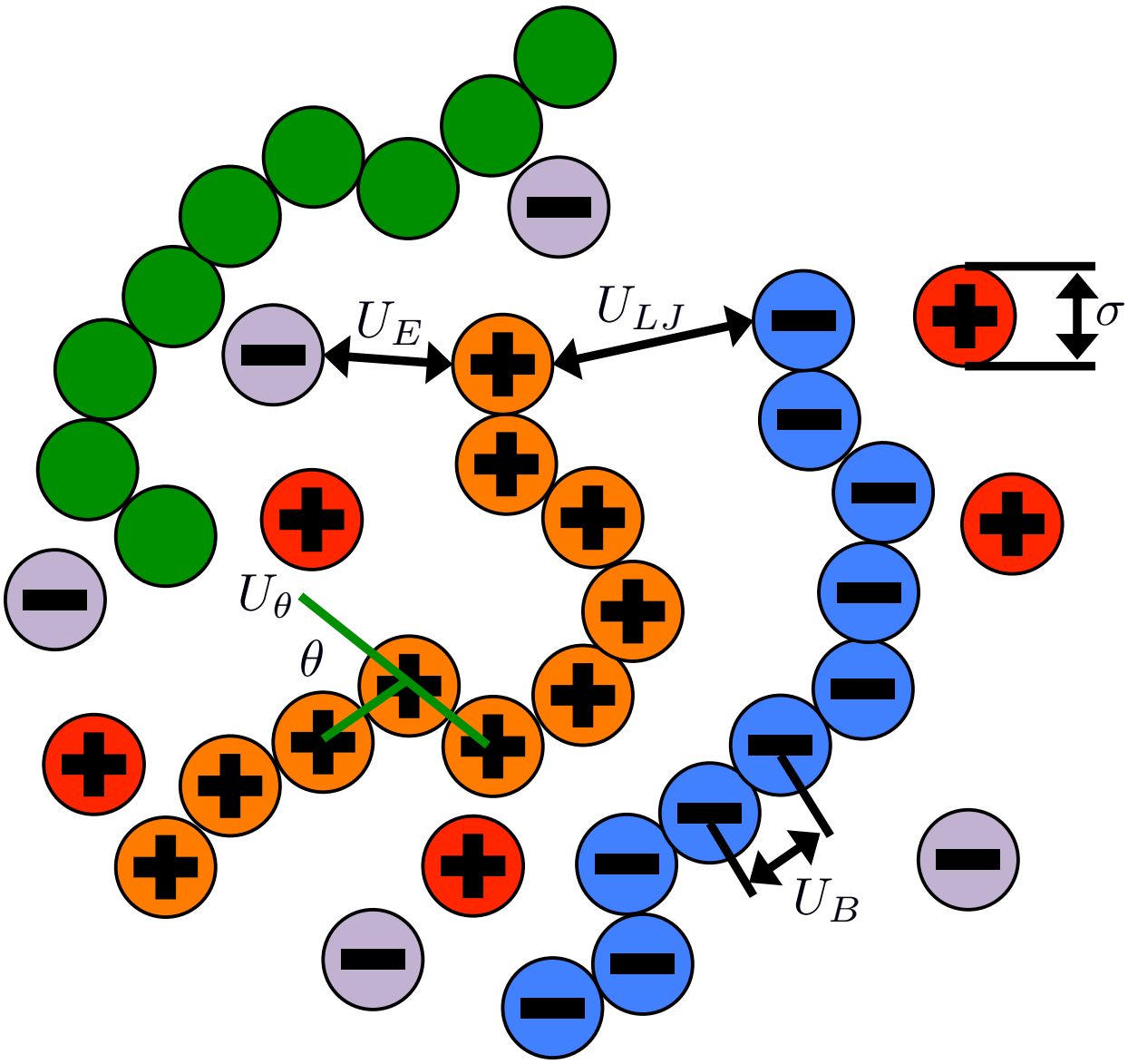

Figure 6.1: Schematic demonstrating the features of both our MD and MC simulation model. All species are represented as beads of diameter σ (including the neutral polymer beads, green), and charged species interact via a Coulomb potential U_E. Polymer charges are connected by a bonding potential U_B, and have a bending potential U_θ. Only minor differences exist between the MD and MC models; in particular, MC has a hard-sphere potential that keeps charges from overlapping, while MD uses a corresponding Lennard-Jones potential parameterized so that both simulations exhibit nearly the same pair correlation functions (see Figure 6.2). There are also minor differences in the bonding potential U_B.

matching for interfacial properties. Importantly, we motivate our use of MC-SCFT and TM-SCFT by comparing with a completely particle-based simulation. To ensure that we have comparable models, we show that the MC used to inform the SCFT yields the same

radial distribution functions when compared to the full-particle MD simulations. Figure 6.2 shows radial distribution functions from both methods (MC and MD) using $n_{A+} = n_{A-} = 6$ in a cubic simulation box for $\phi_A = 0.08$ and $\phi_A = 0.12$ (Figs. 6.2a and b respectively). Both MC and MD simulations agree nearly-quantitatively. Some differences do occur due to differences in the interaction potentials; the MC uses hard-core interactions that are not possible in MD simulations, where a Lennard-Jones potential is used instead. These disparities are apparent at the contact peak near $r/\sigma = 1$, where the differences in these potentials are most pronounced.

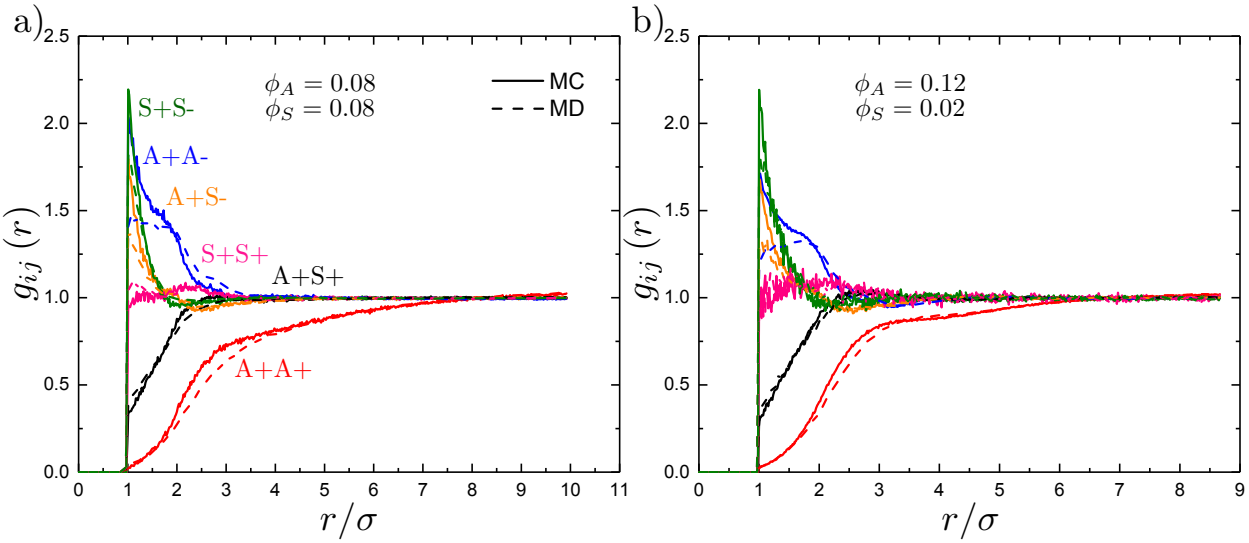

Figure 6.2: Radial distribution functions (RDF), $g_{ij}(\sigma)$ as a function of separation, r/σ, from Monte Carlo (MC, solid lines) simulations and molecular dynamics (MD, dashed lines) simulations. a) RDF at $\phi_A = 0.12$ and $\phi_S = 0.02$. b) RDF at $\phi_A = 0.08$ and $\phi_S = 0.08$. The green line is cation-anion (S+S-) pairs, the blue line is polycation-polyanion (A+A-) pairs, the orange line is polycation-anion (A+S-) pairs, the pink line is cation-cation (S+S+) pairs, the black line is polycation-cation (A+S+) pairs, and the red line is polycation-polycation (A+A+) pairs. Qualitatively, the MC and MD simulations show the same structure. However, some differences are present due to the use of a Lennard-Jones potential for excluded volume interactions as opposed to a hard sphere potential.

The phase behavior of a coacervate with no neutral polymer is shown in Figure 6.3a (calculated from MC-SCFT), showing the two-phase coacervation regime at low salt ϕ_S and polymer ϕ_A concentrations. Sloped tie lines are observed, connecting the large-ϕ_A coacervate phase at a slightly lower ϕ_S than the low-ϕ_A supernatant phase. This is due to the partitioning of salt to the supernatant, which has been demonstrated by previous

computational, theoretical, and experimental work [4, 67, 84, 93, 121]. We also show MD simulation snapshots from phase-separating mixtures along the indicated tie lines, with the orange and blue polymers representing the polycations and polyanions respectively. This structure becomes more diffuse as salt is increased. This is apparent in Figures 6.3b-g, where we plot the interfacial profiles (ϕ_i versus distance x/σ) that form along these same tie lines (Figure 6.3a). These plots include full-particle MD simulations, along with interfacial profiles calculated with both MC-SCFT and TM-SCFT. MD simulations were performed with $n_{A+} = n_{A-} = 15$ in a rectangular prism simulation box with the x-dimension 3 times the length of the y- and z-dimension. Starting volume fractions for each simulation were taken as the midpoint of the tie lines in Figure 6.3a.

All 3 techniques exhibit nearly-quantitative matching in all interfacial profiles shown. This *a posteriori* justifies the approximations we made in the TM-SCFT and MC-SCFT, which is that we have a separation of length scales between the charge correlations (which are treated as a homogeneous system at each SCFT grid point) and the polymer length scales (which span multiple SCFT grid points) [112]. We do note that correlations in Figure 6.2 have a similar range to the gred spacing used in our simulations (0.75σ), which is set relatively small to resolve the interfacial structure. However, this correlation length scale seems to still be sufficiently small compared to the length scales of variation in ϕ_A and ϕ_S such that square gradient corrections to f_{EXC} are unnecessary to match SCFT with MD. The increasingly diffuse interface at higher salt concentrations poses a practical challenge for the full-particle MD, where it is difficult to obtain a good average of the interface; this is why we focus on tie lines far from the critical point. We thus demonstrate that MC-SCFT and TM-SCFT capture the correct interfacial profile, motivating our use of these field-based methods to calculate interfacial properties such as interfacial tension, interfacial width, and the surface excess of salt.

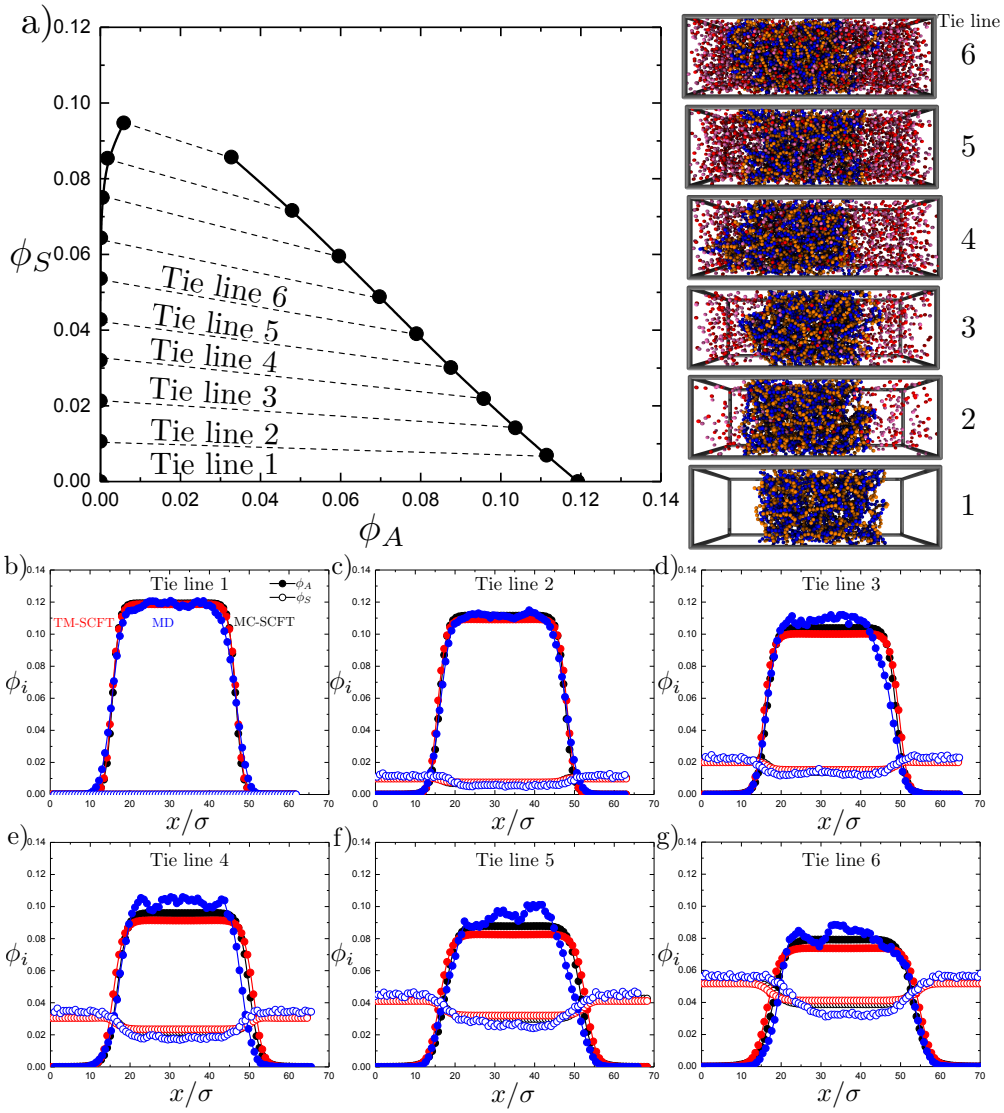

Figure 6.3: a) The phase diagram in the ϕ_S versus ϕ_A plane, determined from MC-SCFT calculations. This phase diagram is consistent with prior theoretical and computational efforts [93]. The labeled tie lines correspond to simulation snapshots shown on the right, showing that phase separation occurs within the simulation box. To quantify this phase separation behavior, we show a comparison of interfacial profiles by plotting ϕ_i versus distance x/σ from MD simulations, MC-SCFT, and TM-SCFT in the limit of no neutral polymer. Blue denotes MD simulations, black denotes MC-SCFT, and red denotes the TM-SCFT simulations. Lines are a guide to the eye. Filled points correspond to the volume fraction of polyelectrolyte ϕ_A, and open points correspond to the volume fraction of salt ϕ_S. MD interfacial profiles have been shifted along the x-axis to overlay the interfaces with SCFT calculations. b) The first tie line interfacial profile contains no salt. c)-g) The interfacial profiles corresponding to tie lines 2-6, respectively. Nearly quantitative matching is demonstrated between all three techniques for the tie lines considered. Interfacial profiles were not obtained above tie line 6, because the relaxation of the interface is on the order of the time for the interface to move inhibiting the ability to determine the average interface using MD simulation.

6.3.2 Interfacial Properties of Coacervates

We can use the results of both MC-SCFT and TM-SCFT to determine the interfacial tension of a coacervate. We use the expression: [172–176]

$$\tilde{\gamma} = \int_{-\infty}^{\infty} \left(\Delta \tilde{f}\left(x\right) + \frac{1}{36\phi_A\left(x\right)} \left(\frac{\partial \phi_A\left(x\right)}{\partial \tilde{x}} \right)^2 + \right. \\ \left. + \frac{1}{36\phi_B\left(x\right)} \left(\frac{\partial \phi_B\left(x\right)}{\partial \tilde{x}} \right)^2 \right) d\tilde{x} \tag{6.26}$$

We have used tildes to denote normalization of energy scales by k_BT and length scales by σ. The second and third terms in the integrand are square gradient expressions for the polyelectrolyte and the neutral polymer, approximated using the result from the Random Phase Approximation (RPA) [175, 176]. The first term in the integrand is the free energy of a homogeneous system with the volume fractions at a point x relative to the bulk free energy of the system, given by the expression: [173, 174]

$$\Delta f\left(x\right) = \sum_{i=A,B,S,W} \frac{\phi_i}{N_i} \left(\mu_i\left(x\right) - \mu_i^{\infty} \right) \tag{6.27}$$

Here, μ_i^{∞} is the chemical potential of species i in the bulk phase.

We show a calculation of this interfacial tension $\tilde{\gamma}$ for a coacervate without the presence of a neutral polymer, shown in Figure 6.4a. Consistent with previous experimental and theoretical literature, [79, 109, 177–179] we plot the decrease in $\tilde{\gamma}$ as a function of salt concentration, where we choose the supernatant salt concentration ϕ_S^{β}. We will typically denote phases by a superscript α (coacervate) and β (supernatant). Indeed, we demonstrate that both MC-SCFT and TM-SCFT exhibit nearly-identical values of $\tilde{\gamma}$, with only a small horizontal offset of the $\tilde{\gamma}$ versus ϕ_S^{β} curve. We can also show that our results exhibit the scaling law described by Qin, et al. [109] for the interfacial tension. $\tilde{\gamma}/\tilde{\gamma}_0 \sim (1 - \phi_S^{\beta}/\phi_S^{crit})^{3/2}$ as ϕ_S^{β} approaches its critical point value ϕ_S^{crit} (Figure 6.5). Here, interfacial tension is normalized by its zero-salt value, $tilde\gamma_0$. Qin demonstrated matching between this prediction and with experimental data [109, 177–179], despite the use of Voorn-Overbeek theory in the derivation of the scaling behavior. Our results are consistent with the Qin prediction, showing a 3/2 slope in a log-log

plot in Figure 6.5 for both TM-SCFT and MC-SCFT; our results are also consistent with the experimental results from the literature [109,177–179], which are also included in Figure 6.5 as open symbols. We note that these results are based on mean-field SCFT models; a different power law will likely be observed as the critical point is approached, which would require beyond-mean-field polymer field theories.

This is consistent with other the interfacial properties, such as the interfacial width D. We define D using the interfacial profile for the polyelectrolyte [172]:

$$D = \frac{2\left(\phi_A^\alpha - \phi_A^\beta\right)}{\left|\frac{\partial \phi_A(x)}{\partial x}\right|_{x=\frac{\left(\phi_A^\alpha + \phi_A^\beta\right)}{2}}} \tag{6.28}$$

Here, the derivative in the denominator is taken at the midpoint concentration between the polyelectrolyte concentrations in the coacervate phase ϕ_A^α and the supernatant phase ϕ_A^β. We plot D/σ as a function of ϕ_S^β for both MC-SCFT and TM-SCFT in Figure 6.4b. Similar to Figure 6.4a, we again see mainly small differences in this quantity between the two methods. The exception to this comes at large values of ϕ_S^β, which is close to the critical point such that D/σ becomes large. The curves do not become large at the same rate, consistent with Figure 6.4a which shows that the critical value of ϕ_S^β appears to be shifted. The physical observation that D increases is consistent with traditional polymer theory, [175, 180–182] where a decrease in the driving force for phase separation broadens the interface. In non-charged systems, this is usually controlled by temperature, however we are instead weakening the electrostatic interaction by using salt concentration ϕ_S^β instead.

This system has effectively 3 species, the polyelectrolytes, salt ions, and water; thus, we can calculate the surface excess of salt at the interface as the overall salt concentration is increased. The surface excess of any species i can be calculated via the relationship: [173,174]

$$\Gamma_i = \frac{1}{D}\left[\int \phi_i(x)\,\mathrm{d}x - D^\alpha \phi_i^\alpha - D^\beta \phi_i^\beta\right] \tag{6.29}$$

Here, D is defined in equation 6.28, and D^i is the size of the phase. This definition, however, depends on the choice of interface position; a related value is independent of this choice:

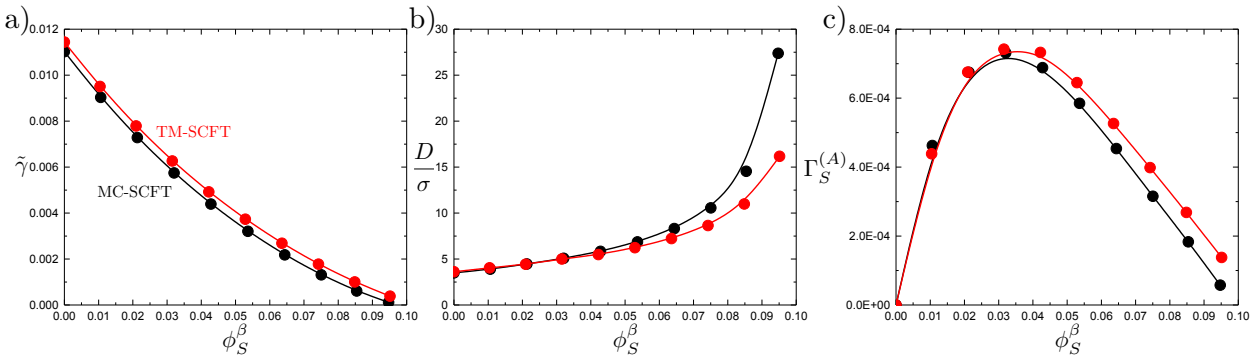

Figure 6.4: Interfacial properties for the coacervate-forming system calculated using both MC-SCFT (black) and TM-SCFT (red) as a function of supernatant salt concentration, ϕ_S^β. Lines are guides for the eye. a) The interfacial tension decreases with increasing salt concentration. b) The interfacial width increases with increasing salt concentration. c) The interfacial excess of salt initially increases with increasing salt concentration, but at large enough salt concentrations the interfacial excess of salt decreases. Observed trends are seen using both MC-SCFT and TM-SCFT. Both techniques qualitatively agree.

[173, 174]

$$\Gamma_i^{(j)} = \Gamma_i - \Gamma_j \frac{\phi_i^\alpha - \phi_i^\beta}{\phi_j^\alpha - \phi_j^\beta}, j \neq i \tag{6.30}$$

This value of $\Gamma_i^{(j)}$ describes the surface excess of i, using a reference of $j \neq i$, such that it does not depend on the choice of $j \neq i$. This physically represents the deviation in excess ϕ_i (captured by the first term in Equation 6.30) away from any excess ϕ_j calculated from the renormalized interfacial structure in the other species j (second term in Equation 6.30). We plot $\Gamma_S^{(A)}$, the surface excess of salt, as a function of ϕ_S^β in Figure 6.4c [173,174]. We once more observe only small differences between MC-SCFT and TM-SCFT, and show that the surface excess approaches $\Gamma_S^{(A)} = 0$ at the limits of ϕ_S^β (where there is no salt) and at the critical value of ϕ_S^β where the system becomes homogeneous. At intermediate values, the surface excess reaches a maximum, indicating that salt preferentially partitions to the interface. The surface excess salt remains quite small, however, with $\Gamma_S^{(A)} \sim 7 \times 10^{-4}$ indicating that any deviations of ϕ_S from what would be expected from the ϕ_A profile are between one or two orders of magnitude smaller than the overall variations in ϕ_S.

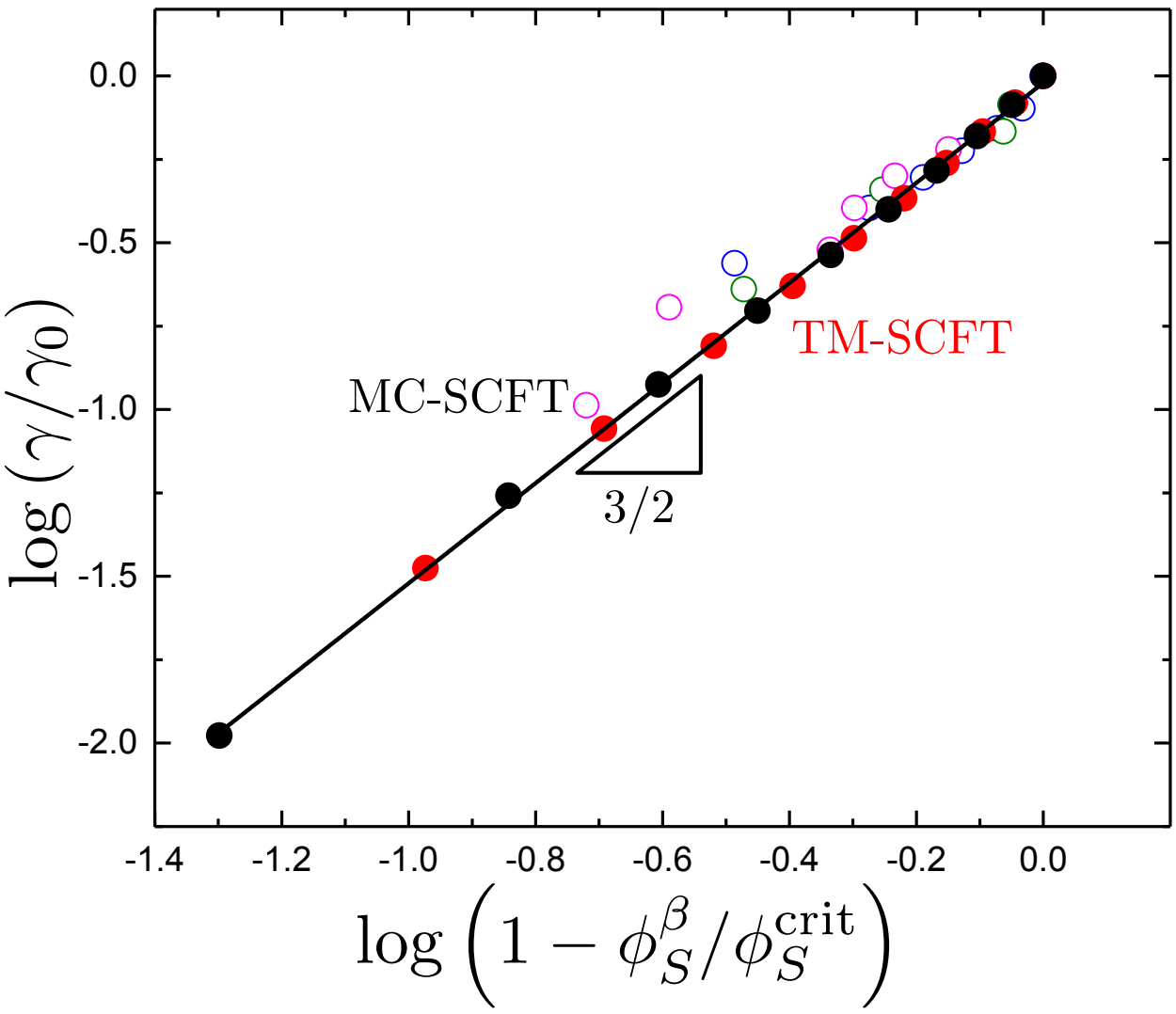

Figure 6.5: Log-log plot showing the scaling of interfacial tension $\tilde{\gamma}/\tilde{\gamma}_0$ versus $1-\phi_S^{\beta}/\phi_S^{crit}$ using both MC-SCFT and TM-SCFT. This exhibits the scaling predicted by Qin et al. [109], $\tilde{\gamma}/\tilde{\gamma}_0 \sim (1-\phi_S^{\beta}/\phi_S^{crit})^{3/2}$, with the black fit line showing the exponent to be 1.50 ± 0.01. For MC-SCFT, $\phi_S^{crit} = 0.0997$, and for TM-SCFT $\phi_S^{crit} = 0.1065$. We also plot the experimental data (open symbols) used in the work of Qin et al., compiled from the studies of Priftis et al. [177] (magenta), Riggleman et. al. [79] (green), and Cohen Stuart et al. [178] (blue). Our predictions are consistent with those experimental results.

6.3.3 Coacervation Phase Diagrams with Neutral Polymer

Interfacial tension plays a significant role in the classical theoretical work on the self-assembly of block copolymers [180–185]. The form of the interfacial free energy follows that of a simple polymer-polymer interface, and is driven by a positive short-range Flory χ parameter [82, 175, 181, 182]. Self-assembled structures formed due to coacervation are driven by long-

range electrostatic attractions, that are not well-represented by χ; [186] instead, we use the analogous interface between a coacervate and a neutral polymer to determine the interfacial tensions that would arise in coacervate-driven self-assembly. Furthermore, the presence of neutral polymer has implications for biological coacervates, which are often in crowded macromolecular environments [187, 188]. Recent reports from experiment demonstrate that 'crowding' can have a significant impact on the formation of bio-inspired coacervates [188].

First, we show that the addition of a neutral polymer species significantly affects the phase diagram depending upon the concentration of neutral polymer (Figure 6.6a and b). To plot the effect of the neutral polymer, we note that it primarily partitions into the supernatant phase. We thus adjust the neutral polymer concentration by fixing its value in this phase ϕ_B^β. The corresponding neutral polymer concentration in the coacervate phase ϕ_B^α is typically negligible, except near the critical point. We thus emphasize that Figure 6.6 is the projection of a three-dimensional phase diagram onto the ϕ_S versus ϕ_A plane.

The inclusion of the neutral polymer results in a large extension of the two-phase region at high ϕ_S and low ϕ_A, which extends further to the right as the concentration ϕ_B^β increases. This trend is observed in both MC-SCFT and TM-SCFT. We interpret this trend as due to the matching of pressure between the supernatant and coacervate phases; the coacervate phase in the absence of neutral polymer is limited to low ϕ_A and ϕ_S due in part to the high pressure due to excluded volume in the polymer-dense coacervate [4]. This phase would expand except this would dilute the combinatoric entropy of polymer-polymer interactions that primarily drives phase separation [93, 121]. With the addition of the neutral polymer, this polymer partitions to the supernatant and applies a counterpressure. When $\phi_A \sim \phi_B$, the pressures of the two phases balance essentially removing the pressure-based driving force for miscibility; this results in an extended two-phase region. These observations are supported by the phase diagram in Figure 6.6c, which shows largely no change in phase behavior if the B-polymer has no explicit excluded volume.

This observation is further supported by the examination of the salt partitioning $\lambda = \phi_S^\alpha/\phi_S^\beta$, where ϕ_S^α is the volume fraction of salt in the coacervate phase and ϕ_S^β is the volume fraction of salt in the supernatant phase. This is plotted as a function of ϕ_S^β in Figures 6.6d and e, corresponding to parts a and b directly above. In the limit of no neutral

polymer, the salt partitions such that the salt concentration in the supernatant is greater than in the coacervate phase ($\lambda < 1$). This is consistent with previous experiment and simulation, [4, 93, 121, 189] and we attribute this to the excluded volume of the polymer in the coacervate phase. Upon addition of neutral polymer, the salt partitioning behavior is altered, in different ways depending on the value of ϕ_S^β. At low ϕ_S^β, salt partitioning becomes increasingly even between the two phases ($\lambda \to 1$). We attribute this to the neutral polymer in the supernatant, which begins to equalize the excluded volume in the two phases as its concentration increases. This occurs below the critical salt concentration of the phase diagram in the absence of neutral polymer, however at high ϕ_S^β the opposite trend is observed. Here, larger values of ϕ_B^β lead to smaller values of λ. We attribute this 'switch' to the large extent that the coacervate phase is increasingly pushed to large ϕ_A and ϕ_S, where excluded volume effects become enhanced.

Our excluded volume argument is consistent with the differences between TM-SCFT and MC-SCFT, particularly with respect to the value of λ. While some aspects of the qualitative trends are very similar, there are some differences; namely the lack of a critical point in the region tested for TM-SCFT and the different magnitudes for the plots of λ. We attribute this to the phenomenological argument for the excluded volume term in Equation 6.11, which is chosen to approximate the free energy associated with packing the species [93, 121]. We also note that Figure 6.6d becomes non-monotonic at large values of ϕ_S^β, with an increase in partitioning at intermediate salt concentrations. This does not occur for the TM-SCFT predictions in Figure 6.6e. We not that this non-monotonicity occurs at high-ϕ_A *and* high-ϕ_S regions of the phase diagram in Figure 6.6a and b, where there are also different shapes in the binodal curves. We once more attribute these differences to the phenomenological excluded volume term in TM-SCFT, which should become significant in this region.

We chose a point in the phase diagrams in Figure 6.6 to demonstrate that these large shifts in the phase diagram are indeed observed in the full MD simulation. We selected a value of $\phi_B^\beta = 0.03$, and average concentrations of $\langle\phi_A\rangle = 0.025$ and $\langle\phi_S\rangle = 0.12$ for all simulation/theory methods (MD, TM-SCFT, MC-SCFT). We plot the resulting volume fraction profiles in Figure 6.7, demonstrating that all three methods exhibit near-quantitative matching. Indeed, this choice of salt and polymer concentrations will not phase separate

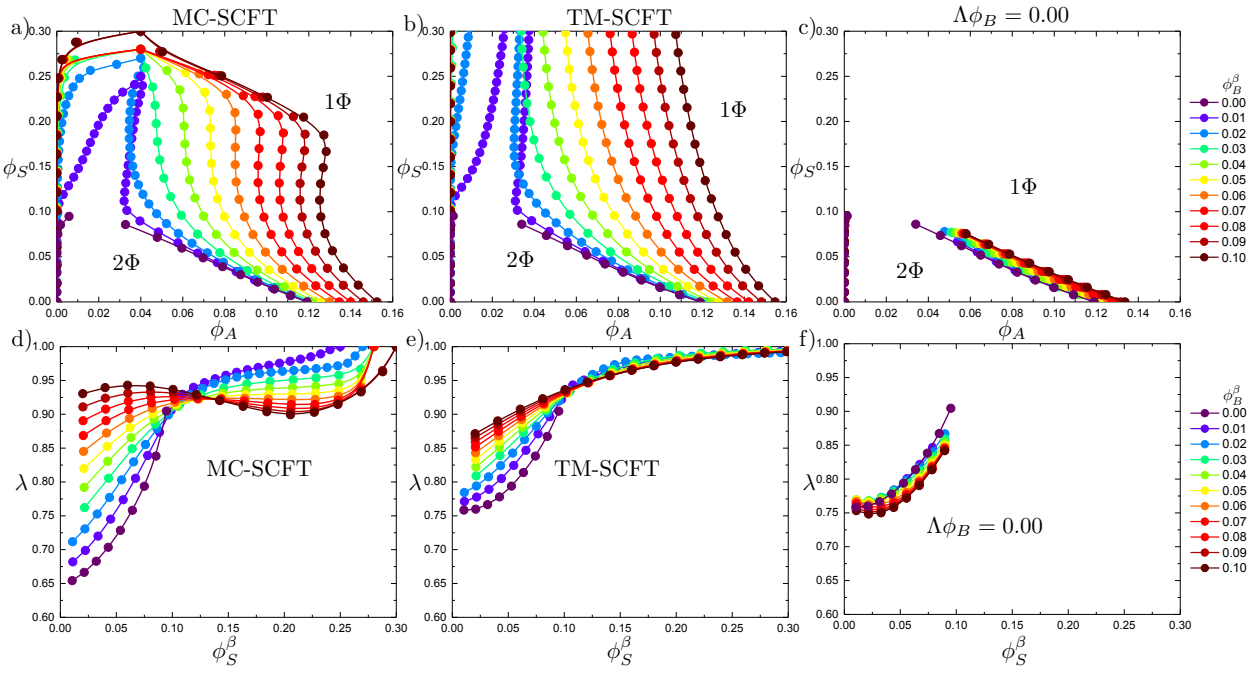

Figure 6.6: Phase diagrams and salt partitioning including a neutral polymer species. Lines are a guide to the eye. a) MC-SCFT phase diagram as a function of polyelectrolyte volume fraction ϕ_A and salt volume fraction ϕ_S for a number of supernatant neutral polymer volume fractions ϕ_B^β. b) TM-SCFT phase diagram as a function of polyelectrolyte volume fraction ϕ_A and salt volume fraction ϕ_S for a number of supernatant neutral polymer volume fractions ϕ_B^β. Qualitatively, both methods show a large increase in the immiscible region with larger increases corresponding to more supernatant neutral polymer volume fraction. However, TM-SCFT does not show the same critical point behavior as MC-SCFT. This is probably due to the use of a simple cubic term for excluded volume, which does not fully capture the complex interplay of all species excluded volume. c) We demonstrate the importance of this excluded volume term by removing the effect of excluded volume for the B-polymer. We see that, with the finite excluded volume of B, only minor shifts in the phase boundary are observed with increasing ϕ_B^β. d) Salt partitioning, $\lambda = \phi_S^\alpha/\phi_S^\beta$, as a function of supernatant salt volume fraction ϕ_S^β for MC-SCFT. e) Salt partitioning as a function of ϕ_S^β for TM-SCFT. Differences between panels d) and e) are observed, which we attribute to the use of a third-order term to approximate the excluded volume in the TM theory. f) Similar to c), the removal of the finite excluded volume of the neutral B-polymer leads to only small changes in the partitioning of other components.

without the presence of the neutral polymer. Snapshots at the bottom of Figure 6.7 show the MD simulation corresponding to the interfacial profile. Both show the same system, however the top snapshot includes the ions and the bottom snapshot removes the ions to show the polymer components more clearly. Consistent with the expectations from the SCFT calculations, the neutral polymer (green) is almost completely in the supernatant phase and

the polycation and polyanion (blue and orange) are completely in the coacervate phase.

6.3.4 Interfacial Properties of Coacervates with Neutral Polymer

We use both MC-SCFT and TM-SCFT to determine how the interfacial tension $\tilde{\gamma}$ changes as ϕ_B^β is increased. These results correspond to the phase diagrams in Figure 6.6, and are shown in Figure 6.8a and d for the two different methods. For both sets of results, the interfacial tension monotonically increases with ϕ_B^β, including both above and below the critical ϕ_S^β at $\phi_B = 0$. Interestingly, for small quantities of ϕ_B^β the surface tension remains very close to $\tilde{\gamma} \approx 0$ for a large range of ϕ_S^β. This trend is also apparent in the interfacial width D (Figure 6.8b and e), which exhibits significantly broader interfaces at small values of ϕ_B^β. After the initial addition of ϕ_B^β, the width of the interface begins to decrease to what appears to be a limiting value of D at high ϕ_B^β. Finally, increase in ϕ_B^β drastically increases the surface excess of salt $\Gamma_S^{(A)}$ (Figure 6.8c and f), which we attribute to the increase of excluded volume in *both* the coacervate and supernatant phases. In this case, the salt preferentially partitions to the interface where excluded volume is minimized. This is directly observed in Figure 6.7, where the profile shows a significant increase of salt at the interface for all methods (MD, MC-SCFT, and TM-SCFT). The calculated value of $\Gamma^(A)_S \approx 3 \times 10^{-3}$ is similar to the magnitude of the positive deviation in ϕ_S at the interface.

For all interfacial properties in Figure 6.8, MC-SCFT and TM-SCFT both capture the same qualitative trends. However, there are differences connected to the lack of critical points in TM-SCFT seen in Figure 6.6. This manifests as a decrease in the interfacial tension $\tilde{\gamma}$ and interfacial excess of salt $\Gamma_S^{(A)}$ to 0, along with a sharp increase in D for the MC-SCFT results. Similar to the phase diagram, we primarily attribute these differences to our approximate treatment of the excluded volume in the TM theory [93, 121].

6.4 Conclusion

In this chapter, we show that we can use a range of computational and theoretical routes to understand the interfacial properties of polymeric complex coacervates. We can directly sim-

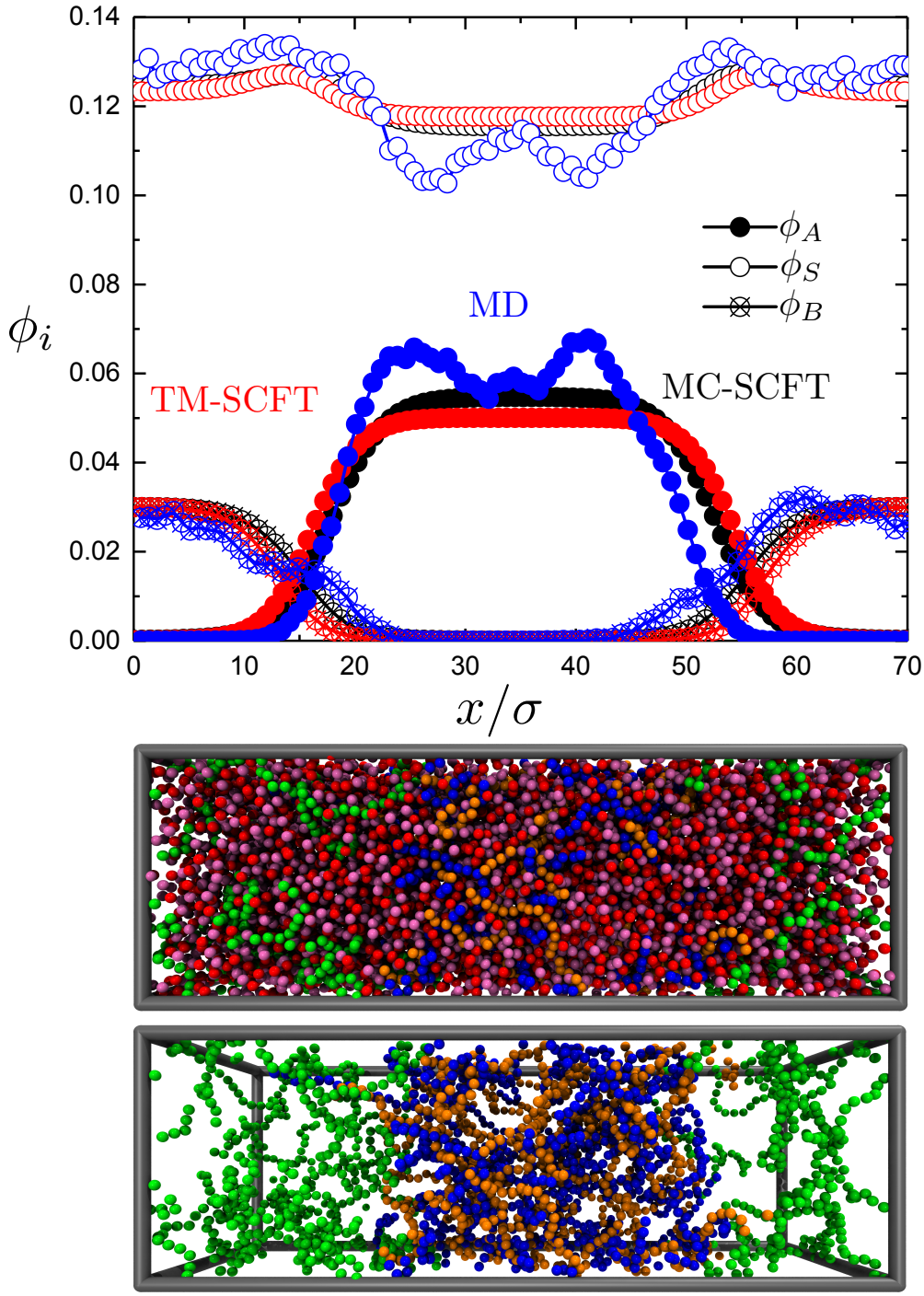

Figure 6.7: Interfacial profiles for a system with neutral polymers plotted with the volume fractions ϕ_i as a function of x, for MD, MC-SCFT, and TM-SCFT. $\phi_B^\beta = 0.03$, $\langle\phi_A\rangle = 0.025$, and $\langle\phi_S\rangle = 0.12$, which in the absence of neutral polymer does not undergo phase separation. We indeed observe phase separation, and our theoretical and simulation-informed SCFT models are capable of matching all-particle MD calculations nearly quantitatively. We show snapshots from simulations on the bottom, from the same simulation. In the top snapshot, salt is included, while in the lower snapshot it is removed to show that the neutral polymer (green) has phase separated completely from the charged polymers (orange and blue).

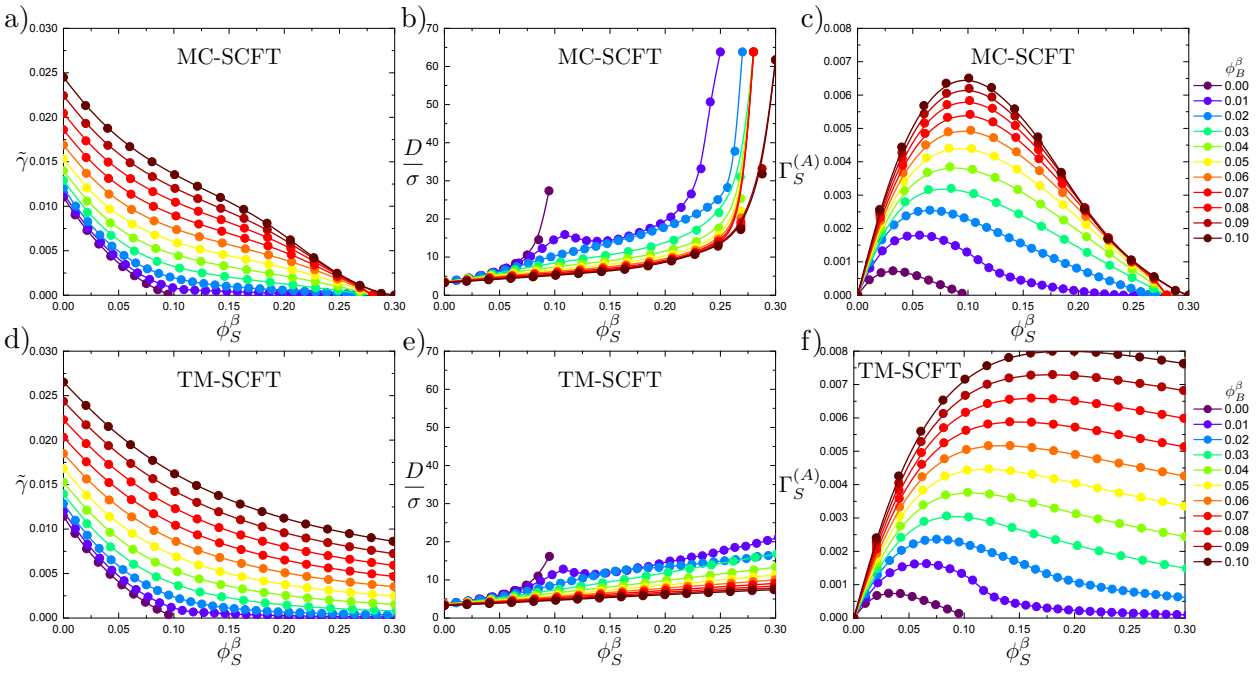

Figure 6.8: Interfacial properties calculated including a neutral polymer species. Lines are a guide to the eye. a) The interfacial tension, $\tilde{\gamma}$, calculated using MC-SCFT as a function of supernatant salt volume fraction ϕ_S^β for a number of supernatant neutral polymer volume fractions ϕ_B^β. With increasing ϕ_S^β, the interfacial tension decreases, consistent with the trends in Figure 6.4. With increasing ϕ_B^β, the interfacial tension increases due to an increase in the density of interactions. b) The interfacial width, D/σ, calculated using MC-SCFT. The width increases with increasing ϕ_S^β, because the phase separation is weaker making the interface more diffuse. Increasing ϕ_B^β the width to decrease. c) The interfacial excess of salt, $\Gamma_S^{(A)}$, calculated using MC-SCFT. This is a non-monotonic function of ϕ_S^β. Increasing ϕ_B^β causes an increase in the amount of excess salt at the interface. This is due to the supernatant phase being rich in neutral polymer causing both phases to have a large excluded volume. Salt adsorbs to the interface where there is excluded volume. d) The interfacial tension, $\tilde{\gamma}$, calculated using TM-SCFT. e) The interfacial width, D/σ, calculated using TM-SCFT. f) The interfacial excess of salt, $\Gamma_S^{(A)}$, calculated using TM-SCFT. Qualitatively, MC-SCFT and TM-SCFT show similar trends for all of the interfacial properties. However, differences between the two methods is observed at higher ϕ_B^β due to the approximate form of the excluded volume in the TM theory.

ulate interfaces using molecular dynamics, using a restricted primitive model representation that considers all polymeric and salt species as explicit particles. We match these results to SCFT predictions, which capture charge correlations using either a Monte-Carlo based method (MC-SCFT) or a transfer matrix theory of coacervation (TM-SCFT); we demonstrate nearly-quantitative matching among the interfacial profiles of all three methods, as

well as matching between the pair correlation functions in the MC and MD simulations. We subsequently use both MC-SCFT and TM-SCFT to probe the interfacial thermodynamics of coacervates, demonstrating trends in the interfacial tension γ consistent with previous observations in the literature [177, 178]. Similarly, we provide predictions for the interfacial width D and surface excess of salt $\Gamma_S^{(A)}$.

We subsequently consider the effect of adding neutral polymer, due to its relevancy for the interface of self-assembling coacervate block copolymers. The coacervation phase behavior changes drastically, with the neutral polymer partitioning strongly to the supernatant phase and 'balancing' the excluded volume pressure of the coacervate phase. This results in a large increase in the region of coacervation, seen in both MC-SCFT and TM-SCFT calculations. This change in the phase behavior is commensurate with large changes in the interfacial properties, with a large region of low-γ observed upon initially including neutral polymer. There are corresponding changes in interfacial width D, and significant increases in the surface-excess salt $\Gamma_S^{(A)}$ that are due to the presence of significant excluded volume in both phases.

Nearly quantitative agreement with full-particle MD, as well as field theories informed by both simulation and theory, provides insight into the important features needed to understand the physics of coacervation. First, the separation of length scales between the polymer conformation and the charge correlations is reflected in the SCFT calculations and does not seem to adversely effect the predictive power of the theory. Second, quantitative prediction hinges on the accuracy of the excluded volume model, which plays a large role near the critical point when there is neutral polymer present; small differences in this term lead to large changes in observed phase behavior. Finally, the complexity of the phase behavior when the neutral polymer is present poses a challenge for developing intuitive scaling arguments; in contrast to χ-driven phase separation, [175, 181, 182] it will likely be difficult to distill quantities like γ down to compact scaling expressions.

While the agreement between the different methods is excellent, we note the limitations of our current approach. In particular, all of the polymers considered possessed a high charge density. This is crucial for the transfer matrix theory, which assumes that most of the charges along the chain are matched with a condensed counterion or oppositely-charged chain [93].

It may be possible to extend the theory to low charge densities, however in these limits we approach regions where field theoretic approaches may be more apt [70, 72, 73, 78, 79, 91, 92, 109, 190]. Nevertheless, we use realistic parameters in our model that are roughly consistent with standard polyelectrolytes used in complex coacervates and have exhibited qualitative matching to experiment in a number of circumstances [4, 10, 11]. We further note that all methods used in this chapter (MC-SCFT,TM-SCFT, and MD) in principle have challenges in describing systems where both ϕ_S and ϕ_A are small. For MD and MC, we can easily go to low salt concentrations but do not see a large enough simulation box to explicitly capture the polymer concentrations seen on the low-ϕ_A branch of the binodal curve. We instead rely on extrapolation of f_{EXC} from finite concentrations of A to this limit. Alternatively, TM does not consider spatial correlations between oppositely-charged polyelectrolytes nor does it exhibit changes in polymer conformations that are known to play a role in polyelectrolyte thermodynamics. These may limit the accurate determination of the low-ϕ_A branch of the binodal curve, but we expect this to have little quantitative effect on our predictions of the high-ϕ_A branch.

We anticipate that this work will inform the further development of an understanding of coacervates, in particular the self-assembly of coacervate-based block copolymers. Models of block copolymer self-assembly incorporate surface free energies via interfacial tension γ, [183] and we have provided an initial picture of how this term would behave in the case of block copolyelectrolyte solution self-assembly.

To further provide a foundation to understand coacervate-driven block copolymer self-assembly, simulation phase diagrams are determined in the next chapter. We use our MC simulation as an input to a single chain in a mean field simulation, which allows block copolymer morphologies to be determined. Common block copolymer morphologies (hexagonally packing, inverted hexagonal packing, and lamellar) are observed, and, at large salt and polymer concentrations, a coexistence of morphologies is observed.

CHAPTER 7

COACERVATE-DRIVEN BLOCK COPOLYMER ASSEMBLY IN THE HIGH CHARGE DENSITY LIMIT

7.1 Introduction

Assembly using complex coacervate motifs has been extensively studied in a number of situations, all involving pairs of oppositely-charged block copolymers that can self-assemble into nano-structured morphologies [25,29,68,191–199]. Early research focused on coacervation or complexation-driven micelles, [191–193] which have been promising as drug-delivery vehicles and can encapsulate hydrophilic, charged drugs (in contrast to micelles formed by dispersive or hydrophobic interactions, which can only deliver hydrophobic drugs) [25, 197]. Increasing the concentration of these micelles, or synthesizing triblock copolymers, has been shown to form gel materials that can demonstrate elastic material properties and responsiveness to the charge environment (via pH or salt concentration) [29, 68, 194–196, 200]. Similar self-assembly motifs can lead to stimuli-responsive sensors that change color due to swelling and deswelling coacervate materials [29].

In this chapter, we demonstrate a method for embedding molecular-level Monte Carlo (MC) simulations into field theoretic calculations. MC simulations are performed using the model in Sections 2.2 and 6.2.2 to capture the excess free energy according to Equation 6.10. This free energy landscape is incorporated into a field theoretic calculation. For this work, we use single chain in mean field (SCMF) calculations that use coarse-grained Monte Carlo to calculate heterogeneous polymers in equilibrium [201–205].

This hybrid 'Monte Carlo-Single Chain in Mean Field' (MC-SCMF) method is capable

of providing new insight into an important class of material problem. We are capable of describing the phase behavior of coacervate-driven self assembly in charged block copolymers. Unlike previous work, our method extends to the limit that charge density along the polymer is high. This is a noted limitation of the one-loop approximation in RPA, [70] used by the embedded fluctuation model, [68] and is representative of a system where the molecular detail plays an important role in the macroscopic thermodynamic behavior.

We can use this new approach to coacervate self-assembly to demonstrate new or interesting physical behaviors that may arise. In particular, we predict the presence of a salt-induced ordering transition that is due to the partitioning of salt ions between a charged A-block and an uncharged B-block. The swelling of the B-block due to an abundance of added salt can stabilize a hexagonal phase. Similarly, this partitioning plays a major role in transitions to other morphologies (lamellar and inverse hexagonal) observed in our model. We compare our results to experimental results in the literature to show that, despite the underlying simplicity of the model, it nevertheless captures many of the essential physical features driving coacervate phase behavior.

7.2 Method

Our overall approach is to assume a *separation of length scales* between the local, molecular features of complex coacervates and the larger length-scale phase and morphological features of the overall polyelectrolyte systems (which can be composed of polymer or block copolymer). For the local, molecular features we use Monte Carlo (MC) techniques detailed in Sections 2.2 and 6.2.2 with $N_P = N_{MC} = 20$, for all polymer species, and an $\epsilon_{LJ} = 0.25 k_B T$. Thermodynamic values can be obtained from these simulations that are then useful at larger length scales. For these large length scales, we use Single Chain in Mean Field (SCMF) calculations. This method maps coarse-grained polymers to a grid, which in our approach has properties informed by the MC portion of the calculation. We demonstrate this general scheme in Figure 7.1, and describe each portion in detail below.

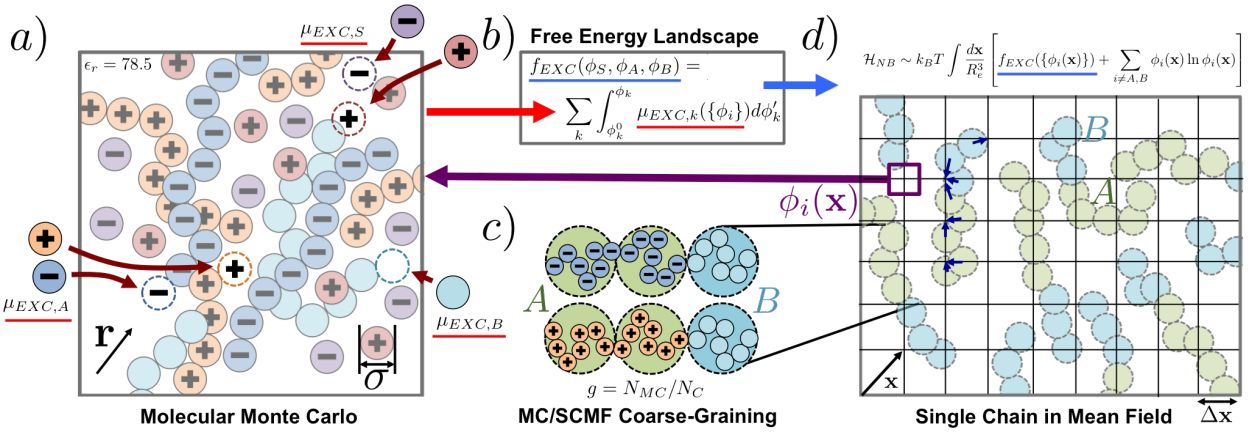

Figure 7.1: Schematic of the hybrid MC-SCMF scheme. (a) Molecular MC simulates solutions of polymer (polycation, orange; polyanion, blue; neutral polymer, cyan) and salt (cation, red; anion, purple). The RPM is used, with charged species represented as hard spheres of diameter σ in a dielectric solvent medium with $\epsilon_r = 78.5$. Spatial coordinate is $\mathbf{r}$. Widom insertion of salt/polymer species (dark red arrows) yields $\mu_{EXC,i}$ of species i. (b) $\mu_{EXC,i}$ is an input into the calculation of the free energy landscape $f_{EXC}(\phi_S, \phi_A, \phi_B)$, see Eq. 2.11. (c) SCMF simulations consider coarse-grained representions of (for example) block copolymers. g monomers make up individual coarse-grained beads, which are connected by Gaussian springs (Eq. 7.2). In our scheme, polycation versus polyanion beads are indistinguishable. (d) f_{EXC} from part (b) contributes to a non-bonded Hamiltonian $\mathcal{H}_{NB}$ (see full Eq. 7.3) calculated by assigning beads to grid points (blue arrows). Grid has coordinate $\mathbf{x}$ and informs MC updates of coarse-grained polymers. These chains do not interact except through the contribution of each coarse-grained bead to the ϕ_A or ϕ_B at a given grid point. The f_{EXC} informs the distribution of SCMF chains, which set the values of ϕ_i at a grid point $\mathbf{x}$ used to calculate f_{EXC}, establishing consistency between the two simulation methods.

7.2.1 Single Chain in Mean Field Simulations

We use Single Chain in Mean Field (SCMF) simulations that use MC to solve field theoretical representations of polymer systems [201–205]. Our system consists of connected polymer beads that only interact due to their contribution to a density field that sets the system Hamiltonian, as well as fields associated with the ions in the system. Molecular MC calculations consider a five-component system, with two polyelectrolytes, two ions, and an implicit water solvent. We make the assumption that the polycations and polyanions are indistinguishable and in equal concentration at any point (Figure 7.1c [1, 66]. The same assumption can be made regarding the ion species. This simplifies the system to a charged polymeric species A that represents both the polycation and polyanion, an ion species S that

represents both the cation and anion, and water W. We will also consider block copolymers with an uncharged block B.

The interaction energy between all species is described by the Hamiltonian $\mathcal{H}$: [201–204]

$$\mathcal{H} = \mathcal{H}_B[\{\mathbf{x}_i\}] + \mathcal{H}_{NB}[\phi_A, \phi_B, \phi_S, \phi_W] \tag{7.1}$$

where $\mathcal{H}_B[\{\mathbf{x}_i\}]$ is the bonded energy as a function of the position $\mathbf{x}_i$ of all beads i. We note the use of the position variable $\mathbf{x}$ for SCMF simulations in contrast with the coordinate $\mathbf{r}$ used by the MC portion of the calculation; this reflects the different level of molecular resolution between the two methods. $\mathcal{H}_{nb}[\phi_A, \phi_B, \phi_S, \phi_W]$ is the nonbonded energy functional of the local densities $\phi_A(\mathbf{x})$, $\phi_B(\mathbf{x})$, and $\phi_S(\mathbf{x})$ ($\phi_W = 1 - \phi_A - \phi_B - \phi_S$).

We consider n_C coarse-grained chains that consist of N_C Gaussian segments, with bonded energy $\mathcal{H}_B$ given by:

$$\mathcal{H}_B[\{\mathbf{x}_i\}] = \frac{3}{2} k_B T \sum_{i=0}^{n_C} \sum_{s=1}^{N_C - 1} \frac{(N_C - 1)[\mathbf{x}_i(s+1) - \mathbf{x}_i(s)]^2}{R_e^2} \tag{7.2}$$

R_e^2 is the mean-squared end-to-end distance for a chain that is isolated and noninteracting.

The nonbonded Hamiltonian functional is given by: [201–205]

$$\frac{\mathcal{H}_{NB}[\phi_A, \phi_B, \phi_S, \phi_W]}{g N_C k_B T \sqrt{\bar{\mathcal{N}}}} = \int_V \frac{d\mathbf{x}}{R_e^3} f_{EXC}(\{\phi_i(\mathbf{x})\}) + \int_V \frac{d\mathbf{x}}{R_e^3} \sum_{i \neq A,B} \phi_i(\mathbf{x}) \ln \phi_i(\mathbf{x}) \tag{7.3}$$

where $i = A, B, S, W$ and g is the number of molecular monomers per coarse-grained monomer. g accounts for the interaction of a coarse-grained monomer, which is equivalent to the interaction of g molecular monomers (Figure 7.1c). $\sqrt{\bar{\mathcal{N}}} = \rho_0 R_e^3 / N_C$ is an interdigitation number that estimates the average number of chains interacting with a single chain. $\rho_0 = n_C N_C / V \langle \phi_P \rangle$ is the average bulk number density of coarse-grained polymer beads, where $\langle \phi_P \rangle$ is the average volume fraction of polymer beads in the system. The first term in Equation 7.3 represents the excess free energy of the charged species f_{EXC} and the second term is the translational entropy of all of the non-polymer species (the translational entropy of the polymers is captured by the bonded portion of the Hamiltonian $\mathcal{H}_B$).

Simulation beads are mapped to a grid (Figure 7.1d) to define the local densities used in the evaluation of the non-bonded portion of the Hamiltonian (Equation 7.3). We use the PM_0 mappings considered in previous implementations of the SCMF method, [201,202] and use random grid-shifting to remove the effect of a discrete, fixed grid. Each bead contributes a volume fraction $\delta\phi_P = n_G\langle\phi_P\rangle/(n_C N_C)$ that is related to the number of grid points n_G in the system. Local salt densities are not determined using explicit beads, and instead are simply tracked using the presence of a field variable $\phi_S(\mathbf{x})$ at each grid point $\mathbf{x}$.

MC moves for polymers are carried out in the same fashion as for the molecular-level simulations, with random translational movements of particles. Additional moves such as block flips are implemented as necessary. MC moves for salt consists of moving a randomly chosen volume fraction of salt $\delta\phi_S$ from one grid point to another $(\phi_S(\mathbf{x}), \phi_S(\mathbf{x}') \rightarrow \phi_S(\mathbf{x}) + \delta\phi_S, \phi_S(\mathbf{x}') - \delta\phi_S)$. All moves include corresponding changes to ϕ_W via the constraint $\phi_S + \phi_A + \phi_B + \phi_W = 1$.

The form for the excess free energy density f_{EXC} can be taken from the landscape determined via the small length-scale MC results. Self-consistency between the length scales is maintained by ensuring that the value of $f_{EXC}(\{\phi_i\})$ calculated from molecular MC is representative of the local concentrations determined in the SCMF portion of the calculation. We note that this self-consistency includes an assumption that $\mu_{EXC,i}(\{\phi_i\}, N_{MC}) \approx \mu_{EXC,i}(\{\phi_i\}, N_C)$; in other words, we use the $N_{MC} = 20$ result in molecular MC to represent the thermodynamics of any chain length in the SCMF portion of the calculation. The inset of Figure 2.2 demonstrates that this approximation is reasonable except for short N (ca. < 10) where deviations of $\mu_{EXC,i}$ become significant. We expect the short-N limit to be roughly defined by the overlap concentration ϕ_P^* of the solution, above which thermodynamic properties are nearly N-independent [206]. We calculate this to be $\phi_P^* \sim 0.006$ for our system with $N_{MC} = 20$, an order of magnitude less than the concentrations used in our f_{EXC} calculations. The combined use of the local MC with the large-scale SCMF simulations is what we call the MC-SCMF method, and will be used as the primary method in this chapter for determining the behavior of coacervate-driven block copolymer assemblies.

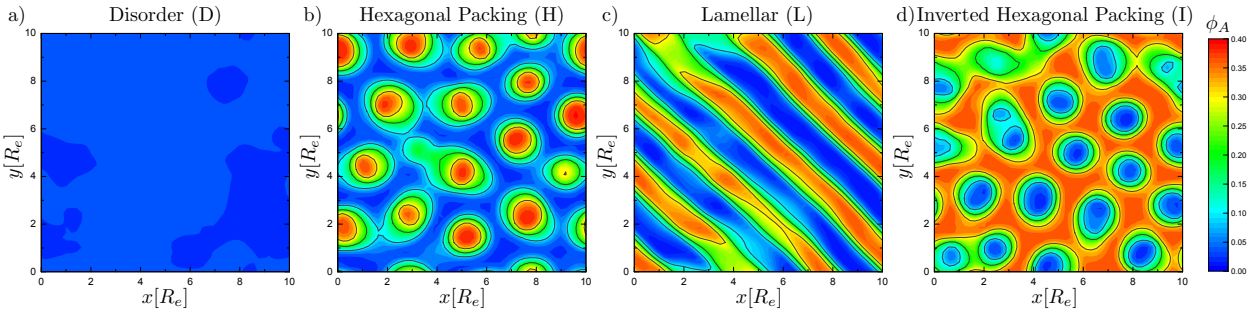

Figure 7.2: Representative pictures of the morphologies observed in 2-D SCMF simulations of complex coacervate block copolymers. Spatial coordinates in units of the unperturbed chain end-to-end distance R_e. (a) Disordered morphology *(D)*. (b) Hexagonal Packing *(H)* exhibits hexagonally-packed micelles, with a coacervate core. (c) Lamellar morphology *(L)*. (c) Inverted Hexagonal Packing *(H)* occurs when the continuous phase is composed of the charged, coacervate blocks.

7.3 Results

7.3.1 Block Coacervate Morphologies

MC-SCMF provides the basis to understand the effect of molecular structure on the phase behavior of complex coacervates that self-assemble into structures on large length scales. It incorporates molecular MC calculations into a larger-length scale field theory, using a separation of length scales between charge ordering and polymer dimensions. Self-assembly behavior such as in block copolymers requires a method that captures behaviors at these multiple length scales, due to the assembly of large 10nm-1μm features due to electrostatic driving forces at small $<$ 1nm length scales.

We use MC-SCMF to predict and understand phase behaviors when coacervate-forming polycation/polyanion (A) blocks forms a copolymer with a neutral block (B). These systems are known to undergo microphase separation due to the associative phase separation of an A block that must remain covalently bonded to the B block. We identify three parameters that influence block copolymer morphology; the volume fraction of salt ϕ_S and the volume fraction of polymers ϕ_P correspond to the parameters used to map macroscopic complex coacervation. The fraction of A monomers f_A and the chain length N provide other parameters to control block copolymer coacervates.

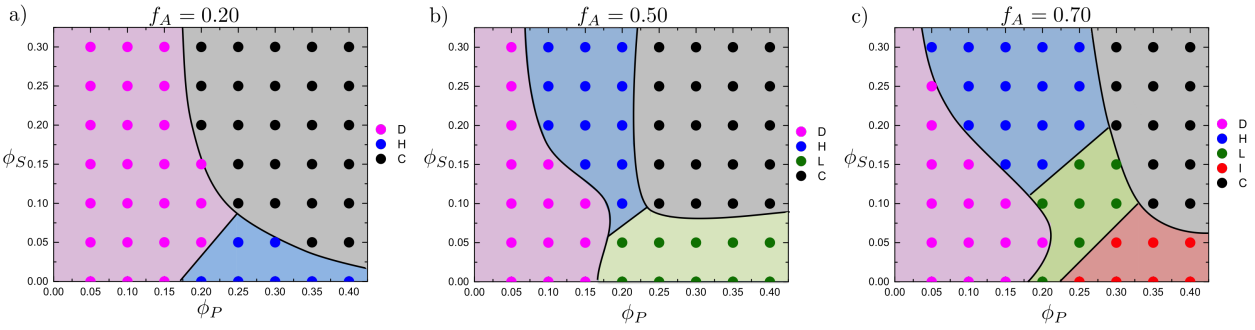

Figure 7.3: Phase diagrams in ϕ_S versus ϕ_P space, demonstrating the observed morphology (representative snapshots in Figure 7.2) using MC-SCFM. $N = 50$. Here we show the effect of changing the fraction of the charged A-blocks; (a) $f_A = 0.20$, (b) $f_A = 0.50$, (c) $f_A = 0.70$. Low ϕ_P regions demonstrate disordered phases, but at high polymer concentration ordered phases emerge depending on ϕ_S and f_A. Consistent features include transitions to phases that exhibit increasing curvature in the direction of the A-block (i.e. $I \rightarrow L \rightarrow H$) as ϕ_S is increased. We attribute this to increasing osmotic expansion of the B-rich phase. A coexistence (C) region also shows up at high ϕ_S and ϕ_P regions, which we attribute to the high excluded volume penalties associated with these high-density regions. Lines are drawn to guide the eye, and do not represent the precise location of phase boundaries.

7.3.2 Morphological Phase Behavior

We consider a two-dimensional MC-SCMF calculation; this simplifies the morphological possibilities while retaining a sufficient number of observed structures. We visually demonstrate these in Figure 7.2. A lack of structure is indicated as *disordered* (D). Microphase separation can occur, leading to a hexagonal ordering of circular coacervate-cores of A blocks surrounded by B blocks. These are *hexagonally packed* (H) phases. Striped *lamellar* (L) phases can also form, as well as *inverse hexagonally packed* (I) structures, that are similar to H structures except with B blocks in the cores. We note that there are effectively three components in this system: block copolymer, salt, and water. This means that it is possible to observe coexistence (C) between two different morphologies.

We plot the phase diagrams obtained using the MC-SCMF method in Figure 7.3. We consider different lengths for the charged block of the copolymer, given as a fraction of the overall chain $f_A = 0.20$, 0.50, and 0.70. These three values are plotted in Figure 7.3. The general trends are similar - for example, at low polymer concentrations (ϕ_P) ordering is not observed for any f_A or ϕ_S. As the polymer concentration is increased, there is an increased tendency to form ordered phases. At low ϕ_S and high ϕ_P, hexagonal, lamellar,

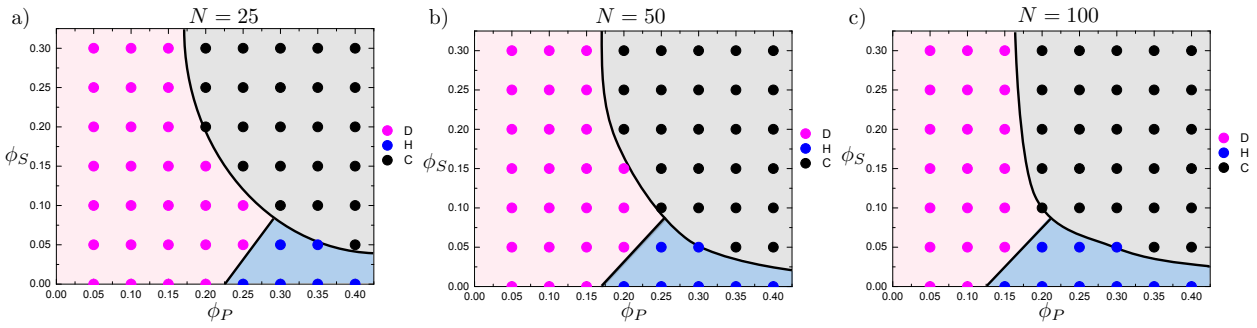

Figure 7.4: Phase diagrams in ϕ_S versus ϕ_P space, demonstrating the observed morphology (representative snapshots in Figure 7.2) using MC-SCFM. $f_A = 0.20$. We show the effect of changing the overall chain length N; (a) $N = 25$, (b) $N = 50$, (c) $N = 100$. The features are essentially the same as N is varied, however the location of the ordered phase shifts continuously to lower values of ϕ_P at large N. The same is apparent in the coexistence portion of the phase diagram. We attribute these small changes to the decrease in the chain translational entropy with respect to the charge driving force for phase separation.

or inverse hexagonal phases depending on the block fraction f_A; this is consistent with the morphologies expected for standard block copolymers with similar block fractions, where the interface curves due toward the minority component. This is physically attributed to the relative 'sizes' of the two blocks. At high values of salt and f_A, transitions occur toward interfaces that curve toward the A-block (from I to L to H), and the disordered phase can undergo a salt-induced ordering transition. At large values of ϕ_P and ϕ_S, all block fractions f_A demonstrate a coexistence. We elaborate on these features later in this chapter.

Figure 7.4 demonstrates phase diagrams associated with different chain lengths, $N = 25$, 50, and 100, with $f_A = 0.20$. These phase diagrams demonstrate similar features, with the primary difference being a movement of the order-disorder transition to lower values of ϕ_P. We attribute this to a decrease in the chain translational entropy with respect to the charge driving force for phase separation..

7.3.3 High Salt/Polymer Phase Coexistence

A consistent aspect of the phase diagrams in Figure 7.3 is the appearance of a coexistence region at high ϕ_S and ϕ_P, between two different morphologies. While larger simulations, or Gibbs Ensemble field theory calculations [207] would be required to accurately reproduce tie

lines, we observe that they would run from high ϕ_S and low ϕ_P to low ϕ_S and high ϕ_P. In Figure 7.3a, coexistence would be between H and D, in Figure 7.3b between H and L, and in Figure 7.3c between L or H and I.

We attribute the presence of this coexistence region to the large penalty due to excluded volume between the salt, polymer components. This region occurs at high ϕ_P and ϕ_S, where the volume fraction of both becomes close to $\phi_P + \phi_S \to 1$. We hypothesize that this is highly unfavorable due to the enhanced excluded volume felt specifically by the salt in the proximity of highly-connected polymers. By separating into a high-ϕ_S/low-ϕ_P system, these interactions are minimized.

7.3.4 Order-Disorder Transition and Interfacial Properties

We note the appearance of a salt-induced ordering transition at high f_A (Figure 7.5a). At first glance this is counterintuitive; the increase in salt may be expected to screen the electrostatic attractions and thus decrease the driving force for phase separation. To investigate this inverted behavior, we monitor the composition of salt and polymer across the A-B interface (see schematic in Figure 7.5b). We consider a constant polymer concentration path shown in Figure 7.3, which is exclusively in the hexagonal region of the phase diagram. We plot concentration profiles from the center of the charge-rich core region to the surrounding B-block rich region (see Figure 7.5c). Two observations provide an explanation for the salt-induced ordering transition: salt localization at the interface and salt partitioning to the B-rich region.

Indeed, these interfacial profiles demonstrate how complicated phase separation is in complex coacervate assembly. Figure 7.6 demonstrates the interfacial profiles for the complete set of morphologies observed in our calculations. In particular, we note that while the excess of ϕ_S in the B-rich phase is apparent in the H morphology (Figure 7.6a), this is enhanced because the osmotic expansion of this block facilitates this structure. However, in L and I structures where the B-block becomes increasingly confined, salt partitions in a less pronounced manner. Indeed, the highly-confined B-block in the I morphology leads to $\phi_S^A > \phi_S^B$, which is inverted when compared to the bulk phase separation. This also leads to the accu-

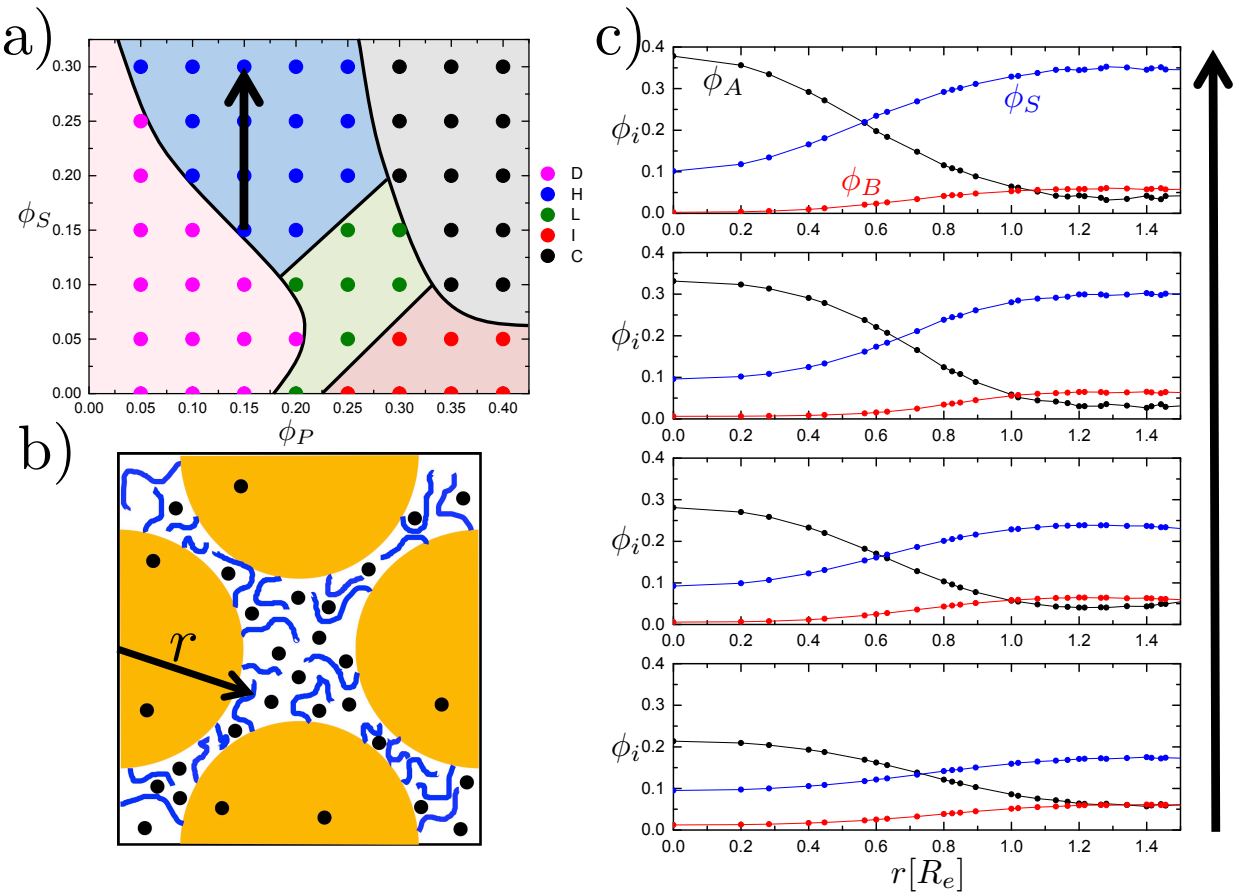

Figure 7.5: (a) Phase diagram in ϕ_S versus ϕ_P space from Figure 7.3 ($f_A = 0.7$, $N = 50$), demonstrating a trajectory upon passing through a salt-induced ordering transition. (b) We attribute the salt-induced ordering transition to the osmotic pressure in the B-rich region, which expands the minority block sufficiently to drive interfacial curvature toward the A-block. This stabilizes the H phase. (c) This mechanism is supported by the increased salt concentration ϕ_S in the B-rich phase, which is apparent in the interfacial density profile measured from the center of the H-phase cores. These profiles exhibit an increasing concentration ϕ_S in the B-rich region as ϕ_S is increased.

mulation of salt at the interface between A and B-rich regions, which is observed in both L and I morphologies.

7.3.5 Comparison to Literature, Experiment

The results of our MC-SCFM calculations are qualitatively consistent with previous theory and experiment of coacervate-driven self-assembly. Audus, et al. [68] considers the no-salt $\phi_S = 0$ limit, which demonstrates similar morphology at low salt concentration; there is

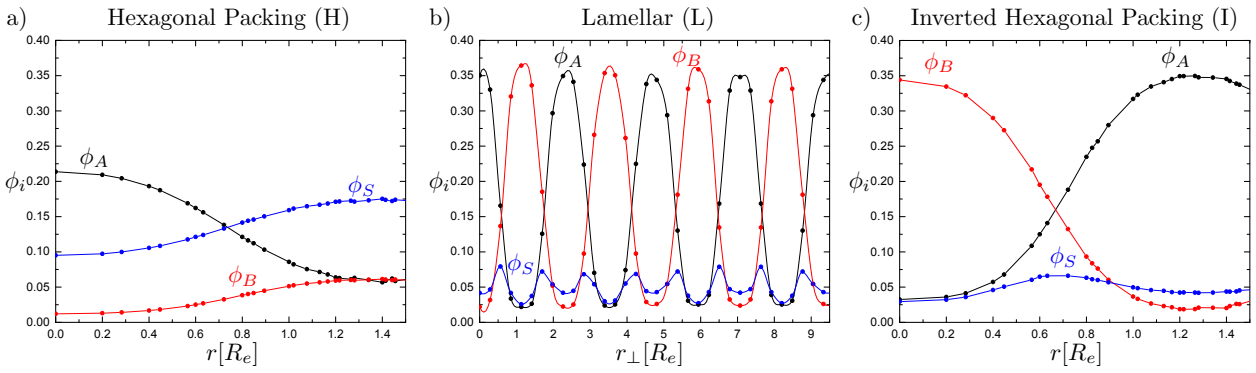

Figure 7.6: Interfacial density profiles for (a) hexagonal packing morphologies, measured from the charged core to the corona; (b) lamellar morphologies, measured across the entire simulation box; (c) inverted hexagonal packing, measured from the uncharged core. We note that, as the curvature moves toward the B-rich region ($H \rightarrow L \rightarrow I$), preferential partitioning of salt to the B-rich region decreases and instead the salt partitions to the interface.

an order-disordered transition at ϕ_P (in weight percent) around $\phi_P \approx 10 - 20\%$ that does not change drastically with block fraction. Furthermore, increasing block fraction leads to lamellar phases. Some differences are observed in the theoretical predictions of Audus, et al. [68], such as a predicted coexistence at low ϕ_P, however these may be attributed to these predictions being for triblocks and for polymers with low charge density.

Figure 7.7 used chain length $N = 250$ and block fraction $f_A = 0.15$, corresponding roughly to the chain dimensions of experimental phase diagrams from Krogstad, et al. [22] We note that we still use the simple restricted primitive model polymer, without explicitly parameterizing to the molecular structure in that article. Nevertheless, we note the similarity between both phase diagrams. At low salt, there is a disorder to hexagonal transition around $\phi_P \approx 0.1 - 0.15$. As salt increases, a region of hexagonal/disorder coexistence appears for both experiment and simulation. We observe this transition at a slightly higher value of ϕ_S than in experiment, and the ordering transition moves to the right much more quickly in experiment; we attribute this to the use of a weak LJ attraction between beads in our model, which may overestimate the strength of association between the polyelectrolyte A-blocks.

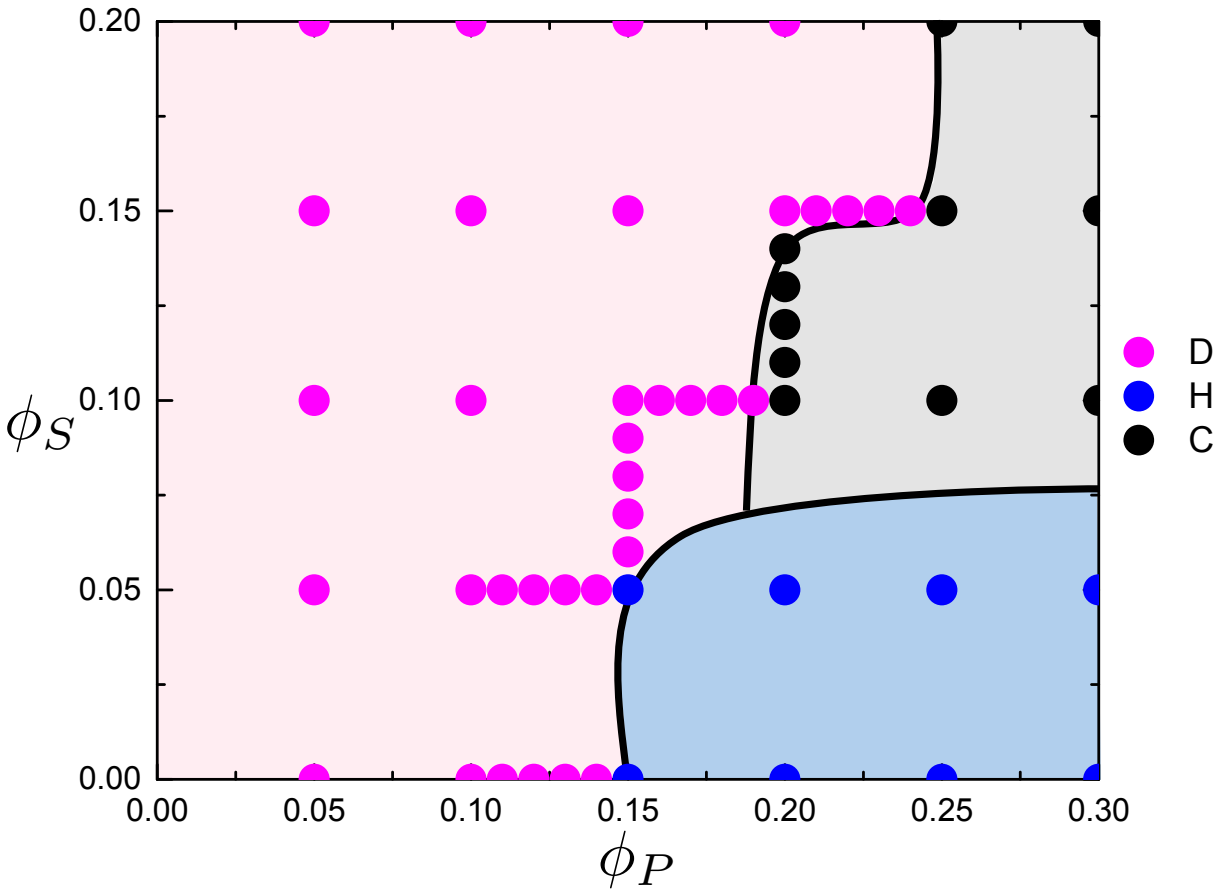

Figure 7.7: ϕ_S versus ϕ_P for $N = 250$ and $f_A = 0.15$, which corresponds to the experimental system considered in Krogstad, et al. [22] We note the similarity between the two phase diagrams, including a D-H transition at $\phi_P \approx 15\%$ and the appearance of a coexistence region at $\phi_P \approx 20\%$. The similarities are striking, especially considering that no significant parameterization was attempted on the model at the molecular MC level of the calculation.

7.4 Conclusions

We have developed a hybrid method that is capable of linking both the molecular structure that is crucial to understanding polymeric complex coacervate materials with the large-scale morphological features of polymer self-assembly. This is performed by using standard Monte Carlo methods (Gibbs Ensemble, Widom insertion) to capture how local charge correlations in highly charge-dense polymers drive both the macroscopic phase behavior as well as the thermodynamic parameters of coacervate-forming systems. These thermodynamic parameters are subsequently used as inputs to Single Chain in Mean Field (SCMF) calculations,

which are capable of rapidly determining block copolymer morphologies using field theory. Therefore, we can demonstrate the self-assembly properties of charge-neutral block copolymers. Coacervation-driven self-assembly and the MC-SCMF calculations described in this chapter match well with previous experimental, theoretical results.

We investigate a number of new phenomena that arise, such as a morphological coexistence region that exists at high ϕ_P and ϕ_S, and a salt-induced ordering especially at large f_A. The salt-induced ordering is attributed to salt partitioning effects that stabilize the same phase at high ϕ_P, and plays a role in the transitions between morphologies at high f_A.

Simultaneously considering the local, molecular structure as well as polymer morphology is crucial to understanding the phase behavior when the polymer components become strongly correlated (i.e. high linear charge density). Our results suggest that there is a rich phenomenological landscape of phase behaviors to be explored when the local charge-density is considered and subsequently tuned. We expect chain architecture and stiffness to play an important role in coacervate-driven assembly, and potentially an interesting way to tune phase behavior via local charge correlations [208]. MC-SCFM represents a tool that will enable more detailed studies of the underlying physical causes for the observed phase diagrams, and thus provide insight into the physical driving forces governing self-assembly in coacervates.

Our results demonstrate similarities to features observed in previous literature. To our knowledge, only a few experimental phase diagrams have been created, [22, 68] especially those investigating the salt dependency. In particular, we are able to qualitatively reproduce the phase behavior observed by Krogstad et al., including a phase coexistence between the disordered and hexagonal phase that mirrors their observed coexistence between disordered and BCC-packed phase [22]. We plan to investigate this further to understand how the choice of physical parameters may lead to better matching, and provide insight into the predictive capabilities and limitations of this model.

CHAPTER 8

CONCLUSION

In this dissertation, I developed a transfer matrix theory to describe complex coacervation phase separation behavior. This approach maps the three-dimensional, correlated structure of a polyelectrolyte/salt mixture to a one-dimensional adsorption model, which is solved via a transfer matrix. Transition probabilities were calculated from Monte Carlo simulations, and used to parameterize the transfer matrix parameters in order to capture the local structure of the coacervate. Free energies calculated from this theory produced a phase diagram in nearly quantitative agreement with the simulation phase diagram. Upon coacervation this theory shows that the average fraction of monomers with a salt ion adsorbed decreases, which agrees with counterion condensation and release arguments. Additionally, the average fraction of monomers with an oppositely-charged polymer chain adsorbed increases upon coacervation, suggesting that the number of ways for oppositely-charged chains to interact is crucial to coacervation phase behavior

To further understand the relationship between coacervation phase behavior and this chain interaction entropy, I modified this theory to investigate how chain stiffness, charge valency, and polymer architecture affect coacervation phase behavior. Increasing the chain stiffness resulted in a decrease in the phase separation region, because the number of ways for oppositely-charged chains to interact decreased. Decreases in the phase separation region were also observed due to increasing salt valency, which is attributed to the salt ions being able to absorb to multiple monomers and decreasing the chain interaction entropy. Comb architecture also decreased the phase separation region by decreasing the number of ways oppositely-charged chains interact. These results suggest coacervation is strongly affected by the chain interaction entropy in addition to the counterion release entropy.

With an understanding of how physical molecular features affect coacervation phase be-

havior, I investigated how charge sequence affects coacervation by investigating coacervation occuring between a sequence-defined polycation and a homopolyanion using Monte Carlo simulations, which were compared to experimental results. As charge 'blockiness' increases, the size of the immiscible region increases, because the entropy gain upon counterion release increases. Blocky patterns localize counterions near the charged blocks more than less blocky patterns, such that upon coacervation the released counterions gain more entropy compared to less blocky patterns, which is supported by both simulation and experimental results.

Using this physical insight, I extended the transfer matrix theory to study charge sequence. Simulation was used to calculate an effective binding energy per monomer to capture the local electrostatic environment along the chain, which is used as an input for the transfer matrix. This modification allowed the blockiness trend to be captured in qualitative agreement with experimental results. Investigations into charge fraction revealed that increasing charge fraction can increase the critical salt concentration, but blockiness also affects this critical salt concentration. Non-regular patterns demonstrated that the charged block positions affect the phase separation behavior as well. This showed that the transfer matrix theory is able to capture precise, monomer-level charge sequence effects.

In order to implement this understanding of how physical molecular features affect coacervation to understand self-assembly, I extended this transfer matrix theory of coacervation to study the interfacial properties between the coacervate and the supernatant, which is key for understanding coacervate-driven self-assembly. Interfacial profiles calculated via the transfer matrix showed qualitative matching with molecular dynamics simulations. This indicates that the transfer matrix theory can describe the structure and thermodynamics of this interface, enabling us to calculate properties such as interfacial tension, width, and excess of salt. My results showed that adding salt decreases the interfacial tension while increasing the interfacial width.Addition of a neutral polymer species to the system dramatically alters the phase separation behavior, which qualitatively matches molecular dynamics simulations. This neutral species increases the interfacial tension, decreases the interfacial width, and increases the concentration of salt at the interface. It is hypothesized that the excluded volume of the neutral species causes this alteration in the phase diagram and interfacial properties.

To further develop the foundation for understanding coacervate self-assembly, I performed Monte Carlo simulations to determine initial morphological phase diagrams for coacervate-driven block copolymer self assembly. These investigations showed that at large salt and polymer concentrations, a coexistence of phases was observed. As the salt concentration in the system was increased, disorder to order transitions were observed, and attributed to partitioning of the salt to the interface and the neutral-block phase.

These investigations provide a method to study further questions about complex coacervation phase behavior. Coacervate-driven block copolymer self-assembly can be studied using the transfer matrix theory to develop a molecular-level understanding of how block copolymer self-assembly can be altered using physical molecular features. A more specific study would be to develop a theory of block copolymer micellization driven by complex coacervation in a similar manner to L. Leibler et. al. [183], who developed free energy expressions to determine the stability of the micelle phase.

In addition to block copolymer self-assembly, charge sequence provides a host of unanswered questions. Charge sequences herein studied only contained 2 types of monomers: positively-charged and neutral. These neutral beads only interacted via excluded volume, but additional interactions could be considered such as hydrophobicity or hydrogen bonding, and negatively-charged monomers could be added to the polymer backbone to investigate polyampholyte coacervation. Increasing sequence complexity could allow access to more sophisticated phase behavior that can be tuned in a controllable way. A complementary method to access more complex phase behaviors could be considering mixtures of sequence-defined polyelectrolytes, which might be able to access the formation of hierarchal structures such as the core-shell structure seen in membraneless organelles [56,64]. These mixtures could result in the formation of multiple coexisting coacervate and supernatant phases, depending on the system composition.

Coexisting phases formed from sequenced-defined coacervate systems could exhibit unusual interfacial properties. Polymer chains could adopt folded configurations across the interface in order to minimize unfavorable contacts between coexisting phases. This type of folding behavior could be similar to the folding of tapered block copolymers across interfaces formed between microphase domains [156, 209–211]. Interfaces could potentially be

broadened, which might allow interfacial design using sequence-defined polyelectrolytes.

Inclusion of sequence-defined polyelectrolytes as blocks in block copolymers could potentially be used to design self-assembling systems with hierarchal structure. This could be a path towards designing self-assembling systems from the monomer length scale to the chain length scale, which might result in sophisticated structures beyond those which can be realized using simple block copolymers. My work has set the stage to potentially use charge sequence as a tool to engineer materials self-assembly.

REFERENCES

[1] E. Spruijt, A. H. Westphal, J. W. Borst, M. A. Cohen Stuart, and J. van der Gucht, "Binodal compositions of polyelectrolyte complexes," *Macromolecules*, vol. 43, pp. 6467–6484, 2010.

[2] J. van der Gucht, E. Spruijt, M. Lemmers, and M. A. Cohen Stuart, "Polyelectrolyte complexes: bulk phases and colloidal systems," *J. Colloid Interface Sci.*, vol. 361, pp. 407–422, 2011.

[3] P. K. Jha, P. S. Desai, J. Li, and R. G. Larson, "ph and salt effects on the associative phase separation of oppositely charged polyelectrolytes," *Polymers*, vol. 6, pp. 1414–1436, 2014.

[4] M. Radhakrishna, K. Basu, Y. Liu, R. Shamsi, S. L. Perry, and C. E. Sing, "Molecular connectivity and correlation effects on polymer coacervation," *Macromolecules*, p. DOI: 10.1021/acs.macromol.6b02582, 2017.

[5] L. Li, S. Srivastava, M. Andreev, A. B. Marciel, J. J. de Pablo, and M. V. Tirrell, "Phase behavior and salt partitioning in polyelectrolyte complex coacervates," *Macromolecules*, p. DOI: 10.1021/acs.macromol.8b00238, 2018.

[6] J. Lou, S. Friedowitz, J. Qin, and Y. Xia, "Tunable coacervation of well-defined homologous polyanions and polycations by local polarity," *ACS Cent. Sci.*, vol. 5, pp. 549–557, 2019.

[7] A. Veis and C. Aranyi, "Phase separation in polyelectrolyte systems i. complex coacervates of gelatin," *J. Phys. Chem.*, vol. 64, pp. 1203–1210, 1960.

[8] S. L. Perry, Y. Li, D. Priftis, L. Leon, and M. Tirrell, "The effect of salt on the complex coacervation of vinyl polyelectrolytes," *Polymers*, vol. 6, pp. 1756–1772, 2014.

[9] A. Veis, "Phase separation in polyelectrolyte solutions ii. interaction effects," *J. Phys. Chem.*, vol. 65, pp. 1798–1803, 1961.

[10] B. M. Johnston, C. W. Johnston, R. Letteri, T. K. Lytle, C. E. Sing, T. Emrick, and S. L. Perry, "The effect of comb architecture on complex coacervation," *Org. Biomol. Chem.*, vol. 15, pp. 7630–7642, 2017.

[11] L. Chang, T. K. Lytle, M. Radhakrishna, J. J. Madinya, J. Velez, and C. E. Sing, "Sequence and entropy-based control of complex coacervates," *Nat. Comm.*, vol. 8, p. 1273, 2017.

[12] T. K. Lytle, L. Chang, N. Markiewicz, S. L. Perry, and C. E. Sing, "Designing electrostatic interactions via polyelectrolyte monomer sequence," *ACS Cent. Sci.*, vol. 5, pp. 709–718, 2019.

[13] C. Schmitt and S. L. Turgeon, "Protein/polysaccharide complexes and coacervates in food systems," *Advances in Colloid and Interface Science*, vol. 167, pp. 63–70, 2011.

[14] S. Leclercq, C. Milo, and G. A. Reineccius, "Effects of cross-linking, capsule wall thickness and compound hydrophobicity on aroma release from complex coacervate microcapsules," *Journal of Agricultural and Food Chemistry*, vol. 57, pp. 1426–1432, 2009.

[15] H. M. Shewan and J. R. Stokes, "Review of techniques to manufacture micro-hydrogel particles for the food industry and their applications," *Journal of Food Engineering*, vol. 119, pp. 781–792, 2013.

[16] L. A. Bosnea, T. Moschakis, and C. G. Biliaderis, "Microencapsulated cells of lactobacillus paracasei subsp. paracasei in biopolymer complex coacervates and their function in a yogurt matrix," *Food and Function*, vol. 8, p. 554, 2017.

[17] T. Moschakis and C. G. Biliaderis, "Biopolymer-based coacervates: Structures, functionality, and applications in food products," *Current Opinion in Colloid and Interface Science*, vol. 28, pp. 96–109, 2017.

[18] T. Wasilewski, "Coacervates as a modern delivery system of hand dishwashing liquids," *Journal of Surfactants and Detergents*, vol. 13, pp. 513–520, 2010.

[19] J. Boutique, P. F. A. Delplancke, R. Wagner, M. D. Butts, S. E. Genovese, and S. Scialla, "Liquid laundry detergent comprising a cationic silicone polymer and a coacervate phase forming cationic polymer," Patent 7,439,217.

[20] A. Seweryn, T. Wasilewski, and T. Bujak, "Effect of salt on the manufactureing and properties of hand dishwashing liquids in the coacervate form," *Industrial and Engineering Chemistry Research*, vol. 55, pp. 1134–1141, 2016.

[21] T. H. Kalantar, C. J. Tucker, A. S. Zalusky, T. A. Boomgaard, D. E. Wilson, M. Ladika, S. L. Jordan, W. K. Li, and X. Zhang, "High throughput workflow for coacervate formation and characterization in shampoo systems," *Journal of Cosmetic Science*, vol. 58, pp. 375–383, 2007.

[22] D. V. Krogstad, N. A. Lynd, D. Miyajima, J. D. Gopez, C. J. Hawker, E. J. Kramer, and M. V. Tirrell, "Structural evolution of polyelectrolyte complex core micelles and ordered-phase bulk materials," *Macromolecules*, vol. 47, pp. 8026–8032, 2014.

[23] S. Srivastava, M. Andreev, A. E. Levi, D. J. Goldfield, J. Mao, W. T. Heller, V. M. Prapbu, J. J. de Pablo, and M. V. Tirrell, "Gel phase formation in dilute triblock copolyelectrolyte complexes," *Nat. Comm.*, vol. 8, pp. 1–9, 2017.

[24] C. X. Wang, S. Utech, J. D. Gopez, M. F. Mabesoone, C. J. Hawker, and D. Klinger, "Non-covalent microgel particles containing functional payloads: Coacervation of peg-based triblocks via microfluidics," *ACS Appl. Mater. Interfaces*, vol. 8, pp. 16 914–16 921, 2016.

[25] I. K. Voets, A. de Keizer, and M. A. Cohen Stuart, "Complex coacervate core micelles," *Advances in Colloids and Interface Science*, vol. 147-148, pp. 300–318, 2009.

[26] K. A. Black, D. Priftis, S. L. Perry, J. Yip, W. Y. Byun, and M. V. Tirrell, "Protein encapsulation via polypeptide complex coacervation," *ACS Macro Lett.*, vol. 3, pp. 1088–1091, 2014.

[27] M. Zhao and N. S. Zacharia, "Protein encapsulation via polyelectrolyte complex coacervation: Protection against protein denaturation," *J. Chem. Phys.*, vol. 149, p. 163326, 2018.

[28] J. Wang, A. H. Velders, E. Gianolio, S. Airne, F. J. Vergeldt, H. V. As, Y. Yan, M. Drechsler, A. de Keizer, M. A. Cohen Stuart, and J. van der Gucht, "Controlled mixing of lanthanide(iii) ions in coacervate core micelles," *Chem. Commun.*, vol. 49, pp. 3736–3738, 2013.

[29] Y. Fan, S. Tang, E. L. Thomas, and B. D. Olsen, "Responsive block copolymer photonics triggered by protein-polyelectrolyte coacervation," *ACS Nano*, vol. 8, pp. 11 467–11 473, 2014.

[30] R. J. Stewart, C. S. Wang, and H. Shao, "Complex coacervates as a foundation for synthetic underwater adhesives," *Advances in Colloid and Interface Science*, vol. 167, pp. 85–93, 2011.

[31] X. Meng, S. L. Perry, and J. D. Schiffman, "Complex coacervation:chemically stable fibers electrospun from aqueous polyelectrolyte solutions," *ACS Macro. Lett.*, vol. 6, pp. 505–511, 2017.

[32] J. Wang, A. Groeneveld, M. Oikonomou, A. Prusova, H. V. As, J. W. M. van Lent, and A. H. Velders, "Revealing and tuning the core, structure, properties and function of polymer micelles with lanthanide-coordination complexes," *Soft Matter*, vol. 12, pp. 99–105, 2016.

[33] J. Wang, A. de Keizer, R. Fokkink, Y. Yan, M. A. Cohen Stuart, and J. van der Gucht, "Complex coacervate core micelles from iron-based coordination polymers," *J. Phys. Chem. B.*, vol. 11, pp. 8313–8319, 2010.

[34] Y. Yan, N. A. M. Besseling, A. de Keizer, and M. A. Cohen Stuart, "Characteristic differences in the formation of complex coacervate core micelles from neodymium and zinc-based coordination polymers," *J. Phys. Chem. B*, vol. 111, pp. 5811–5818, 2007.

[35] R. Stewart and H. Shao, "Adhesive complex coacervates and methods of making and using thereof," Patent 9.272,069 B2.

[36] X. Meng, J. D. Schiffman, and S. L. Perry, "Electrospinning cargo-containing polyelectrolyte complex fibers: Correlating molecular interactions to complex coacervate phase behavior and fiber formation," *Macromolecules*, vol. 65, pp. 8821–8832, 2018.

[37] C. W. Pak, M. Kosno, A. S. Holehouse, S. B. Padrick, A. Mittal, R. Ali, A. A. Yuyus, D. R. Liu, R. V. Pappu, and M. K. Rosen, "Sequence determinants of intracellular phase separation by complex coacervation of a disordered protein," *Mol. Cell*, vol. 63, pp. 72–85, 2016.

[38] M. Feric, N. Vaidya, T. S. Harmon, D. M. Mitrea, L. Zhu, T. M. Richardson, R. W. Kriwacki, R. V. Pappu, and C. P. Brangwynne, "Coexisting liquid phases underlie nucleolar subcompartments," *Cell*, vol. 165, pp. 1686–1697, 2016.

[39] R. K. Das and R. V. Pappu, "Conformations of intrinsically disordered proteins are influenced by linear sequence distributions of oppositely charged residues," *Proc. Natl. Acad. Sci. USA*, vol. 110, pp. 13 392–13 397, 2013.

[40] C. J. Oldfield and A. K. Dunker, "Intrinsically disordered proteins and intrinsically disordered proteins regions," *Annu. Rev. Biochem.*, vol. 83, pp. 553–584, 2014.

[41] F. G. Quiroz and A. Chilkoti, "Sequence heuristics to encode phase behaviour in intrinsically disordered protein polymers," *Nat. Mat.*, vol. 14, pp. 1164–1172, 2015.

[42] Y. Lin and H. S. Chan, "Phase separation and single-chain compactness of charged disordered proteins are strongly correlated," *Biophys. J.*, vol. 112, pp. 2043–2046, 2017.

[43] J. Wang, J.-M. Choi, A. S. Holehouse, H. O. Lee, X. Zhang, M. Jahnel, S. Maharana, R. Lemaitre, A. Pozniakovsky, D. Dreschel, I. Poser, R. V. Pappu, S. Alberti, and A. A. Hyman, "A molecular grammar governing the driving forces for phase separation of prion-like rna binding proteins," *Cell*, vol. 174, pp. 688–699, 2018.

[44] K. M. Ruff, S. Roberst, A. Chilkoti, and R. V. Pappu, "Advances in understanding stimulus-responsive phase behavior of intrinsically disordered protein polymers," *J. Mol. Bio.*, vol. 430, pp. 4619–4635, 2018.

[45] S. Das, A. N. Amin, Y. Lin, and H. S. Chan, "Coarse-grained residue-based models of disordered proteins condensates: utility and limiations of simple charge pattern parameters," *Phys. Chem. Chem. Phys.*, vol. 20, p. 28558, 2018.

[46] C. P. Brangwynne, T. J. Mitchison, and A. A. Hyman, "Active liquid-like behavior of nucleoli determines their size and shape in xenopus laevis oocytes," *Proc. Natl. Acad. Sci. USA*, vol. 108, pp. 4334–4339, 2011.

[47] S. Koga, D. S. Williams, A. W. Perriman, and S. Mann, "Peptide-nucleotide microdroplets as a step towards a membrane-free protocell model," *Nat. Chem.*, vol. 3, pp. 720–724, 2011.

[48] A. A. Hyman and K. Simons, "Beyond oil and water - phase transitions in cells," *Science*, vol. 337, pp. 1047–1049, 2012.

[49] A. A. Hyman, C. A. Weber, and F. Julicher, "Liquid-liquid phase separation in biology," *Annu. Rev. of Cell and Dev. Bio.*, vol. 30, pp. 39–58, 2014.

[50] C. P. Brangwynne, P. Tompa, and R. H. Pappu, "Polymer physics of intracellular phase transitions," *Nat. Phys.*, vol. 11, pp. 899–904, 2015.

[51] L. Zhu and C. P. Brangwynne, "Nuclear bodies: the emerging biophysics of nucleoplasmic phases," *Curr. Opin. Cell Biol.*, vol. 34, pp. 23–30, 2015.

[52] S. Elbaum-Garfinkle, Y. Kim, S. Szczepaniak, C. C. Chen, C. R. Eckmann, S. Myong, and C. P. Brangwynne, "The disordered p granule protein laf-1 drives phase separation into droplets with tunable viscosity and dynamics," *Proc. Natl. Acad. Sci. U. S. A.*, vol. 112, pp. 7189–7194, 2015.

[53] T. J. Nott, E. Petsalaki, P. Farber, D. Jervis, E. Fussner, A. Plochowietz, T. D. Craggs, D. P. Bazett-Jones, T. Pawson, J. D. Forman-Kay, and A. J. Baldwin, "Phase transition of a disordered nuage protein generates environmentally responsive membraneless organelles," *Mol. Cell*, vol. 57, pp. 936–947, 2015.

[54] N. Martin, M. Li, and S. Mann, "Selective uptake and refolding of globular proteins in coacervate microdroplets," *Langmuir*, vol. 32, pp. 5881–5889, 2016.

[55] Y. Lin, J. D. Forman-Kay, and H. S. Chan, "Sequene-specific polyampholyte phase separation in membraneless organelles," *Phys. Rev. Lett.*, vol. 117, 178101, 2016.

[56] J. R. Simon, N. J. Carroll, M. Rubinstein, A. Chilkoti, and G. P. López, "Programming molecular self-assembly of intrinsically disordered proteins containing sequences of low complexity," *Nat. Chem.*, vol. 9, pp. 509–538, 2017.

[57] M. Wei, S. Elbaum-Garfinkle, A. S. Holehouse, C. C. Chen, M. Feric, C. B. Arnold, R. D. Priestley, R. V. Pappu, and C. P. Brangwynne, "Phase behaviour of disordered proteins underlying low density and high permeability of liquid organelles," *Nat. Chem.*, vol. 9, pp. 1118–1125, 2017.

[58] S. C. Weber, "Sequence-encoded material properties dictate the structure and function of nuclear bodies," *Curr. Opin. Cell Bio.*, vol. 46, pp. 62–71, 2017.

[59] S. F. Banani, H. O. Lee, A. A. Hyman, and M. K. Rosen, "Biomolecular condensates: organizers of cellular biochemistry," *Nat. Rev. Mol. Cell Biol.*, vol. 18, pp. 285–298, 2017.

[60] E. W. Martin and T. Mittag, "Relationship of sequence and phase separation in protein low-complexity regions," *Biochemistry*, vol. 57, pp. 2478–2487, 2018.

[61] G. L. Dignon, W. Zheng, R. B. Best, Y. C. Kim, and J. Mittal, "Relation between single-molecule properties and phase behavior of intrinsically disordered proteins," *Proc. Natl. Acad. Sci. USA*, vol. 115, pp. 9929–9934, 2018.

[62] J. Berry, C. P. Brangwynne, and M. Haataja, "Physical principles of intracellular organization via active and passive phase transitions," *Rep. Prog. Phys.*, vol. 81, p. 046601, 2018.

[63] S. C. Weber and C. P. Brangwynne, "Getting rna and protein in phase," *Cell*, vol. 149, pp. 1188–1191, 2012.

[64] S. Boeynaems, A. S. Holehous, V. Weinhardt, D. Kovacs, J. Van Lindt, C. Larabell, L. Van Den Boxch, R. Das, P. S. Tompa, R. V. Pappu, and A. D. Gitler, "Spontaneous driving forces give rise to protein-rna condensates with coexisting phases and complex material properties," *Proc. Natl. Acad. Sci. USA*, vol. 116, pp. 7889–7898, 20189.

[65] I. Michaeli, J. T. G. Overbeek, and M. J. Voorn, "Phase separation of polyelectrolye solutions," *Journal of Polymer Science*, vol. 23, pp. 443–450, 1957.

[66] J. T. G. Overbeek and M. J. Voorn, "Phase separation in polyelectrolye solutions. theory of complex coacervation," *Journal of Cellular Physiology*, vol. 49, pp. 7–26, 1957.

[67] S. L. Perry and C. E. Sing, "Prism-based theory of complex coacervation: Excluded volume versus chain correlation," *Macromolecules*, vol. 48, pp. 5040–5053, 2015.

[68] D. J. Audus, J. D. Gopez, D. V. Krogstad, N. A. Lynd, E. J. Kramer, C. J. Hawker, and G. H. Fredrickson, "Phase behavior of electrostatically complexed polyelectrolyte gels using an embedded fluctuation model," *Soft Matter*, vol. 11, p. 1214, 2015.

[69] V. Y. Borue and I. Y. Erukhimovich, "A statistical theory of weakly charged polyelectrolytes: Fluctuations, equations of state, and microphase separation," *Macromolecules*, vol. 21, pp. 3240–3249, 1988.

[70] M. Castelnovo and F. J. Joanny, "Complexation between oppositely charged polyelectrolytes: Beyond the random phase approximation," *The European Physical Journal E*, vol. 6, pp. 377–386, 2001.

[71] K. T. Delaney and G. H. Fredrickson, "Theory of polyelectrolyte complexation-complex coacervates are self-coacervates," *J. Chem. Phys.*, vol. 146, p. 225902, 2017.

[72] A. Kudlay, A. V. Ermoshkin, and M. Olvera de la Cruz, "Complexation of oppositely charged polyelectrolytes: Effect of ion pair formation," *Macromolecules*, vol. 37, pp. 9231–9241, 2004.

[73] A. Kudlay and M. Olvera de la Cruz, "Precipitation of oppositely charged polyelectrolytes in salt solutions," *J. Chem. Phys.*, vol. 120, p. 404, 2004.

[74] R. Kumar, D. Audus, and G. H. Fredrickson, "Phase separation in symmetric mixtures of oppositely charged rodlike polyelectrolytes," *J. Phys. Chem. B*, vol. 114, pp. 9956–9976, 2010.

[75] J. Lee, Y. O. Popov, J. Lee, and G. H. Fredrickson, "Complex coacervation: A field theoretic simulation study of polyelectrolyte complexation," *J. Chem. Phys.*, vol. 128, p. 224908, 2008.

[76] Y. O. Popov, J. Lee, and G. H. Fredrickson, "Field-theoretic simulations of polyelectrolyte complexation," *J. Polym. Sci. B: Polym. Phys.*, vol. 45, pp. 3223–3230, 2007.

[77] I. I. Potemkin and V. V. Palyulin, "Complexation of oppositely charged polyelectrolytes: Effect of discrete charge distribution along the chain," *Phys. Rev. E*, vol. 81, p. 041802, 2010.

[78] J. Qin and J. J. de Pablo, "Criticality and connectivity in macromolecular charge complexation," *Macromolecules*, vol. 49, pp. 8789–8800, 2016.

[79] R. A. Riggleman, R. Kumar, and G. H. Fredrickson, "Investigation of the interfacial tension of complex coacervates using field-theoretic simulations," *J. Chem. Phys.*, vol. 136, p. 024903, 2012.

[80] J. Hansen and I. R. McDonald, *Theory of Simple Liquids*. Boston: Academic Press, 2013.

[81] A. Nakajima and H. Sato, "Phase relationships of an equivalent mixture of sulfated polyvinyl alcohol and aminoacetalyzed polyvinyl alcohol in microsalt aqueous solution," *Biopolymers*, vol. 10, pp. 1345–1355, 1972.

[82] G. H. Fredrickson, *The Equilibrium Theory of Inhomogeneous Polymers*. Boston: Oxford University Press, 2006.

[83] C. B. Bucur, Z. Sui, and J. B. Schlenoff, "Ideal mixing in polyelectrolyte complexes and multilayers: Entropy driven assembly," *J. Am. Chem. Soc.*, vol. 128, pp. 13 690–13 691, 2006.

[84] J. Fu and J. B. Schlenoff, "Driving Forces for Oppositely Charged Polyion Association in Aqueous Solutions: Enthalpic, Entropic, but Not Electrostatic," *J. Am. Chem. Soc.*, vol. 138, pp. 980–990, 2016.

[85] D. Priftis, N. Laugel, and M. Tirrell, "Thermodynamic characterization of polypeptide complex coacervation," *Langmuir*, vol. 28, pp. 15 947–15 957, 2012.

[86] V. Ball, M. Winterhalter, P. Schwinte, P. Lavalle, J.-C. Voegel, and P. Schaaf, "Complexation mechanism of bovine serum albumin and poly(allylamine hydrochloride)," *J. Phys. Chem. B*, vol. 106, pp. 2357–2364, 2002.

[87] F. M. Lounis, J. Chamieh, L. Leclercq, P. Gonzalez, A. Geneste, B. Prelot, and H. Cottet, "Interactions between oppositely charged polyelectrolytes by isothermal titration calorimetry: Effect of ionic strength and charge density," *J. Phys. Chem. B*, vol. 121, pp. 2684–2694, 2017.

[88] G. S. Manning, "Limiting laws and counterion condensation in polyelectrolyte solutions i. colligative properties," *J. Chem. Phys.*, vol. 51, pp. 924–933, 1969.

[89] A. Salehi and R. G. Larson, "A molecular thermodynamic model of complexation in mixtures of oppositely charged polyelectrolytes with explicit account of charge association/dissociation," *Macromolecules*, vol. 49, pp. 9706–9719, 2016.

[90] S. Friedowitz, A. Salehi, R. G. Larson, and J. Qin, "Role of electrostatic correlations in polyelectrolyte charge association," *J. Chem. Phys.*, vol. 149, p. 163335, 2018.

[91] P. Zhang, N. M. Alsaifi, J. Wu, and Z. Wang, "Polyelectrolyte complex coacervation: Effects of concentration asymmetry," *J. Chem. Phys.*, vol. 149, p. 163303, 2018.

[92] P. Zhang, K. Shen, N. M. Alsaifi, and Z. Wang, "Salt partitioning in complex coacervation of symmetric polyelectrolytes," *Macromolecules*, vol. 51, pp. 5586–5593, 2018.

[93] T. K. Lytle and C. E. Sing, "Transfer matrix theory of polymer complex coacervation," *Soft Matter*, vol. 13, pp. 7001–7012, 2017.

[94] M. Radhakrishna and C. E. Sing, "Charge correlations for precise, coulombically driven self assembly," *Macromol. Chem. Phys.*, vol. 217, pp. 126–136, 2016.

[95] A. Salis and B. W. Ninham, "Models and mechanisms of hofmeister effects in electrolyte solutions, and colloid and protein systems revisited," *Chem. Soc. Rev.*, vol. 43, pp. 7358–7377, 2014.

[96] A. Levy, D. Andelman, and H. Orland, "Dielectric constant of ionic solutions: A field-theory approach," *Phys. Rev. Lett.*, vol. 108, p. 227801, 2012.

[97] X. Duan and I. Nakamura, "A new lattice monte carlo simulation for dielectric saturation in ion-containing liquids," *Soft Matter*, vol. 11, pp. 3566–3571, 2015.

[98] Y. Wei, P. Chiang, and S. Sridhar, "Ion size effects on the dynamic and static dielectric properties of aqueous alkali solutions," *J. Chem. Phys.*, vol. 96, pp. 4569–4573, 1992.

[99] I. Nakamura, "Synergistic effects of ion pairs on the dielectric properties of diblock copolymer melts," *Soft Matter*, vol. 10, pp. 9596–9600, 2014.

[100] I. Nakamura, N. P. Balsara, and Z. Wang, "Thermodynamics of ion-containing polymer blends and block copolymers," *Phys. Rev. Lett.*, vol. 107, p. 198301, 2011.

[101] M. Muthukumar, "Theory of counter-ion condensation on flexible polyelectrolytes: Adsorption mechanism," *J. Chem. Phys.*, vol. 120, pp. 9343–9350, 2004.

[102] P. K. Jha, J. W. Zwanikken, and M. Olvera de la Cruz, "Understanding swollen-collapsed and re-entrant transitions in polyelectrolyte nanogels by a modified donnan theory," *Soft Matter*, vol. 8, pp. 9519–9522, 2012.

[103] M. P. Allen and D. J. Tildesley, *Computer Simulation of Liquids*. Oxford: Clarendon Press, 1989.

[104] D. Frenkel and B. Smit, *Understanding Molecular Simulation, 2nd. Ed.: From Algorithms to Applications*. San Diego CA: Academic Press, 2001.

[105] S. K. Kumar, I. Szleifer, and A. Z. Panagiotopoulos, "Determination of the chemical potentials of polymeric systems from monte carlo simulations," *Phys. Rev. Lett.*, vol. 66, pp. 2935–2938, 1991.

[106] Y. J. Sheng, A. Z. Panagiotopoulos, S. K. Kumar, and I. Szleifer, "Monte carlo calculation of phase equilibria for a bead-spring polymeric model," *Macromolecules*, vol. 27, pp. 400–406, 1994.

[107] J. Towns, T. Cockerill, M. Dahan, I. Foster, K. Gaither, A. Grimshaw, V. Hazlewood, S. Lathrop, D. Lifka, G. D. Peterson, R. Roskies, J. R. Scott, and N. Wilkins-Diehr, "Xsede: Accelerating scientific discovery," *Comp. Sci. and Eng.*, vol. 16, pp. 62–74, 2014.

[108] A. Z. Panagiotopoulos, "Direct determination of phase coexistence properties of fluids by monte carlo simulation in a new ensemble," *Mol. Phys.*, vol. 61, pp. 813–826, 1987.

[109] J. Qin, D. Priftis, R. Farina, S. L. Perry, L. Leon, J. Whitmer, K. Hoffmann, M. Tirrell, and J. J. de Pablo, "Interfacial tension of polyelectrolyte complex coacervate phases," *ACS Macro Lett.*, vol. 3, no. 6, pp. 565–568, 2014.

[110] D. A. McQuarrie, *Statistical Mechanics*. Sausalito: University Science Books, 2000.

[111] C. E. Sing, "Development of the modern theory of polymeric complex coacervation," *Advances in Colloid and Interface Science*, vol. 239, pp. 2–16, 2017.

[112] T. K. Lytle, M. Radhakrishna, and C. E. Sing, "High charge-density coacervate assembly via hybrid monte carlo-single chain in mean field theory," *Macromolecules*, vol. 49, pp. 9693–9705, 2016.

[113] A. N. Semenov and M. Rubinstein, "Thermoreversible gelation in solutions of associative polymers. 1. statics," *Macromolecules*, vol. 31, pp. 1373–1385, 1998.

[114] E. E. Dormidontova, "Role of competitive peo-water and water-water hydrogen bonding in aqueous solution peo behavior," *Macromolecules*, vol. 35, pp. 987–1001, 2002.

[115] C. Ren, I. Nakamura, and Z. Wang, "Effects of ion-induced cross-linking on the phase behavior in salt-doped polymer blends," *Macromolecules*, vol. 49, pp. 425–431, 2016.

[116] P. M. Biesheuvel and M. A. Cohen Stuart, "Electrostatic free energy of weakly charged macromolecules in solution and intermacromolecular complexes consisting of oppositely charged polymers," *Langmuir*, vol. 20, pp. 2785–2791, 2004.

[117] R. Zhang and B. I. Shklovskii, "Phase diagram of solution of oppositely charged polyelectrolytes," *Physica A*, vol. 352, pp. 216–238, 2005.

[118] R. S. Dias, P. Linse, and A. A. C. C. Pais, "Stepwise disproportionation in polyelectrolyte complexes," *J. Comp. Chem.*, vol. 32, pp. 2697–2707, 2011.

[119] S. Liu and M. Muthukumar, "Langeving dynamics simulation of counterion distribution around isolated flexible polyelectrolyte chains," *J. Chem. Phys.*, vol. 116, p. 9975, 2002.

[120] Z. Ou and M. Muthukumar, "Entropy and enthalpy of polyelectrolyte complexation: Langevin dynamics simulations," *J. Chem. Phys.*, vol. 124, p. 154902, 2006.

[121] T. K. Lytle and C. E. Sing, "Tuning chain interaction entropy in complex coacervation using polymer stiffness, architecture, and salt valency," *Mol. Syst. Des. Eng.*, vol. 3, pp. 183–196, 2018.

[122] A. Siber, A. L. Bozic, and R. Podgornik, "Energies and pressures in viruses: contribution of nonspecific electrostatic interactions," *Phys. Chem. Chem. Phys.*, vol. 14, pp. 3746–3765, 2012.

[123] C. Forrey and M. Muthukumar, "Langevin dynamics simulations of genome packing in bacteriophage," *Biophys. J.*, vol. 91, pp. 25–41, 2006.

[124] A. J. Spakowitz and Z. Wang, "Dna packaging in bacteriophage: Is twist important," *Biophys. J.*, vol. 88, pp. 3912–3923, 2005.

[125] R. M. Elder and A. Jayaraman, "Coarse-grained simulation studies of effects of polycation architecture on structure of the polycation and polycation-polyanion complexes," *Macromolecules*, vol. 45, pp. 8083–8096, 2012.

[126] R. M. Elder, T. Emrick, and A. Jayaraman, "Understanding the effect of polylysine architecture on dna binding using molecular dynamics simulations," *Biomacromolecules*, vol. 12, pp. 3870–3879, 2011.

[127] H. S. Antila, M. Harkonen, and M. Sammalkorpi, "Chemistry specificity of dna-polycation complex salt response: a simulation study of dna, polylysine and polyethyleneimine," *Phys. Chem. Chem. Phys.*, vol. 17, pp. 5279–5289, 2015.

[128] H. S. Antila and M. Sammalkorpi, "Polyelectrolyte decomplexation via addition of salt: Charge correlation driven zipper," *J. Phys. Chem. B*, vol. 118, pp. 3226–3234, 2014.

[129] M. Kim, H. R. Kim, S. Y. Chae, R. G. Larson, H. Lee, and J. C. Park, "Effect of arginine-rich peptide length on the structure and binding strenght of sirna-peptide complexes," *J. Phys. Chem. B*, vol. 117, pp. 6917–6926, 2013.

[130] R. M. Elder and A. J. Jayaraman, "Molecular simulations of polycation–dna binding exploring the effect of peptide chemistry and sequence in nuclear localization sequence based polycations," *J. Phys. Chem. B*, vol. 117, pp. 11 988–11 999, 2013.

[131] P. Welch and M. Muthukumar, "Dendrimer-polyelectrolyte complexation: A model guest-host system," *Macromolecules*, vol. 33, pp. 6159–6167, 2000.

[132] J. Ruhe, M. Ballauff, M. Biesalski, P. Dziezok, F. Grohn, D. Johannsmann, N. Houbenov, N. Hugenberg, R. Konradi, S. Minko, M. MOtornov, R. R. Netz, M. Schmidt, C. Seidel, M. Stamm, T. Stephan, D. Usov, and H. Zhang, "Polyelectrolyte brushes," *Adv. Polym. Sci.*, vol. 165, pp. 79–150, 2004.

[133] L. C. Bosule and J. A. Schellman, "Compact form of dna induced by spermidine," *Nature*, vol. 259, pp. 333–335, 1976.

[134] B. K. Brettmann, N. Laugel, N. Hoffmann, P. Pincus, and M. V. Tirrell, "Bridging contributions to polyelectrolyte brush collapse in multivalent salt solutions," *J. Polym. Sci. Poly. Chem.*, vol. 54, pp. 284–291, 2016.

[135] B. Brettmann, P. Pincus, and M. V. Tirrell, "Lateral structure formation in polyelectrolyte brushes induced by multivalent ions," *Macromolecules*, vol. 50, pp. 1225–1235, 2017.

[136] C. E. Sing, J. W. Zwanikken, and M. Olvera de la Cruz, "Effect of ion-ion correlations on polyelectrolyte gel collapse and reentrant swelling," *Macromolecules*, vol. 46, pp. 5053–5065, 2013.

[137] D. Yin, F. Horkay, J. F. Douglas, and J. J. de Pablo, "Molecular simulation of the swelling of polyelectrolyte gels by monovalent and divalent counterions," *J. Chem. Phys.*, vol. 129, p. 154902, 2008.

[138] E. Raspaud, M. Olvera de la Cruz, J. L. Sikorav, and F. Livolant, "Precipitation of dna by polyamines: a polyelectrolyte behavior," *Biophys. J.*, vol. 74, pp. 381–393, 1998.

[139] M. Olvera de la Cruz, L. Belloni, M. Delsanti, J. P. Dalbiez, O. Spalla, and M. Drifford, "Precipitation of highly charged polyelectrollyte solutions in the presence of multivalent salts," *J. Chem. Phys.*, vol. 103, pp. 5781–5791, 1995.

[140] J. Zwanikken and M. Olvera de la Cruz, "Tunable soft structure in charged fluids confined by dielectric interfaces," *Proc. Natl. Acad. Sci. USA*, vol. 110, pp. 5301–5308, 2013.

[141] J. F. Lutz, M. Ouchi, D. R. Liu, and M. Sawamoto, "Sequence-controlled polymers," *Science*, vol. 341, p. 1238149, 2013.

[142] J. F. Lutz, J. M. Lehn, E. W. Meijer, and K. Matyjaszewski, "From precision polymers to complex materials and systems," *Nat. Rev. Mater.*, vol. 1, pp. 1–14, 2016.

[143] J. Dudowicz and K. F. Freed, "Relation of effective interaction parameters for binary blends and diblock copolymers: Lattice cluster theory predictions and comparisons with experiment," *Macromolecules*, vol. 26, pp. 213–220, 1993.

[144] P. J. Flory, *Principles of Polymer Chemistry.* Ithaca, NY: Cornell University Press, 1953.

[145] T. Miller, M. C. Goude, T. C. McDevitt, and J. S. Temenoff, "Molecular engineering of glycosaminoglycan chemistry for biomolecule delivery," *Acta Biomaterialia*, vol. 10, pp. 1705–1719, 2014.

[146] Y. Lin and H. S. Chan, "Phase separation and single-chain compactness of charged disordered proteins are strongly correlated," *Biophys. J.*, vol. 112, pp. 2043–2046, 2017.

[147] R. B. Merrifield, "Solid phase pepetide synthesis. i. the synthesis of a tetrapeptide," *J. Am. Chem. Soc.*, vol. 85, pp. 2149–2154, 1963.

[148] J. C. Barnes, D. J. C. Ehrlich, A. X. Gao, F. A. Leibfarth, Y. Jiang, E. Zhou, T. F. Jamison, and J. A. Johnson, "Iterative exponential growth of stereo- and sequence-controlled polymers," *Nat. Chem.*, vol. 7, pp. 810–815, 2015.

[149] S. C. Solleder, D. Zengel, K. S. Wetzel, and M. A. R. Meier, "A scalable and high-yield strategy for the synthesis of sequence-defined macromolecules," *Angewandte Chemie Int. Ed.*, vol. 55, pp. 1204–1207, 2016.

[150] N. Zydziak, F. Feist, B. Huber, J. O. Mueller, and C. Barner-Kowollik, "Photo-induced sequence defined macromolecules via hetero bifunctional synthons," *Chem. Comm.*, vol. 51, pp. 1799–1802, 2015.

[151] M. E. Seitz, C. D. Chan, K. L. Opper, T. W. Baughman, K. B. Wagener, and K. I. Winey, "Nanoscale morphology in precisely sequenced poly(ethylene-co-acrylic acid) zinc ionomers," *J. Am. Chem. Soc.*, vol. 132, pp. 8165–8174, 2010.

[152] L. M. Hall, M. E. Seitz, K. I. Winey, K. L. Opper, K. B. Wagener, M. J. Stevens, and A. L. Frischknecht, "Ionic aggregate structure in ionomer melts: Effect of molecular architecture on aggregates and the ionomer peak," *J. Am. Chem. Soc.*, vol. 134, pp. 574–587, 2012.

[153] S. Mao, Q. J. MacPherson, S. S. He, E. Coletta, and A. J. Spakowitz, "Impact of conformational and chemical correlations on microphase segregation in random copolymers," *Macromolecules*, vol. 49, pp. 4358–4368, 2016.

[154] S. Mao, Q. MacPherson, J. Qin, and A. J. Spakowitz, "Field-theoretic simulations of random copolymers with structural rigidity," *Soft Matter*, p. DOI: 10.1039/C7SM00164A, 2017.

[155] V. Meenakshisundaram, J.-H. Hung, T. K. Patra, and D. S. Simmons, "Designing sequence-specific copolymer compatibilizers using a molecular-dynamics-simulation-based genetic algorithm," *Macromolecules*, vol. 50, pp. 1155–1166, 2017.

[156] W. G. Levine, Y. Seo, J. R. Brown, and L. M. Hall, "Effect of sequence dispersity on morphology of tapered diblock copolymers from molecular dynamics simulations," *J. Chem. Phys.*, vol. 145, p. 234907, 2016.

[157] S. L. Perry, L. Leon, K. Q. Hoffmann, M. J. Kade, D. Priftis, K. A. Black, D. Wong, R. A. Klein, C. F. Pierce III, K. O. Margossian, J. K. Whitmer, J. Qin, J. J. de Pablo, and M. Tirrell, "Chirality-selected phase behaviour in ionic polypeptide complexes," *Nat. Commun.*, vol. 6, p. 6052, 2015.

[158] K. Q. Hoffmann, S. L. Perry, L. Leon, D. Priftis, M. Tirrell, and J. J. de Pablo, "A molecular view of the role of chirality in charge-driven polypeptide complexation," *Soft Matter*, vol. 11, pp. 1525–1538, 2015.

[159] N. M. Pacalin, L. Leon, and M. V. Tirrell, "Directing the phase behavior of polyelectrolyte complexes using chiral patterned peptides," *Eur. Phys. J. Special Topics*, vol. 225, pp. 1805–1815, 2016.

[160] F. S. Bates, M. A. Hillmyer, T. P. Lodge, C. M. Bates, K. T. Delaney, and G. H. Fredrickson, "Multiblock polymers: Panacea or pandora's box," *Science*, vol. 336, pp. 434–440, 2012.

[161] R. Wuttke, H. Hofmann, D. Nettels, M. B. Borgia, J. Mittal, R. B. Best, and B. Schuler, "Temperature-dependent solvation modulates the dimensions of disordered proteins," *Proc. Natl. Acad. Sci. USA*, vol. 111, pp. 5213–5218, 2014.

[162] P. E. Brumby, A. J. Haslam, E. de Miguel, and G. Jackson, "Subtelties in the calculation of the pressure and pressure tensor of anisotropic particles from volume-perturbation methods and the apparent asymmetry of the compressive and expansive contributions," *Mol. Phys.*, vol. 109, pp. 169–189, 2011.

[163] K. G. Honnell, C. K. Hall, and R. Dickman, "On the pressure equation for chain molecules," *J. Chem. Phys.*, vol. 87, p. 664, 1987.

[164] G. Orkoulas, I. Szleifer, and A. Z. Panagiotopoulos, "Free energy and phase equilibria for the restricted primitive model of ionic fluids from monte carlo simulations," *J. Chem. Phys.*, vol. 101, p. 1452, 1994.

[165] T. K. Lytle, A. J. Salazar, and C. E. Sing, "Interfacial properties of polymeric complex coacervates from simulation and theory," *J. Chem. Phys.*, vol. 149, p. 163315, 2018.

[166] M. Andreev, V. M. Prabhu, J. F. Douglas, M. V. Tirrell, and J. J. de Pablo, "Complex coacervation in polyelectrolytes from a coarse-grained model," *Macromolecules*, vol. 51, pp. 6717–6723, 2018.

[167] P. Debye and E. Huckel, "Theory of electrolytes," *Phys. Z.*, vol. 24, p. 185, 1923.

[168] K. R. Shull, "Mean-field theory of block copolymers: Bulk melts, surfaces, and thin films," *Macromolecules*, vol. 25, pp. 2122–2133, 1992.

[169] K. R. Shull and E. J. Kramer, "Mean-field theory of polymer interfaces in the presence of block copolymers," *Macromolecules*, vol. 23, pp. 4769–4779, 1990.

[170] K. R. Shull, "Theory of end-adsorbed polymer brushes in polymeric matrices," *J. Chem. Phys.*, vol. 94, pp. 5723–5738, 1991.

[171] S. Plimpton, "Fast parallel algorithms for short-range molecular dynamics," *J. Comp. Phys.*, vol. 117, pp. 1–19, 1995.

[172] J. W. Cahn and J. E. Hilliard, "Free energy of a nonuniform system. i. interfacial free energy," *J. Chem. Phys.*, vol. 28, pp. 258–267, 1958.

[173] C. Huang, M. Olvera de la Cruz, and B. W. Swift, "Phase separation of ternary mixtures: symmetric polymer blends," *Macromolecules*, vol. 28, pp. 7996–8005, 1995.

[174] C. Huang and M. Olvera de la Cruz, "Adsorption of a minority component in polymer blend interfaces," *Phys. Rev. E*, vol. 53, pp. 812–819, 1996.

[175] H. Tang and K. F. Freed, "Interfacial studies of incompressible binary blends," *J. Chem. Phys.*, vol. 94, pp. 6307–6322, 1991.

[176] C. E. Sing, J. W. Zwanikken, and M. Olvera de la Cruz, "Theory of melt polyelectrolyte blends and block copolymers: Phase behavior, surface tension, and microphase periodicity," *J. Chem. Phys.*, vol. 142, p. 034902, 2015.

[177] D. Priftis, R. Farina, and M. Tirrell, "Interfacial energy of polypeptide complex coacervates measured via capillary adhesion," *Langmuir*, vol. 28, pp. 8721–8729, 2012.

[178] E. Spruijt, J. Sprakel, M. A. Cohen Stuart, and J. van der Gucht, "Interfacial tension between a complex coacervate phase and its coexisting aqueous phase," *Soft Matter*, vol. 6, pp. 172–178, 2010.

[179] S. Lim, D. Moon, H. J. Kim, S. H. Seo, I. S. Kang, and H. J. Cha, "Interfacial tension of complex coacervated mussel adhesive protein according to the hofmeister series," *Langmuir*, vol. 30, pp. 1108–1115, 2014.

[180] M. W. Matsen and F. S. Bates, "Unifying weak- and strong-segregation block copolymer theories," *Macromolecules*, vol. 29, pp. 1091–1098, 1996.

[181] E. Helfand and Y. Tagami, "Theory of the interface between immiscible polymers," *J. Poly. Sci. Part C: Poly. Lett.*, vol. 9, pp. 741–746, 1971.

[182] E. Helfand and Y. Tagami, "Theory of the interface between immiscible polymers. ii," *J. Chem. Phys.*, vol. 56, pp. 3592–3601, 1972.

[183] L. Leibler, H. Orland, and J. C. Wheeler, "Theory of critical micelle concentration for solutions of block copolymers," *J. Chem. Phys.*, vol. 79, pp. 3550–3557, 1983.

[184] A. Halperin, "Polymeric micelles: A star model," *Macromolecules*, vol. 20, pp. 2943–2946, 1987.

[185] M. W. Matsen and F. S. Bates, "Origins of complex self-assembly in block copolymers," *Macromolecules*, vol. 29, pp. 7641–7644, 1996.

[186] C. E. Sing and M. Olvera de la Cruz, "Polyelectrolyte blends and nontrivial behavior in effective flory-huggins parameters," *ACS Macro Lett.*, vol. 3, pp. 698–702, 2014.

[187] R. J. Ellis, "Macromolecular crowding: an important but neglected aspect of the intracellular environment," *Curr. Opin. Struct. Biol.*, vol. 11, pp. 114–119, 2001.

[188] A. M. Marianelli, B. M. Miller, and C. D. Keating, "Impact of macromolecular crowding on rna/spermine complex coacervation and oligonucleotide compartmentalization," *Soft Matter*, vol. 14, pp. 368–378, 2018.

[189] P. Schaaf and J. B. Schlenoff, "Saloplastics: Processing compact polyelectrolyte complexes," *Adv. Mater.*, vol. 27, pp. 2420–2432, 2015.

[190] V. Y. Borue and I. Y. Erukhimovich, "A statistical theory of globular polyelectrolyte complexes," *Macromolecules*, vol. 23, pp. 3625–3632, 1990.

[191] M. A. Cohen Stuart, N. A. M. Besseling, and R. G. Fokkink, "Formation of Micelles with Complex Coacervate Cores," *Langmuir*, vol. 14, no. 24, pp. 6846–6849, 1998. [Online]. Available: http://dx.doi.org/10.1021/la980778m

[192] A. Harada and K. Kataoka, "Formation of Polyion Complex Micelles in an Aqueous Milieu from a Pair of Oppositely-Charged Block Copolymers with Poly(ethylene glycol) Segments," *Macromolecules*, vol. 28, no. 15, pp. 5294–5299, 1995. [Online]. Available: http://pubs.acs.org/doi/abs/10.1021/ma00119a019

[193] A. Harada and K. Kataoka, "Chain Length Recognition: Core-Shell Supramolecular Assembly from Oppositely Charged Block Copolymers," *Science*, vol. 283, no. 5398, pp. 65–67, 1999.

[194] "Tunable, high modulus hydrogels driven by ionic coacervation," *Adv. Mat.*, vol. 23, pp. 2327–2331, 2011.

[195] D. V. Krogstad, N. A. Lynd, S. Choi, J. M. Spruell, C. J. Hawker, E. J. Kramer, and M. V. Tirrell, "Effects of Polymer and Salt Concentration on the Structure and Properties of Triblock Copolymer Coacervate Hydrogels.pdf," *Macromolecules*, vol. 46, pp. 1512–1518, 2013.

[196] J. H. Ortony, S. Choi, J. M. Spruell, J. N. Hunt, N. A. Lynd, D. V. Krogstad, V. S. Urban, C. J. Hawker, E. J. Kramer, and S. Han, "Fluidity and water in nanoscale domains define coacervate hydrogels," *Chem. Sci.*, vol. 5, no. 1, pp. 58–67, 2013. [Online]. Available: http://xlink.rsc.org/?DOI=c3sc52368c\npapers3://publication/doi/10.1039/c3sc52368c

[197] D. V. Pergushov, A. H. E. Müller, and F. H. Schacher, "Micellar Interpolyelectrolyte Complexes," *Chem. Soc. Rev.*, vol. 41, no. 21, p. 6888, 2012.

[198] H. M. Van Der Kooij, E. Spruijt, I. K. Voets, R. Fokkink, M. A. Cohen Stuart, and J. Van Der Gucht, "On the stability and morphology of complex coacervate core micelles: From spherical to wormlike micelles," *Langmuir*, vol. 28, no. 40, pp. 14 180–14 191, 2012.

[199] A. C. Obermeyer, C. E. Mills, X. H. Dong, R. J. Flores, and B. D. Olsen, "Complex coacervation of supercharged proteins with polyelectrolytes," *Soft Matter*, p. DOI: 10.1039/C6SM00002A, 2016.

[200] D. V. Krogstad, S. Choi, N. A. Lynd, D. J. Audus., S. L. Perry, J. D. Gopez, C. J. Hawker, E. J. Kramer, and M. V. Tirrell, "Small angle neutron scattering study of complex coacervate micelles and hydrogels formed from ionic diblock and triblock copolymers," *J. Phys. Chem. B*, vol. 118, pp. 13 011–13 018, 2014.

[201] F. A. Detcheverry, H. Kang, K. C. Daoulas, M. Müller, P. F. Nealey, and J. J. de Pablo, "Monte carlo simulations of a coarse grain model for block copolymers and nanocomposites," *Macromolecules*, vol. 41, pp. 4989–5001, 2008.

[202] D. Q. Pike, F. A. Detcheverry, M. Müller, and J. J. de Pablo, "Theoretically informed coarse grain simulations of polymeric systems," *J. Chem. Phys.*, vol. 131, p. 084903, 2009.

[203] K. C. Daoulas and M. Müllers, "Single chain in mean field simulations: Quasi-instantaneous field approximation and quantitative comparison with Monte Carlo simulations," *J. Chem. Phys.*, vol. 125, no. 18, p. 184904, 2006. [Online]. Available: http://scitation.aip.org/content/aip/journal/jcp/125/18/10.1063/1.2364506

[204] F. A. Detcheverry, D. Q. Pike, P. F. Nealey, M. Müller, and J. J. de Pablo, "Monte Carlo Simulation of Coarse Grain Polymeric Systems," *Phys. Rev. Lett.*, vol. 102, no. 19, p. 197801, 2009. [Online]. Available: http://link.aps.org/doi/10.1103/PhysRevLett.102.197801

[205] K. C. Doulas, M. Müller, J. J. de Pablo, P. F. Nealey, and G. D. Smith, "Morphology of multi-component polymer systems: single chain in mean field simulation studies," *Soft Matter*, vol. 2, pp. 573–583, 2006.

[206] P. G. De Gennes, *Scaling Concepts in Polymer Physics*. Ithaca: Cornell University Press, 1979.

[207] R. A. Riggleman and G. H. Fredrickson, "Field-theoretic simulations in the gibbs ensemble," *J. Chem. Phys.*, vol. 132, p. 023103, 2010.

[208] M. Radhakrishna and C. E. Sing, "Charge Correlations for Precise, Coulombically Driven Self Assembly," *Macromolecular Chemistry and Physics*, vol. 217, pp. 126–136, 2016. [Online]. Available: http://doi.wiley.com/10.1002/macp.201500278

[209] J. R. Brown, Y. Seo, S. W. Sides, and L. M. Hall, "Unique phase behavior of inverse tapered block copolymers: Self-consistent field theory and molecular dynamics simulations," *Macromolecules*, vol. 50, pp. 5619–5626, 2017.

[210] Y. Seo, J. R. Brown, and L. M. Hall, "Effect of tapering on morphology and interfacial behavior of diblock copolymers from molecular dynamics simulations," *Macromolecules*, vol. 48, pp. 4974–4982, 2015.

[211] M. Luo, J. R. Brown, R. A. Remy, D. M. Scott, M. E. Mackay, L. M. Hall, and T. H. Epps III, "Determination of interfacial mixing in tapered block polymer thin films: Experimental and theoretical investigations," *Macromolecules*, vol. 49, pp. 5213–5222, 2016.